Cooperative Spin Excitations in Quantum Materials Studied by Neutron Spectroscopy

Stephen M. Gaw

A thesis submitted for the degree of
Doctor of Philosophy

Balliol College, University of Oxford
Hilary Term, 2014

Cooperative Spin Excitations in Quantum Materials Studied by Neutron Spectroscopy

Stephen M. Gaw
Balliol College, University of Oxford
Hilary Term, 2014

Thesis submitted for the degree of Doctor of Philosophy

This thesis describes the experimental investigation of three different strongly correlated transition-metal oxide systems. The magnetic behaviour of each has been probed using inelastic neutron spectroscopy.

A distinctive hour-glass excitation spectrum has been observed in the layered cobaltate $La_{1.75}Sr_{0.25}CoO_4$. This spectrum is similar to that measured in a related cobaltate $La_{1.67}Sr_{0.33}CoO_4$, although it appears broader. The spectrum has been reproduced using a spin wave model derived from a disordered cluster spin glass ground state. Signatures of spin glass behaviour have also been observed in bulk magnetisation measurements of $La_{1.75}Sr_{0.25}CoO_4$. These findings, once more, demonstrate the emergence of an hour-glass spectrum from a ground state that combines quasi-one dimensional magnetic correlations and disorder. Additionally, this study shows that charge and magnetic stripe order persists to lower dopings in $La_{2-x}Sr_xCoO_4$ than previously thought.

The complete magnetic excitation spectrum of the multiferroic compound CuO has been measured for the first time. A high energy, one-dimensional magnetic spectrum is observed and modelled using the Müller ansatz derived for the $S = 1/2$ Heisenberg antiferromagnetic chain. At lower energies, a three-dimension spectrum is observed. The measured spectrum is inconsistent with all previous theoretical estimates of the dominant inter-chain exchange interactions in CuO. The inter-chain dispersion is successfully described by a phenomenological model based on linear spin wave theory.

The third material investigated, $LuFe_2O_4$ demonstrates complex charge and magnetic order, the precise nature of which is still under debate. The full spectrum of in-plane excitations in $LuFe_2O_4$ has been measured and a complicated dispersion consistent with six magnetic modes is observed. These findings are compatible with structures described by a magnetic unit cell containing six spins. The dispersion can be described by a spin wave model derived from a bilayer structure comprised of charge-rich and charge-poor monolayers. This structure is consistent with the original site-specific model for the 3D magnetic ordering in $LuFe_2O_4$.

Acknowledgements

I have so many people to thank for helping me to produce this thesis and making my time in Oxford a delight. First and foremost, my supervisor Andrew Boothroyd has been a constant source of support and enthusiasm. His seemingly-endless knowledge has never failed to amaze me and without his incredible efforts this thesis would be lying in a gutter, incomplete and awash with hanging participles.

My thanks must also go to those that have help me with experiments. Particularly, Prabhakaran, who has created so many excellent samples in the course of my studies, and has always been happy to explain how he does it. Also, the mind-bogglingly productive Russell Ewings for helping with pretty much everything; and Toby Perring, for his great insights into neutron scattering and my data analysis. Additionally, I must thank the other instrument scientist with whom I have had the pleasure of working, including Chris Frost, Jiří Kulda, Devashibhai Adroja, and Elisa Wheeler. They have never failed to help this DPhil student in his hour(s) of need.

During my frequent battles with neutron data, Radu Coldea has usually provided both a practical solution and a physical understanding. I am incredibly grateful for the time he has afforded me and for his patience when I wanted to know more. Roger Johnson has almost been able to explain symmetry to me – which is no mean feat – in addition to instigating many crucial trips to the pub alongside Paul Goddard. Ivelisse Cabrera continues to inspire me with her knowledge of inelastic neutron scattering and her incredible positivity. I must also thank Steve Blundell, for his enthusiasm for science and its history, and his constant willingness to share that enthusiasm with others.

My time in the Clarendon would not have been the same without the volume of Alice Taylor; the grumpiness of Graeme Johnstone; or the Babbers – Peter Babkevich. Additionally, I would like to thank Andrew Steele, Jack Wright, Ben Heathcote Williams (CMP), Bill Hayes, Danielle Kaminskii, Liam 'Mmmm' Gannon, Natasha Perks, Jordan Thompson, Sam Blake and Marein Rahn who have all made tea times special.

Finally, I would like to thank my parents, Moira and Allan; my sister, Alex; and SJ, who have all inadvertently learned about magnets with me.

For my parents

Contents

Chapter 1

Magnetic Order and Excitations in Quantum Materials

Contents

1.1 Introduction

Many complex phenomena in physics emerge from the collective behaviour of relatively simple building blocks. An example of this is the vast array of magnetic behaviour observed in different condensed matter systems. The origins of an atom's magnetic moment is well understood using quantum mechanics. However,

a plethora of magnetic orders and effects are found when moments are grouped together in crystal structures and there exist strong interactions between the electrons (ie. the electrons are strongly correlated). Subtle effects become significant in these many-body systems and a lot of the emergent behaviours are still not understood. In this chapter, I will introduce some of the key physical concepts relevant to the study of magnetic systems, upon which this thesis is based. I shall introduce the Heisenberg Hamiltonian as a description of magnetic interactions and discuss how it can be used to model the magnetic excitation spectra measured in later chapters. Finally, I shall introduce some broad classes of materials which my research aims to better understand.

1.2 Magnetism and Magnetic Order

1.2.1 Magnetic Ions

The magnetism of an atom or ion arises, primarily, from the properties of the electrons [1]. Electrons within an atom have both an intrinsic spin angular momentum $\boldsymbol{s}$ (with magnitude $\hbar/2$) in addition to an orbital angular momentum $\boldsymbol{l}$. Electrons occupy shells, and summing the electrons' individual momenta in the outer most shell determine the spin $\boldsymbol{S}$ and orbital $\boldsymbol{L}$ quantum numbers of the atom. Due to the Pauli exclusion principle, only two electrons with opposite spin can occupy the same orbital. Hence, in atoms with fully occupied electron shells, the different electronic contributions of the angular momenta cancel. This is not the case in an atom with unfilled electron shells, however, which can carry a magnetic moment $\boldsymbol{\mu}$.

The moment is associated with the total angular momentum $\boldsymbol{J}$, which is related to the individual spin and orbital contributions by the expression

$$\boldsymbol{J} = \boldsymbol{S} + \boldsymbol{L}. \tag{1.1}$$

The effective magnetic moment for an isolated atom is therefore defined as

$$\mu_{\text{eff}} = g_J \mu_{\text{B}} \sqrt{J(J+1)}, \tag{1.2}$$

where μ_{B} is the Bohr magneton and

$$g_J = \frac{3}{2} + \frac{S(S+1) - L(L+1)}{2J(J+1)}. \tag{1.3}$$

This is the Landé g-factor.

In an isolated atom, the arrangement of the electrons giving rise to the effective moment is predicted by Hund's rules [1]. These are a set of empirical rules that emerge from a minimisation of the Coulomb repulsion in an atom. They state that the electronic configuration must first maximise $\boldsymbol{S}$, then maximise $\boldsymbol{L}$. The value of $\boldsymbol{J}$ is then found to be $J = |L - S|$ for shells less than half full or $J = |L + S|$ for shells with greater than half occupancy. When a shell is half occupied $L = 0$ and the orbital angular momentum is quenched. Therefore, the total angular momentum is only dependant on $\boldsymbol{S}$ and the magnetic moment has the form

$$\mu_{\text{eff}} = g_S \mu_{\text{B}} \sqrt{S(S+1)}, \tag{1.4}$$

where $g_S = 2$ for a spin-only system. Orbital quenching is common in the 3d transition metal ions where the outer d shell is nearly half-filled. Therefore, a spin-only description is typically sufficient to describe the magnetism in certain materials. For those cases, the effects of a small spin orbit coupling can be accommodated by scaling the value of g_S. Although Hund's rules are derived for isolated atoms, they are often a good first approximation of the electronic configuration of atoms in a material. However, the additional effect of the material's crystal field must be considered to find the true ground state configuration.

1.2.2 Diamagnetism and Paramagnetism

In bulk materials, a weak magnetisation can be induced by an externally applied magnetic field. This is the diamagnetic moment and opposes the applied field [1]. Therefore, materials with a predominately diamagnetic response are characterised by a negative magnetic susceptibility χ, where

$$\boldsymbol{M} = \chi \boldsymbol{H}. \tag{1.5}$$

In this expression, $\boldsymbol{M}$ is the magnetisation of the material and $\boldsymbol{H}$ is the applied magnetic field. Diamagnetism is a weak effect and is not significant for the materials investigated in this thesis. Paramagnetism is characterised by a positive susceptibility [1]. This corresponds to an induced magnetisation parallel to the applied field. Such a response is due to the individual magnetic moments of the atoms aligning with the field. Therefore, in the absence of a field the moments are randomly orientated in a paramagnetic state.

1.2.3 Magnetic Exchange Interactions

Interactions between neighbouring magnetic moments open up the possibility of correlated behaviour beyond simple paramagnetism. Such behaviour results in the magnetic ordering seen in many materials. The magnetic dipole interaction is the most obvious candidate to describe magnetic interactions but its effect is actually very weak. Instead, exchange interactions dominate within magnetic materials and can be understood by considering a simple system of two electrons in the absence of spin-orbit coupling [1]. The electrons (as fermions) are described by an overall antisymmetric wave function. Therefore, when two electrons, a and b, are at the positions $\boldsymbol{r}_1$ and $\boldsymbol{r}_2$, their total wavefunction can be written as

$$\Psi_{\mathrm{S}} = \frac{1}{\sqrt{2}}[\psi_a(\boldsymbol{r}_1)\psi_b(\boldsymbol{r}_2) + \psi_a(\boldsymbol{r}_2)\psi_b(\boldsymbol{r}_1)]\chi_{\mathrm{S}}, \tag{1.6}$$

or

$$\Psi_{\mathrm{T}} = \frac{1}{\sqrt{2}}[\psi_a(\boldsymbol{r}_1)\psi_b(\boldsymbol{r}_2) - \psi_a(\boldsymbol{r}_2)\psi_b(\boldsymbol{r}_1)]\chi_{\mathrm{T}}. \tag{1.7}$$

These expressions contain a spin wavefunction in either the singlet χ_{S} or triplet χ_{T} state. To ensure Ψ is antisymmetric, the combined form of the spatial wavefunctions $\psi_a(\boldsymbol{r}_1)$ and $\psi_b(\boldsymbol{r}_2)$ have the symmetric or antisymmetric form. From Eqs. 1.6 and 1.7, the difference in energy between the singlet and triplet wavefunctions is found to be

$$J = E_{\mathrm{S}} - E_{\mathrm{T}} = 2\int \psi_a^*(\boldsymbol{r}_1)\psi_b^*(\boldsymbol{r}_2)\mathcal{H}\psi_a(\boldsymbol{r}_2)\psi_b(\boldsymbol{r}_1)d\boldsymbol{r}_1\boldsymbol{r}_2. \tag{1.8}$$

This expression defines the exchange constant J. The energy difference between singlet and triplet state can also be similarly quantified using an effective spin Hamiltonian containing the expression $\boldsymbol{S}_a \cdot \boldsymbol{S}_b$. This has the form

$$\mathcal{H} = \frac{1}{4}(E_{\mathrm{S}} + 3E_{\mathrm{T}}) - (E_{\mathrm{S}} - E_{\mathrm{T}})\boldsymbol{S}_a \cdot \boldsymbol{S}_b. \tag{1.9}$$

Therefore, omitting the constant term, $\mathcal{H}$ can be expressed as an effective spin Hamiltonian

$$\mathcal{H} = -J\boldsymbol{S}_a \cdot \boldsymbol{S}_b. \tag{1.10}$$

Considering Eq. 1.10, the triplet state is favoured when $J > 0$ and therefore the spins are aligned parallel. Conversely, $J < 0$ energetically favours the singlet state and spins are aligned antiparallel.

This concept has been generalised to describe a system of many spins in the Heisenberg Hamiltonian

$$\mathcal{H} = \sum_{\langle i,j \rangle} J_{ij}\boldsymbol{S}_i \cdot \boldsymbol{S}_j, \tag{1.11}$$

where $\boldsymbol{S}_i$ is the spin operator for the i^{th} spin in the system, and J_{ij} describes the exchange interaction between the spins i and j (and has been redefined such that $J > 0$ favours antiparallel spins). The notation $\langle i, j \rangle$ denotes that the summation is over all pairs of spins, with each pair counted once.

Although Eq. 1.11 is expressed in relatively simple terms, this belies the vast array of magnetic behaviour that the Heisenberg Hamiltonian can describe. It can only be solved exactly for the most simple cases. However, approximate solutions provide excellent descriptions for many magnetic phenomena observed. Nearest neighbour exchange interactions are all that is required to understand the ferromagnetic (FM) or antiferromagnetic (AFM) ordering arising in many physical systems. The value of the exchange parameters J_{ij} depend nominally on the overlap of atomic orbitals which facilitates the exchange process. However, this simple picture is complicated by the various types of exchange interaction. These include direct exchange and superexchange which will be described below.

Direct Exchange

Direct exchange arises when electrons on neighbouring magnetic atoms interact directly via some overlapping orbital. In reality, this is typically a very weak interaction, as the overlap is usually very small even for the large 3d orbitals in the transition metal ions studied in this thesis. Therefore, most exchange is indirect, conducted through some intermediary.

Superexchange

Superexchange is an indirect exchange process whereby magnetic atoms interact via a non-magnetic intermediary [1]. This process can be used to explain the majority of magnetic orders seen in the transition metal oxides, where exchange is via the non-magnetic oxygen atom. An example of AFM ordering arising from superexchange is shown in Figure 1.1. The outer electron orbitals involved in the M–O–M bond (where M is a 3d transition metal ion and O is oxygen with a 2p bonding orbital) is depicted in Figure 1.1. The system can minimise the kinetic energy of all the electrons by allowing them to spread across all orbitals. However, to satisfy the Pauli exclusion principle, the spins on the M ions must align antiparallel. Therefore,

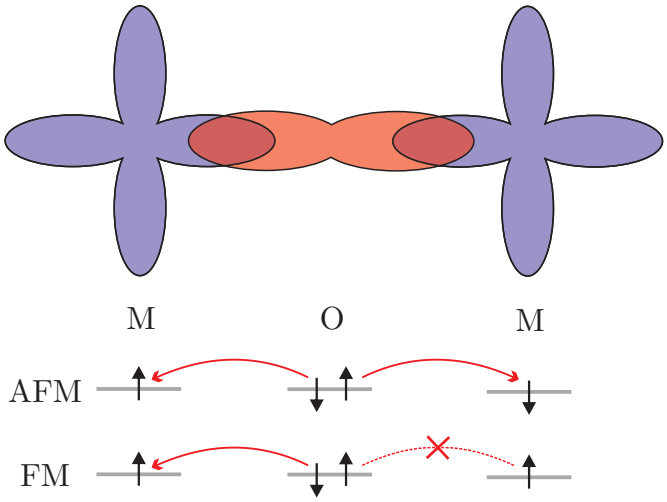

Figure 1.1: Schematic diagram of the atomic orbitals involved in AFM ordering via superexchange. Two $d_{x^2-y^2}$ orbitals – typically involved in the bonding of 3d transitional metals (M) – are shown. They overlap with the 2p bonding orbital of an oxygen atom (O). Possible spin configurations of the electrons involved in the M-O-M bond are shown below the orbitals. An AFM arrangement of electrons in the M orbitals allows the O electrons to hop to either M orbital and is, thus, energetically favourable. In contrast, a FM ordering of the M spins only allows a single O electron to hop. The second hopping process is forbidden by the Pauli exclusion principle.

superexchange typically gives rise to AFM order, although there are situations where it can favour ferromagnetism.

The Goodenough-Kanamori-Anderson (GKA) rules provide a phenomenological model to predict the strength and sign of the superexchange interaction J based on the details of the orbital overlap and bonding angle. Full details of the GKA rules can be found elsewhere [2, 3] but at the simplest level there exist two basic cases:

(i) Strong AFM exchange is favoured by an M–O–M system when there is reasonably large overlap between all orbitals and the two metal ions are separated by a bond angle of 180°.

(ii) Weak FM exchange is favoured when the M–O–M bond angle approaches 90° and there is little orbital overlap.

There exist many materials with bond angles lying between the extremes of 90° and

180°. For these cases, the GKA rules provide a indication to the most likely strength and sign of the superexchange interaction, depending on the relative proximity of a material's bonding to either extreme scenario.

1.2.4 Higher Order Exchange

Superexchange is formally a second-order process as it involves an intermediate atom. Therefore, it is treated using second-order perturbation theory. Higher order terms also exist, such as the fourth-order biquadratic exchange with the form $\mathcal{K}(\boldsymbol{S}_i \cdot \boldsymbol{S}_j)^2$. This and other higher-order terms are much weaker than the second-order superexchange interaction. Therefore, they do not play as significant a role in most magnetic materials, although they can be important in frustrated systems, when Heisenberg coupling terms cancel.

1.2.5 Anisotropy and Magnetic Ordering

The superexchange interaction is able to explain the orientation of spins with respect to each other, in many magnetic materials. However, the isotropic form of the Heisenberg Hamiltonian in Eq. 1.11, does not differentiate the possible directions of collinear spins with respect to the crystal structure. Instead, the easy spin direction is determined by the spin-orbit coupling and the crystal field from the surrounding atoms which determines the energies and degeneracies of the electronic orbitals. These give rise to anisotropic effects in all real materials.

When there is little or no spin-orbit coupling and a system is described with a spin-only model, anisotropies can be introduced through a single or two ion process. A single ion anisotropy describes an energetically favoured direction for each individual spin in the system. This can be included in the Hamiltonian using terms such as $-\mathcal{D}(S_i^z)^2$, where S_i^z is the component of the i^{th} spin parallel to the easy axis. Two-ion anisotropy terms depend on the details of the bonding within a material, which may favour stronger exchange between one spin component over the others.

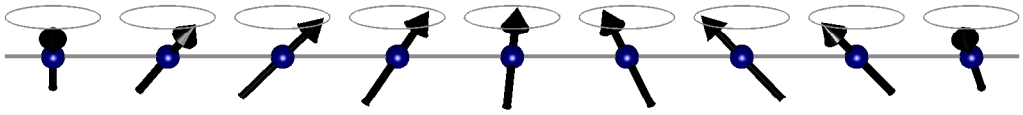

Figure 1.2: Representation of a propagating spin wave in a FM chain. Spins precess around their easy axis. Neighbouring spins are correlated due to the exchange interactions. Hence, the precession propagates as a wave along the FM chain.

In this case, an anisotropic form of the Heisenberg Hamiltonian must be used to replicate the behaviour. The scalar exchange interaction J_{ij} becomes a vector quantity $\boldsymbol{J}_{ij} = (J_{ij}^x, J_{ij}^y, J_{ij}^z)$ and so energetically favours the alignment of spins parallel to a specific direction.

1.3 Magnetic Excitations

In any ordered system, thermal fluctuations allow for excitations away from the ground state [1]. In the case of a magnetically ordered material, such excitations are most commonly spin waves. A spin wave is a correlated fluctuation of the magnetisation away from its average. It is quantised by the magnon and described by a dispersion relation, analogous to lattice excitations quantised by phonons. Figure 1.2 provides a visual representation of a spin wave propagating in a FM chain.

1.3.1 Linear Spin Wave Theory

The dispersion of a magnon in a particular system depends on the interactions between spins in that system. Therefore, the spin wave dispersion can be approximately calculated using an appropriate expression of the system's Hamiltonian. Linear spin wave theory outlines the process of diagonalising the Hamiltonian to

find the energy eigenvectors describing the dispersion. Below, I shall introduce this theory using the example of isotropic exchange in an antiferromagnet on a square lattice [2].

Figure 1.3(a) shows the ground state AFM order. The system is described by the magnetic unit cell (shaded in grey) and only the nearest neighbour exchange interaction J is considered. This system can be adequately described by the Heisenberg Hamiltonian introduced in Eq. 1.11. The AFM order can be considered to comprise two inter-penetrating sublattices A and B, with opposite FM ordering. Fluctuations of the spins can be easily introduced by expressing the spin operators $\boldsymbol{S} = (S^x, S^y, S^z)$ in terms of raising and lowering operators $S^{\pm} = S^x \pm iS^y$. In this definition, z is parallel to the spin easy direction, while x and y are perpendicular to z and form a set of Cartesian coordinates. The raising (lowering) operators have the effect of increasing (decreasing) the z component of spin by one.

A Holstein-Primakoff (HP) transformation is made between these spin operator and bosonic creation and annihilation operators. This transformation is defined for spins on sublattice A as

$$S_A^+ = \sqrt{2S}a, \qquad S_A^- = \sqrt{2S}a^\dagger, \quad \text{and} \quad S_A^z = S - a^\dagger a. \tag{1.12}$$

Similarly, spins oppositely aligned on the B sublattice are transformed as

$$S_B^+ = \sqrt{2S}b^\dagger, \qquad S_B^- = \sqrt{2S}b, \quad \text{and} \quad S_B^z = -S + b^\dagger b. \tag{1.13}$$

The HP transformation assumes that fluctuating spins behave as simple harmonic oscillators. Using Eqs. 1.12 and 1.13, the Heisenberg Hamiltonian can be expressed as

$$\mathcal{H} = -4NS^2J + \frac{SJ}{2}\sum_{\langle i,j\rangle}(a_i^\dagger a_i + b_j^\dagger b_j + a_i^\dagger b_j^\dagger + a_i b_j). \tag{1.14}$$

To find the dispersion of a spin wave, the Hamiltonian must be defined in terms of

wave vector $\boldsymbol{q}$. This is done using the Fourier transforms

$$a_i = \frac{1}{\sqrt{N}} \sum_{\boldsymbol{q}} e^{i\boldsymbol{q}\cdot\boldsymbol{r}_i} a_{\boldsymbol{q}}, \quad \text{and} \quad a_i^\dagger = \frac{1}{\sqrt{N}} \sum_{\boldsymbol{q}} e^{-i\boldsymbol{q}\cdot\boldsymbol{r}_i} a_{\boldsymbol{q}}^\dagger, \tag{1.15}$$

where $\boldsymbol{r}_i$ is the real space position of the i^{th} spin and N is the total number of spins contained within the magnetic unit cell. Transforming Eq. 1.14 gives

$$\mathcal{H} = -4NJS^2 + \sum_{\boldsymbol{q}} 2JS[2(a_{\boldsymbol{q}}^\dagger a_{\boldsymbol{q}} + b_{\boldsymbol{q}}^\dagger b_{\boldsymbol{q}}) + \gamma(\boldsymbol{q})(a_{\boldsymbol{q}} b_{-\boldsymbol{q}} + a_{\boldsymbol{q}}^\dagger b_{-\boldsymbol{q}}^\dagger)], \tag{1.16}$$

where

$$\gamma(\boldsymbol{q}) = \cos(\boldsymbol{q}\cdot\boldsymbol{a}) + \cos(\boldsymbol{q}\cdot\boldsymbol{b}). \tag{1.17}$$

In this expression, $\boldsymbol{a}$ and $\boldsymbol{b}$ are the 2D lattice vectors defined in Figure 1.3(a). Using the Bogoliubov transformation for bosons, Eq. 1.16 can be diagonalised to find the energy of the magnon excitation as a function of wave vector. This is the dispersion relation and has the form

$$E(\boldsymbol{q}) = \hbar\omega(\boldsymbol{q}) = 4SJ\sqrt{1 - \frac{1}{4}\gamma(\boldsymbol{q})^2}. \tag{1.18}$$

The dispersion is plotted in Figure 1.3(b) and is characterised by a cone-like mode emerging from the AFM Bragg position at $\boldsymbol{q} = (1/2, 1/2)$ and dispersing up to a maximum energy of $4JS$ at the Brillouin zone (BZ) boundary. The maximum energy corresponds to the energy cost associated with the complete reversal of a spin in the square lattice (where each nearest neighbour interaction contributes JS to the total energy).

Linear spin wave theory, outlined above, is a semi-classical treatment of magnetic excitations. The assumption that spins behave as simple harmonic oscillators is most appropriate for large spins ($S \gg 1/2$), but it has been shown to give a good description for long-range ordered spins approaching the quantum limit. However, the magnetic excitation spectra of materials with $S = 1/2$ also exhibit behaviour

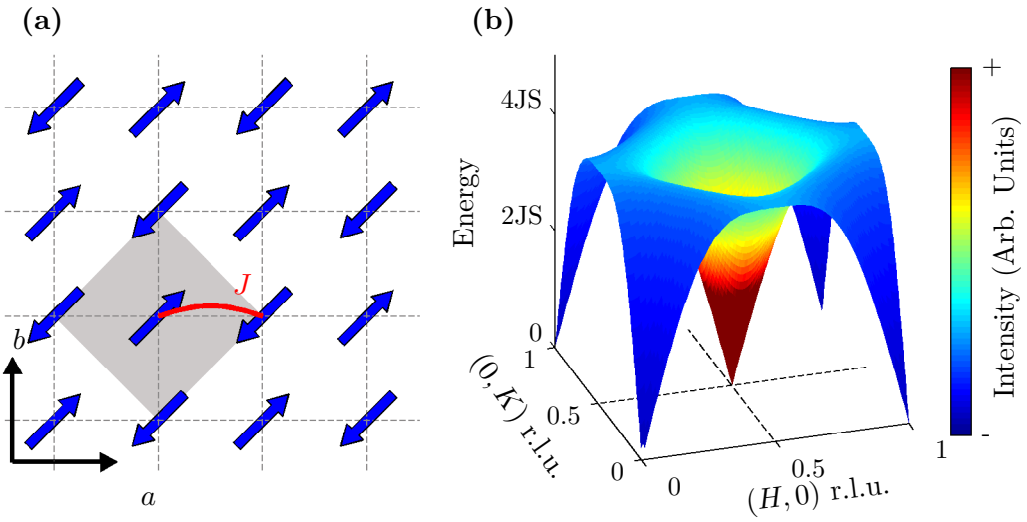

Figure 1.3: Schematic diagram of a simple AFM on a square lattice. (a) AFM order on a square lattice. Two spins are contained within the magnetic unit cell (grey area). The nearest-neighbour exchange interaction J is labelled (red line). (b) The spin wave dispersion for an isotropic Heisenberg antiferromagnet on the square lattice shown in (a). The intensity of the mode is wave vector dependent and is denoted by the colour scale.

not described by LSWT, such as scattering continua and quantum renormalisation effects. Such excitations are best introduced through the canonical example of a quantum spin system, the $S = 1/2$ Heisenberg AFM chain, discussed in the next section.

1.3.2 The $S = 1/2$ Heisenberg AFM Chain

Figure 1.4 shows a representative excitation process in an $S = 1/2$ AFM chain. The ground state AFM order is depicted in Figure 1.4(a). Figure 1.4(b) shows an $S = 1$ excitation (analogous to a magnon) which corresponds to the reversal of a single spin in the chain. The flipped spin is effectively a distinct AFM domain in the system. The energy cost associated with a spin flip in this 1D case is J, where $J/2$ is associated with each of the nearest neighbour exchange interactions at the domain walls. There is no additional energetic cost associated with the propagation

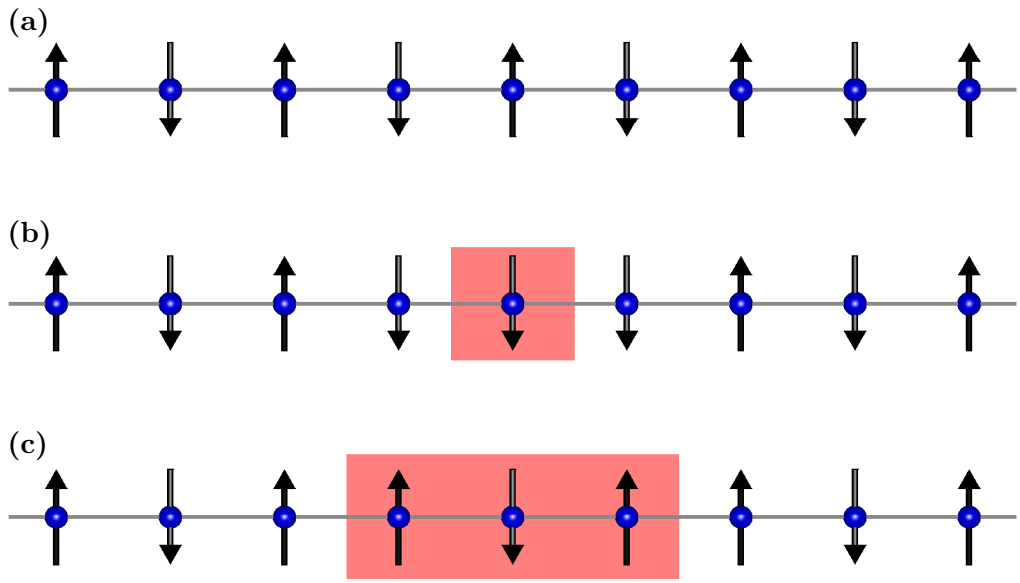

Figure 1.4: Spin excitations in an $S = 1/2$ AFM chain. (a) The ground state magnetic order of the AFM chain. (b) A $S = 1$ magnetic excitation (such as that created in a neutron scattering experiment) acts to reverse a spin in the AFM chain. This single reversed spin effectively forms a second AFM domain within the chain, indicated by the red shaded area. (c) The domain walls are able to propagate along the chain with no added energy cost. Each domain wall carries a spin of $S = 1/2$ and is quantised as a spinon excitation.

of this new domain as there remain only two domain walls – Figure 1.4(c). Therefore, the initial magnon excitation decays into two decoupled $S = 1/2$ excitations corresponding to the domain walls. These excitations are called spinons [4].

An $S = 1/2$ AFM chain is a case where the Heisenberg Hamiltonian can be solved exactly. The solution for the ground state is known as the Bethe ansatz [5] and the excitations are described by the des Cloizeaux-Pearson dispersion [6]. For a single spinon, this has the form

$$E(q) = \frac{\pi J}{2} |\sin(2\pi q)|, \quad \text{for} \quad 0 < q < \pi. \tag{1.19}$$

This is illustrated in Figure 1.5(a). A continuum of scattering is observed when measuring the magnetic excitation spectrum of $S = 1/2$ chains because spinons are

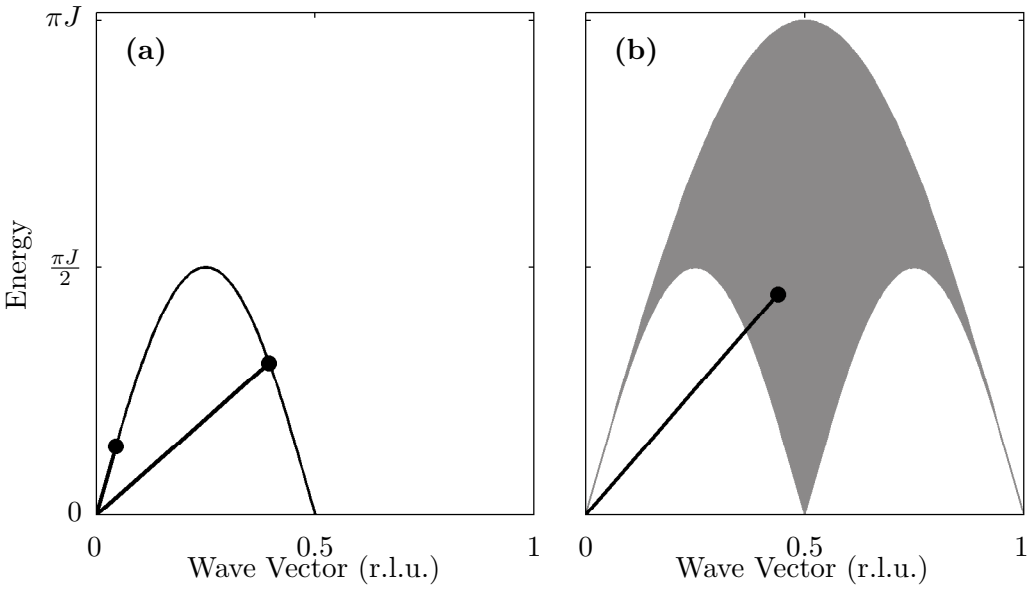

Figure 1.5: Spinon dispersion and the two-spinon continuum. (a) The des Cloizeaux-Pearson dispersion relation for a single spinon. (b) The 2-spinon continuum of scattering. The continuum arises as spinons are created in pairs. Therefore, the sum of any two positions on the single spinon dispersion lies within this continuum. This is illustrated for two points on the dispersion in (a) and shown by black markers. The sum of the two vector positions is shown by the black marker in (b) and lies within the continuum. Figure adapted from Ref. [7].

created in pairs. Two individual spinon excitations are shown at different points on the dispersion in Figure 1.5(a). When an $S = 1$ scattering process creates these spinons simultaneously, the measured spectrum reveals the sum of the two – shown in Figure 1.5(b). All possible two-particle scattering processes consistent with Eq. 1.19 define the grey continuum shown in Figure 1.5(b), with sharp upper and lower boundaries.

1.4 Materials of Note

The concepts outlined in the previous sections have been used to successfully describe magnetic order and excitations in numerous correlated electron systems. These include materials similar to those studied in this thesis. Two broad classes of materials are introduced below, namely the cuprate unconventional supercon-

ductors and multiferroics. The experimental investigations presented in subsequent chapters were motivated by a desire to better understand both classes.

1.4.1 The Cuprate Superconductors

Superconductivity was first observed in elemental Hg below the critical temperature $T_C = 4.2\,K$ in 1911 by Onnes [8]. It is a state of matter characterised by various unusual behaviours, most notably an infinite electrical conductivity and the complete expulsion of a magnetic field from a sample's interior (otherwise known as the Meissner effect) [9]. It was not until 1957 that a theory for superconductivity was successfully derived. This was proposed by Bardeen, Cooper and Schrieffer, and is commonly referred to as BCS theory [10]. It describes the means by which electrons with opposite wave vectors form pairs (so-called 'Cooper pairs') via a phonon-mediated attractive interaction when they exist close to the Fermi surface [9]. Cooper pairs share many of the same attributes as bosons, and are able to condense into a ground state. This ground state is separated from the Fermi surface by a small energy gap. As Cooper pairs have zero net wave vector (hence, an infinite de Broglie wavelength) and the pair-forming electrons are separated from other states by the gap, only scattering which destroys the Cooper pair is possible. At low temperatures a system does not have sufficient energy to break apart the Cooper pairs, and an infinite conductivity arises from their unimpeded motion.

This conventional picture of superconductivity has been hugely successful in explaining the behaviour of superconducting elements and simple compounds. However, there exist various unconventional superconductors that cannot be understood in the context of BCS theory. The most lauded of these unconventional superconductors are the cuprates. This family of materials was found to superconduct below approximately 30 K in 1986 by Bednorz and Müller [11]. Cuprates currently hold the record for the highest superconducting temperature $T_C \approx 134\,K$ at atmospheric pressure [12] and $T_C \approx 160\,K$ at higher pressures [13] in Hg-doped samples.

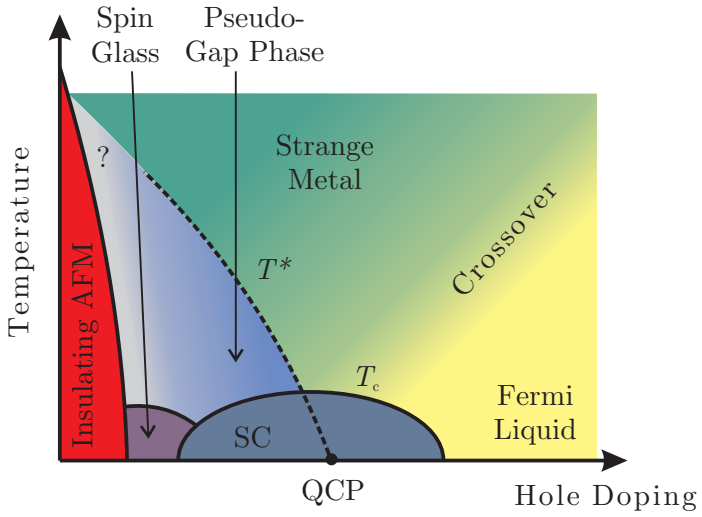

Figure 1.6: Generalised phase diagram of the cuprate unconventional superconductors. The different phases are defined in terms of temperature and hole doping. The phases are labelled. T_c denotes the critical temperature of the superconducting (SC) phase. T^* denotes the transition temperature of the pseudo-gap phase and is suspected to extend down to a quantum critical point (QCP) at $T = 0$. Figure adapted from Ref. [14].

Cuprates come in various compositions. Common to all varieties are Cu-O planes, which are stacked to form a perovskite crystal structure. One or more cations separate these planes in the stacked structure. Chemical substitutions of the cations separating the layers can introduce additional holes. Therefore, Cu ions exist in mixed valence states. Through this process the system is doped. A superconducting phase exists at low temperatures in the cuprates across a specific doping range. A generalised phase diagram of the cuprates is shown in Figure 1.6.

This diagram also features various other phases in addition to superconductivity [15, 16]. In the parent undoped compound and at low dopings, the cuprates are insulating antiferromagnets [16]. Between this phase and superconductivity, spin glass behaviour has been reported at low temperatures. The mixture of Cu valence states in the doped cuprates also leads to charge ordering phenomena driven by strong electronic correlations. Specifically, in some single-layer cuprates there exist quasi-one-dimensional charge correlations, creating charge and magnetically ordered

stripes at certain doping levels [15]. In contrast, different incommensurate charge correlations have been observed in some bilayer cuprates [17].

Where magnetism is known to destroy Cooper pairs in conventional superconductivity, it is crucial to the pairing interaction in the cuprates (in place of the conventional phonon) [18, 19]. Although magnetic interactions are recognised as important, the mechanism through which they can form Cooper pairs remains unknown. Emergent phenomena in condensed matter physics are often understood as fluctuations of the background order. Therefore, to reveal the mechanism behind unconventional superconductivity, there is an ongoing effort to understand the various correlated behaviours observed across the phase diagram of the cuprates.

1.4.2 Multiferroic Materials

Multiferroics are materials that have two or more coexisting ferroic orders. These orders include ferromagnetism, ferroelectricity, ferroelasticity and ferrotoroidicity. This definition is often relaxed to include the related antiferro- orders (eg. the antiparallel alignment of magnetic moments observed in antiferromagnetic order) [20]. Multiferroics with coexisting magnetic order and ferroelectric polarisation are of particular interest because of the potential technological implications for data storage and processing. Recent multiferroics research has principally focused on such materials and two distinct classes of multiferroics have been identified. Proper (or Type-I) multiferroics, exhibit coexisting orders that arise from distinct mechansims [21]. A prototypical example of this class is $BiFeO_3$, a multiferroic that exhibits a large ferroelectric polarisation and antiferromagnetic order [22]. In this case, the magnetic ordering arises from the collective behaviour of the Fe^{3+} ions, whereas the polarisation is due to the ordering of the Bi ion's lone pair (formed by the 6s orbital electrons).

The separate origin for the magnetism and polarisation in proper multiferroics is not surprising as magnetism arises in many transition metal ions due to half

filled d electron shells; while a polarisation is typically produced when d shells are empty [21]. Such conflicting origins indicate that multiferroicity is unlikely to arise from a common source. However, such materials do exist and are called improper (or Type-II) multiferroics. In these cases, a polarisation can spontaneously arise in certain incommensurate magnetic orders. Specifically, helicoidal magnetic order where the rotation axis $\boldsymbol{R}$ (perpendicular to the plane in which spins are rotated in the spiral) and the spiral propagation vector $\boldsymbol{\kappa}$ are not parallel. This breaks inversion symmetry and allows for a polarisation $\boldsymbol{P}$ in the direction parallel to $\boldsymbol{R} \times \boldsymbol{\kappa}$. These conditions are found in cycloidal magnetic structures which often exhibit improper multiferroicity [21, 23].

The shared origin of magnetism and polarisation in improper multiferroics strongly couples the two orders. There are various mechansims proposed to give rise to this magnetoelectric coupling. A likely candidate in many materials, is the weak Dyaloshinskii-Moriya (DM) interaction [24, 25]. This is a non-linear exchange interaction of the form $\boldsymbol{D} \cdot (\boldsymbol{S}_i \times \boldsymbol{S}_j)$. With a better understanding of observed magnetoelectric coupling, it is hoped that a strongly-coupled multiferroic can be found at room temperatures. To this end, research has focussed on identifying and modelling experimental signatures of the magnetoelectric coupling. A material's magnetic excitation spectrum offers the perfect experimental test bed for such studies.

1.5 Work Presented in this Thesis

This thesis deals with three different materials $La_{1.75}Sr_{0.25}CoO_4$, CuO, and $LuFe_2O_4$. To understand each I have employed a common methodology: experimentally measuring the magnetic excitation spectrum and simulating the results with a model of the dominant exchange interactions. Inelastic neutron scattering (INS) is used to measure the excitation spectrum in the materials. Chapter 2 describes the theory behind INS as a technique and introduces the experimental procedures used to col-

lect all the measured data. Chapter 3 describes the study of $La_{1.75}Sr_{0.25}CoO_4$. A broad hour-glass magnetic spectrum is measured in this system similar to spectra measured in some cuprates. Its spectrum is successfully reproduced by modelling the ground state Co-O plane as a disordered cluster spin glass. Chapter 4 introduces the comprehensive measurements of the high energy 1D and low energy 3D magnetic spectrum of the high temperature multiferroic CuO. Existing models describing the dominant interactions using a Heisenberg Hamiltonian are tested against the data and are shown to fail. A new phenomenological model is introduced which successfully describes the measured dispersion. Chapter 5 documents measurements of the excitation spectrum of $LuFe_2O_4$. A spin wave model is successfully used to describe the measured dispersion comprised of six modes and its implications on the debate over the specific charge ordering in $LuFe_2O_4$ are discussed. Finally, Chapter 6 concludes this thesis and suggests possible future work.

Chapter 2

Experimental Techniques

Contents

2.1 Introduction

Neutron scattering is a central experimental technique in the study of condensed matter physics. The neutron, initially discovered in 1932 by James Chadwick [26],

was shown to diffract from crystalline matter in 1936 by the separate groups of von Halban and Preiswerk [27], and Mitchell and Powers [28]. Their experiments demonstrated that thermal neutrons have a de Broglie wavelength similar to interatomic distances (in the order of angstroms) and so the neutron is an ideal probe for determining the structure of solids. Additionally, thermal neutrons have energies of a similar magnitude to the quanta of excitations found in condensed matter (such as phonons and magnons). This allows excitations created through inelastic neutron scattering (INS) to be measured with high resolution, as any relative change in neutron energy is comparatively large with respect to the total energy (ie. $\Delta E/E \not\approx 0$). This was first shown by Brockhouse and Stewart in 1955 by measuring phonon excitations in aluminium [29]. Neutron scattering remains complementary to other scattering techniques because neutrons are a very weakly interacting probe and so penetrate and scatter from the bulk of a sample. Additionally, the neutron possesses a small magnetic moment. A weakly interacting moment allows the neutron to scatter from a sample's magnetisation in a simple and easily-quantifiable way. This is in contrast to other scattering probes, such as X-rays, which must typically exploit resonance enhancement to probe magnetic order and dynamics [30]. Furthermore, the orientation of the neutron's magnetic moment (or polarisation) leads to scattering by different mechanisms but only from certain components of a sample's magnetisation. Neutron scattering with polarisation analysis was first performed by Moon, *et al* in 1969 [31]. They showed that different scattering components can be separated when the change in neutron polarisation is measured. This opened the door for detailed studies of a sample's magnetic order and excitation spectrum previously shrouded by stronger features.

The research presented in this thesis is centred around using INS to measure magnetic excitation spectra and describing the results with a physical model. To do this, various aspects of the neutron's interaction with matter must be understood; diffraction and spectroscopic techniques must be utilised; and the required single

crystal samples must be extensively characterised and quality-checked. This chapter outlines the basic theory required to interpret the results I shall present throughout the thesis. Additionally, it reviews the different experimental techniques employed to collect the data.

2.2 Neutron Scattering Theory

One of the strengths of neutron scattering is that the neutron-matter interaction is relatively simple and can be very accurately quantified theoretically. This is a great benefit when testing a theoretical model against experimental data. In this section I shall outline the key theoretical results that will be used in the thesis. There are several textbooks which present a more comprehensive treatment of the theory, including derivations of many of the results quoted here, such as Refs. [32] and [33].

2.2.1 Basic Scattering Concepts

To understand how neutrons interact with a given system, the changes a neutron undergoes during a scattering process must be defined. In doing this, I shall define what is measured in a given experiment.

Consider a neutron with wave vector $\boldsymbol{k}_\mathrm{i}$ incident on a sample. Through some interaction with the sample matter, the neutron is scattered in a direction specified by the wave vector $\boldsymbol{k}_\mathrm{f}$. Through the conservation of momentum and energy, it can be stated that

$$\boldsymbol{Q} = \boldsymbol{k}_\mathrm{i} - \boldsymbol{k}_\mathrm{f} \tag{2.1}$$

$$E = E_\mathrm{i} - E_\mathrm{f} = \frac{\hbar^2}{2m}(|\boldsymbol{k}_\mathrm{i}|^2 - |\boldsymbol{k}_\mathrm{f}|^2). \tag{2.2}$$

This defines the *scattering vector* $\boldsymbol{Q}$ and the *energy transfer* E. These are the wave vector and energy that have been imparted to the sample through the scattering

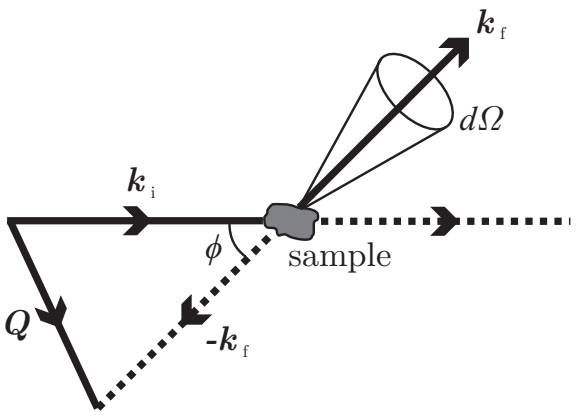

Figure 2.1: Schematic diagram of the basic scattering geometry. Neutrons incident on a sample are described by an incident wave vector $\boldsymbol{k}_\mathrm{i}$. The neutrons scattered from the sample are similarly described by a final wave vector $\boldsymbol{k}_\mathrm{f}$ which is at an angle ϕ (the scattering angle) to $\boldsymbol{k}_\mathrm{i}$. This defines the scattering vector $\boldsymbol{Q}$ through Eq. 2.1. $d\Omega$ defines the solid angle subtended by the detector in a given scattering direction.

process. *Elastic scattering* refers to the situation where there is no energy transfer and so $|\boldsymbol{k}_\mathrm{i}| = |\boldsymbol{k}_\mathrm{f}|$. Conversely, *inelastic scattering* refers to the case of a non-zero energy transfer and so an excitation has been created or destroyed within the sample. Figure 2.1 depicts this scattering geometry.

In order to quantify the number of scattered neutrons defined by a specific $\boldsymbol{Q}$ and E, first the total number of neutrons scattered by a system must be considered. This is done by defining the sample's *cross-section* which can be stated as

$$\sigma = \frac{(\text{total number of neutrons scattered per second})}{\Phi_0}. \tag{2.3}$$

Here, Φ_0 is the incident flux of neutrons and so has dimensions of [area^{-1} time^{-1}]. Therefore, the cross-section σ has units of area and can be considered the effective area presented by the sample to the neutrons during scattering. As Eq. 2.3 specifies the total number of scattered neutrons in all directions, the *differential cross-section*

must be introduced to define the scattering in a particular direction,

$$\frac{d\sigma}{d\Omega} = \frac{\left(\begin{smallmatrix}\text{number of neutrons scattered per second into}\\ \text{the small solid angle } d\Omega \text{ in a given direction}\end{smallmatrix}\right)}{\Phi_0}. \tag{2.4}$$

$d\Omega$ defines a small solid angle (also shown in Figure 2.1) which represents the finite size of the detector used to experimentally measure the scattered neutrons. While the differential cross-section is an adequate description of elastic scattering in diffraction experiments, a further generalisation is required to describe inelastic scattering. The scattered neutron energy needs to be specified, and the *partial differential cross-section* is defined as

$$\frac{d^2\sigma}{d\Omega dE} = \frac{\left(\begin{smallmatrix}\text{number of neutrons scattered per second into}\\ \text{the small solid angle } d\Omega \text{ in a given direction}\\ \text{with a final energy between } E_\mathrm{f} \text{ and } E_\mathrm{f}+dE\end{smallmatrix}\right)}{\Phi_0}. \tag{2.5}$$

This quantity is what is measured in a general neutron scattering experiment with energy analysis. To calculate the partial differential cross-section from a model of the scattering system we can apply the Born approximation.[1] This assumes that the scattered neutrons behave as spherical waves. The approximation is valid for neutron scattering as the interaction between neutrons and matter is very weak. Through this treatment, the partial differential cross-section for one particular change of state can be expressed in terms of the neutron-matter interaction potential $V(\boldsymbol{r})$, through the equation

$$\left.\frac{d^2\sigma}{d\Omega dE}\right|_{\lambda_\mathrm{i},\sigma_\mathrm{i}\to\lambda_\mathrm{f},\sigma_\mathrm{f}} = \frac{k_\mathrm{f}}{k_\mathrm{i}}\left(\frac{m}{2\pi\hbar^2}\right)|\langle\lambda_\mathrm{f}\sigma_\mathrm{f}|V(\boldsymbol{Q})|\lambda_\mathrm{i}\sigma_\mathrm{i}\rangle|^2\delta(E_\mathrm{i}-E_\mathrm{f}-E). \tag{2.6}$$

In this expression, λ_i and λ_f denote the initial and final states of the scattering system with which the neutron interacts. Similarly, σ_i and σ_f denote the neutron's initial and final spin states. $\delta(E_\mathrm{i}-E_\mathrm{f}-E)$ is the Dirac delta function and introduces the conservation of energy (Eq. 2.2) into the expression. m is the mass of the neutron

[1] More commonly known as 'Fermi's Golden Rule' when not taken in the context of scattering.

and $\hbar$ is the reduced Planck constant. $V(\boldsymbol{Q})$ is the the Fourier transform of the real-space interaction potential defined by

$$V(\boldsymbol{Q}) = \int_{-\infty}^{\infty} V(\boldsymbol{r}) e^{i\boldsymbol{Q}.\boldsymbol{r}} d\boldsymbol{r}. \tag{2.7}$$

The vector $\boldsymbol{r}$ is a general position of the neutron relative to the atom or ion from which it scatters.

As an experiment does not probe a single transition, but rather the sum of all transitions in a system, the initial state of the system must be averaged and all final states must be summed. In doing this, the general expression of the partial differential cross-section is obtained:

$$\frac{d^2\sigma}{d\Omega dE} = \frac{k_\mathrm{f}}{k_\mathrm{i}}\Big(\frac{m}{2\pi\hbar^2}\Big) \sum_{\substack{\sigma_\mathrm{i},\sigma_\mathrm{f} \\ \lambda_\mathrm{i},\lambda_\mathrm{f}}} p_{\sigma_\mathrm{i}} p_{\lambda_\mathrm{i}} |\langle \lambda_\mathrm{f}\sigma_\mathrm{f}|V(\boldsymbol{Q})|\lambda_\mathrm{i}\sigma_\mathrm{i}\rangle|^2 \delta(E_\mathrm{i} - E_\mathrm{f} - E), \tag{2.8}$$

where p_{λ_i} and p_{σ_i} are the probabilities of the system and neutron being in the initial states λ_i and σ_i respectively.

It becomes apparent from this expression that the task of calculating the intensity measured in a particular experiment becomes a problem of evaluating the matrix elements $\langle \lambda_\mathrm{f}\sigma_\mathrm{f}|V(\boldsymbol{Q})|\lambda_\mathrm{i}\sigma_\mathrm{i}\rangle$. Hence, the states of a system must be understood and the neutron-sample interaction must be known. The following sections will define the nuclear and magnetic interaction potentials experienced by the neutron. Elastic and inelastic neutron scattering cross-sections will be presented. First, I shall only consider the system's change of state ($\lambda_\mathrm{i} \rightarrow \lambda_\mathrm{f}$) before introducing the particular case of polarised neutron scattering, where transitions between neutron spin states are also differentiated.

2.2.2 Nuclear Scattering

Neutrons scatter from atoms by interacting with their nuclei through the strong force. The strong force is very short range and so any expression of the interaction

potential (introduced in Eq. 2.7) must reflect this. An expression known as the *Fermi pseudopotential* is used to describe this interaction, which has the form

$$V_{\mathrm{N}}(\boldsymbol{r}) = \frac{2\pi\hbar^2}{m}\sum_j b_j\delta(\boldsymbol{r}-\boldsymbol{r}_j), \tag{2.9}$$

where b_j is the scattering length of the j^{th} nucleus and $\boldsymbol{r}_j$ is the position of that nucleus. Scattering lengths have been experimentally measured and are tabulated in Ref. [34]. When this interaction is considered across a system of nuclei (as found in a crystal structure) interference effects arise from the spatial correlation between nuclei. This is the origin of the nuclear Bragg peaks measured in neutron diffraction experiments and is called *coherent* scattering. Similarly, correlations also arise between the position of an individual nucleus at different times. This leads to *incoherent* scattering, and manifests itself as a constant scattering background. Therefore, the partial differential cross-section can be separated into two components

$$\frac{d^2\sigma}{d\Omega dE} = \Big(\frac{d^2\sigma}{d\Omega dE}\Big)_{\mathrm{coh.}} + \Big(\frac{d^2\sigma}{d\Omega dE}\Big)_{\mathrm{incoh.}} \tag{2.10}$$

As the coherent scattering is due to the correlated behaviour of the whole system, I shall only be considering it in the remaining theory and the subsequent analysis of neutron data in other chapters. At low temperatures, incoherent scattering is purely elastic and can be accommodated by subtracting a constant background from a measured diffraction pattern.

By substituting the Fourier transform of Eq. 2.9 into Eq. 2.8, in addition to considering only zero energy transfer scattering, the general expression for coherent elastic nuclear scattering is found

$$\Big(\frac{d^2\sigma}{d\Omega dE}\Big)_{\substack{\mathrm{coh.}\\ \mathrm{elas.}}} = N\frac{(2\pi)^3}{V_0}\sum_{\boldsymbol{G}}\delta(\boldsymbol{Q}-\boldsymbol{G})|F_{\mathrm{N}}(\boldsymbol{Q})|^2\delta(E). \tag{2.11}$$

In this expression, the Bragg law is included in the form $\delta(\boldsymbol{Q}-\boldsymbol{G})$, where $\boldsymbol{G}$ is the

reciprocal lattice wave vector; N is the number of unit cells in the measured crystal; V_0 is the volume of one unit cell; and $F_{\mathrm{N}}(\boldsymbol{Q})$ is the nuclear structure factor, which can be expressed as

$$F_{\mathrm{N}}(\boldsymbol{Q}) = \sum_j b_j e^{i\boldsymbol{Q}\cdot\boldsymbol{r}_j} e^{-W_j}. \tag{2.12}$$

The exponent W_j is the Debye-Waller factor and has the effect of attenuating the scattering intensity due to the random thermal motion of atoms in a crystal. For a cubic crystal it has the form $W_j = \frac{1}{3}\boldsymbol{Q}^2\langle u_j^2\rangle$, where u_j is the displacement of atom j from its equilibrium position, $\boldsymbol{r}_j$. The atomic displacements are due to thermal fluctuations in the crystal and hence $\langle u_j^2\rangle$ becomes negligibly small as the temperature of the crystal tends to zero. As all of the measurements in this thesis are performed at cryogenic temperatures the effect of the Debye-Waller factor is negligible and so will not be considered in my analysis.

The general form of the partial differential cross-section in Eq. 2.8 also allows the neutron to inelastically scatter from a nuclei. This process creates or destroys a lattice excitation, the quantum of which is the phonon. This thesis is principally concerned with the magnetic equivalent of phonon scattering, which will be introduced in Section 2.2.3. However, phonon scattering often contributes to the background intensity measured in an INS experiment. This intensity occurs as a result of the direct measurement of the phonon spectrum or through indirect multiple scattering processes. An example of multiple scattering is incoherently scattered neutrons undergoing a second scattering process with a phonon. Inelastic background intensities are modelled in a variety of ways so as to separate them from the relevant spectral features.

2.2.3 Magnetic Scattering

An intrinsic property of the neutron is that it has a small magnetic moment ($\sim 0.001\,\mu_{\mathrm{B}}$). This distinguishes neutron scattering over other scattering techniques using different probes (such as X-rays) as the neutron is able to interact directly

with an atom's magnetic moment via the Zeeman interaction – see Eq. 2.15 below. In this section, I shall outline the principal mechanism of magnetic scattering, the dipole interaction between the neutron and an atom's unpaired electrons.[2]

The magnetic dipole moment of the neutron can be defined as

$$\boldsymbol{\mu}_{\mathrm{n}} = -\gamma \mu_{\mathrm{N}} \boldsymbol{\sigma}, \tag{2.13}$$

where $\mu_{\mathrm{N}} = e\hbar/2m_{\mathrm{p}}$ is the nuclear magneton and $\boldsymbol{\sigma}$ is the Pauli spin operator with eigenvalues ± 1. $\gamma = 1.913$ is the gyromagnetic ratio of the neutron. In a scattering process, this moment will interact with the magnetic field created by unpaired electrons orbiting the atom. This field can be expressed in terms of components arising due to the spin and orbital angular momentum ($\boldsymbol{B}_{\mathrm{S}}$ and $\boldsymbol{B}_{\mathrm{L}}$ respectively) as follows:

$$\boldsymbol{B}(\boldsymbol{r}) = \boldsymbol{B}_{\mathrm{S}}(\boldsymbol{r}) + \boldsymbol{B}_{\mathrm{L}}(\boldsymbol{r}) = \frac{\mu_0}{4\pi}\Big[\nabla \times \Big(\frac{\boldsymbol{\mu}_{\mathrm{e}} \times \hat{\boldsymbol{r}}}{r^2}\Big) - \frac{2\mu_{\mathrm{B}}}{\hbar}\frac{\boldsymbol{\rho} \times \hat{\boldsymbol{r}}}{r^2}\Big]. \tag{2.14}$$

In this equation μ_0 is the permeability of free space; $\boldsymbol{\mu}_{\mathrm{e}} = -2\mu_{\mathrm{B}}\boldsymbol{s}$ is the magnetic dipole moment of the electron (where $\boldsymbol{s}$ is the electron's spin angular momentum operator); $\boldsymbol{r}$ is the vector specifying a position relative to the electron; $\boldsymbol{p}$ is the momentum of the electron; and $\mu_{\mathrm{B}} = e\hbar/2m_{\mathrm{e}}$ is the Bohr magneton. The interaction between the neutron and this magnetic field can, therefore, be defined as the dot product of Eqs. 2.13 and 2.14

$$V_{\mathrm{M}}(\boldsymbol{r}) = -\boldsymbol{\mu}_{\mathrm{n}} \cdot \boldsymbol{B}(\boldsymbol{r}). \tag{2.15}$$

Using Maxwell's equations to introduce the magnetisation $\boldsymbol{M}$ in place of $\boldsymbol{B}$ and the definition of the Fourier transform presented in Eq. 2.7, the interaction potential

[2]The neutron also interacts with the atom's nuclear moment but this is an even weaker interaction and is outside the scope of this thesis.

can be expressed as a function of wave vector

$$V_{\mathrm{M}}(\boldsymbol{Q}) = \mu_0 \boldsymbol{\mu}_{\mathrm{n}} \cdot \boldsymbol{M}_{\perp}(\boldsymbol{Q}), \tag{2.16}$$

where $\boldsymbol{M}_{\perp}(\boldsymbol{Q})$ is the component of $\boldsymbol{M}(\boldsymbol{Q})$ (the Fourier transform of the real-space magnetisation) perpendicular to $\boldsymbol{Q}$ and can be expressed as

$$\boldsymbol{M}_{\perp}(\boldsymbol{Q}) = \hat{\boldsymbol{Q}} \times (\boldsymbol{M}(\boldsymbol{Q}) \times \hat{\boldsymbol{Q}}). \tag{2.17}$$

This quirk, that the neutron is only sensitive to the component of magnetisation perpendicular to the scattering vector, is rooted in how the expression of the magnetic field (Eq. 2.14) behaves under Fourier transformation. Finally, substitution of Eq. 2.16 into Eq. 2.8 leads to the general expression of the partial differential cross-section for magnetic scattering

$$\frac{d^2\sigma}{d\Omega dE} = \frac{k_{\mathrm{f}}}{k_{\mathrm{i}}} \Big(\frac{\gamma r_0}{2\mu_{\mathrm{B}}} \Big) \sum_{\lambda_{\mathrm{i}},\lambda_{\mathrm{f}}} p_{\lambda_{\mathrm{i}}} |\langle \lambda_{\mathrm{f}} | \boldsymbol{M}_{\perp}(\boldsymbol{Q}) | \lambda_{\mathrm{i}} \rangle|^2 \delta(E_{\mathrm{i}} - E_{\mathrm{f}} - E). \tag{2.18}$$

$\boldsymbol{M}(\boldsymbol{Q})$ in the Dipole Approximation

The general expression for $\boldsymbol{M}(\boldsymbol{Q})$ is very complicated. However, in most practical applications the *dipole approximation* is valid and can be used to simplify the expression for $\boldsymbol{M}(\boldsymbol{Q})$. The approximation assumes that the scattering vector is much smaller than the inverse radius of the orbital wavefunction ($|\boldsymbol{Q}| < r_{orb}^{-1}$). Furthermore, in the 3d transition metal oxides the orbital angular momentum is typically quenched such that $\boldsymbol{L} = 0$. Hence, the magnetisation is defined by the good quantum number $\boldsymbol{S}$ describing the spin. Any small orbital contribution to the moments arising from spin-orbit coupling can be accommodated by using an effective g-factor. Therefore,

$$\boldsymbol{M}(\boldsymbol{Q}) \approx -g\mu_{\mathrm{B}} f(\boldsymbol{Q}) \boldsymbol{S} = \boldsymbol{\mu} f(\boldsymbol{Q}), \tag{2.19}$$

where $\boldsymbol{\mu}$ is the ion's magnetic moment and $g \approx 2$ for a spin-only system. $f(\boldsymbol{Q})$ is the magnetic form factor and is defined as the Fourier transform of the magnetisation distribution of an ion, such that

$$\boldsymbol{\mu} f(\boldsymbol{Q}) = \boldsymbol{\mu} \int m(\boldsymbol{r}) e^{i\boldsymbol{Q}\cdot\boldsymbol{r}} d\boldsymbol{r}, \tag{2.20}$$

where $m(\boldsymbol{r})$ is the normalised density of unpaired electrons. In the dipole approximation for spin only scattering, the magnetic form factor can be described by an integral expression containing the zeroth order Bessel function:

$$f(\boldsymbol{Q}) = \langle j_0(\boldsymbol{Q}) \rangle. \tag{2.21}$$

This can, in turn, be parameterised by a sum of exponential terms of the form

$$\langle j_0(\boldsymbol{Q}) \rangle = Ae^{-as^2} + Be^{-bs^2} + Ce^{-cs^2} + D, \tag{2.22}$$

where $s = |\boldsymbol{Q}|/4\pi$, and the other coefficients have been experimentally measured. The values for the magnetic ions have been tabulated in Chapter 2 of Ref. [35] and online [36].

Elastic Magnetic Scattering

Elastic magnetic scattering measures the Fourier transform of the static magnetic ordering within a crystal. Hence, magnetic Bragg peaks are measured, directly analogous to the structural Bragg peaks arising due to nuclear elastic scattering. To understand these peaks, the magnetic unit cell defined in real space must be considered in place of the crystallographic unit cell. In many cases these units cells are the same (such as in a ferromagnet), however, the antiferromagnetic materials studied in this thesis all require a larger unit cell to describe their magnetic structure.

Using the expressions presented in Eqs. 2.18 and 2.19, the partial differential

cross-section describing the elastic magnetic scattering is found to be

$$\left(\frac{d^2\sigma}{d\Omega dE}\right)_{\substack{\text{coh.}\\ \text{elas.}}} = \left(\frac{\gamma r_0}{2\mu_\text{B}}\right)^2 |\boldsymbol{M}_\perp(\boldsymbol{Q})|^2 \delta(E) \tag{2.23}$$

$$= (\gamma r_0)^2 N \frac{(2\pi)^3}{V_0} \sum_{\boldsymbol{G}} \delta(\boldsymbol{Q} - \boldsymbol{G}_\text{M}) \sum_{\alpha,\beta} (\delta_{\alpha,\beta} - \hat{Q}^\alpha \hat{Q}^\beta) F_\text{M}^{\alpha *}(\boldsymbol{Q}) F_\text{M}^{\beta}(\boldsymbol{Q}) \delta(E). \tag{2.24}$$

In Eq. 2.24, the neutron's sensitivity to the components of $\boldsymbol{M}(\boldsymbol{Q})$ perpendicular to $\boldsymbol{Q}$ is introduced through the orientation factor $(\delta_{\alpha,\beta} - \hat{Q}^\alpha \hat{Q}^\beta)$. $\delta_{\alpha,\beta}$ is the Kronecker delta function and $\hat{Q}^{\{\alpha,\beta\}}$ are the components of the unit vector parallel to $\boldsymbol{Q}$. The components are defined in cartesian coordinates such that $\{\alpha, \beta\} = \{x, y, z\}$. The Bragg law is now satisfied when the scattering vector corresponds to a magnetic reciprocal lattice vector, $\boldsymbol{G}_\text{M}$. Finally, $F_\text{M}^\alpha(\boldsymbol{Q})$ is the α-component of the magnetic structure factor defined as

$$F_\text{M}(\boldsymbol{Q}) = \sum_j f_j(\boldsymbol{Q}) \boldsymbol{\mu}_j e^{i\boldsymbol{Q}\cdot\boldsymbol{r}_j} e^{-W_j}, \tag{2.25}$$

where $f_j(\boldsymbol{Q})$ is the form factor (defined in Eq. 2.20) and $\boldsymbol{\mu}_j$ is the moment (defined in Eq. 2.19) of the j^th ion. $\boldsymbol{r}_j$ is the position of the ion within the magnetic unit cell and e^{-W_j} is the Debye-Waller factor introduced in Section 2.2.2.

Considering Eqs. 2.24 and 2.25, the intensity of neutrons scattered via a magnetic interaction will be scaled by the square of the form factor. This has been plotted for Co^{2+} and Cu^{2+} ions (as outlined in Eqs. 2.21 and 2.22) in Figure 2.2.

Inelastic Magnetic Scattering

The majority of the work in this thesis aims to measure magnetic excitations in condensed matter systems so as to better understand the microscopic magnetic interactions. The expression for magnetic elastic scattering presented in Eq. 2.24 must be extended to describe inelastic scattering. In the dipole approximation, the

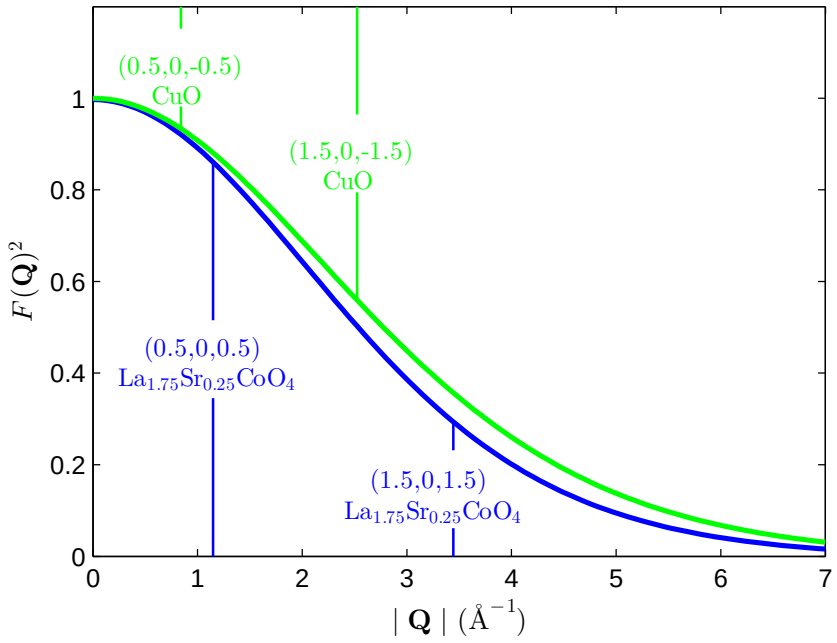

Figure 2.2: Q dependence of the approximate spin-only, squared magnetic form factors of Co^{2+} and Cu^{2+}. The values of $|\boldsymbol{Q}|$ for several of the measured magnetic Brillouin zone centres in CuO and $La_{1.75}Sr_{0.25}CoO_4$ are depicted.

partial differential cross-section is defined as

$$\frac{d^2\sigma}{d\Omega dE} = \frac{k_\mathrm{f}}{k_\mathrm{i}}\left(\frac{\gamma r_0}{2}\right)^2 \mu_B^2 g^2 f^2(Q) \sum_{\alpha,\beta}(\delta_{\alpha,\beta} - \hat{Q}^\alpha \hat{Q}^\beta) S^{\alpha\beta}(\boldsymbol{Q}, E). \tag{2.26}$$

In this expression the g-factor and form factor are still present, as introduced in Eq. 2.19. However, in place of the magnetic moment $\boldsymbol{\mu}$, the *scattering function*[3] $S^{\alpha\beta}(\boldsymbol{Q}, E)$ is introduced. This describes the correlations between the different components of the magnetisation $\boldsymbol{M}(\boldsymbol{Q})$ and, through the approximation in Eq. 2.19, is defined in terms of the spin operator $\boldsymbol{S}$

$$S^{\alpha\beta}(\boldsymbol{Q}, E) = \sum_{\lambda_\mathrm{i},\lambda_\mathrm{f}} \langle\lambda_\mathrm{i}|S^{\alpha *}(\boldsymbol{Q})|\lambda_\mathrm{f}\rangle\langle\lambda_\mathrm{f}|S^{\beta}(\boldsymbol{Q})|\lambda_\mathrm{i}\rangle \delta(E_\mathrm{i} - E_\mathrm{f} - E), \tag{2.27}$$

where $S^{\{\alpha,\beta\}}(\boldsymbol{Q})$ are the components of $\boldsymbol{S}(\boldsymbol{Q})$ in cartesian coordinates, $\{\alpha, \beta\} = \{x, y, z\}$.

[3] Alternatively called the 'response function' in some references.

It is convenient to express the partial differential cross-section in this way as the physical description of the correlations are contained within the expression of $S^{\alpha\beta}(\boldsymbol{Q}, E)$. Experimental coefficients and factors relating to the specific neutron scattering process are separated from this in Eq. 2.26. This form is especially useful in comparing the measured scattering intensity to theoretical work, as I will do throughout this thesis.

Theoretical studies typically investigate the generalised susceptibility which is related to the magnetisation, $\boldsymbol{M} = \chi \boldsymbol{H}$, and defined as complex, $\chi(\boldsymbol{Q}, E) = \chi'(\boldsymbol{Q}, E) - i\chi''(\boldsymbol{Q}, E)$. The imaginary part of the generalised susceptibility is related to the scattering function by the *fluctuation-dissipation theorem*,

$$S^{\alpha\beta}(\boldsymbol{Q}, E) = \frac{1}{\pi}[1 + n(E)]\chi''(\boldsymbol{Q}, E). \tag{2.28}$$

Here, $n(E) = (e^{E/k_{\mathrm{B}}T} - 1)^{-1}$ is the Bose-Einstein population factor. This relation is advantageous as the susceptibility can be readily calculated from a given Hamiltonian, whereas calculating the magnetisation (or the spin operator, in the case of Eq. 2.27) can be more difficult.

The form of Eq. 2.27 allows for both neutron energy loss and gain scattering processes. While these processes are allowed with an equal probability, neutron energy gain requires the system to initially be in an excited state. Therefore, the scattering function for energy gain scattering is suppressed by the Boltzmann factor with respect to energy loss scattering, such that

$$S^{\alpha\beta}(\boldsymbol{Q}, -E) = \exp(-E/k_{\mathrm{B}}T) S^{\alpha\beta}(\boldsymbol{Q}, E). \tag{2.29}$$

This relation is known as the *principle of detailed balance*. As all the measurements in this thesis are performed at cryogenic temperatures and the typical energies of magnetic excitations are in the thermal range, neutron energy gain scattering can be ignored.

2.2.4 Polarised Neutron Scattering

As introduced in the general expression for the partial differential cross-section in Eq. 2.8, the spin state of the neutron also affects its interaction with matter. Eq. 2.13 shows that the neutron spin has two eigenstates, which I shall denote spin up and down (represented in Dirac notation as $|\uparrow\rangle$ and $|\downarrow\rangle$). In an applied magnetic field, the neutron spin must align parallel or antiparallel to the field. Therefore, the polarisation of a neutron beam can be expressed in terms of the relative ratios of these polarisation states

$$P = \frac{n_\uparrow - n_\downarrow}{n_\uparrow + n_\downarrow}, \tag{2.30}$$

where $n_\uparrow$ ($n_\downarrow$) is the total number of spin up (down) neutrons in the beam. In an unpolarised neutron beam, there are equal proportions of each state so the net polarisation is zero. However, through various experimental techniques, it is possible to preferentially select one spin state and so create a polarised beam of neutrons where $P = \pm 1$. The polarisation defined above is a scalar, however, it requires an applied magnetic field (a vector quantity) to create the two allowed spin states. Therefore, by manipulating the applied field, the direction with which the polarisation is aligned must also change. I shall refer to this alignment as the 'polarisation direction', to distinguish it from the scalar polarisation.[4] Typically, the polarisation direction is defined with respect to the scattering vector (and hence the instrument geometry).

I shall restrict attention here to experiments where the neutron is at all times in a magnetic field (before, during, and after scattering), which defines the two spin states of the neutron. This arrangement is called uniaxial or longitudinal polarisation analysis. As there are two neutron spin states, there are four possible permutations of the interaction matrix elements, $\langle\sigma_\mathrm{f}|V(\boldsymbol{Q})|\sigma_\mathrm{i}\rangle$. Hence, two types of scattering process exist: spin-flip (SF) scattering where the neutron's spin changes;

[4] In a full treatment, the beam polarisation is defined as a vector in the absence of a magnetic field (being related to the ensemble average of the neutron spin vectors). However, this is only required to understand spherical neutron polarimetry, which is outside of the scope of this thesis.

and non-spin-flip (NSF) scattering where the neutron's spin remains the same. In this section, I shall use the forms of the interaction potential introduced in Sections 2.2.2 and 2.2.3 to evaluate the spin dependent matrix elements.

First, consider the matrix elements for coherent nuclear scattering. The interaction potential is defined by a constant scattering length according to Eq. 2.9. Therefore, the spin transition matrix elements can be evaluated as

$$\langle \boldsymbol{\sigma}_{\mathrm{f}} \mid b \mid \boldsymbol{\sigma}_{\mathrm{i}} \rangle = b \langle \boldsymbol{\sigma}_{\mathrm{f}} \mid \boldsymbol{\sigma}_{\mathrm{i}} \rangle = \left\{ \begin{array}{ll} b & \left. \begin{array}{l} |\uparrow\rangle \rightarrow |\uparrow\rangle \\ |\downarrow\rangle \rightarrow |\downarrow\rangle \end{array} \right\} \text{NSF} \\ 0 & \left. \begin{array}{l} |\uparrow\rangle \rightarrow |\downarrow\rangle \\ |\downarrow\rangle \rightarrow |\uparrow\rangle \end{array} \right\} \text{SF} \end{array} \right. \tag{2.31}$$

This equation shows that for coherent nuclear scattering, only NSF terms are non-zero (ie. neutrons scattered coherently by nuclei maintain their initial polarisation). Similarly, the matrix elements for magnetic scattering can be evaluated using Eq. 2.16, the results being

$$\langle \boldsymbol{\sigma}_{\mathrm{f}} \mid V_{\mathrm{m}}(\boldsymbol{Q}) \mid \boldsymbol{\sigma}_{\mathrm{i}} \rangle = \left\{ \begin{array}{ll} M_{\perp}^{z}(\boldsymbol{Q}) & \left. \begin{array}{l} |\uparrow\rangle \rightarrow |\uparrow\rangle \\ |\downarrow\rangle \rightarrow |\downarrow\rangle \end{array} \right\} \text{NSF} \\ -M_{\perp}^{z}(\boldsymbol{Q}) & \\ M_{\perp}^{x}(\boldsymbol{Q}) - iM_{\perp}^{y}(\boldsymbol{Q}) & \left. \begin{array}{l} |\uparrow\rangle \rightarrow |\downarrow\rangle \\ |\downarrow\rangle \rightarrow |\uparrow\rangle \end{array} \right\} \text{SF} \\ M_{\perp}^{x}(\boldsymbol{Q}) + iM_{\perp}^{y}(\boldsymbol{Q}) & \end{array} \right. \tag{2.32}$$

Here, $\{x, y, z\}$ denote the orthogonal components of $\boldsymbol{M}_{\perp}(\boldsymbol{Q})$ with respect to the neutron polarisation direction defined to be parallel to z.[5] Hence, by measuring the SF and NSF scattering for different neutron polarisations all the components of $\boldsymbol{M}_{\perp}(\boldsymbol{Q})$ can be separated.

The results quoted in Eqs. 2.31 and 2.32 highlight the power of polarised neutron scattering. With the ability to polarise an incident neutron beam; experimentally

[5]Not to be confused with the x, y, z coordinate system, defined with $x \parallel \boldsymbol{Q}$, denoting the polarisation direction of the incident neutron beam in Section 2.3.3

control the polarisation direction; and differentiate the polarisations of the scattered neutrons the nuclear and magnetic scattering can be separated and all the components of the magnetisation can be resolved.

2.3 Neutron Instrumentation

There is a wide array of neutron sources and instrumentation across the world. Each is optimised for a specific experiment and all have strengths and weaknesses. In this section, I will outline the basic workings of two classes of instrument: the *triple axis spectrometer* (TAS) and the *direct-geometry chopper spectrometer*. The work in this thesis was mainly performed using the MAPS and MERLIN chopper spectrometers at the ISIS Spallation Neutron Source, Didcot, UK. Additionally, some measurements were performed using the IN8 and IN20 TAS at the ILL Neutron Reactor Source, Grenoble, France. A more comprehensive description of these two types of spectrometer, and the associated technologies, can be found in Ref. [37]. A more extensive discussion of the TAS can be found in Ref. [38].

2.3.1 Neutron Sources

There are two methods of producing the high flux neutron beams needed for scattering experiments. The first is using a *reactor source*. This produces neutrons through a self-sustaining nuclear fission reaction and has a very high, constant flux. The neutrons are produced with energies in the MeV range. A *moderator* is used to reduce the energy of the neutrons to the thermal energies required for the study of condensed matter systems (typically in the meV range). Moderators are made of a material with light nuclei (such as water or graphite) and held at a constant temperature. When the neutrons pass through a moderator, they scatter and equilibrate their energy. This produces neutrons with a Boltzmann distribution of energies characterised by the temperature of the moderator. A scattering experiment will then go on to select a specific energy from this distribution for its incident beam.

The second method uses a *spallation source*. This involves accelerating a beam of charged particles (ie. protons) onto a heavy metal target. The ensuing collision causes neutrons to be ejected from the target nuclei through a spallation reaction. Like the reactor source, neutrons are produced with very high energies and so a moderator is used to reduce the energy to the thermal range. Spallation sources have a lower average neutron flux but have the benefit that the neutrons are produced in pulses. Having well defined pulses allows the neutron's 'time-of-flight' (TOF) to be exploited. The TOF is the time taken for a neutron to travel through the instrument and varies with the neutron's wave vector. Understanding the time structure of the neutron pulse and measuring the detection time of the scattered neutrons allows for a much more efficient use of the flux generated compared to a reactor source.

2.3.2 The Direct-Geometry Chopper Spectrometer

The direct-geometry chopper spectrometer utilises the neutron's TOF to select an incident wave vector and distinguish the final wave vectors. For this reason, chopper spectrometers are typically used at pulsed spallation sources. There are techniques to allow a reactor source to create neutron pulses but these have not been used for the work in this thesis and will not be discussed. Therefore, in this section neutrons emitted from the moderator are considered to be pulsed, and it is with respect to this pulse that the TOF is defined.

Figure 2.3(a) shows a schematic diagram of a direct-geometry chopper spectrometer. In order to create a monochromatic incident beam, the neutrons emitted from the moderator pass through two *choppers*. The nimonic chopper is a rotating disc with a slit cut into it. As it rotates, the spectrometer is only open to the moderator when the slit is aligned with the beam direction. By setting the phase and frequency of rotation to coincide with the pulse of neutrons emitted from the moderator, the nimonic chopper reduces the detected background of high energy neutrons and gamma rays outside of the pulse. Next, the *Fermi chopper* is used

to select a particular incident energy. This chopper is typically a drum of neutron absorbent material (eg. B) with small slits of neutron transparent material (eg. Al) running through it. This is rotated in the beam and neutrons can only pass through the chopper when the slits align with the beam direction. Hence, by setting the phase of the rotating Fermi chopper with respect to the pulse of neutrons emanating from the moderator, the intensity pulse can be reduced to a narrow peak centred around a specific energy. The frequency of the Fermi chopper determines the energy width of this peak by setting the length of time during which neutrons can pass. Therefore, a higher frequency of chopper leads to a better defined incident energy; however, it also reduces the flux incident on the sample. The uncertainty of the incident energy leads to a finite energy resolution, which shall be discussed in more detail later in the section. While there are at least two choppers on a chopper spectrometer, only the Fermi chopper is adjusted during a typical experiment. For this reason, the term chopper is commonly used to refer solely to the Fermi chopper, as I shall do for the remainder of the thesis.

Once the incident energy has been specified, the neutrons go on to scatter from the sample. A large area detector bank of position sensitive detectors (eg. ^{3}He-gas tube detectors) record the angular direction and flight time of the scattered neutrons. By knowing the distance between sample and detector, L_3, the speed and hence the kinetic energy of the neutron can be calculated. This leads to an expression for the energy transfer in terms of the TOF, t,

$$E = E_\mathrm{i} - E_\mathrm{f} = E_\mathrm{i} - \frac{mL_3^2}{2t^2}. \tag{2.33}$$

As the neutron energy is related to the wave vector, as outlined in Eq. 2.2, the scattering vector can be subsequently found. An example of the changing $\boldsymbol{Q}$ measured by a single detector as TOF increases is shown in Figure 2.3(b). Typically, large area detector banks are used in chopper spectrometers so as to survey wide areas of reciprocal space simultaneously.

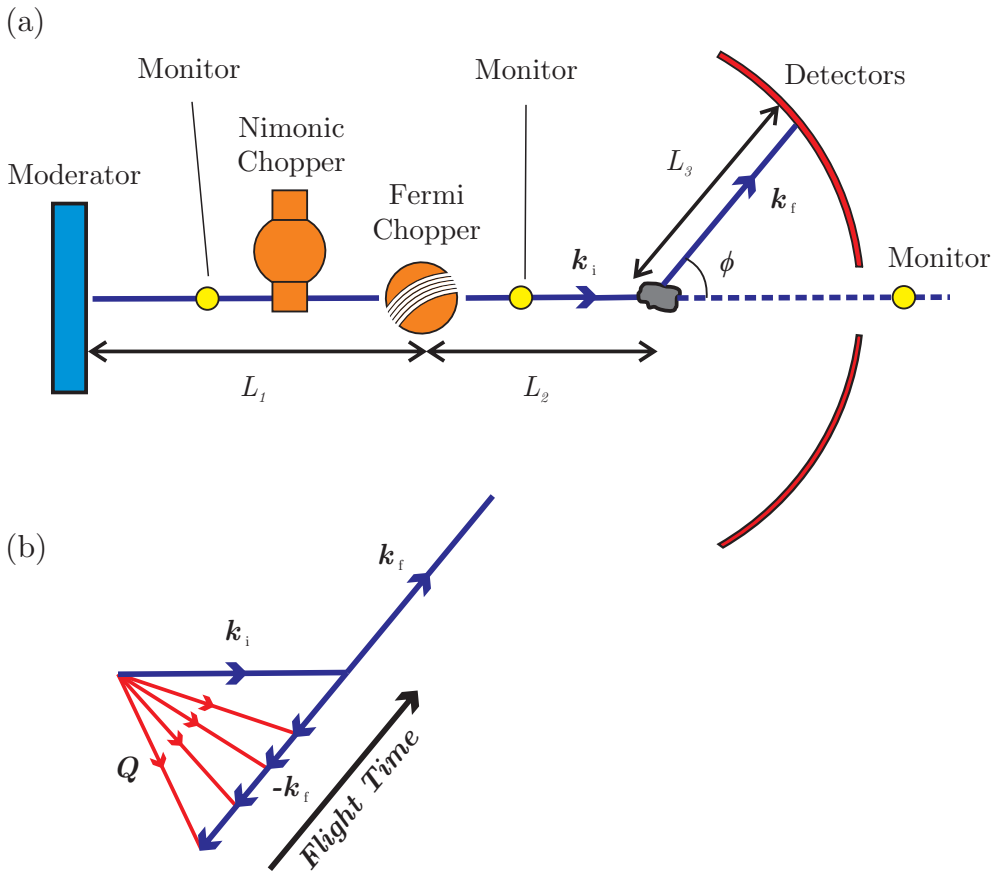

Figure 2.3: The direct-geometry chopper spectrometer and TOF scattering triangle. (a) Schematic diagram of a direct geometry chopper spectrometer. See the main text for a description of the labelled components and variables. (b) Diagram of the scattering triangle for a fixed scattering angle, ϕ. The changing $-\boldsymbol{k}_\mathrm{f}$ (and subsequent change in $\boldsymbol{Q}$) with increasing TOF is shown by the black arrow.

A consequence of using TOF is that, in any single measurement, the component of $\boldsymbol{Q}$ parallel to the direction of the $\boldsymbol{k}_\mathrm{i}$ (denoted, $\boldsymbol{Q}_\parallel$) varies with E because of the definitions in Eqs. 2.1 and 2.2. Figure 2.4 illustrates the coupling of $\boldsymbol{Q}_\parallel$ to the energy transfer for a bank of detectors covering a 20° arc of detectors in the horizontal scattering plane. The shaded grey surface – which originates from the 20° arc at $E = 0$ – illustrates how the wave vector coverage of these fixed detectors changes with E. This feature of TOF spectrometers does not affect the analysis of a one or two-dimensional magnetic system where there are no correlations in one

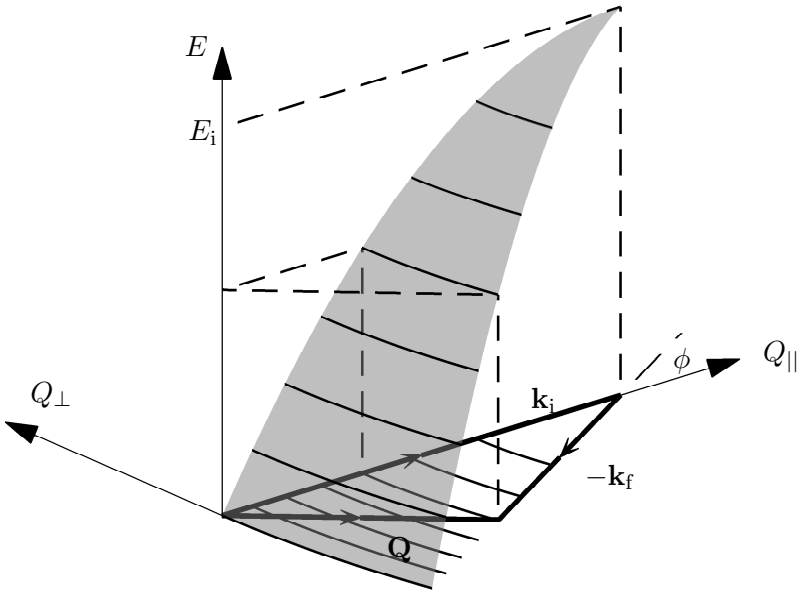

Figure 2.4: The accessible $(\boldsymbol{Q}, E)$-region of a fixed orientation measurement using a direct-geometry chopper spectrometer. An example scattering triangle is plotted on the wave vector plane defined by the directions parallel ($\boldsymbol{Q}_{\|}$) and perpendicular ($\boldsymbol{Q}_{\perp}$) to $\boldsymbol{k}_i$. In any single orientation, the component of $\boldsymbol{Q}$ parallel to $\boldsymbol{k}_i$ is coupled to E. For a 20° arc of fixed detectors this leads to a curved area of accessible $(\boldsymbol{Q}, E)$ values (shaded in grey). The black curves across this area show equally spaced constant energy contours. These contours are also projected onto the $E = 0$ wave vector plane for comparison.

or more directions. Typically, the uncorrelated direction is orientated parallel to $\boldsymbol{k}_i$ and the data are integrated across the $\boldsymbol{Q}_{\|}$ direction. However, in three-dimensional (3D) systems, the variation of $\boldsymbol{Q}_{\|}$ with E makes a single measurement with a fixed orientation an insufficient description of all the correlations. To circumvent this problem a series of measurements is made while incrementally changing the sample orientation. This is referred to as a *multi-angle scan*. Software is then used to combine all of the scattering information into a four-dimensional data volume.

The MAPS and MERLIN spectrometers use the HORACE software suite [39] to combine the multi-angle scan into a data volume. Figure 2.5 illustrates a 2D example of this by considering the reciprocal space coverage of elastic scattering that

can be achieved within the scattering plane (in contrast to Figure 2.4). The $E = 0$ detector coverage is plotted for a series of incrementally rotated measurements with respect to a sample's reciprocal lattice. In this example, a square lattice is aligned in the horizontal scattering plane and is rotated through 90°, around the out-of-plane direction. The detector coverage sweeps out an area across the in-plane reciprocal lattice. Subsequent analysis can take cuts through this area, isolating the spectrum along any given high-symmetry direction independent of coupling between $\boldsymbol{Q}_{\parallel}$ and E.

Scattered neutrons detected in a spectrometer are described by their position in $(\boldsymbol{Q}, E)$-space. However, in reality there is a small distribution of energies and wave vectors which contribute to the intensity at any given position. This distribution is centred around the position that is being measured, denoted $(\boldsymbol{Q}_0, E_0)$. The distribution arises because of uncertainties in the energy transfer and scattering angle and is described by the resolution function, $R(\boldsymbol{Q}, E)$. The measured intensity in a neutron experiment is a convolution of the partial differential cross-section, which describes the sample's scattering, and the resolution function. Mathematically, this can be expressed as

$$I(\boldsymbol{Q}_0, E_0) = \int \frac{d^2\sigma}{d\Omega dE}(\boldsymbol{Q}, E)\ R(\boldsymbol{Q} - \boldsymbol{Q}_0, E - E_0) d\boldsymbol{Q} dE, \tag{2.34}$$

where $I(\boldsymbol{Q}_0, E_0)$ is the intensity measured at the point $(\boldsymbol{Q}_0, E_0)$. The resolution function is most commonly expressed as a constant deviation contour centred around $(\boldsymbol{Q}_0, E_0)$. This describes a four-dimensional ellipsoid and is defined for each detector position in a spectrometer. The full resolution function is dependant on various instrumental parameters and is very complicated. Computer programs, such as TobyFit [40], allow the complete resolution function to be calculated for a chopper spectrometer and convolved with an analytic model of the scattering function. However, in most cases this is computationally intensive and unnecessary. Instead an approximate broadening function is applied, based on the dominant resolution

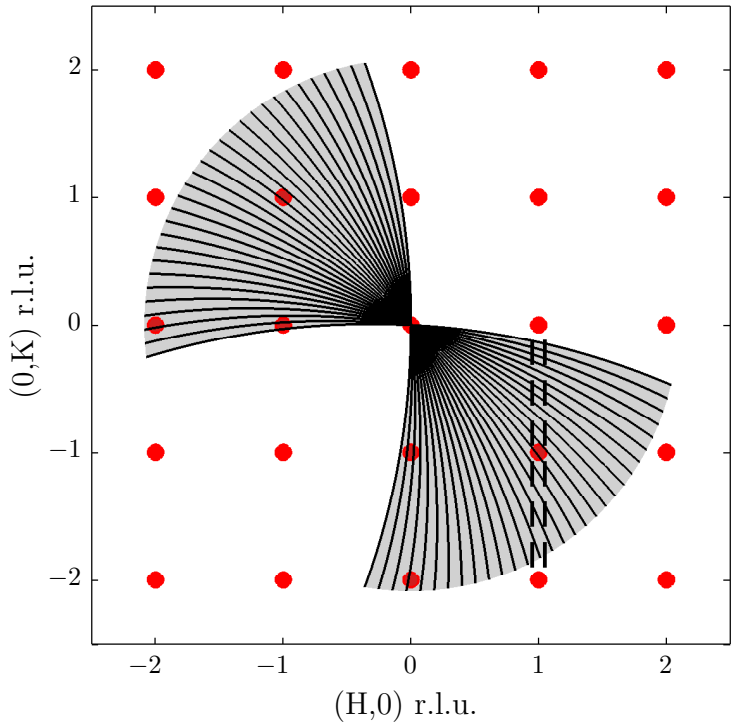

Figure 2.5: Schematic diagram of the combined reciprocal space coverage of a multi-angle scan made using a chopper spectrometer. The in-plane detector coverage for elastic scattering is shown for each 3° incremental measurement by the black arcs. The detector coverage is calculated for a 40° detector bank (such as the MAPS low-angle bank) using $E_\mathrm{i} = 75$ meV. The reciprocal lattice for a square lattice with $a = 2\pi$ Å is plotted (red circles) as an example crystal. The grey region shows the area of reciprocal space contained in the Horace data volume after combining the information from the individual measurements. The black dashed lines illustrates the limits of an example integrated line cut through the data volume. This cut along the $(1, K)$-direction combines the measured intensity from many of the fixed orientation scans.

effects, along a single dimension of $(\boldsymbol{Q}, E)$.

Commonly, the E resolution (and equivalently the $\boldsymbol{Q}_\parallel$ resolution) is the most significant broadening effect on a measured spectrum. It is dependent on the slit size and frequency of the chopper, and the initial pulse width from the moderator (see Ref. [41]). The energy uncertainty arising from the Fermi chopper can be expressed as

$$\Delta E_\mathrm{ch} = 2E_\mathrm{i}\Big(\frac{\Delta t_\mathrm{ch}}{t_\mathrm{ch}}\Big)\Big[1 + \frac{L_1 + L_3}{L_2}\Big(1 - \frac{E}{E_\mathrm{i}}\Big)^{3/2}\Big], \tag{2.35}$$

where Δt_{ch} is the time duration neutrons can pass through the chopper; t_{ch} is the neutron's TOF from the chopper to the sample; and L_1, L_2, and L_3 are the moderator to chopper, chopper to sample, and sample to detector distances respectively. Similarly, the energy uncertainty due to the moderator is expressed as

$$\Delta E_{\mathrm{mod}} = 2E_{\mathrm{i}}\Big(\frac{\Delta t_{\mathrm{mod}}}{t_{\mathrm{mod}}}\Big)\Big[1+\frac{L_3}{L_2}\Big(1-\frac{E}{E_{\mathrm{i}}}\Big)^{3/2}\Big], \tag{2.36}$$

where, Δt_{mod} is the width of the moderator pulse and t_{mod} is the neutron's TOF from the moderator to chopper. These expressions can be added in quadrature to give an expression for the total energy uncertainty. It is apparent from the above expressions that ΔE will decrease with increasing E.

The $\boldsymbol{Q}_{\perp}$ resolution is due to the uncertainty of the scattering angle and so is dependent on the beam divergence. The finite size of the sample and detector can affect the beam divergence, however, it is the angular width of the moderator as seen from the sample that is the dominate contribution. Neutron guides (like that on the MERLIN spectrometer) will also increase the beam divergence and further diminish the $\boldsymbol{Q}_{\perp}$ resolution. While the $\boldsymbol{Q}_{\perp}$ resolution introduces a $\boldsymbol{Q}$ dependent broadening, it is significantly overshadowed by the E resolution in nearly all experimental cases. For this reason, a separate treatment of the $\boldsymbol{Q}_{\perp}$ resolution is typically omitted from any data analysis. The $\boldsymbol{Q}_{\parallel}$ resolution is equivalent to the energy resolution (because of the coupling of $\boldsymbol{Q}_{\parallel}$ and E) so is not considered separately.

The chopper spectrometer also allows the measured scattering intensities to be easily converted into absolute units. This requires a normalisation of all the detector efficiencies and is achieved by measuring a known vanadium standard sample. Results obtained in absolute units can then be directly compared to derived models of the partial differential cross-section.

2.3.3 The Triple-Axis Spectrometer

The triple-axis spectrometer (TAS) is the original and most commonly used method of measuring excitations within condensed matter systems. Figure 2.6 shows a schematic diagram of a TAS. In place of a chopper, a *monochromator* is used to select the incident neutron wave vector. The monochromator is a single crystal positioned such that the scattering angle, $2\theta_{\mathrm{M}}$, corresponds to a strong Bragg peak for a particular neutron wave vector. Typically, the monochromator crystal is pyrolytic graphite (PG), Si, or Cu. A *filter* (typically made from PG or sapphire) is placed before the sample to reduce the intensity of higher order Bragg peaks (ie. $2\boldsymbol{k}_{\mathrm{i}}$, $3\boldsymbol{k}_{\mathrm{i}}$, etc). The *analyser* is functionally the same as the monochromator, but it selects the measured final wave vector through the choice of the $2\theta_{\mathrm{A}}$ scattering angle. Hence, by specifying $2\theta_{\mathrm{M}}$, ϕ, and $2\theta_{\mathrm{A}}$ a specific $\boldsymbol{k}_{\mathrm{i}}$ and $\boldsymbol{k}_{\mathrm{f}}$ are selected, which correspond to an individual position in $(\boldsymbol{Q}, E)$-space. Experiments are then performed by measuring the intensity along a particular high-symmetry $\boldsymbol{Q}$ or E direction so that a line cut is taken through the spectrum.

High intensity background scattering can significantly affect the ability of a TAS to measure weakly scattering excitations. Spurious peaks can arise due to Bragg scattering from instrumental components exposed to any section of the beam as well as higher order scattering effects within the sample. The detector, monochromator and analyser all have extensive shielding to reduce the effects of background radiation and neutrons. Additionally, monitors (low efficiency neutron detectors) are placed in the incident and final beams to track the relative intensities at each stage of the scattering process. In many cases, this provides an indication as to whether a measured signal is spurious, but only an understanding of the physics of the sample allows spurious peaks to be identified unambiguously.

As with the chopper spectrometer, the resolution function of the TAS must be considered when analysing data. The resolution of a TAS is principally determined by the beam divergence along all three axes. To improve the flux, arrays of single

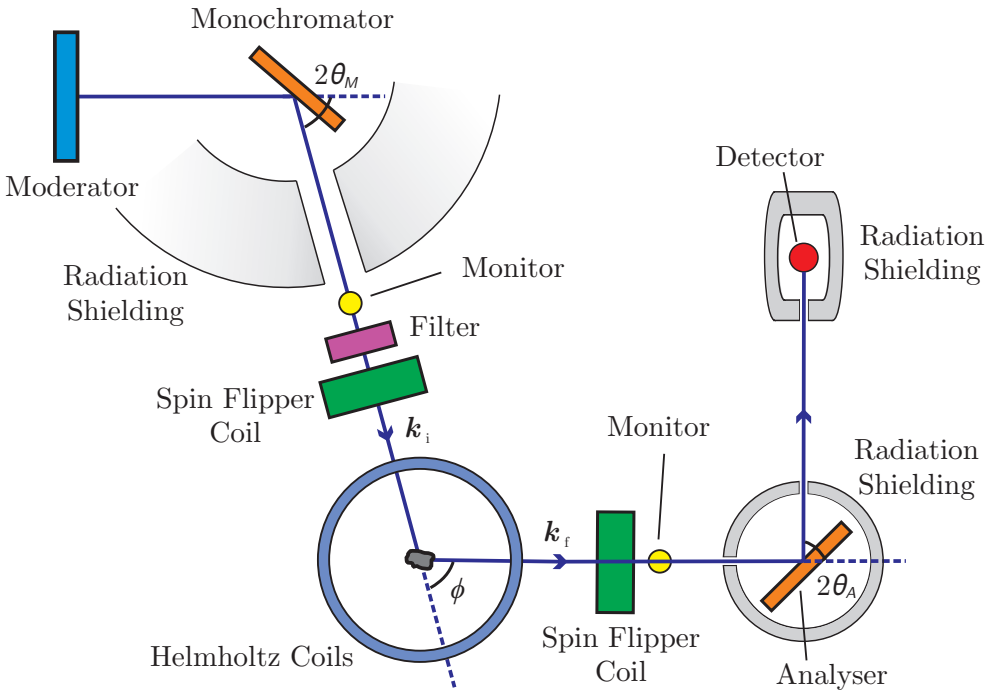

Figure 2.6: Schematic diagram of a triple-axis spectrometer with polarisation analysis capabilities. The components and variables labelled are described in the main text. Note, the guide field, necessary for polarisation analysis is not depicted to simplify the diagram.

crystals are used as the monochromator and analyser, aligned to focus the neutron beam horizontally and vertically. However, focussing will reduce the resolution. Horizontally focussing the monochromator increases the incident flux at the expense of wave vector resolution (but not energy resolution). Vertical focussing on either monochromator or analyser will increases the flux but worsen the out-of-plane wave vector resolution. Flat, single or double focussing monochromators and analysers are all used in different experiments depending on the requirements. The orientation of the resolution ellipsoid in a TAS is dependent upon the particular orientation of the spectrometer axes for a given $(\boldsymbol{Q}, E)$-position. Therefore, the resolution changes across a line cut and can be substantially different when measuring in different Brillouin zones. This changing resolution can complicate the analysis of TAS data as symmetric features in the spectrum can be measured with different widths and

intensities. Programs, such as RESCAL [42] and RESTRAX [43], exist to calculate the resolution function and simulate its effect on a given line cut.

TAS with Polarisation Analysis

A great benefit of the triple-axis spectrometer is the relative ease with which polarised neutrons can be produced and analysed. In this section I will introduce the additional instrumentation required to perform uniaxial polarisation analysis on a TAS. While there are various techniques that can be employed to polarise neutrons and subsequently manipulate that polarisation, I shall introduce the specific examples used on the IN20 spectrometer at the ILL and employed to study CuO in Chapter 4.

Any polarised neutron experiment first requires a method of polarising the incident neutron beam. This is achieved in a TAS by using a ferromagnetic monochromator crystal. The ferromagnetic moment is aligned perpendicular to the scattering vector and the cross-section is polarisation dependent. Therefore, there are two expressions of the differential cross-section describing scattering for the spin-up and spin-down neutrons,

$$\left(\frac{d\sigma}{d\Omega}\right)_{\uparrow} = \mid F_{\mathrm{N}}(\boldsymbol{Q}) + F_{\mathrm{M}}(\boldsymbol{Q}) \mid^2 \tag{2.37}$$

$$\left(\frac{d\sigma}{d\Omega}\right)_{\downarrow} = \mid F_{\mathrm{N}}(\boldsymbol{Q}) - F_{\mathrm{M}}(\boldsymbol{Q}) \mid^2 . \tag{2.38}$$

To obtain a fully polarised neutron beam a monochromator with $F_{\mathrm{N}}(\boldsymbol{Q}) = F_{\mathrm{M}}(\boldsymbol{Q})$ is used to suppress the spin-down cross-section. This condition is well satisfied by a Heusler crystal.[6]

Once the incident neutron beam is polarised, this polarisation is maintained by applying a constant *guide field* along the neutron flight path. The polarisation can then be manipulated by two components: the spin-flipper coils; and the Helmhotz

[6] 'Heusler alloy' refers to a group of ferromagnetic intermetallic materials. However, in polarised neutron scattering 'Heusler cyrstal' has come to refer specifically to the Heusler alloy Cu_2MnAl which can be grown as a large single crystal.

coil (Figure 2.6).

The spin-flipper is included to rotate the polarisation by 180° with respect to the spectrometer. This is achieved by applying a magnetic field $\boldsymbol{B}_{\mathrm{SF}}$ perpendicular to the initial polarisation. The neutron will precess around the field and, hence, the polarisation can be set to any arbitrary direction in the plane perpendicular to $\boldsymbol{B}_{\mathrm{SF}}$. By considering the velocity of the neutron, v, and the distance, d, it travels through the coil, the field can be tuned to produce a 180° rotation of the polarisation using the relation $|\boldsymbol{B}_{\mathrm{SF}}| = \pi v/\gamma_{\mathrm{n}} d$.

The spin-flipper in conjunction with a Heusler crystal monochromator and analyser enables uniaxial polarisation analysis. This allows the four matrix elements introduced in Eqs. 2.31 and 2.32 to be individually measured. However, due to the imperfect nature of instrumentation, each measured matrix element (or channel) can also include some signal associated with the other channels. The combined effects of imperfect polarisation, flipper efficiency, and guide field inhomogeneity can be quantified by the *flipping ratio*, R, which is defined as

$$R = \frac{I_{\mathrm{NSF}}}{I_{\mathrm{SF}}} = \frac{1 + f_1 f_2}{1 - f_1 f_2}, \tag{2.39}$$

where f_1 and f_2 are the polarising efficiencies of the incident and final neutron flight paths and take values in the range $0 < f < 1$. Figure 2.7 shows the relative ratios of the four scattering processes in terms of these efficiencies. The neutron beam is considered to start in a 100% spin-up polarised state and undergoes NSF nuclear scattering at the sample. Hence, in a perfect instrument only $|\uparrow_1\uparrow_2\rangle$ scattering should have any measured intensity. However, the figure shows that there will be neutrons detected in the SF channel due to NSF scattering, and vice-versa. This is due to the polarisation efficiencies not being 100% in both the incident and final flight paths. By measuring the flipping ratio on a purely nuclear or magnetic Bragg peak, this leakage of intensity can be corrected after the measurements.

The Helmholtz coil allows the different components of the magnetisation to be

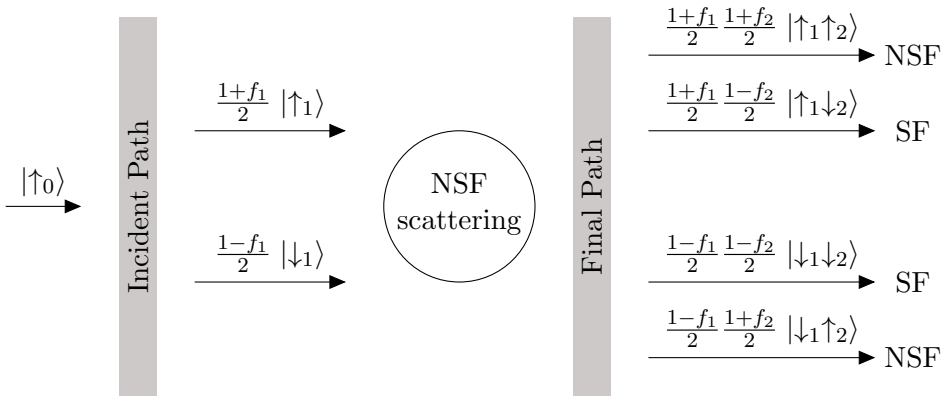

Figure 2.7: Neutron depolarisation and the measured matrix elements in a nuclear scattering (NSF) process. Before scattering, a fully polarised neutron beam (labelled $|\uparrow_0\rangle$) will depolarise due to stray fields before it reaches the sample. Therefore, upon reaching the sample, the neutron beam is comprised of both polarised ($|\uparrow_1\rangle$) and depolarised ($|\downarrow_1\rangle$) neutrons. The population of neutrons in each state is characterised by the efficiency f_1. Scattering via the nuclear interaction does not change the neutron's polarisation. After scattering, the neutrons are again subjected to stray fields on the final beam flight path, again causing depolarisation (characterised by the efficiency f_2). The detected polarisation states are indicated by $|\uparrow_2\rangle$ and $|\downarrow_2\rangle$. All four matrix elements from Eqs. 2.31 and 2.32 are present in the final beam. Each is labelled SF or NSF to denote which channel the intensity will be attributed to in the experiment.

distinguished by adiabatically changing the polarisation direction to any arbitrary direction at the sample. Conventionally, three orthogonal polarisations are used, defined as x parallel to $\boldsymbol{Q}$; y perpendicular to x and within the scattering plane; and z perpendicular to both x and y.

2.3.4 Sample Environment

All of the INS measurements were performed at low temperatures. This ensured that the measured excitations arose from the sample's ground state. On MAPS and MERLIN, this was achieved by using a closed-cycle refrigerator (CCR) which reached a base temperature of approximately 6K. The sample space was filled with low pressure ^{4}He-gas to act as a thermal exchange medium. The IN8 and IN20 experiments used top-loading ^{4}He cryostats. ^{4}He-gas was again used as an exchange medium. The sample achieved a base temperature of approximately 1.5K using this method.

The samples were secured in the sample space on custom made aluminium mountings. These were designed to position the sample in a particular crystallographic orientation while minimising the amount of Al in the beam. While Al is generally regarded as being transparent to neutrons, it does have a very small scattering cross-section. Hence, a background Al powder diffraction pattern is measured in INS experiments due to the mounting. Ensuring the use of the smallest amount of Al minimises this background. Additionally, Cd – as a strong absorber of thermal neutrons – is used to shield all the components of the mounting outside of the beam. This reduces intensity from secondary scattering processes which can cause spurious peaks.

2.4 Sample Characterisation Techniques

Samples used in each INS experiment had to undergo rigorous characterisation to understand their chemical composition, crystal structure and magnetic behaviour. This section describes the variety of characterisation techniques employed.

2.4.1 SQUID Magnetometry

Magnetometry can characterise the magnetic order and phase transitions exhibited by a material. Typically, the magnetic susceptibility is measured which allows a direct comparison of the magnetic properties of different samples. A superconducting quantum interference device (SQUID) magnetometer has been used for all the results presented in this thesis. A SQUID is comprised of a superconducting ring with two Josephson junctions dividing it into semi-circles. Each semi-circular piece is connected to an external current source. The current flowing through the SQUID varies with the phase difference across each Josephson junction as well as the flux through the ring. This effect can be exploited to measure a magnetic field by measuring the critical current of the SQUID ring which oscillates with increasing flux [9]. For the purposes of magnetometry, a sample is passed through the SQUID

ring allowing the sample's magnetisation perpendicular to the ring to be measured. In materials with no net magnetisation (such as an antiferromagnet), a magnetic field must be applied to induce a net moment which can then be measured by the SQUID.

A Quantum Designs MPMS SQUID was used for all the magnetometry measurements presented. Small fragments of the single crystal used in the neutron experiments were aligned with respect to the SQUID ring, accurate to within 10°. The SQUID samples typically had the dimensions $2 \times 2 \times 2$ mm and the sample mass was accurately measured to allow the susceptibility to be expressed per mole of material.

2.4.2 EPMA

Electron Probe Microanalysis (EPMA) is an electron-in-photon-out technique that is able to measure the relative proportion of elements in a given sample with respect to a known standard material [44]. X-rays are produced by the inelastic collision of incident electrons with an atom's core electrons. The core electrons are ejected by the collisions, leaving holes which are filled as electrons in higher energy atomic orbitals fall to the lower energy state through the emission of an X-ray. The X-rays have characteristic wavelengths associated with the particular transitions within an atom. Therefore, measuring the relative intensity of X-rays produced by known atomic transitions allows the relative chemical composition of a sample to be measured. EPMA is most sensitive to heavier elements with more clearly defined electron energy levels. Lighter elements, where the electronic structure is significantly altered due to bonding are harder to measure accurately. Therefore, EPMA offers an accurate measure of the heavy element composition of a sample. A Jeol JXA-8600 was used to determine the precise doping in a series of $La_{2-x}Sr_xCoO_4$ sample, reported in Chapter 3.

2.4.3 X-ray Powder Diffraction

X-ray powder diffraction (XRPD) is a scattering technique similar to the neutron case outline in Section 2.2. Using X-rays as the scattering probe has the advantage that high fluxes can be easily produced. Therefore, X-ray diffraction can be performed in a laboratory experiment. X-rays interact with the electrons within an atom and so the scattering cross-section is proportional to atomic number. This means X-rays are not very sensitive to lighter elements if heavier elements are also present in a material.

The X'Pert PRO PANalytical diffractometer was used for all XRPD sample characterisation measurements in this thesis. The diffractometer uses X-rays created by accelerating electrons in a potential difference and targeting them onto a metal plate. The ensuing collision creates X-rays through the same process as described for EPMA. The target material (typically Cu or Mo) is chosen such that the emission spectrum is dominated by a single wavelength, λ. These X-rays go on to scatter from the powdered sample when satisfying the Bragg equation,

$$n\lambda = 2d_{hkl}\sin(\theta), \tag{2.40}$$

where n is an integer; d_{hkl} is the inter-atomic distance defined by the Miller indices (h, k, l). The scattering angle, 2θ, and relative intensities of the measured Bragg peaks allow the lattice parameters and crystal structure of the sample to be found through Reitveld refinement of the data (using software such as FullProf [45]). Relative site occupation in doped materials can also be quantified.

2.4.4 X-ray and Neutron Laue Diffraction

Laue diffraction is a single-crystal scattering technique. A incident beam of polychromatic neutrons or X-rays is used to simultaneously satisfy all Bragg scattering conditions (in accordance with Eq. 2.40). A large area detector is used to measure

the resulting Bragg peaks. This technique is principally used to align a sample on its mounting or check the quality of a single crystal by measuring the mosaic and identifying any additional grains. X-ray Laue was primarily performed on a custom built diffractometer in the Clarendon Laboratory. Neutron Laue was performed on the OrientExpress instrument at the ILL and the ALF instrument at the ISIS facility.

2.4.5 Thermo-Gravimetric Analysis

Thermo-gravimetric analysis (TGA) is a technique in which the mass of a small powdered sample is very accurately measured as a function of temperature. The application of heat while the sample is in a reducing atmosphere will breakdown a material into a selection of constituent compounds. Knowing what final compounds are produced and measuring the initial and final mass of the sample allows any difference from the expected stoichiometry to be quantified. This is an especially useful technique for testing the oxygen stoichiometry of a sample where TGA is accurate enough to measure $\sim 1\%$ shifts away from the stoichiometric values. This far exceeds the accuracy of X-ray probes which are not sensitive to the lighter elements. TGA measurements for this thesis were performed on a Perkin Elmer Diamond TG/DTA.

Chapter 3

Hour-Glass Magnetic Excitation Spectrum in $La_{1.75}Sr_{0.25}CoO_4$

Contents

3.1 Introduction

The hour-glass spectrum is a special form of magnetic excitation spectrum which has been observed in neutron scattering measurements on a variety of quasi-two

dimensional (2D) layered systems. It is characterised by low-energy incommensurate excitation branches dispersing inwards to the antiferromagnetic (AFM) wave vector [$\boldsymbol{Q}_{\mathrm{AFM}} = (0.5, 0.5)$ when defined in reciprocal lattice units for a square lattice]; a broad, near-vertically dispersing intensity centred on $\boldsymbol{Q}_{\mathrm{AFM}}$ at intermediate energies; and high-energy outwardly dispersing modes rotated 45° with respect to the low energy branches. This spectrum was initially measured in a variety of the cuprate high-T_{c} superconductors [46–56]. In the cuprates, the distinctive form has been attributed to either stripe-like correlations in strong coupling models or to quasiparticle transitions across the Fermi surface in itinerant, weak-coupling models [15]. Unravelling the origins of the hour-glass spectrum will reveal more about the nature of magnetism in the doped cuprates. This is crucial in order to better understand the superconductivity, which is so intimately related to magnetism in these compounds.

Recently, a similar hour-glass spectrum has been discovered in layered cobaltate [57, 58] and manganate materials [59]. These insulating materials provide an interesting comparison to the cuprates due to their significantly different electronic properties. The existence of an hour-glass spectrum in each of these varied systems points toward some common origin arising from particular magnetic correlations. The localised electrons in the cobaltates and manganates allow the hour-glass spectrum to be understood through the lens of linear spin wave theory (LSWT). Such an analysis indicates that short-range quasi-one-dimensional (1D) magnetic correlations give rise to an hour-glass spectrum. These conditions are found in layered materials with disordered stripe phases.

Stripe ordering is a simultaneous charge and magnetic ordering. It occurs in doped AFM systems whereby the charges arrange themselves into 1D arrays and form domain walls, which modulate the background AFM order. Different varieties of such order have been observed in the cuprates [54, 55, 60, 61], nickelates [62–64], manganates [65], and cobaltates [66]. Stripe ordering is found alongside

magnetic disorder in many of these materials. This is evidenced by spin glass behaviour measured in the magnetisation of stripe ordered cuprates [67], nickelates [68], and cobaltates [69]. How disorder affects the hour-glass is of particular interest in systems which are subtly tuned by doping.

In this chapter, I shall present inelastic neutron scattering (INS) measurements of the excitation spectrum of $La_{1.75}Sr_{0.25}CoO_4$. The spectrum of a quarter-doped layered cobaltate has not been reported before. As I shall show, the data reveals an hour-glass magnetic spectrum consistent with short range period-4 stripe order. The spectrum differs from previously measured hour-glasses as it exhibits a greater level of disorder. To model the results, the cluster glass model proposed for $La_{1.67}Sr_{0.33}CoO_4$ by Andrade, *et al.* [70] has been extended for the case of one-quarter doping. I shall demonstrate that this model qualitatively reproduces all the main features of the spectrum.

3.1.1 Charge and Magnetic Order in $La_{2-x}Sr_xCoO_4$

The $La_{2-x}Sr_xCoO_4$ family crystallises into a perovskite structure as shown in Figure 3.1(a). Two-dimensional CoO_2 layers are separated by La ions, and Co exists in an octahedral crystal field environment created by the surrounding oxygen atoms. In the $x = 0$ parent compound, the Co ions exist in the Co^{2+} valence state. Due to the particular crystal field, the e_g and t_{2g} 3d orbitals are non-degenerate. The outer electrons of the Co^{2+} ions experience a dominant coulomb repulsion in this crystal field and therefore occupy an $S = 3/2$ high-spin (HS) state – see Figure 3.1(b). Furthermore, the crystal field in combination with spin-orbit coupling constrains the spins to lie within the CoO planes and they subsequently order antiferromagnetically. The simple AFM structure of the parent compound is shown in Figure 3.2(a).

The system can be doped through the substitution of Sr in place of La atoms. Sr is in a lower valence state than La and so doping creates Co^{3+} ions in the CoO layers. Crystal field calculations show that Co^{3+} ions can occupy the near degenerate $S = 0$

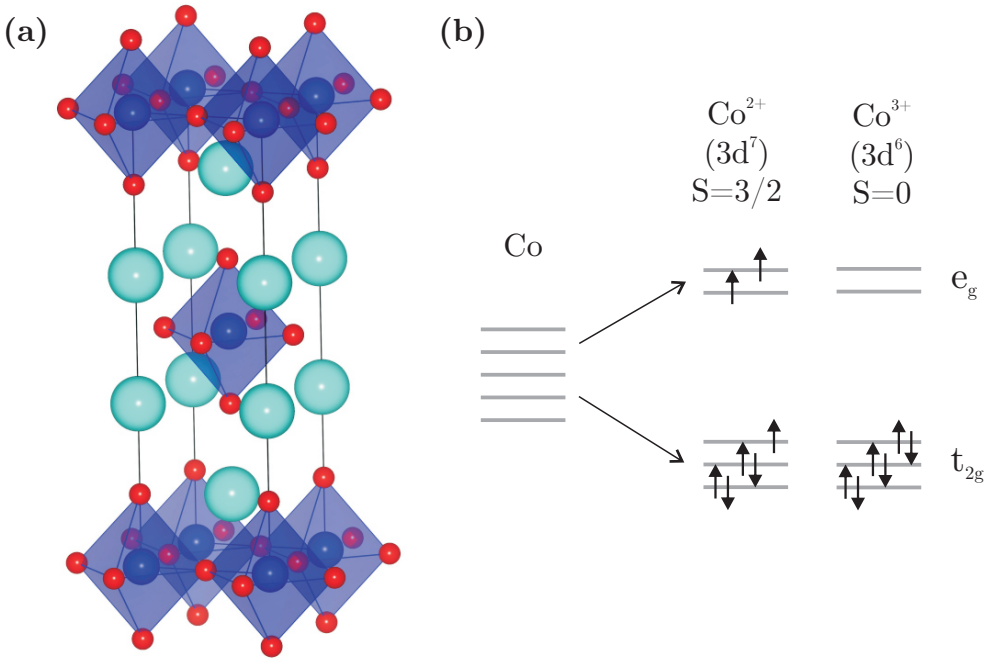

Figure 3.1: Crystal structure of $La_{2-x}Sr_xCoO_4$ and the spin state of Co^{2+} and Co^{3+} ions. (a) $La_{2-x}Sr_xCoO_4$ is described by a tetragonal crystal structure at low temperatures. Co, O and La (or Sr) atoms are shown as blue, red and cyan spheres respectively. The Co ions are at the centre of a locally octahedral oxygen environment (as depicted by the blue shaded octahedron). The octahedral crystal field lifts the e_g and t_{2g} orbital degeneracy in $La_{2-x}Sr_xCoO_4$. (b) This crystal field creates an $S = 3/2$ HS state in the Co^{2+} ion and an $S = 0$ LS state in the Co^{3+} ion in the low doped $La_{2-x}Sr_xCoO_4$ compounds, with depicted electronic configurations.

low-spin (LS), $S = 1$ intermediate-spin (IS), or $S = 2$ HS states. The measured anisotropic susceptibility has been shown by Hollmann, *et al.* [71] to rule out all but the LS state of Co^{3+} ions in $0.4 < x < 0.8$ samples – see Figure 3.1(b). This analysis was extended to describe the spin state of $x = 0.33$ samples, which showed similar anisotropies [57]. Across the different dopings, Co^{2+} ions remain in the HS state.

Checkerboard charge ordering of the Co^{2+} and Co^{3+} ions has been directly measured in $x = 0.5$ doped samples [72]. Additionally, in-plane AFM ordering of the Co^{2+} ions has been measured in these half doped samples [72, 73]. This ordering is depicted in Figure 3.2(d). At lower dopings with $0.3 \leq x < 0.5$, magnetic order

consistent with stripe order is observed [66], however, no direct measurements of the charge ordering have so far been reported. This has called into question how accurately the perfect stripe description applies to lower doped $La_{2-x}Sr_xCoO_4$ samples. On the basis of measurements of an $x = 0.4$ doped sample, it was suggested that a chiral or non-collinear magnetic state emerges from the well defined checkerboard order at half doping [58]. Alternatively, a model for $x = 0.33$ doped samples points to short range stripe correlations in a cluster glass ground state [70]. Both these states combine short-range magnetic order with some amount of charge disorder.

Generally, $La_{2-x}Sr_xCoO_4$ stripes have the non-magnetic Co^{3+} ions condense into 1D chains parallel to the $[1, 1, 0]$ and equivalent $[1, \bar{1}, 0]$ directions. The Co^{2+} ions order antiferromagnetically in the regions between the Co^{3+} ions. Figure 3.2(c) illustrates the perfect period-3 stripe order measured in $x = 0.33$ samples. Figure 3.2(b) shows perfect period-4 stripe order proposed for $La_{2-x}Sr_xCoO_4$ with $x = 0.25$.

Stripe order has a longer periodicity than the underlying AFM order and so is described by a larger magnetic unit cell – see Figure 3.2. Therefore, striped correlations lead to incommensurate magnetic peaks distributed around the AFM wave vector. In the case of the diagonal stripes observed in the cobaltates, these magnetic peaks are at wave vectors $\mathbf{Q}_{\mathrm{m}} = \mathbf{Q}_{\mathrm{AFM}} \pm (\zeta, \zeta)$ and $\mathbf{Q}_{\mathrm{AFM}} \pm (\zeta, -\zeta)$. The value of the incommensurate splitting ζ is related to the periodicity of the stripe order [74]. Hence, it depends on the total doping of the system by the relation

$$2\zeta = n_{\mathrm{h}} = x + 2\delta, \tag{3.1}$$

where the total number of holes in the system n_{h} is related to both the Sr doping x and oxygen excess δ.

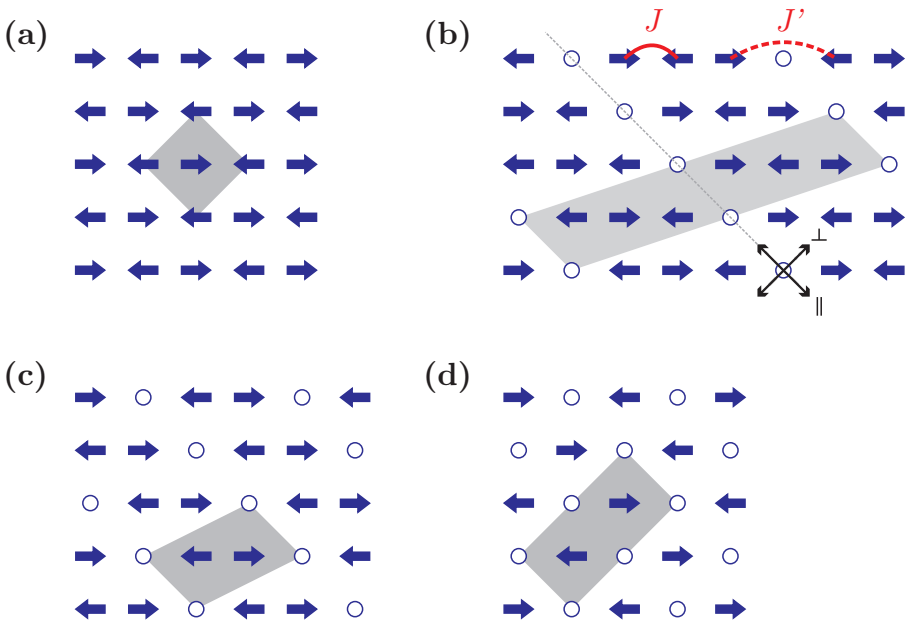

Figure 3.2: The 2D magnetic order in $La_{2-x}Sr_xCoO_4$. In all diagrams, the Co^{2+} spin direction is represented by the blue arrow while the non-magnetic Co^{3+} ions are denoted by open blue circles. (a) The nearest neighbour AFM order in the La_2CoO_4 compound. (b) Perfect period-4 stripe order proposed for $La_{1.75}Sr_{0.25}CoO_4$. The dashed line highlights a 1D stripe of Co^{3+} ions. The black arrows indicate the directions parallel (||) and perpendicular ($\perp$) to the stripe. Intra- and inter-stripe exchange interactions are labelled as J and J' respectively. (c) The perfect period-3 stripe order reported in $La_{1.67}Sr_{0.33}CoO_4$. (d) Checkerboard charge ordering with AFM order of the Co^{2+} ions measured in $La_{1.5}Sr_{0.5}CoO_4$. In all structures, the magnetic unit cell is shown as a shaded grey area.

3.1.2 Description of Magnetic Excitations in $La_{2-x}Sr_xCoO_4$

Excitation spectra have been measured in a variety of the layered cobaltates. Various models have been used to describe the magnetic excitations observed. An effective $S = 1/2$ Heisenberg exchange model successfully describes the low energy spectral features in $x = 0.5$ and $x = 0$ samples [73, 75]. For both dopings, this simplified model was extended to spin $S = 3/2$ and the $L = 3$ orbital angular momentum was introduced to describe the full spectrum. This same $S = 3/2$ model was shown in Ref. [57] to provide a good description of the hour-glass spectrum measured in samples with $x = 0.33$ after some phenomenological broadening was introduced to the simulated spectrum. The narrowed intensity centred on $\boldsymbol{Q}_{\mathrm{AFM}}$ at

intermediate energies – creating the thin waist of the hourglass – is formed because of the respective strengths of intra- and inter-stripe exchange. Hence, the ratio of the exchange parameters determines the energy position of the waist and can lead to a suppression of the hour-glass spectrum, as observed in the stripe ordered nickelates [76, 77].

In order to better understand the disorder which broadens the spectrum in the cobaltates, a disordered cluster spin glass (DCSG) model was developed for $x = 0.33$ doped samples [70]. This uses the simplified $S = 1/2$ model and neglects spin orbit coupling and the crystal field effects present in layered cobaltates. The proposed DCSG ground state is characterised by both local stripe and AFM orders, which leads to frustrated magnetic behaviour. This model demonstrates that both the energy position of the hour-glass waist and the suppression of the outwardly dispersing low energy branches are tuned by the disorder. In the case of the waist position, this is in addition to the ratio of inter- and intra-stripe exchange parameters. It is interesting to note that the suppression of the outwardly dispersing branches has been experimentally tuned in a manganate system by introducing thermal disorder [59].

3.2 Sample Growth and Characterisation

3.2.1 Crystal Growth

Three single crystals with different Sr doping were grown using the optical floating-zone method by Dr Prabhakaran in the Clarendon Laboratory. Initially, polycrystalline $La_{1.75}Sr_{0.25}CoO_4$, $La_{1.7}Sr_{0.3}CoO_4$, and $La_{1.67}Sr_{0.33}CoO_4$ were separately prepared from La_2O_3, $SrCO_3$ and Co_3O_4 (>99.99% purity) by solid-state reaction. The starting materials were reacted in air at 1200 °C for 48 h then reground and sintered in air at 1225 °C for 48 h. No impurity phases could be detected in the product by x-ray powder diffraction (XRPD). The powders were then pressed into rods and sintered in air at 1250 °C for 24 h. The crystal growth was performed in a four-

mirror image furnace in flowing high purity argon at a growth speed of 2 mm h^{-1} with counter-rotation of the feed and seed rods at 25 rpm for each sample. Previous experimental growths of $La_{2-x}Sr_xCoO_4$ compounds have shown that it is difficult to achieve oxygen stoichiometry, with most as-grown crystals having an excess of oxygen when $x \lesssim 0.3$. To achieve stoichiometry, the three as-grown crystals underwent an anneal in a reducing atmosphere of CO_2:CO at 850 °C for 12 h. This process produced single crystals of 14.3 g ($La_{1.75}Sr_{0.25}CoO_4$), 13.6 g ($La_{1.7}Sr_{0.3}CoO_4$), and 9.1 g ($La_{1.67}Sr_{0.33}CoO_4$) for INS experiments.

3.2.2 Compositional Analysis

$La_{2-x}Sr_xCoO_4$ samples with low doping are difficult to grow as large single crystals and, as mentioned above, have shown a tendency to stray from their stoichiometric oxygen composition. Therefore, various techniques were employed to check the quality of each single crystal and determine its chemical composition. These checks have revealed discrepancies between the composition expected from the ratio of initial oxides in the growth and in the final samples. The discrepancy was very small for the $La_{1.75}Sr_{0.25}CoO_4$ crystal but the $La_{1.7}Sr_{0.3}CoO_4$ and $La_{1.67}Sr_{0.33}CoO_4$ crystals exhibited significant deviations from their nominal composition. In this section I shall introduce the compositional analysis performed and the conclusions that can be drawn about each crystal.

XRPD was used to test that the crystals were single-phase and of high-quality. Figure 3.3(a) shows an example diffraction pattern using a powdered sample of the $La_{1.75}Sr_{0.25}CoO_4$ single crystal. Powdered measurements of all single crystals were performed at 300 K. No secondary phases can be seen in the $La_{1.75}Sr_{0.25}CoO_4$ or $La_{1.7}Sr_{0.3}CoO_4$ samples and the structures were refined in the $I4/mmm$ space group. The lattice parameters were slightly different in each of the samples. The refined parameters were $a = 3.86348(7)$ Å and $c = 12.6193(3)$ Å for $La_{1.75}Sr_{0.25}CoO_4$ and $a = 3.85937(6)$ Å and $c = 12.6299(3)$ Å for $La_{1.7}Sr_{0.3}CoO_4$. The diffrac-

tion pattern of the $La_{1.67}Sr_{0.33}CoO_4$ sample exhibits a slight splitting of some peaks. The $(1, 0, 7)$ ($d \approx 1.63$ Å) and $(1, 1, 6)$ ($d \approx 1.66$ Å) peaks measured in the $La_{1.75}Sr_{0.25}CoO_4$ and $La_{1.67}Sr_{0.33}CoO_4$ samples are presented in Figures 3.3(b) and 3.3(c) respectively. The splitting can be seen in the $La_{1.67}Sr_{0.33}CoO_4$ data, manifesting as a small shoulder at lower d-spacing. Such slight splitting is unlikely due to a different compound being present. Rather, it may indicate a phase with slightly different lattice parameters or a small reduction in the tetragonal symmetry. Either of these possibilities point towards a fluctuation in the oxygen content and similar effects have been seen before in the isostructural cuprates [78] and nickelates [79]. Unfortunately, the splitting is too small to allow an accurate refinement of both $La_{1.67}Sr_{0.33}CoO_{4+\delta}$ phases. A single phase refinement with the $I4/mmm$ space group found $a = 3.85714(6)$ Å and $c = 12.6146(4)$ Å lattice parameters. For the sharper diffraction patterns in $La_{1.75}Sr_{0.25}CoO_4$ and $La_{1.7}Sr_{0.3}CoO_4$ samples, it was possible to refine the content of La and Sr. This was done by assuming the total occupancy of the La/Sr site to be stoichiometric. The results are outlined in Table 3.1.

Electron Probe Microanalysis (EPMA) was also used to measure the relative ratios of the metal ions in the samples. Measurements were taken at ten positions on a sample's surface. These were averaged to improve accuracy and the standard deviation provides an estimate of the random error. The ratios are normalised to the nominal La content.[1] The measured values of x are presented in Table 3.1. The results show that all samples appear to be under-doped with respect to the nominal values. This is very significant in the case of $La_{1.7}Sr_{0.3}CoO_4$, which is closer to the nominal doping of $x = 0.25$. It is important to note that, while the errors recorded are small, they do not account for systematic errors in the calibration.

This compositional analysis demonstrates that $La_{2-x}Sr_xCoO_4$ continues to be a challenging system for large single-crystal growth. The $La_{1.75}Sr_{0.25}CoO_4$ sample

[1]The La content is expected to be closest to its weighed growth value as La_2O_3 has the highest melting point of all the starting oxides and so is least likely to escape the reaction.

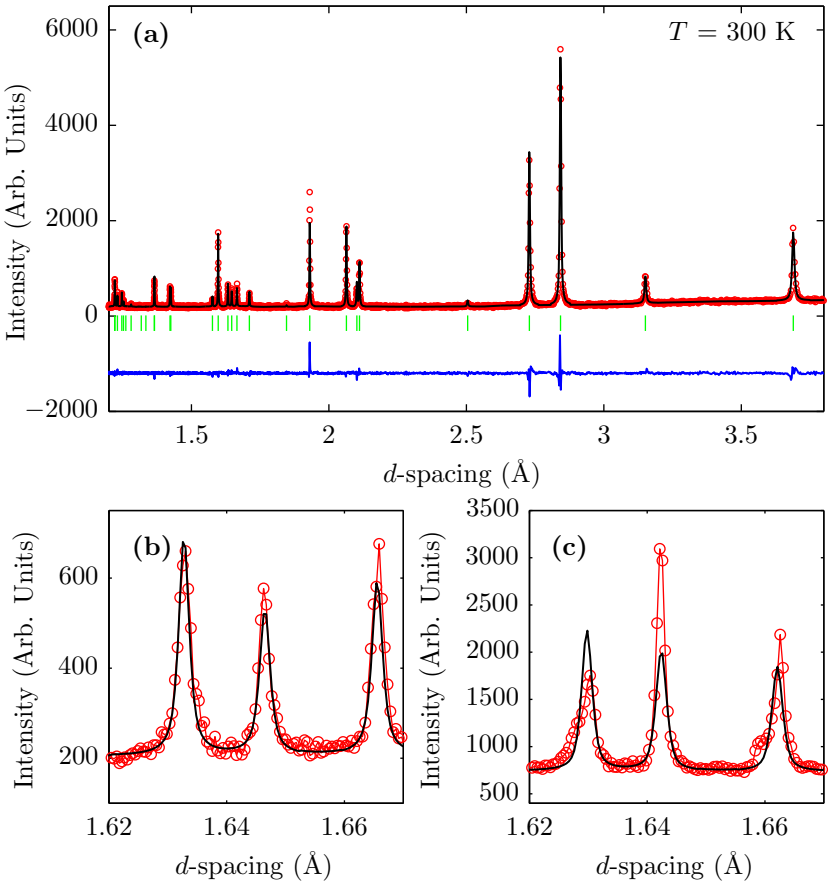

Figure 3.3: X-ray powder diffraction pattern of low-doped $La_{2-x}Sr_xCoO_4$ samples. Red circles denote the measured data points; the black line is the Rietveld profile refinement; green bars indicate the positions of the refined peaks; and the blue line is the residual (difference between the data points and refinement). (a) shows the full diffraction pattern of the $La_{1.75}Sr_{0.25}CoO_4$ sample. (b) and (c) show close up views of specific peaks in the $La_{1.75}Sr_{0.25}CoO_4$ and $La_{1.67}Sr_{0.33}CoO_4$ samples respectively. While the peaks are very well fit in (b), the $d \approx 1.63$ and 1.66 Å peaks in (c) show some splitting.

has the most consistent composition when compared to its nominal values. The $La_{1.7}Sr_{0.3}CoO_4$ appears to have a deficiency in Sr, compared to the nominal value, bringing it closer to $x = 0.25$. The $La_{1.67}Sr_{0.33}CoO_4$ crystal has been grown with the desired Sr content but the splitting of peaks in the XRPD pattern hint at an oxygen content that is not stoichiometric. In light of these results, I shall focus on the $La_{1.75}Sr_{0.25}CoO_4$ sample and the analysis of a $x = 0.25$ doped system throughout the chapter. The findings of the elastic neutron study – presented in Section 3.3.1

Nominal doping	2ζ		x	δ
$x = 0.25$	0.2240(3)	Weighed	0.25	-0.0130(1)
		EPMA	0.238(4)	-0.007(2)
		X-Ray	0.22(3)	0.00(2)
$x = 0.30$	0.258(8)	Weighed	0.30	-0.021(4)
		EPMA	0.228(4)	0.015(4)
		X-Ray	0.25(2)	0.004(4)
$x = 0.33$	0.2507(4)	Weighed	0.33	-0.0396(2)
		EPMA	0.315(3)	-0.032(2)
		X-Ray	–	–

Table 3.1: Summary of $La_{2-x}Sr_xCoO_4$ compositional analysis. The measured Sr contents (x) and calculated oxygen excesses (δ) are presented for all three crystals. The Sr content is determined in three different ways: (i) from weighed starting materials, (ii) from EPMA, and (iii) from XRPD refinement. The parameter ζ is determined from the magnetic ordering vector $\boldsymbol{Q}_{\mathrm{m}} = (0.5, 0.5) \pm (\zeta, \zeta)$ observed by neutron diffraction. The oxygen excess is calculated from Eq. 3.1. All values are per formula unit of $La_{2-x}Sr_xCoO_4$.

– are consistent with the compositional analysis of this material.

3.2.3 Magnetic Characterisation

Figure 3.4 shows the susceptibility and thermoremnant magnetisation (TRM) measured in $La_{1.75}Sr_{0.25}CoO_4$. This exemplifies the qualitatively similar results found for the $La_{1.7}Sr_{0.3}CoO_4$ and $La_{1.67}Sr_{0.33}CoO_4$ samples. Figure 3.4(a) demonstrates divergent behaviour between the zero-field-cooled (ZFC) and field-cooled (FC) susceptibilities when the applied measuring field ($\boldsymbol{H}$) is directed parallel to the a axis. The insert to Figure 3.4(a) depicts the susceptibilities measured parallel to the a and c axes in the temperature range 2 to 300 K. The susceptibility is highly anisotropic, with $\chi_a > \chi_c$, indicating that spins order parallel to the ab-plane. This is qualitatively similar to the strong anisotropy reported in Ref. [57] for a $x = 0.33$ doped sample. Additionally, it resembles the anisotropic susceptibilities in $0.4 < x < 0.7$ $La_{2-x}Sr_xCoO_4$ samples reported in Ref. [71] indicating that Co^{3+} ions occupied the

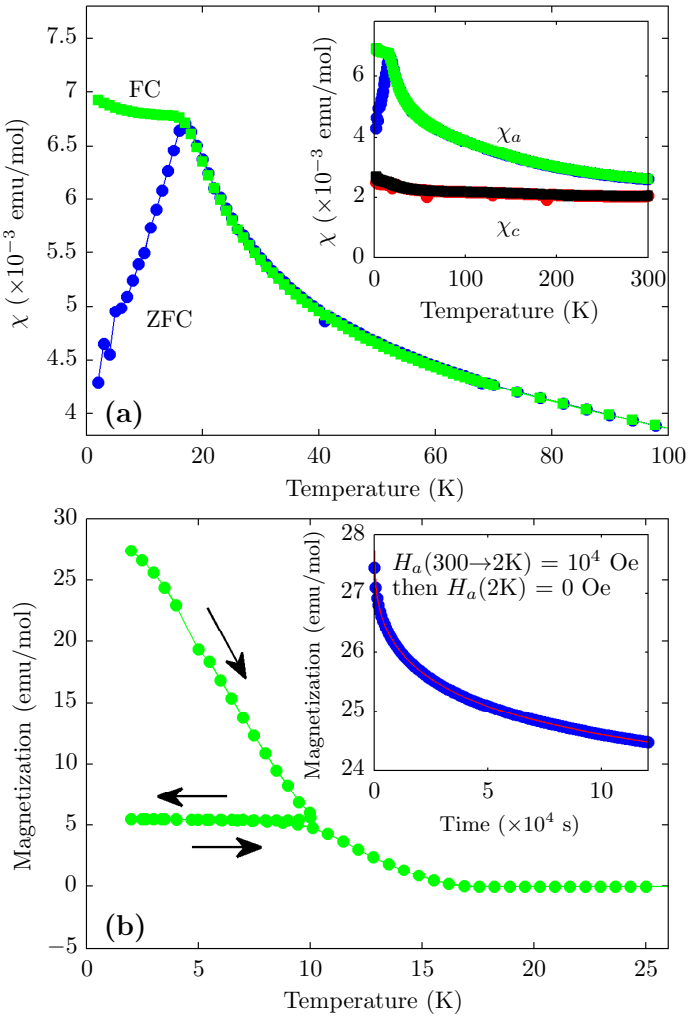

Figure 3.4: Susceptibility and thermoremnant magnetisation of $La_{1.75}Sr_{0.25}CoO_4$. (a) Temperature dependence of the magnetic susceptibility measured with a field of 1000 Oe applied parallel to the a-axis. Insert in (a) shows the anisotropy in the magnetic susceptibility, demonstrated when fields are applied parallel to the a- and c-axes. (b) Memory effect observed in the TRM during the warm-cool-warm cycle (as indicated by the arrows). Insert in (b) is the measured decay of TRM with time (blue points) and a fitted stretched exponential (red line), as described in the text. Reprinted figure from S. M. Gaw *et al.*, Phys. Rev. B, **88**, 165121 (2013) [80]. Copyright (2013) by the American Physical Society.

$S = 0$ low spin state. Hence, the Co^{3+} ions are also expected to be non-magnetic in samples with $x = 0.25$.

The TRM is measured after the sample has been cooled to 2 K in a field of 10^4 Oe. Various irreversibility effects can be seen once this field has been removed.

Figure 3.4(b) shows the variation of TRM with temperature. The temperature is increased through the cycle $2 \rightarrow 10 \rightarrow 2 \rightarrow 30\,\mathrm{K}$. There is a decay of TRM with increasing temperature but on re-cooling ($10 \rightarrow 2\,\mathrm{K}$) the TRM remains constant. Only when the temperature is again increased and re-approaches 10 K does the TRM decrease. It rejoins the initial decay trend above 10 K. The insert of Figure 3.4(b) shows the TRM relaxation behaviour. After the field was removed, the TRM was measured for approximately 32 hours at regular time intervals. A characteristic decay curve can been seen.

The magnetometry results exhibit two key indications of spin glass behaviour in all the samples. First, the divergence of the ZFC and FC susceptibilities, consistent with a spin freezing transition at $T_\mathrm{f} = 18\,\mathrm{K}$. This can be understood as a glassy freezing in of induced magnetic order (in the FC case) or the lack of order (in the ZFC case) [81]. Freezing behaviour is further evidenced by the memory effect observed in Figure 3.4(b). The TRM temperature decay demonstrates a melting of induced frozen order which cannot be regained without the application of a magnetic field. The second spin glass indicator is the characteristic relaxation present in the insert of Figure 3.4(b). The TRM decay is fitted to a stretched exponential of the form $M(t) = M_0 \exp\{-\alpha t^{(1-n)}\} + M_\mathrm{bgd}$. An ideal spin-glass is predicted to have $n = 2/3$ [82].

The fitted exponents for each sample are presented in Table 3.2. Temperature instabilities meant that the TRM of the $La_{1.67}Sr_{0.33}CoO_4$ sample was measured for only a third of the time compared to the other samples. Such a reduction in measuring time has been shown to affect the fitted value of the exponent. The approximate measurement time is, therefore, recorded in Table 3.2. The exponent for the $La_{1.75}Sr_{0.25}CoO_4$ sample approaches that of an ideal spin glass. Similar results have been found for the lightly-doped cuprates [67] and nickelates [68], but with different exponents. The exponents for the $La_{1.7}Sr_{0.3}CoO_4$ and $La_{1.67}Sr_{0.33}CoO_4$ samples are further from the ideal value, however, they are close to the value found

Sample	Approx. Time (h)	n
$La_{1.75}Sr_{0.25}CoO_4$	32	0.6171(8)
$La_{1.7}Sr_{0.3}CoO_4$	32	0.560(2)
$La_{1.67}Sr_{0.33}CoO_4$	11	0.497(9)

Table 3.2: Fitted decay exponents found from the TRM relaxation data. The TRM relaxation for each sample is measured at regular intervals over the approximate time. The decay is then fitted to the stretched exponential outlined in the text. The exponent n is presented for each sample.

in another studied $x = 0.33$ doped sample (see Ref. [83]). These findings suggest that while the precise nature of spin glassy behaviour varies between samples and between different materials it is a universally shared property linked with imperfect stripe order in real-world materials.

3.3 Neutron Scattering Experiments

Direct geometry chopper spectrometers were used to measure the excitation spectra of all three samples. Each sample was aligned with its c axis parallel to the incident neutron beam. Previous measurements on $La_{2-x}Sr_xCoO_4$ have shown that there are only very low energy (several meV) dispersive correlations between the CoO_2 layers [57]. Hence, for energies above this, the interlayer correlations are negligible. Therefore, the L component of the scattering vector ($\boldsymbol{Q}_{\parallel}$ in this orientation) can be integrated to give the spectrum purely in the (H, K) plane (see Section 2.3.2). The $La_{1.75}Sr_{0.25}CoO_4$ and $La_{1.7}Sr_{0.3}CoO_4$ samples were measured using the MAPS spectrometer, with $E_\mathrm{i} = 80,\ 120$, and 300 meV. This allowed the full spectrum to be surveyed. The $La_{1.75}Sr_{0.25}CoO_4$ and $La_{1.67}Sr_{0.33}CoO_4$ samples were subsequently measured using the MERLIN spectrometer with $E_\mathrm{i} = 20$ and 60 meV. The energy resolution in each experiment was approximately 5% of E_i at $E = 0$ and decreased with increasing energy transfer. All measurements were corrected for detector efficiency, time-independent background and the $k_\mathrm{f}/k_\mathrm{i}$ factor in the partial differential

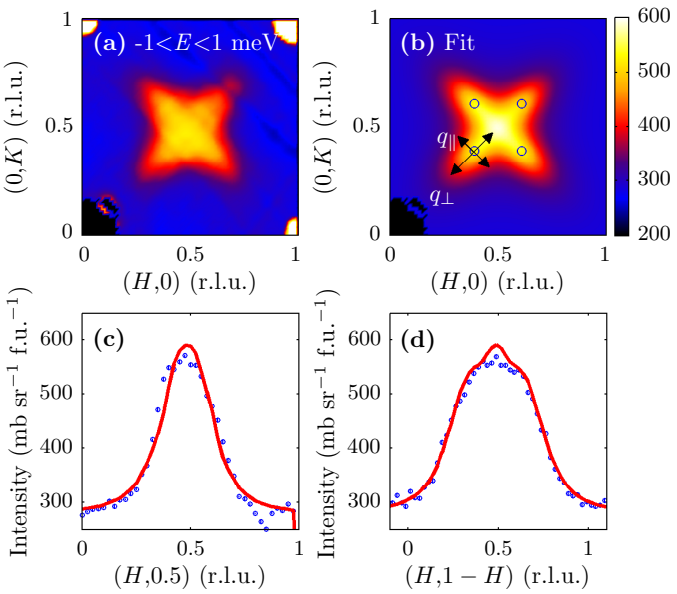

Figure 3.5: Elastic neutron scattering pattern and fit for $La_{1.75}Sr_{0.25}CoO_4$. (a) The elastic scattering intensity in the (H, K) plane, measured with $E_i = 20\,\text{meV}$ and integrated between $-1 < E < 1\,\text{meV}$. The intensity is given in units of $\text{mb}\,\text{sr}^{-1}\,\text{f.u.}^{-1}$. (b) 2D fit to the elastic data using a pattern of four bi-variant and elliptically contoured Lorentzian peaks. The peaks are centred on $\mathbf{Q}_m = \mathbf{Q}_{AFM} \pm (\zeta, \zeta)$ and $\mathbf{Q}_{AFM} \pm (\zeta, -\zeta)$ (positions marked as black circles). Peak widths are measured along the $q_\parallel$ and $q_\perp$ directions (labelled) and used to find the correlation lengths parallel and perpendicular to the stripe direction, respectively. (c) and (d) show line cuts through the data (blue points) and fit (red line) depicted in (a) and (b) along the $(H, 0.5)$ and $(H, 1 - H)$ directions respectively. Figure adapted from Ref. [80].

cross section (see Eq. 2.26). All measured intensities are given in absolute units. Data were recorded at $T = 6\,\text{K}$, unless otherwise stated.

3.3.1 Neutron Diffraction

Figure 3.5(a) shows the elastic scattering from the $La_{1.75}Sr_{0.25}CoO_4$ sample measured with $E_i = 20\,\text{meV}$. This is representative of the similar results found in the $La_{1.7}Sr_{0.3}CoO_4$ and $La_{1.67}Sr_{0.33}CoO_4$ samples. The scattering is diffuse in nature and is centred around $\boldsymbol{Q}_{AFM} = (0.5, 0.5)$. The intensity forms an 'X'-shape with arms stretched along the $(1, 1)$ and $(1, -1)$ directions. Wave vector line cuts along the $(H, 0.5)$ and $(H, 1 - H)$ directions are presented in Figure 3.5(c) and 3.5(d).

The data can be modelled by fitting four peaks at incommensurate wave vec-

tor positions. Figure 3.5(b) shows the 2D fit obtained using elliptically-contoured bivariant Lorentzian peaks, all equally shifted ζ away from $\boldsymbol{Q}_{\mathrm{AFM}}$. This fitting pattern is consistent with that expected from period-4 stripe order as illustrated in Figure 3.2(d). The distinctive 'X'-shape, not seen in previous studies of $0.3 < x < 0.5$ $La_{2-x}Sr_xCoO_4$ samples [57, 66], is created by the lower doping and significantly broader peaks in $La_{1.75}Sr_{0.25}CoO_4$. Attempts were made to model the diffuse scattering with an additional fifth peak centred on $\boldsymbol{Q}_{\mathrm{AFM}}$. However, the best results all attributed a negative intensity to the central peak. These unphysical fits arose as there is already a slight excess of fitted intensity at $\boldsymbol{Q}_{\mathrm{AFM}}$ in the four peak pattern [apparent in Figure 3.5(d)].

Fitting the elastic scattering allows the degree of disorder to be quantified in each of the samples. As the Lorentzian peaks are elliptical, there are two characteristic widths parallel and perpendicular to the stripe direction. The stripe directions are plotted in real space in Figure 3.2(b) and indicated in reciprocal space in Figure 3.5(b). The peak widths are related to the correlation length, defined as the inverse half width at half maximum (HWHM). The magnetic correlation lengths (ξ_{M}) measured for the three samples are presented in Table 3.3. All three samples exhibit shorter correlation lengths than the $x = 0.33$ sample studied in Ref. [57] (where the reported values are $\xi_{\mathrm{M}}^{||} = 10\,\text{Å}$ and $\xi_{\mathrm{M}}^{\perp} = 6.5\,\text{Å}$). Finally, nuclear Bragg peaks were measured to estimate the combined instrumental resolution and crystal mosaic effects on the peak broadening. The nuclear Bragg peaks were found to be narrower than the incommensurate magnetic peaks by a factor of ~ 10. Hence, the instrumental resolution effects are negligible when compared to the intrinsic width of the diffuse magnetic peaks.

The value of of the fitted incommensurability ζ can be used as an estimation of the total doping in each sample, as defined in Eq. 3.1. This estimate is reliant on the existence of long range stripe order and the fidelity of our chosen fitting pattern. Both of these conditions are so far unproven in this study. The broad

Sample	$\xi_{\mathrm{M}}^{\parallel}$ (Å)	$\xi_{\mathrm{M}}^{\perp}$ (Å)
$La_{1.75}Sr_{0.25}CoO_4$	7.16(2)	3.57(7)
$La_{1.7}Sr_{0.3}CoO_4$	8.5(5)	3.9(3)
$La_{1.67}Sr_{0.33}CoO_4$	6.79(2)	3.26(1)

Table 3.3: Summary of the measured correlation lengths. The significantly larger error on the $La_{1.7}Sr_{0.3}CoO_4$ correlation length is due to fitting the E_i=80 meV elastic data. The other two samples were measured using E_i=20 meV. Note, the fitted incommensurate splitting of the peak positions in all three samples are listed in Table 3.1.

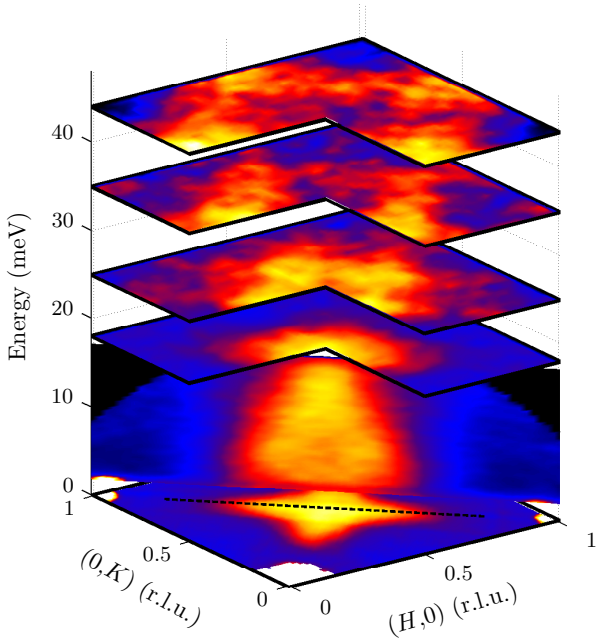

Figure 3.6: Hour-glass magnetic spectrum of $La_{1.75}Sr_{0.25}CoO_4$. Data measured on the MERLIN spectrometer at a temperature of 6 K. Data below and above 17 meV were measured with E_i=20 and 60 meV, respectively. The intensities in each plane have been scaled by different factors to help visualise the overall spectrum. Reprinted figure from S. M. Gaw *et al.*, Phys. Rev. B, **88**, 165121 (2013) [80]. Copyright (2013) by the American Physical Society.

peaks demonstrate that the magnetic order is short range (as discussed above) and the diffuse scattering makes it questionable as to whether any model captures all the features. Therefore, any estimation of the doping from ζ is, perhaps, simplistic. Nevertheless, using Eq. 3.1 the number of Co^{3+} ions can be estimated. Combining this with the previous estimates of the Sr content, δ can be found. These results

are presented in Table 3.1 and agree well with the previous conclusions regarding the chemical composition of each sample. $La_{1.75}Sr_{0.25}CoO_4$ exhibits a δ value close to stoichiometry. $La_{1.7}Sr_{0.3}CoO_4$ shows a lower doping than expected from its nominal content, which arises from a Sr deficiency. Its oxygen content is near stoichiometric when the lower x is considered. $La_{1.67}Sr_{0.33}CoO_4$ demonstrates a significantly different doping than expected. This appears to be due to a sizeable oxygen deficiency, the cause of which is currently not understood.

While the indirect measurements of the total doping and subsequent calculation of δ may be naïve, they are concordant with all the previous compositional analysis. The elastic data shows that the true doping in all the samples is close to that expected for a stoichiometric $x = 0.25$ sample. Only the $La_{1.75}Sr_{0.25}CoO_4$ sample does not show large deviations from its nominal composition. Therefore, the subsequent analysis will be conducted principally on the $La_{1.75}Sr_{0.25}CoO_4$ data and all theoretical modelling based on an $x = 0.25$ doped ground state.

3.3.2 Neutron Spectroscopy

Figure 3.6 shows the magnetic excitation spectrum measured in the $La_{1.75}Sr_{0.25}CoO_4$ sample at a temperature of 6 K. The data exhibit several key features, observed at increasing energies: (i) low energy branches dispersing inwards from the four incommensurate wave vectors $\boldsymbol{Q}_{\mathrm{m}}$ towards $\boldsymbol{Q}_{\mathrm{AFM}}$, (ii) an approximately vertical dispersion between ~ 10 and ~ 18 meV centred on $\boldsymbol{Q}_{\mathrm{AFM}}$, and (iii) intensity above ~ 18 meV dispersing outwards, with a four-peak pattern rotated 45° with respect to the low energy branches. The spectrum has all the characteristic features of an hour-glass spectrum and resembles that observed in the $x = 0.33$ doped sample reported in Ref. [57]. However, the spectra differ in the larger $\boldsymbol{Q}$-broadening that is present in the $La_{1.75}Sr_{0.25}CoO_4$ data. This reflects the much shorter magnetic correlation lengths found in the previous section.

Figures 3.7(a)–3.7(e) show a series of constant energy slices at increasing energies

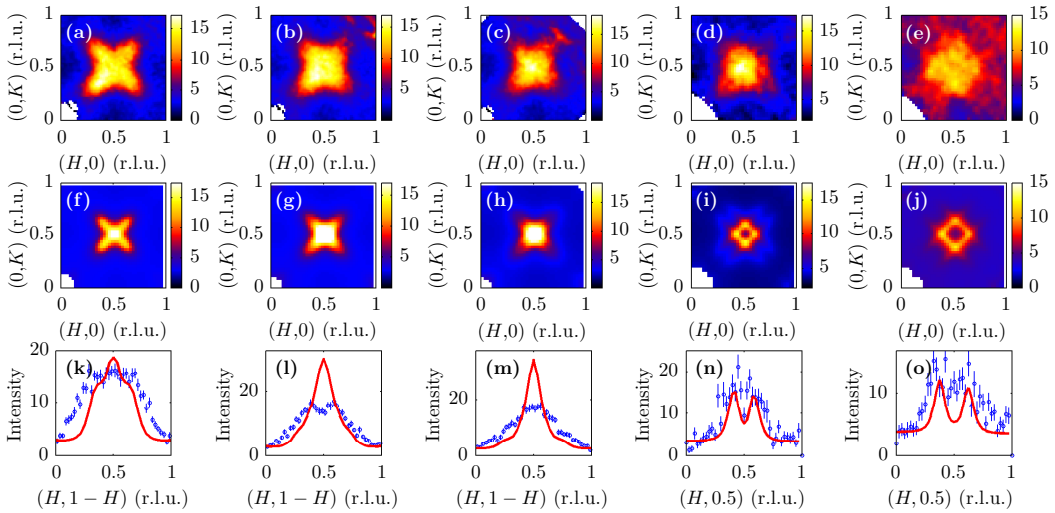

Figure 3.7: Comparison of measured $La_{1.75}Sr_{0.25}CoO_4$ constant-energy slices and DCSG simulations. Constant-energy slices at (a) $\langle E\rangle = 4.5\,\text{meV}$, (b) $\langle E\rangle = 9\,\text{meV}$, (c) $\langle E\rangle = 11.25\,\text{meV}$, (d) $\langle E\rangle = 18\,\text{meV}$ and (e) $\langle E\rangle = 22.5\,\text{meV}$ through the magnetic spectrum of $La_{1.75}Sr_{0.25}CoO_4$. Data were measured on the MERLIN spectrometer using $E_\text{i} = 20\,\text{meV}$ (a–c) and $E_\text{i} = 60\,\text{meV}$ (d,e). The intensity of the data is in absolute units of $\text{mb}\,\text{sr}^{-1}\,\text{meV}^{-1}\,\text{f.u.}^{-1}$. DCSG model simulations are shown at the energies (f) $\omega = 0.2$, (g) $\omega = 0.4$, (h) $\omega = 0.5$, (i) $\omega = 0.8$ and (j) $\omega = 1.0$ expressed in terms of JS. The simulations have been performed with $J'/J = 0.05$, and $JS = 22.5\,\text{meV}$ was chosen to obtain an approximate match between the simulations and data. The simulated charge-disordered ground state was characterized by a correlation length $\xi_\text{C}^{\parallel} = 5a$. The squared magnetic form factor $f^2(Q)$ and the orientation factor for in-plane magnetic fluctuations (see main text) have been included in the simulations. The simulated intensities have been scaled for ease of comparison with the data. (k)–(o) show line cuts through the respective 2D experimental (blue, points) and simulated (red, line) data along the $(H, 1-H)$ (k–m) and $(H, 0.5)$ (n,o) directions. Figure adapted from Ref. [80].

through the hour-glass spectrum. These illustrate the wave vector distribution of intensity in the (H, K) plane. The left half of Figure 3.8 shows dispersive energy-wave vector slices through the hour-glass spectrum. Below $E = 11.25\,\text{meV}$, in the lower panel, the wave vector is along the (H, H) direction and the measurements were made using $E_\text{i} = 20\,\text{meV}$. Above $E = 11.25\,\text{meV}$, in the upper panel, the wave vector axis is along the $(H, 0)$ direction and $E_\text{i} = 60\,\text{meV}$. In both panels, the horizontal axis is centred on $\boldsymbol{Q}_\text{AFM}$ and plots the magnitude of $\boldsymbol{Q}$ in units of $2\pi/a$.

Measurements at higher temperature were carried out to investigate the effect of thermal disorder on the hour-glass. Figure 3.9 depicts dispersive slices along

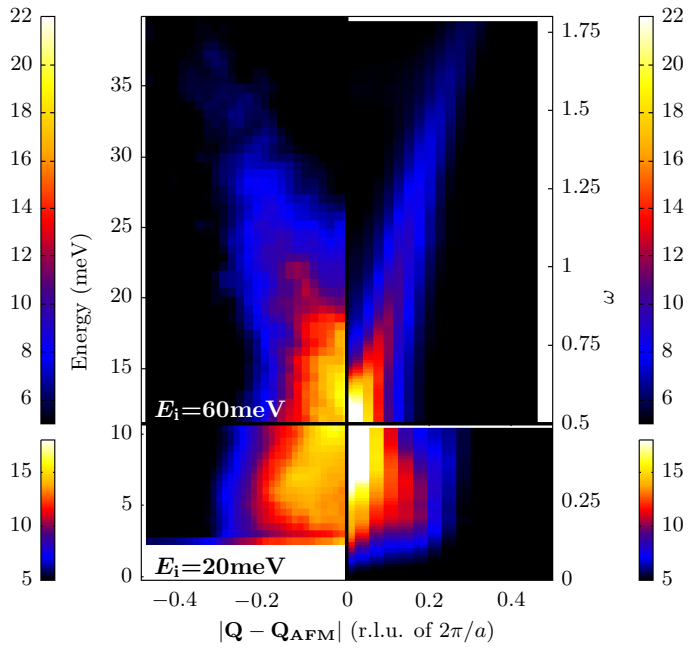

Figure 3.8: Dispersion of the scattering intensity in $La_{1.75}Sr_{0.25}CoO_4$ and comparison to DCSG simulations Lower panels ($E < 11.25\,\text{meV}$, $\omega < 0.5JS$) shows the dispersion along the $\boldsymbol{Q} = (H, H)$ direction. Upper panel ($E > 11.25\,\text{meV}$, $\omega > 0.5JS$) shows the dispersion along the $(H, 0)$ direction. The left half shows neutron scattering data collected on the MERLIN spectrometer. Two incident energies were used, $E_\text{i} = 20\,\text{meV}$ for data in the lower panel, and $E_\text{i} = 60\,\text{meV}$ in the upper panel. The intensity is in absolute units of $\text{mb}\,\text{sr}^{-1}\,\text{meV}^{-1}\,\text{f.u.}^{-1}$. DCSG model simulations are plotted on the right half of the figure. The simulations have been performed with $J'/J = 0.05$, and $JS = 22.5\,\text{meV}$. The simulated charge-disordered ground state was characterized by a correlation length $\xi_\text{C}^{\parallel} = 5a$. The squared magnetic form factor $f^2(Q)$ and the orientation factor for in-plane magnetic fluctuations (see main text) have been included in the simulations. The simulated intensities have been scaled for ease of comparison with the data. Reprinted figure from S. M. Gaw *et al.*, Phys. Rev. B, **88**, 165121 (2013) [80]. Copyright (2013) by the American Physical Society.

the (H, H) (lower panels) and $(0.5, H)$ (upper panels) directions at three different temperatures. The spectra are measured with $E_\text{i} = 60\,\text{meV}$ using the oxygen deficient $La_{1.67}Sr_{0.33}CoO_4$ single crystal, which exhibits a very similar spectrum to the $La_{1.75}Sr_{0.25}CoO_4$ sample at low temperatures. Increasing the temperature will introduce additional thermal disorder and is the same process used by Ulbrich, *et al.* to tune the disorder in certain manganate samples [59]. The hour-glass still exists at the highest measured temperatures of 163 K, though its features are nearly smeared out. An intermediate $T = 124\,\text{K}$ spectrum illustrates the progressive broadening

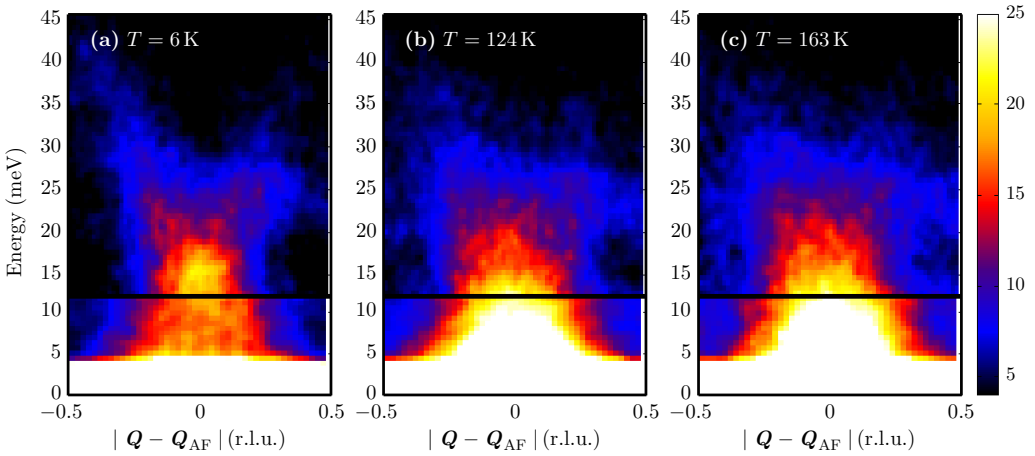

Figure 3.9: Hour-glass dispersion evolving with temperature. Data measured using the $La_{1.67}Sr_{0.33}CoO_4$ sample discussed in Section 3.2 and shown to have a have an effective doping near $n_h = 0.25$. All spectra recorded on the MERLIN spectrometer with $E_i = 60\,\mathrm{meV}$ and (a) $T = 6\,\mathrm{K}$, (b) $T = 124\,\mathrm{K}$, and (c) $T = 163\,\mathrm{K}$. The upper and lower panels show the dispersion along the $\boldsymbol{Q} = (H, H)$ and $(0.5, H)$ directions respectively, as in Figure 3.8.

of the hour-glass across all energies. The high energy features become more diffuse with increasing temperature.

The lower resolution $E_i = 60\,\mathrm{meV}$ measurement at 6 K [Figure 3.9(a)] exhibits low energy branches that can be resolved by fitting. These branches become unresolvable at higher T, but still the intensity visibly narrows in wave vector between $\sim 5\,\mathrm{meV}$ and the waist at $\sim 12\,\mathrm{meV}$. This behaviour is consistent with a broadened hour-glass spectrum. While these measurements are performed using the $La_{1.67}Sr_{0.33}CoO_4$ sample, which carries some ambiguity regarding its true composition, the results qualitatively show the survival of an hour-glass in a low-doped cobaltate at higher temperatures.

3.4 DCSG Ground State and the Hour-Glass Spectrum

To describe the measured excitation spectrum, my collaborators Dr E. Andrade and Prof. M. Vojta simulated the magnetic excitation spectrum arising from short range stripe order. To do this, they have generated systems with disordered ground

states leading to frustrated magnetic interactions. These ground states form local clusters of AFM and striped order and the frustration leads to glassy behaviour. Hence, the states are described as disordered cluster spin glass (DCSG). This theoretical treatment is based on the model proposed for the $La_{1.67}Sr_{0.33}CoO_4$ system in Ref. [70] but has been extended to describe $La_{1.75}Sr_{0.25}CoO_4$.

3.4.1 DCSG Model

The DCSG ground state is generated in two steps. First, a stable configuration of disordered charge stripes is generated, and then the magnetic order is simulated. To derive the charge order, Co^{2+} and Co^{3+} position can be modelled as Ising states ($n_i = 0$ or 1 respectively) in an effective charge Hamiltonian of the form

$$\mathcal{H}_{\mathrm{C}} = \sum_m V_m \sum_{\langle i,j \rangle_m} n_i n_j. \tag{3.2}$$

The relative arrangement of ions is determined by the choice of Coulomb interactions V_m. This model is applied to an initial state with perfect charge stripe order with a $\langle n_{\mathrm{h}} \rangle = 1/4$ filling factor characterised by the charge order wave vectors $\boldsymbol{Q}_{\mathrm{C}} = (0.5 \pm 0.25, 0.5 \mp 0.25)$ and $(0.5 \pm 0.25, 0.5 \pm 0.25)$. The structure is defined on a finite $Na \times Na$ lattice. Monte-Carlo (MC) simulations of this model are used to find charge configurations which depart from the initially perfect order. Instead, the configurations are well defined by short range charge stripe correlations. The disorder can be quantified by the correlation length $\xi_{\mathrm{C}}^{||}$ ($\xi_{\mathrm{C}}^{\perp}$) measured parallel (perpendicular) to the stripe direction. The correlation lengths are found by Fourier transforming the generated structure and measuring the width of the charge order peaks. This is analogous to the experimentally measured magnetic correlation lengths in Section 3.3.1. For large enough N, the charge correlation length scales with the magnetic correlation length [70]. One such disordered charge configuration is shown in Figure 3.10(a).

The spin order is found by placing $S = 1/2$ spins on the Co^{2+} positions in

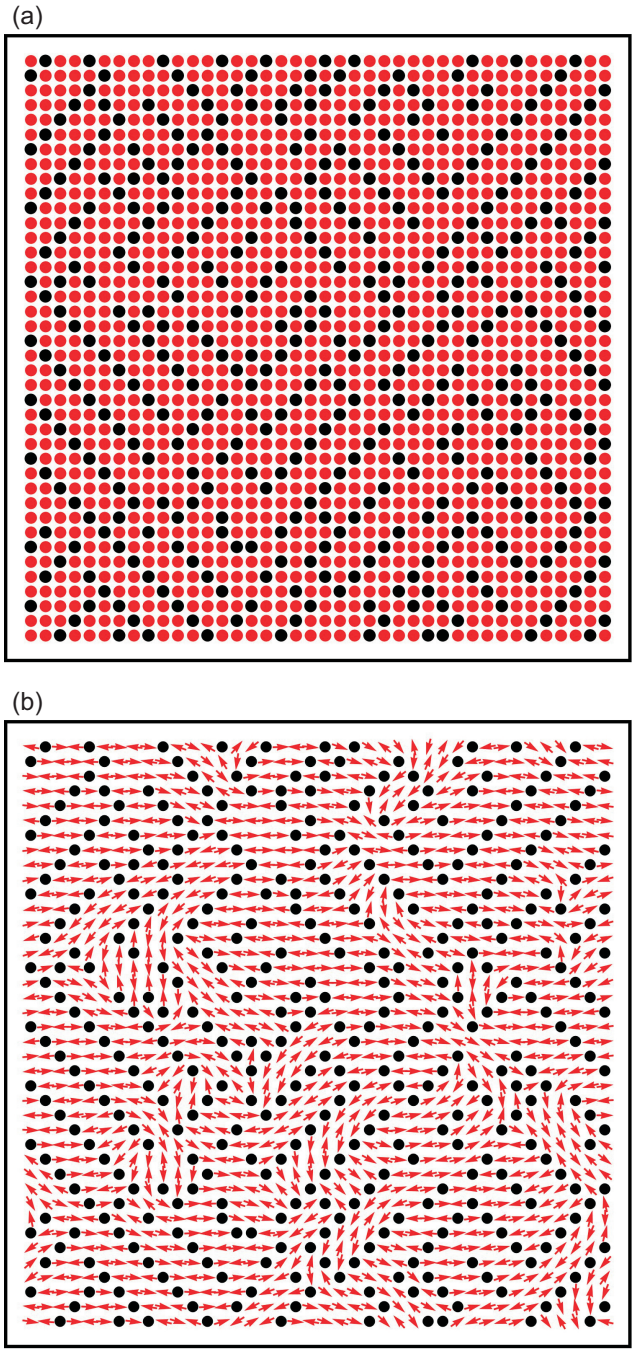

Figure 3.10: Disordered charge and spin states arising from DCSG theory. (a) A disordered charge configuration and (b) the corresponding real-space spin configuration. Black (red) circles indicate the position of Co^{3+} (Co^{2+}) ions. The red arrows denote the direction of the Co^{2+} spins. Reprinted figure from S. M. Gaw *et al.*, Phys. Rev. B, **88**, 165121 (2013) [80]. Copyright (2013) by the American Physical Society.

the charge disordered states. The Co^{3+} sites are assumed to be non-magnetic. To describe the interactions between the neighbouring spins, a Heisenberg Hamiltonian is introduced with the form

$$\mathcal{H}_{\rm sp} = \sum_{\langle i,j \rangle} \sum_{\alpha} J_{ij}^{\alpha} S_i^{\alpha} S_j^{\alpha}, \tag{3.3}$$

where J_{ij} are the exchange parameters and S_i^{α} is the α component of the spin operator corresponding to the $i^{\rm th}$ spin. The $\langle i,j \rangle$ notation indicates that each pair of spins is counted once. Two exchange interactions, J and J', are used, consistent with the spin wave models of the other $La_{2-x}Sr_xCoO_4$ compounds and shown in Figure 3.2(b). Exchange anisotropy is introduced in order to confine the spins to the ab plane. It is assumed the anisotropy has the same form as the parent compound with $J^x = J(1+\varepsilon)$, $J^y = J$, and $J^z = J(1-\delta)$ [75]. The parameters $\delta = 0.28$ and $\varepsilon = 0.013$ are fixed to the values found in La_2CoO_4. The J' exchange is expected to be much weaker than J and so is assumed to be isotropic. Interlayer coupling has been neglected in this treatment. MC simulations using this model are used to find ground state spin structures arising from a particular charge arrangement. An example is shown in Figure 3.10(b).

The excitation spectrum of $\mathcal{H}_{\rm sp}$ can be calculated from each of the derived ground states using LSWT on finite lattices. In the one-magnon approximation, this gives rise to a dynamic susceptibility of the form

$$\chi''(\boldsymbol{Q}, E) = \Big[\sum_{\alpha} \sum_{\nu} |\langle \nu | S^{\alpha}(\boldsymbol{Q}) | 0 \rangle|^2 \delta(E - E_{\nu}) \Big]_{\rm avg}. \tag{3.4}$$

In this expression, $S^{\alpha}(\boldsymbol{Q})$ is the $\alpha = \{x, y, z\}$ component of the Fourier-transformed spin operator and $|0\rangle$ and $|\nu\rangle$ are the magnon vacuum and single magnon state respectively. The energy of the magnon state is E_{ν} and all energies are expressed in terms of JS such that $E = \omega JS$. The $[...]_{\rm avg}$ notation denotes that $\chi''(\boldsymbol{Q}, E)$ is calculated by averaging the expression over the 80 spin states calculated from 40

charge configurations. Numerous states are used to replicate the effect of measuring a large sample. From the fluctuation dissipation theorem introduced in Chapter 2, the dynamical susceptibility is proportional to the scattering function (Eq. 2.28), which is denoted $S^{\text{sim}}(\boldsymbol{Q}, E)$.

3.4.2 Comparison with INS Data

Simulated intensity from the DCSG model is plotted alongside the experimental measurements in Figures 3.7 and 3.8. For the best possible comparison, the $\boldsymbol{Q}$-dependant experimental factors which are present in the magnetic partial differential cross section are applied to the simulation – see Eq. 2.26. This includes the dipole form factor of Co^{2+} [35] and an attenuation factor corresponding to the orientation factor for in-plane fluctuations (which will be discussed below). The δ-function in Eq. 3.4 is replaced by a Lorentzian function to introduce a finite width to the excitations. The Lorentzian has an energy dependent width $\Gamma = 0.1JS$.

From Chapter 2, we have seen that the components of $S^{\alpha\alpha}(\boldsymbol{Q}, E)$ are individually weighted in the summation by their orientation factor. Therefore, the measured INS intensity is related to the components by

$$S^{\text{INS}}(\boldsymbol{Q}, E) = \sum_{\alpha}(1 - \hat{Q}_{\alpha}^{2})S^{\alpha\alpha}(\boldsymbol{Q}, E). \tag{3.5}$$

This is different from the simulated intensity found using Eq. 3.4, where the summation and averaging occur without any weighting of the components. In general, the two expressions in Eqs. 3.4 and 3.5 are not comparable. However, in the particular case of a system having strong in-plane anisotropy and domain-averaged spin configurations the two expressions are proportional. This can be shown by expanding the summation in Eq. 3.5, to show the contributing in-plane spin fluctuations in

the two domains:

$$\begin{aligned}\left\langle S^{\mathrm{INS}}(\boldsymbol{Q},E)\right\rangle &= \frac{1}{2}\left[(1-\hat{Q}_a^2)S^{xx}(\boldsymbol{Q},E)+(1-\hat{Q}_b^2)S^{yy}(\boldsymbol{Q},E)\right] \\ &\quad + \frac{1}{2}\left[(1-\hat{Q}_a^2)S^{yy}(\boldsymbol{Q},E)+(1-\hat{Q}_b^2)S^{xx}(\boldsymbol{Q},E)\right] \\ &= \frac{1}{2}\left[(1-\hat{Q}_a^2)+(1-\hat{Q}_b^2)\right]\left[S^{xx}(\boldsymbol{Q},E)+S^{yy}(\boldsymbol{Q},E)\right] \\ &= \frac{1}{2}(1+\hat{Q}_c^2)S^{\mathrm{sim}}(\boldsymbol{Q},E). \end{aligned} \tag{3.6}$$

Here, $\langle\ldots\rangle$ denotes the domain average in the real crystal. Within each of the orientation factors, the unit vector components of $\boldsymbol{Q}$ are defined along the tetragonal directions a, b, and c. The components of the scattering function are defined in the Cartesian coordinate system, where x is parallel to the spin direction and y lies perpendicular to the spin direction but within the plane. Hence, the $\boldsymbol{Q}$ dependent effects of the in-plane orientation factor can be applied to the simulated intensity through the factor $\frac{1}{2}(1+\hat{Q}_c^2)$. This treatment is possible as both the experimentally measured $S^{\mathrm{INS}}(\boldsymbol{Q},E)$ and simulated $S^{\mathrm{sim}}(\boldsymbol{Q},E)$ are relatively insensitive to out-of-plane spin fluctuations in the energy ranges presented in Figure 3.7 and 3.8. The accuracy of this assumption will be further discussed in Section 3.4.3.

All simulations presented have been scaled such that $JS = 22.5\,\mathrm{meV}$. This value was chosen as it matches the position of the main hour-glass features in the simulations and measurements. The inter-stripe exchange was fixed in the ratio $J'/J = 0.05$. This value was found in Ref. [57] using LSWT based on perfect period-3 stripes to model the hour-glass in $La_{1.67}Sr_{0.33}CoO_4$. Furthermore, the value reproduces the measured $x = 0.33$ sample's spectrum when the ground state is modelled as a DCSG [70]. Introducing more holes into the system is not expected to significantly change the inter-stripe exchange so this J'/J ratio is assumed for $La_{1.75}Sr_{0.25}CoO_4$. The amount of disorder is chosen by comparing a number of simulated spectra to the experimental results. A charge configuration characterised

by $\xi_{\mathrm{C}}^{||} = 5a$ gives the best agreement and is used to simulate the results in Figures 3.7 and 3.8.

The DCSG simulations qualitatively match the experimentally measured hour-glass spectrum. Figures 3.7(f–j) show the distribution of intensity in the Brillouin zone evolving with energy. Line cuts, shown in Figures 3.7(k–o) highlight two differences between the simulation and experiment. First, the $\boldsymbol{Q}$-width of the simulated peaks is narrower than that measured in the experiments. A portion of the additional broadening will be due to the spectrometry resolution but this does not account for all of it. The small energy Lorentzian broadening applied to the simulations is not enough to introduce any phenomenological broadening which previous studies have relied upon. The second discrepancy is the overestimation of the scattering intensity at the $\boldsymbol{Q}_{\mathrm{AFM}}$ wave vector. This is particularly apparent in Figures 3.7(l) and 3.7(m), and the lower panels in Figure 3.8. At energies between 5 and 15 meV, intensity in the experimental data forms two resolvable branches dispersing inwards from the incommensurate $\boldsymbol{Q}_{\mathrm{m}}$ positions to the hour-glass waist. The simulations, however, have the greatest intensity centred on $\boldsymbol{Q}_{\mathrm{AFM}}$ across the same energy range. This suggests that the simulations include more locally coordinated AFM regions than are measured in the INS experiment.

While there are discrepancies between the DCSG simulations and measured data, it is feasible that a better reproduction of the INS data could be achieved if all the parameters could be exhaustively refined. In this study the parameters J', J, $\xi_{\mathrm{C}}^{||}$, and $\xi_{\mathrm{C}}^{\perp}$ are all interdependent. An exhaustive fit would involve the simultaneous fitting of these interdependent parameters. Unfortunately, due to the very long computation times involved in a single simulation this is unfeasible.

3.4.3 $S(E)$ and Proposed High Energy Spectral Features

The momentum-averaged scattering function provides further insight into the DCSG ground state. For the individual components of the scattering function, this is de-

fined as

$$S^{\alpha\alpha}(E) = \frac{\int S^{\alpha\alpha}(\boldsymbol{Q}, E)\,\mathrm{d}\boldsymbol{Q}}{\int \mathrm{d}\boldsymbol{Q}}. \tag{3.7}$$

The quantity $S^{\alpha\alpha}(E)$ can be considered the density of magnetic states for a given polarisation. Using the simulated components of the scattering function, the relative sensitivity to out-of-plane spin fluctuations can be explored. Figure 3.11(a) shows the individual components of the momentum averaged scattering function found from the DCSG model. The in-plane S^{xx} and S^{yy} components dominate at low energies $< 25\,\mathrm{meV}$, while the out-of-plane S^{zz} component is the largest at energies $> 35\,\mathrm{meV}$. These contributions are significantly altered when the components are weighted by their associated orientation factors in Figure 3.11(b). The orientation factor has been calculated using the mean value of $\boldsymbol{Q} = (0.5, 0.5)$ for the in-plane component of scattering vector. The out-of-plane $\boldsymbol{Q}$ component increases with E. This causes the orientation factor to increasingly suppress S^{zz} at increasing energy transfers. Therefore, Figure 3.11(b) now shows that in-plane fluctuations dominate the entire spectrum. A comparison of the in-plane fluctuations $S^{xx}(E) + S^{yy}(E)$ against a combined in-plane and contributing out-of-plane fluctuations summation $S^{xx}(E) + S^{yy}(E) + \eta S^{zz}(E)$ is shown in Figure 3.11(c). The scaling factor $\eta = 2(1 - \hat{Q}_c^2)/(1 + \hat{Q}_c^2)$ is the ratio of out-of-plane to in-plane orientation factors – see Eq. 3.6. The out-of-plane fluctuations contribute at most 15% of the total scattering intensity, as seen from Figure 3.11(c). This confirms that the experimental spectrum is dominated by in-plane magnetic fluctuations.

Following on from this treatment, the simulated $S^{xx}(E) + S^{yy}(E)$ intensity can be compared to the experimental value. To extract $S(E)$ from the measured spectrum, the four-peak pattern of bivariant Lorentzians was fitted to constant E slices in the same way as described for the elastic data in Section 3.3.1. The form factor and the effective orientation factor for in-plane fluctuations (Eq. 3.6) are included in the fitting pattern to remove their influence from the total scattering intensity found. The plotted values can be expressed as $(\gamma r_0/2)^2 S^{\mathrm{expt}}(E)$. Alongside the ex-

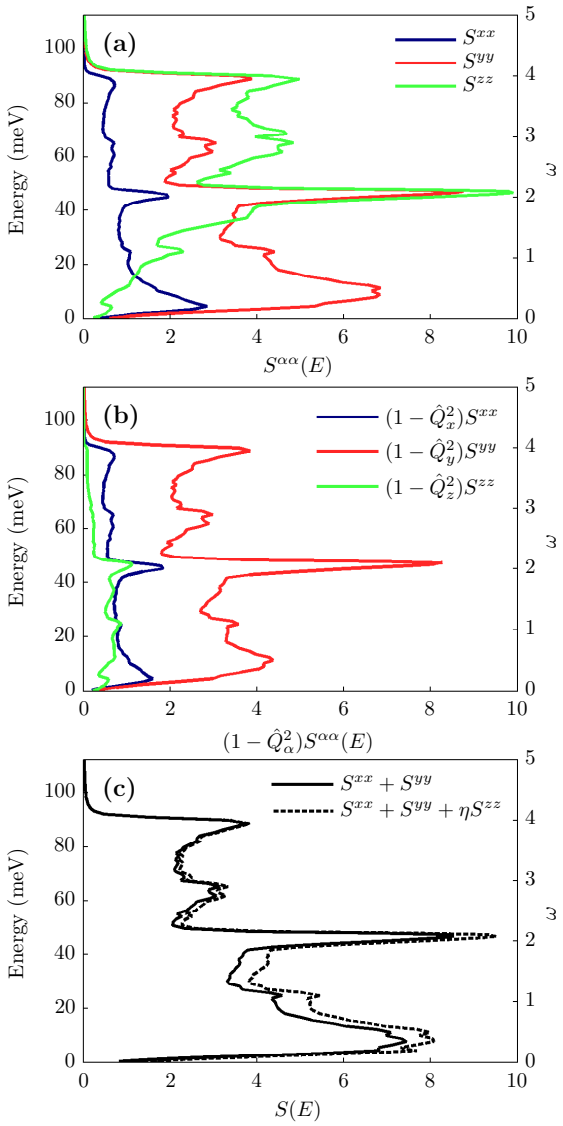

Figure 3.11: The effect of the orientation factor on the components of the scattering function. (a) Momentum-averaged partial scattering functions S^{xx} (blue line), S^{yy} (red line) and S^{zz} (green line), simulated for the case where $\xi_{\mathrm{C}}^{\parallel} = 5a$, $J = 22.5$ meV and $J'/J = 0.05$. (b) The partial scattering functions weighted by the orientation factors in the INS cross-section. The orientation factors are calculated from the variation of $\boldsymbol{Q}$ with energy in the time-of-flight spectrum, with the in-plane component of $\boldsymbol{Q}$ fixed at $(0.5, 0.5)$. The neutron incident energy was $E_{\mathrm{i}} = 60$ meV, as used in the experiment. (c) Comparison of the scattering from the in-plane fluctuations $S^{xx} + S^{yy}$ (solid black line) with the actual combination of scattering functions present in the experimental INS spectrum, $S^{xx}(E) + S^{yy}(E) + \eta S^{zz}(E)$ with $\eta = 2(1 - \hat{Q}_c^2)/(1 + \hat{Q}_c^2)$ (dashed black line). The in-plane fluctuations are seen to dominate the experimental spectrum over the entire bandwidth. Reprinted figure from S. M. Gaw *et al.*, Phys. Rev. B, **88**, 165121 (2013) [80]. Copyright (2013) by the American Physical Society.

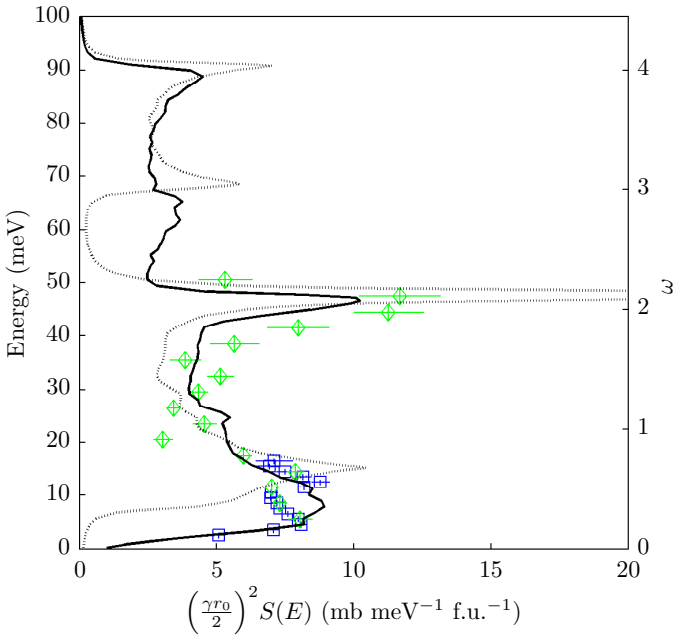

Figure 3.12: Momentum-averaged scattering of $La_{1.75}Sr_{0.25}CoO_4$and scaled DCSG simulations. Experimental points are calculated by the method described in the text from the INS spectra recorded on MERLIN. Blue (green) points indicate values fitted to data measured with $E_i = 20$ meV (60 meV). DCSG simulations of the in-plane magnetic scattering for $\xi_C^{\parallel} = 5a$ disordered stripes (solid line) and $\xi_C^{\parallel} = \infty$ perfect stripe order (dotted line) are also plotted. Both simulations are performed with $JS = 22.5$ meV and $J'/J = 0.05$. The simulated intensities have been scaled for ease of comparison with the data. Reprinted figure from S. M. Gaw *et al.*, Phys. Rev. B, **88**, 165121 (2013) [80]. Copyright (2013) by the American Physical Society.

perimental data points, the simulated in-plane scattering function $[S^{xx}(E)+S^{yy}(E)]$ is plotted for the cases of perfect period-4 stripes (dashed line) and the $\xi_C^{\parallel} = 5a$ DCSG ground state (solid line). The simulations have been scaled for comparison with the experimental data.

The DCSG simulation matches the experimental data points well at low energies in Figure 3.12. This is in contrast to the results for perfect stripes which show some discrepancies. Most prominently, the introduction of disorder in the model lowers the waist of the hour-glass from 15 meV in the perfect stripe spectrum to approximately 12 meV in the DCSG simulation. A similar down shift was observed in the DCSG simulations of $La_{1.67}Sr_{0.33}CoO_4$ [70]. At higher energies, additional features are present in the simulations. These features extend up to energies of $4JS$,

corresponding to the maximum bandwidth due to reversing a spin in a four-nearest neighbour AFM arrangement. Such an environment exists for spins in the middle of the Co^{2+} region of period-4 stripes. Unfortunately, these features are too weak in the measured data to analyse meaningfully.

3.5 Conclusions

This Chapter reports evidence for short-range stripe order in $La_{1.75}Sr_{0.25}CoO_4$ as well as measurements of an hour-glass spectrum. These results demonstrate that stripe order exists at lower doping in the layered cobaltates than previous proposed by Cwik, *et al.* [66]. The hour-glass exhibits broader features than those previously reported in cobaltates, cuprates, or manganates. This highlights the robustness of the hour-glass to disorder, further evidenced by the measurements of the hour-glass at higher temperatures. Such a broadened hour-glass is qualitatively reproduced by LSWT based on a DCSG ground state. Further study of the higher energy spectrum above the hour-glass may reveal more about the local AFM correlations in this highly disorder system. Understanding the emergence of AFM in this striped region of the phase diagram may shed light on the true nature of disorder in the DCSG state.

Chapter 4

Spin Waves and Spinons in Multiferroic CuO

Contents

4.1 Introduction

Cupric oxide, or tenorite, is a naturally occurring binary compound containing Cu^{2+} ions and oxygen. It has been studied at various times in various fields, and is one of the initial magnetic compounds investigated by Brockhouse after the development of neutron scattering [84]. With the discovery of the cuprate unconventional superconductors, CuO was the target of extensive study as the simplest cuprate material. However, interest waned as it became apparent that CuO demonstrates very different physics from that of the layered cuprates which exhibit superconductivity. Instead of the quasi-two dimensional (2D) magnetism exhibited by the superconducting cuprates, CuO shows strong quasi-one dimensional (1D) magnetism, leading to it being described as a $S = 1/2$ antiferromagnetic (AFM) spin chain system [85, 86].

In 2008, interest in CuO was renewed after Kimura, *et al.* [87] demonstrated that it exhibits multiferroic behaviour within a narrow but relatively high temperature phase. Strong magnetoelectric coupling has been demonstrated in this phase [88]. The existence of the multiferroic phase at high temperatures has led many to speculate over the mechanism coupling the magnetism and ferroelectricity in CuO [89–91]. To date, the experimental data measured on CuO is unable to distinguish between the proposed theorectical mechanisms. Therefore, the precise nature of multiferroicity within CuO is currently not understood. The aim of the work described in this thesis was to obtain quantitative information on the magnetic interactions that determine the unusual magnetic and magnetoelectric properties of CuO.

4.1.1 Crystal and Magnetic Structure

Cupric oxide crystallises in the monoclinic C2/c space group with room temperature lattice parameters $a = 4.684\,\text{Å}$, $b = 3.423\,\text{Å}$, and $c = 5.129\,\text{Å}$ [92]. The lattice angle $\beta = 99.54°$ separates the a and c axes. The unit cell contains four Cu atoms and

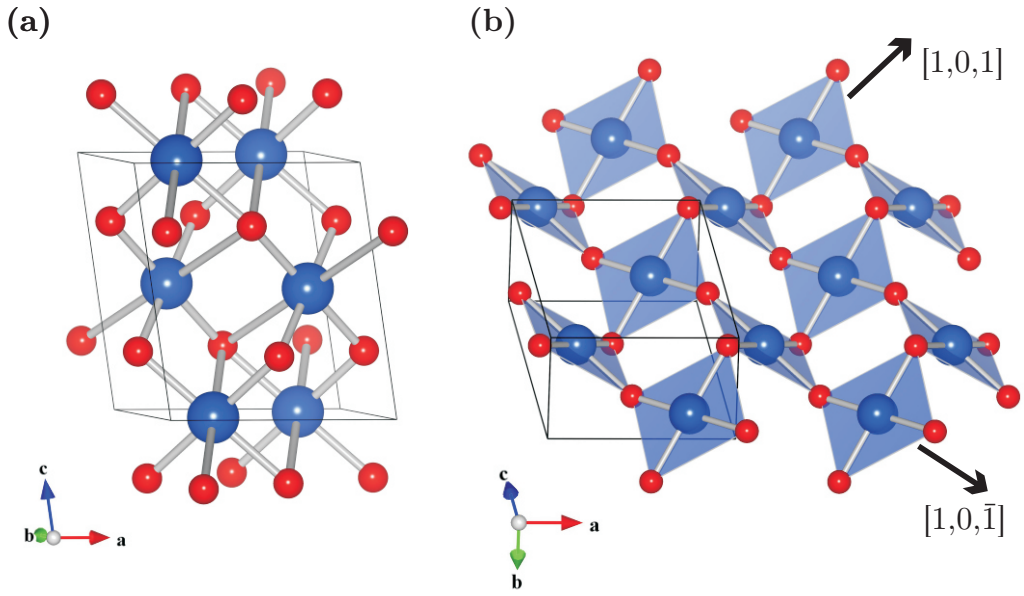

Figure 4.1: The crystal structure of CuO. (a) The monoclinic unit cell of CuO. Cu and O atoms are depicted as blue and red spheres respectively. (b) The square planar oxygen environment of each Cu atom is shaded in blue. The crystal structure is comprised of buckled Cu-O-Cu ribbons parallel to the $[1, 0, 1]$ and $[1, 0, \bar{1}]$ directions. The square planar oxygen arrangement surrounding successive Cu atoms along the ribbons are tilted in alternating directions.

this structure is shown in Figure 4.1(a). Each Cu atom is surrounded by four O, creating a local square-planar environment. Neighbouring CuO_4 plaquettes corner share oxygen atoms and the relative Cu-Cu and Cu-O distances mean that the plaquettes are tilted out of the *ac* plane in alternating directions. This feature of the structure is highlighted in Figure 4.1(b). CuO can, therefore, be considered as buckled Cu-O-Cu ribbons parallel to the $[1, 0, 1]$ and $[1, 0, \bar{1}]$ directions.

Certainly two, and probably three, long range magnetic orders develop in CuO below $T_{N3} = 230\,\mathrm{K}$. Cupric oxide adopts a collinear AFM ground state spin structure below $T_{N1} = 213\,\mathrm{K}$ [85, 93]. Spins align parallel to the b axis and are antiferromagnetically aligned along $[1, 0, \bar{1}]$ and ferromagnetically aligned in the $[1, 0, 1]$ direction. This structure is designated AF1 and is characterised by the ordering wave vector $\boldsymbol{Q} = (1/2, 0, -1/2)$. It is shown in Figures 4.2(a) and 4.2(b).

The stability of this magnetic ordering is understood by considering the Cu-O-Cu bond angles in each direction [93]. The bond angle along the $[1, 0, \bar{1}]$ direction is 146° which approaches the 180° angle favoured by AFM exchange according to the Goodenough-Kanamori-Anderson (GKA) rules [2, 3]. The bond angle in the $[1, 0, 1]$ direction is 109°, much closer to the 90° which promotes ferromagnetic (FM) interactions. These two directions connect Cu^{2+} ions equally displaced along the b axis. Therefore, the magnetic structure can be viewed as two inter-penetrating AFM sublattices separated by an offset along b.

Between T_{N1} and $T_{N2} \approx 229.3\,\mathrm{K}$, an incommensurate spin structure develops [93–95]. It is characterised by the propagation vector $\boldsymbol{\kappa} = (0.506, 0, -0.483)$ and the spins adopt a spiral structure, rotating in the plane defined by the $\boldsymbol{b}^*$ and $(0.506\boldsymbol{a}^* + 1.517\boldsymbol{c}^*)$ vectors [94, 95]. This order is designated AF2. Various mechanisms have been put forward to explain why such a spiral ordering is energetically favourable at higher temperatures. Some of these will be discussed in the next section.

Finally, recent measurements have shown evidence for a third magnetically ordered phase between T_{N2} and $T_{N3} \approx 230.0\,\mathrm{K}$ [96, 97]. Measurements are consistent with this being some collinear AFM arrangement of spins different from the AF1 phase [96], however, the magnetic structure has not been experimentally determined.

4.1.2 Quasi-1D Magnetic Behaviour

Above T_{N3} significant magnetic correlations persist in CuO and there is evidence for one-dimensional (1D) magnetic behaviour. This was first reported based on measurements of the magnetic susceptibility. There is significant deviation from the expected Curie-Weiss susceptibility behaviour in the high-temperature paramagnetic phase of CuO. This manifests as a broad peak centred on 540 K [98] and is consistent with the paramagnetism of 1D AFM chains [99, 100].

Subsequent inelastic neutron scattering (INS) measurements reported the low

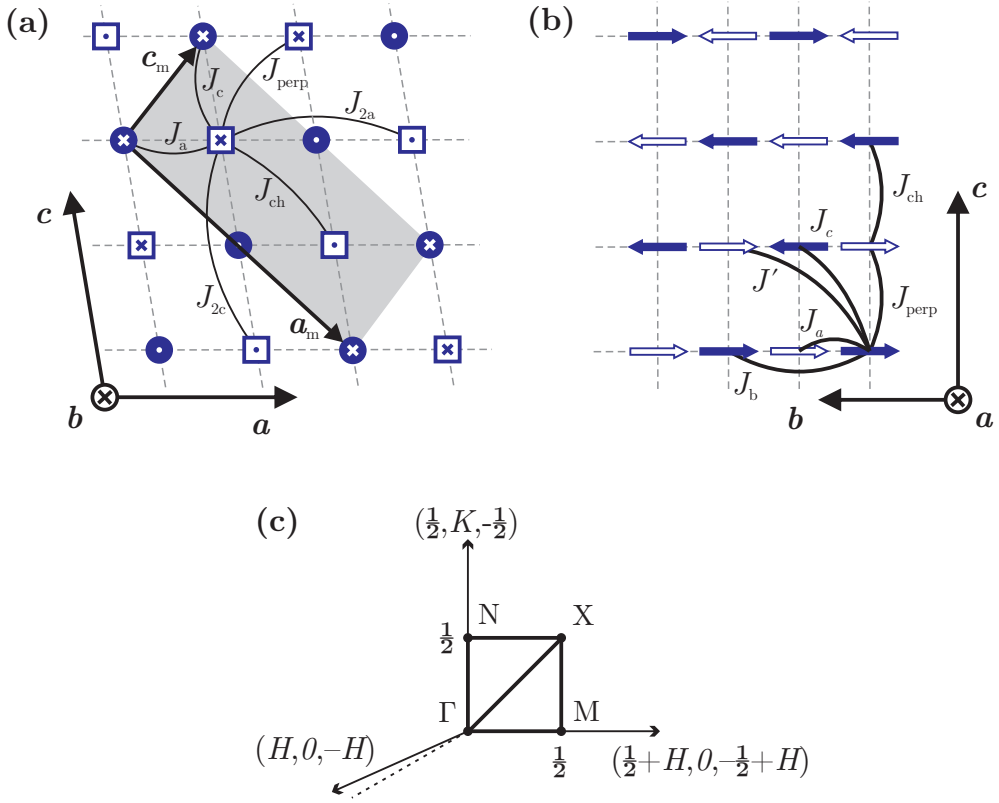

Figure 4.2: Schematic diagram of the AF1 magnetic order and inter-chain Brillouin zone of CuO. (a) The magnetic order projected onto the ac plane. The displacement along the b axis is shown by plotting atoms as filled circles (open squares) which correspond to Cu atoms located at $b = 0$ ($b = 1/2$). This b axis displacement divides the magnetic structure into two sublattices. Spin are orientated parallel to the b axis, with dots (crosses) denoting spins pointing out of (into) the page. The simplified magnetic unit cell containing four Cu atoms is depicted by the grey shaded area and the a_m and c_m magnetic lattice vectors are labelled. (b) The magnetic order projected onto the bc plane. Only atoms on the left-most half of (a) are shown (ie. those Cu^{2+} ions with the two lowest a axis components). The displacement of the atoms along a is denoted by filled ($a = 0$) and open ($a = 1/2$) arrows. The arrow denotes the spin directions of each Cu^{2+} ion. In both (a) and (b) the exchange parameters considered in the analysis are labelled. (c) Diagram of the relevant reciprocal space directions of CuO. The dashes line indicates the direction perpendicular to both $(0, K, 0)$ and $(H, 0, H)$. The path through the inter-chain dispersion direction is shown. This path begins at an AFM zone centre at $\Gamma = (1/2, 0, -1/2)$. The other high symmetry points are labelled.

energy spin wave dispersion along several reciprocal lattice directions [85, 86]. The dispersions are consistent with a large discrepancy between the exchange interactions parallel to the $(H, 0, -H)$ direction compared to those along the $(H, 0, H)$ and

$(0, K, 0)$ directions. The differences between the interaction strengths are also consistent with the GKA theory for different Cu-O-Cu bond angles. These differences lead to quasi-1D magnetic behaviour in CuO. Further INS measurements probed the high energy part of the magnetic spectrum along the AFM chain direction [101] and successfully modelling it using the the Müller ansatz, a phenomenological model for $S = 1/2$ Heisenberg AFM chains [102].

4.1.3 Multiferroicity in CuO

In 2008, Kimura, *et al.* [87] reported that the AF2 phase of CuO has a reversible ferroelectric polarisation. This polarisation is induced by the spiral magnetic order, which breaks inversion symmetry. CuO is, therefore, an improper multiferroic. A strong magnetoelectric coupling has been reported, evidenced by an applied electric field switching the relative domain populations associated with the chiral AF2 magnetic order [88] (however, an applied electric field has little effect on the bulk magnetisation [103]).

CuO has created excitement amongst researchers because of the relatively high temperature of its multiferroic phase. Additionally, before the recent evidence for the very narrow commensurate AFM phase between T_{N2} and T_{N3} [96, 97], the emergence of a multiferroic phase directly from a PM state contrasted the typical behaviour of improper multiferroics [104–106]. This, and the relatively high temperature of the multiferroic phase, led to the proposal of various mechanisms explaining how a spiral spin structure could be stabilised in CuO. Giovannetti, *et al.* [89] postulate that the combined effect of the Dzyaloshinskii-Moriya (DM) interaction and spin-lattice coupling act to stabilise the spin-canting and polarisation. Jin, *et al.* [91] theorise that weakly frustrated inter-sublattice interactions drive CuO into its spiral ordered phase. Tolédano, *et al.* [90] put forward a strong triggering-coupling mechanism of two AFM order parameters which explains the relative sequence and nature of the T_{N1} and T_{N2} phase transitions in CuO. All these theories identify the

DM interaction as causing the polarisation but some underlying magnetic interaction is responsible for the creation of the necessary spiral order.

In this Chapter, I shall present INS measurements of CuO in the AF1 collinear phase. The measurements probe the entire extent of the magnon and spinon spectrum, considerably extending previous studies which were restricted to limited energies and directions in momentum space. The observation of magnetic excitations reveal information about the dominant interactions within CuO. This can be used as a test for the proposed mechanisms giving rise to the multiferroic AF2 phase. High energy excitations are measured parallel to the real space $[1, 0, \bar{1}]$ direction and are consistent with quasi-1D spin-1/2 AFM chain behaviour. Furthermore, measurements are shown suggesting the presence of a magnetic mode due to longitudinal fluctuations. Significant inter-chain excitations are observed at lower energies, extending up to 80 meV. The quasi-1D spectrum is analysed using the Müller Ansatz and the dominant exchange parameter is found to be J_{ch} =143.6(8) meV (after quantum renormalisation). The inter-chain spectrum is compared to a linear spin wave model derived from a Heisenberg Hamiltonian. In order to accurately describe the spectrum, two previous unconsidered interactions must be included to produce a phenomenological model for CuO. The first is an additional next-nearest neighbour exchange which describes interactions in the $[1/2, 1, 1/2]$ direction. The second is the redefinition of the nearest neighbour inter-sublattice exchange interaction into two symmetry inequivalent interactions.

4.2 Sample Preparation and Characterisation

4.2.1 Crystal Growth

Single crystal samples of CuO were prepared by Dr D. Prabhakaran using the floating-zone growth technique. The method has been previously reported in Ref. [107]. CuO is difficult to grow as a single crystal and sample quality is highly dependent on the preparation conditions. The monoclinic structure of CuO make the growth

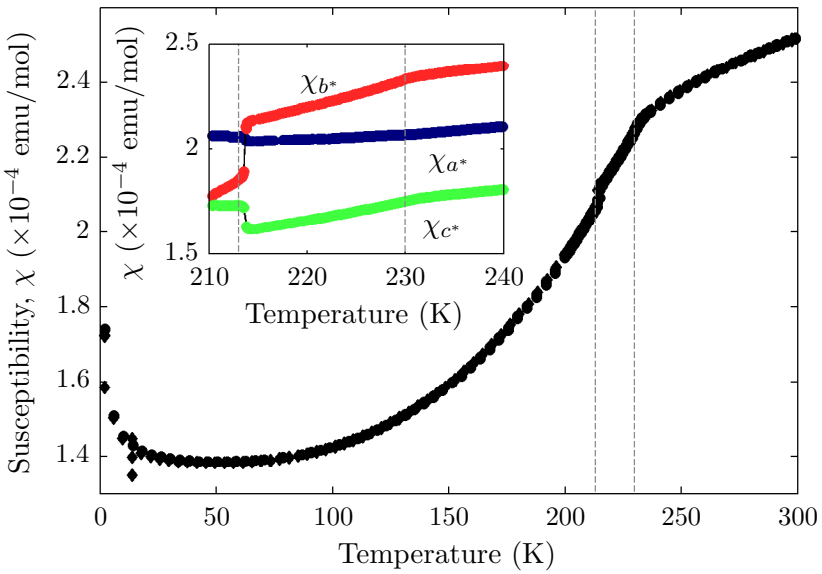

Figure 4.3: Magnetic susceptibility measured in CuO. Data recorded by applying a 1000 Oe field roughly parallel to the b^* axis (black). The FC (circle markers) and ZFC (diamond markers) susceptibilities are approximately equal across the full temperature range measured. The expected transition temperatures of 213 and 230 K are denoted by the dashed lines. The insert shows ZFC data measured by Dr P. Babkevich on a CuO sample from the same batch as used in this study [88]. Clear transitions can be observed in all three reciprocal lattice directions (labelled).

of twinned phases and multi-grain cyrstals very common. In some cases, single crystals could be extracted by cleaving, however, this was not always the case. In total, 20 growths were performed in order to produce six high-quality single crystals used in the neutron scattering experiments.

4.2.2 Magnetic Characterisation

Figure 4.3 shows the measured susceptibility of CuO. The main figure presents the field-cooled (FC) and zero-field-cooled (ZFC) susceptibilities, when a magnetic field of 1000 Oe was applied approximately parallel to the $\boldsymbol{b}^*$ direction. Anomalies are present at 213 and 230 K consistent with the expected behaviour of CuO. For $T > 230$ K, the susceptibility is observed to increase with increasing temperatures. This is consistent with 1D AFM behaviour [100]. Note, that the transitions are not as well defined as those previously reported because of a slight misalignment of the

sample [87, 108]. The insert in Figure 4.3, shows complementary ZFC measurements performed by Dr P. Babkevich on a CuO sample grown in the same batch as those used in this chapter. An applied field of 1000 Oe was aligned parallel with the three reciprocal lattice directions. The data show clear transitions at the expected temperatures. The line shape of the three susceptibilities is in good agreement with previous results. There is no evidence for any magnetic impurity phases.

4.2.3 Crystal Quality Checks and Alignment

As CuO single crystals are difficult to grow, extensive quality checks were performed using X-ray and neutron Laue diffraction to ensure only samples of high crystal quality were used in the subsequent experiments. Figure 4.4(a) shows an example X-ray Laue image centred on the $(1, 0, 1)$ reflection illustrating the high crystal quality of the samples used. A small mosaic spread (characterised by an angle of $\eta = 2^\circ$) was found in the crystals. Such a mosaic appears unavoidable in large crystals of CuO. Due to the small magnetic moment in CuO [85, 109] a large mass of crystal was required to perform inelastic neutron scattering experiments. To achieve this six single crystals, with a combined mass of 32.5 g, were co-aligned – see Figure 4.4(b). The large size of the individual crystals, and their monoclinic structure, made a coalignment within the 50×50 mm cross-sectional area of the ISIS neutron beam difficult. The in-plane mosaic of the coaligned sample was measured for the $(2, 0, 0)$ and $(0, 0, 2)$ Bragg peaks on the MAPS spectrometer and is shown in Figure 4.4(c). The mosaic angle (defined as the Bragg peak half width at half maximum (HWHM) when measured in scattering angle) was found to be $\eta \approx 3^\circ$. This mosaic will be accommodated for in the subsequent resolution convolution when analysing the INS data in Section 4.4.2.

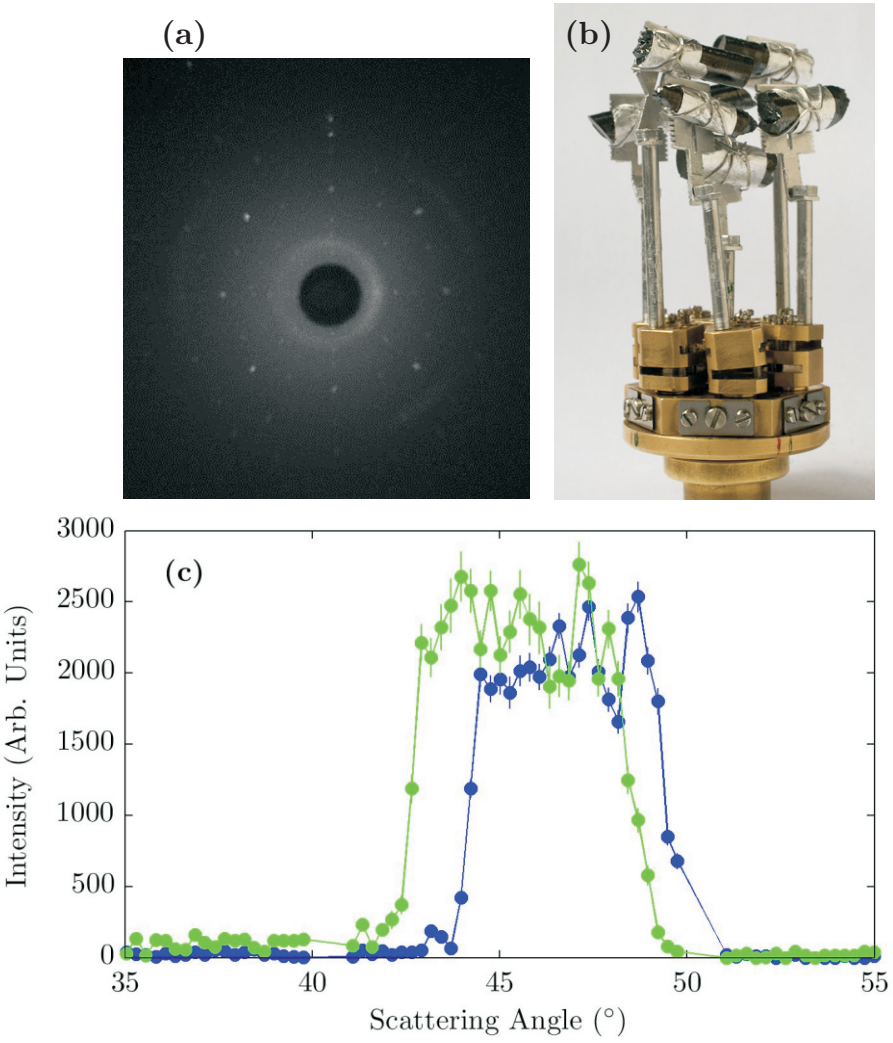

Figure 4.4: Crystal quality and co-alignment of the CuO sample. (a) X-ray Laue diffraction pattern measured with the incident beam parallel to the $(1, 0, 1)$ direction. The sharp peaks demonstrate the high quality of the individual crystals. (b) Photograph of the six co-aligned single crystals of CuO used as the sample in the neutron experiments on the MAPS and MERLIN spectrometers. (c) The in-plane mosaic of the $(2, 0, 0)$ (green) and $(0, 0, 2)$ (blue) Bragg peaks of the co-aligned sample measured on the MAPS spectrometer.

4.3 Inelastic Neutron Scattering Measurements

Neutron experiments were performed on the co-aligned array of single crystals using the MERLIN and MAPS spectrometers at the ISIS facility, UK. Multi-angle scans were performed on MERLIN using $E_\mathrm{i} = 90$, 135, and 180 meV configurations.

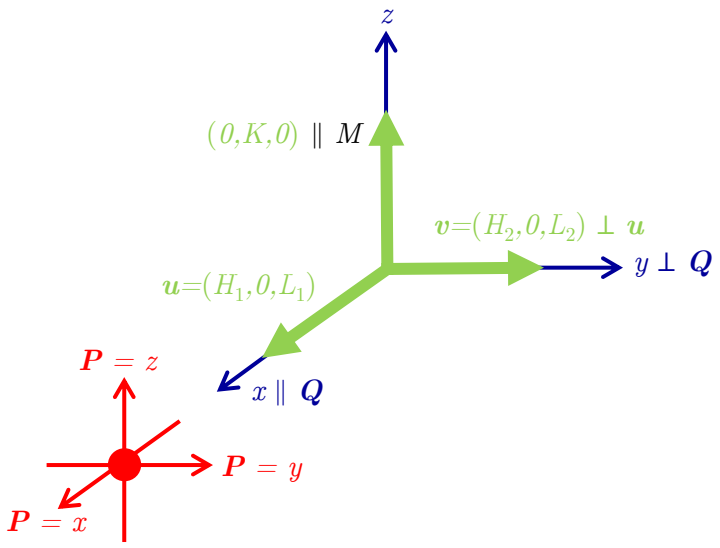

Figure 4.5: Experimental geometry for CuO measured on IN20 with uniaxial polarisation analysis. Blue arrows indicate the spectrometer geometry as defined by the three orthogonal directions x, y, and z. The direction x is parallel to the scattering vector $\boldsymbol{Q}$. The y direction is perpendicular to x and with x defines the horizontal scattering plane. z is perpendicular to both x and y and defines the out-of-plane direction. The crystal orientation (green) is shown with $(H, 0, L)$ in the horizontal scattering plane. Spins in the AF1 phase of CuO are orientated along the b^* direction. Three neutron polarisations (red) are measured, parallel to x, y, and z.

A similar multi-angle scan was performed on MAPS using $E_\mathrm{i} = 160\,\mathrm{meV}$. In each case, $(H, 0, L)$ was in the horizontal scattering plane and the sample was rotated about the b axis in 1° increments. Additionally, fixed orientation scans were performed on MAPS using $E_\mathrm{i} = 300$ and $500\,\mathrm{meV}$. In these measurements the crystal was orientated with the $[1, 0, \bar{1}]$ chain direction perpendicular to $\boldsymbol{k}_\mathrm{i}$ while $(H, 0, L)$ remained in the horizontal scattering plane. The energy resolution of all these measurements is characterised by a full width at half maximum (FWHM) broadening of approximately 5% of E_i at $E = 0$. The broadening decreases with increasing energy transfer. A standard vanadium sample was measured to allow the detector efficiencies to be normalised and all intensities to be expressed in absolute units. Data were recorded at 5 and 6 K for the MERLIN and MAPS experiments respectively.

Polarised inelastic neutron scattering measurements were performed on the

largest individual crystal of CuO used in the co-aligned array. This had a mass of 6.7 g. The experiment was performed on the IN20 triple axis spectrometer (TAS) at the ILL, France. The crystal was aligned with $(H, 0, L)$ parallel to the horizontal scattering plane. Heusler (1,1,1) crystals were used in a doubly focussing monochromator and horizontally focussing analyser to perform uniaxial polarisation analysis. A Helmholtz coil was used to adiabatically change the orientation of the neutron beam polarisation. The polarisation was directed parallel (x) and perpendicular (y, z) to the scattering vector $\boldsymbol{Q}$. The relative directions of the polarisation, and orientations of the crystal and spectrometer are defined in Figure 4.5. This set up allows the magnetic scattering from spin components in the $(H, 0, L)$ plane M_{ac} to be separated from out-of-plane spin components M_b. As the spins in CuO are aligned parallel to the b axis in the AF1 phase, M_{ac} and M_b correspond to transverse and longitudinal magnetic fluctuations, respectively, when $E \neq 0$. Additionally, polarisation analysis allows the nuclear and magnetic scattering to be separated. The sensitivity of each polarisation direction depends on the type of scattering process and is summarised in Table 4.1. Line scans were measured with a fixed final wave vector of either $k_\mathrm{f} = 2.662$ or $4.1\,\mathrm{\AA}^{-1}$. The flipping ratios of all three polarisation directions were measured using $k_\mathrm{f} = 2.662\,\mathrm{\AA}^{-1}$ at the $(2, 0, -2)$ nuclear Bragg peak. The ratios were $R_x = 12$, $R_y = 12$, and $R_z = 21$, corresponding to polarisation efficiencies of between 85–91%. All data were recorded at a temperature of 1.5 K.

4.3.1 1D Magnetic Behaviour

Figure 4.6 shows the high energy excitation spectrum measured on the MAPS spectrometer. The wave vector axis is parallel to the $[1, 0, \bar{1}]$ chain direction which is not exactly parallel to the $(1, 0, -1)$ direction because of the monoclinic lattice [$Q_\mathrm{ch} = (0.93q, 0, -1.09q)$ when defined in reciprocal lattice units (r.l.u.) of $2\pi/d_{[0.5,0,-0.5]}$]. Scattering in perpendicular wave vector directions has been integrated and the dispersion has been symmetrised about the $Q_\mathrm{ch} = 0$ position. The

Polarisation	Interaction Type	Sensitivity	Label
$\boldsymbol{P} = x \parallel \boldsymbol{Q}$	SF	$M_{ac} + M_b$	$x\bar{x}$
	NSF	Nuclear	xx
$\boldsymbol{P} = y \perp \boldsymbol{Q}$	SF	M_b	$y\bar{y}$
	NSF	Nuclear+M_{ac}	yy
$\boldsymbol{P} = z \perp \boldsymbol{Q}$	SF	M_{ac}	$z\bar{z}$
	NSF	Nuclear+M_b	zz

Table 4.1: Summary of the sensitivity of polarisation channels measured during the CuO experiment on IN20. The three orthogonal polarisation directions x, y, and z (defined in Figure 4.5) lead to spin-flip (SF) and non-spin-flip (NSF) scattering processes that are sensitive to different components of the magnetisation and nuclear interactions. The channels are labelled as $\alpha\alpha$ for NSF and $\alpha\bar{\alpha}$ for SF scattering processes, where $\alpha = \{x, y, z\}$.

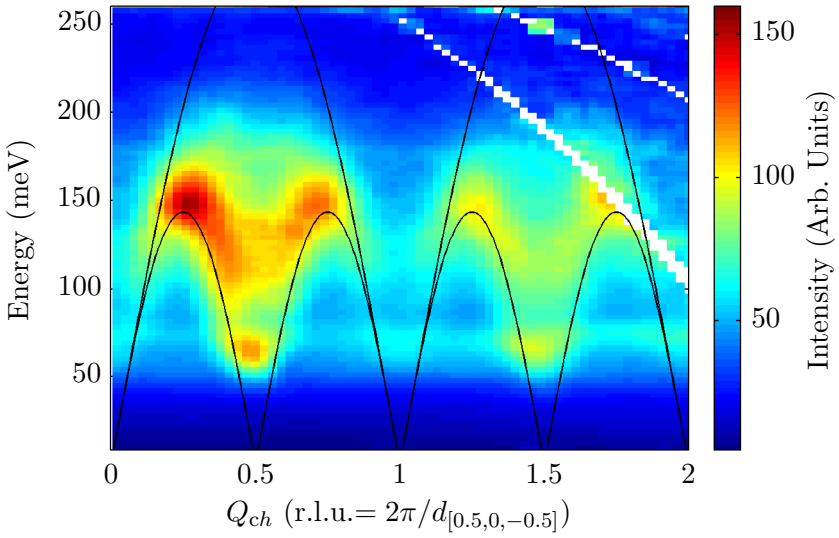

Figure 4.6: The spinon excitation spectrum measured in CuO. Data recorded on the MAPS spectrometer with $E_\mathrm{i} = 300\,\mathrm{meV}$. The inter-chain $(H, 0, H)$ and $(0, K, 0)$ directions have been integrated over and the spectrum has been symmetrised about the $Q_\mathrm{ch} = 0$ position to improve counting statistics. Intensities have been multiplied by the energy dependant scaling factor $[(E\beta)/(1 - \exp(-E\beta))]^2$. This has a similar form to the Bose population factor and $\beta = 1/k_\mathrm{B}100$ was used to best highlight the lower boundary of the spinon continuum. The black lines shows the lower and upper boundary of the spinon continuum calculated for an ideal $S = 1/2$ AFM chain using the des Cloizeax dispersion [6] with $J = 91.4\,\mathrm{meV}$.

intensities have been scaled by an energy dependent factor to ensure that spectral features across a large energy range are visible. A clear sinusoidal dispersion of in-

tensity is observed between 50 and 140 meV. A continuum of scattering is measured at higher energies, extending up to ~ 280 meV. As an alternative view, Figure 4.7 shows unsymmetrised wave vector cuts between $-2 < Q_{\mathrm{ch}} < 2$ r.l.u. measured on MAPS using $E_{\mathrm{i}} = 300$ meV.

For comparison, the upper and lower boundary of the two spinon continuum is plotted alongside the spectrum in Figure 4.6. These boundaries are defined using the des Cloizeax-Pearson dispersion [6] for an ideal $S = 1/2$ AFM chain described by the Heisenberg Hamiltonian

$$\mathcal{H} = J \sum_{\langle i,j \rangle} \boldsymbol{S}_i \cdot \boldsymbol{S}_j, \tag{4.1}$$

and have the form

$$E_{\mathrm{l}}(Q_{\mathrm{ch}}) = \frac{\pi J}{2} |\sin(2\pi Q_{\mathrm{ch}})|, \tag{4.2}$$

$$E_{\mathrm{u}}(Q_{\mathrm{ch}}) = \pi J |\sin(\pi Q_{\mathrm{ch}})|. \tag{4.3}$$

For this comparison, the exchange parameter $J = 91.4$ meV has been used. The dispersing peaks observed in the cuts correspond well to this theoretical continuum and are consistent with $S = 1/2$ AFM chain behaviour.

4.3.2 3D Magnetic Behaviour

At lower energy transfers, the weaker inter-chain exchange couplings become significant and a 3D magnetic excitation spectrum can be observed in CuO. Figure 4.8 shows the measured inter-chain excitations across a plane contained within the full 3D monoclinic Brillouin zone (BZ). A schematic diagram of this inter-chain plane is shown in Figure 4.2(c). This plane is centred on a magnetic Bragg peak position at Γ. The other high symmetry points of the BZ that lie within the 2D plane are labelled in Figure 4.2(c). These positions define the wave vector path of Figure 4.8. Due to the data coverage of the multi-angle scanning technique, data in Figure 4.8

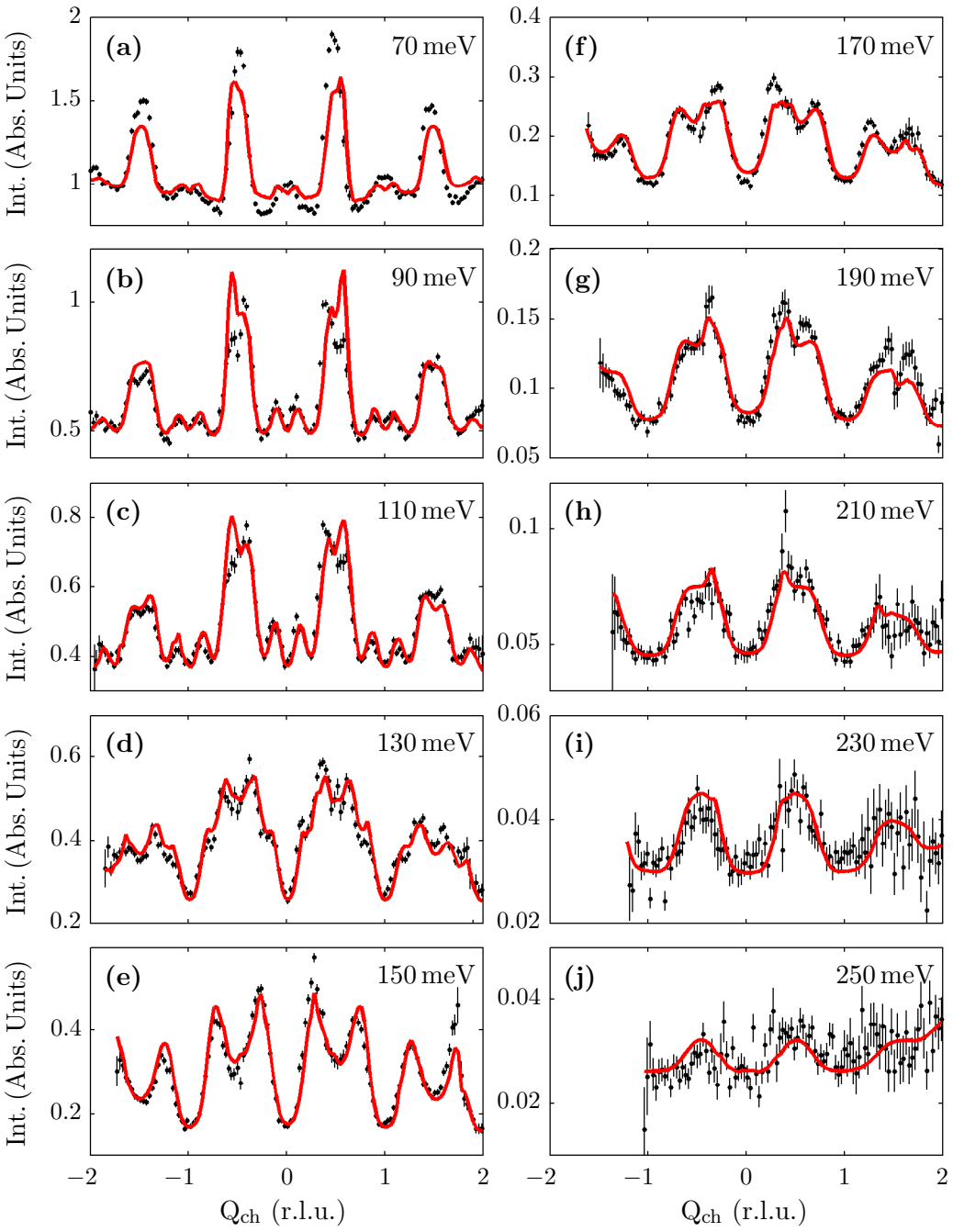

Figure 4.7: Wave vector cuts across the spinon continuum spectrum of CuO and the fit to the Müller ansatz. Data points (black markers) were measured on the MAPS spectrometer using $E_i = 300\,\text{meV}$. The line cuts are measured at constant energies increasing from (a) to (j). All cuts are integrated across a 20 meV range to improve statistics. The average energy $\langle E \rangle$ after this integration is recorded in each sub panel. All intensities are recorded in absolute units of $\text{mb}\,\text{sr}^{-1}\,\text{meV}^{-1}\,\text{f.u.}^{-1}$. The global fit to the Müller ansatz convolved with the MAPS resolution function is shown (red line) and is described in the main text.

derive from planes centred on several magnetic Bragg peaks. Compiling data from these various zones offers an excellent view of the magnetic excitations, however, there are discrepancies in the intensities between some panels. This is most noticeable in the intensity of the lowest energy phonon which appears discontinuous. Note that previous studies of the 3D magnetic excitations in CuO were restricted to the $\Gamma \rightarrow$M and $\Gamma \rightarrow$N directions [86]. Therefore, the $\Gamma \rightarrow$X and X$\rightarrow$M and X$\rightarrow$N paths are reported here for the first time.

The inter-chain spectrum shows clearly dispersing intensity extending up to 80 meV. The modes appear degenerate across most of the spectrum. However, the intensity is broad, suggesting some small splitting of the modes. There is clear evidence for splitting at the minimum of the dispersion at the zone centre position Γ. Unfortunately, the precise position of the gaps at Γ associated with each mode is obscured by low energy phonons (which weakly disperse between $10 - 20$ meV). The energy and nature of the gaps shall be revisited in our measurements using polarised neutrons in the next section.

While Figure 4.8 shows the spectrum in the plane in reciprocal space that is approximately perpendicular to the chains, the true 3D BZ will include additional high symmetry points with a component of $\boldsymbol{Q}$ parallel to the $(H, 0, -H)$ direction. This direction approximately coincides with the quasi-1D chain direction $[1, 0, \bar{1}]$. Therefore, the behaviour of the spectrum along the $(H, 0, -H)$ direction is dominated by the 1D physics observed in the previous section. This makes mapping the spectrum throughout the full 3D BZ very difficult because of two effects. First, the dispersion extends to much higher energy along $(H, 0, -H)$, reaching a maximum at $Q_{\mathrm{ch}} = Q_{\mathrm{AFM}} \pm 0.25$, see Figure 4.6. At such high energies the small dispersion introduced by the inter-chain coupling is impossible to resolve in the data. Secondly, the intensity is suppressed at the minima of the spinon continuum's lower boundary at the 1D zone boundary (ie. at $Q_{\mathrm{ch}} = Q_{\mathrm{AFM}} \pm 0.5$ positions) as seen in Figure 4.6. Hence, no inter-chain dispersion can be observed in the data around the

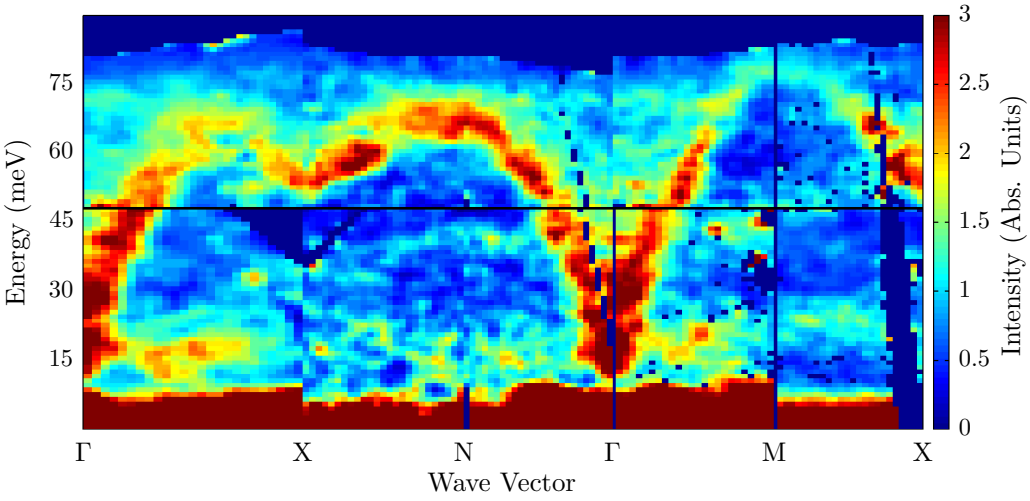

Figure 4.8: The measured inter-chain excitation spectrum of CuO. Data were recorded using the multi-angle scan method on the MAPS spectrometer with $E_\mathrm{i} = 160\,\mathrm{meV}$. The 2D slices shown are centred around several zone centre Γ positions. The high ($> 48\,\mathrm{meV}$) and low ($< 48\,\mathrm{meV}$) energy data are centred on the $\Gamma = (-1.5, K, 1.5)$ and $\Gamma = (-1.5, K, -0.5)$ positions respectively. Both $K = 0$ and 1 are used at different points in the high and low energy data to improve the total data coverage. The labelled high symmetry position are defined in Figure 4.2(c). Data has been integrated across a small wave vector range (0.1 r.l.u. wide), perpendicular to each dispersive direction, to improve statistics. The intensity in each panel is equally scaled and is recorded in absolute units of $\mathrm{mb\,sr^{-1}\,meV^{-1}\,f.u.^{-1}}$.

$Q_\mathrm{ch} = Q_\mathrm{AFM} \pm 0.5$ positions because of the suppression of intensity by the dominant structure factor effects associated with the 1D chain.

4.3.3 3D to 1D Crossover Behaviour

The data presented in Section 4.3.1 gives clear evidence for 1D magnetic behaviour at high energy transfer and Section 4.3.2 demonstrates that 3D magnetic behaviour exists at lower energies. The magnetic behaviour at the crossover between these two regions of the excitation spectrum is expected to be inconsistent with models for either 1D or 3D magnetism. Most prominently, an excitation mode associated with longitudinal magnetic fluctuations is predicted at energies above the transverse fluctuation modes and below the spinon continuum [110, 111]. Such a mode has been measured in $KCuF_3$, a very weakly-coupled quasi-1D $S = 1/2$ Heisenberg AFM [112].

Figure 4.9 outlines the evidence for a longitudinal mode in CuO. The presented line cuts show the subtracted SF intensity isolating the M_b component of magnetic scattering – see Table 4.1. The IN20 spectrometer is not optimised for high energy measurements. Hence, the incident flux at high energies is relatively low, which leads to relatively large statistical errors associated with each data point. As the measured flipping ratios are large, any leakage between SF and NSF channels will be small. Therefore, no correction for the imperfect flipper efficiency has not been applied to avoid any further worsening of the errors on the data.

Figure 4.9(a) presents an energy line cut showing the M_b scattering at the $\boldsymbol{Q}_{\mathrm{AFM}} = (2.5, 0, -2.5)$ BZ centre. The mean intensity – around which the data points fluctuate – markedly increases above 63 meV. This is consistent with the onset of weak longitudinally fluctuating excitations. Figures 4.9(b) and 4.9(c), show M_b wave vector line cuts along the $(H, 0, -H)$ direction at $E = 65$ and 70 meV respectively. A single peak is observed centred approximately on the $\boldsymbol{Q}_{\mathrm{AFM}}$ position at 65 meV. This branches into two peaks at 70 meV. The localisation of M_b scattering intensity in wave vector and the subsequent splitting of the intensity is consistent with the dispersive behaviour of a mode. Such behaviour does not arise due to continuum scattering, where longitudinal fluctuations are also expected. Unfortunately, a spurious signal [centred on 83 meV in Figure 4.9(a)] and a further decrease of incident flux prevented higher energies from being investigated. Hence, the onset of the spinon continuum could not be measured for comparison.

The large statistical errors in Figure 4.9 make any analysis of the high-energy polarised neutron data difficult and so further measurements are required to confirm these findings. The current data can, however, be compared to the theory proposed in Refs. [110, 111]. This model is described by Lake, *et al.* [112], who also show that it is an excellent description of the behaviour of $KCuF_3$. However, CuO is not well described by this theory. The expression for the dispersion of the the longitudinal

fluctuation mode, defined in Ref. [112] and applied to the case of CuO, is

$$E_{\mathrm{L}}(\boldsymbol{Q}) = \sqrt{\frac{\pi^2 J^2}{4}\sin^2(2\pi Q_{\mathrm{ch}}) + M^2\Big(3 - \frac{\gamma[\cos(2\pi Q_{(1,0,1)}) + \cos(2\pi K)]}{2}\Big)}, \quad (4.4)$$

where $\gamma \approx 0.491$ is a constant and M is the transverse fluctuation mode energy at the inter-chain zone boundary (ie. at positions M or N). Note, that the model is derived for a single inter-chain coupling. Therefore, an average value of the mode energy at M and N was used for CuO. $Q_{(1,0,1)}$ defines the wave vector direction perpendicular to the chains and within the *ac*-plane. Using the expression, the model predicts the energy minimum to lie at $\sim 120\,\mathrm{meV}$. Only if the zone boundary energy M is significantly underestimated (to be $\sim 40\,\mathrm{meV}$ at the M and N positions) does the theory predict the measured minima at 63 meV. Why the model would over-estimate the energy of the mode in a material with more significant inter-chain coupling is an open question. However, it should be noted that the model is derived for an unfrustrated system [112] and so deviations from the theory should perhaps be expected in highly frustrated CuO.

4.3.4 Anisotropic Magnetic Excitation Gap

Figure 4.10 shows the measured gap of the magnetic excitation spectrum at three magnetic zone centre positions. Uniaxial polarisation analysis was used to separate the magnetic and phonon scattering at low energies. The measured polarisation channels, outlined in Table 4.1, have been subtracted to separate the individual components of magnetic and nuclear scattering while also removing the instrumental background. The intensity measured has been corrected for the magnetic form factor of Cu^{2+} ions. Figure 4.10(a) depicts the gap associated with transverse magnetic fluctuations measured at $\boldsymbol{Q}_{\mathrm{AFM}} = (0.5, 0, -0.5)$ and $(1.5, 0, -1.5)$. As outlined in Section 2.2.3, neutrons are only sensitive to the component of magnetisation perpendicular to the scattering vector. Therefore, measurements with $\boldsymbol{Q} \parallel (H, 0, -H)$ are only sensitive to one component of the in-plane spin fluctuations, denoted M'_{ac}.

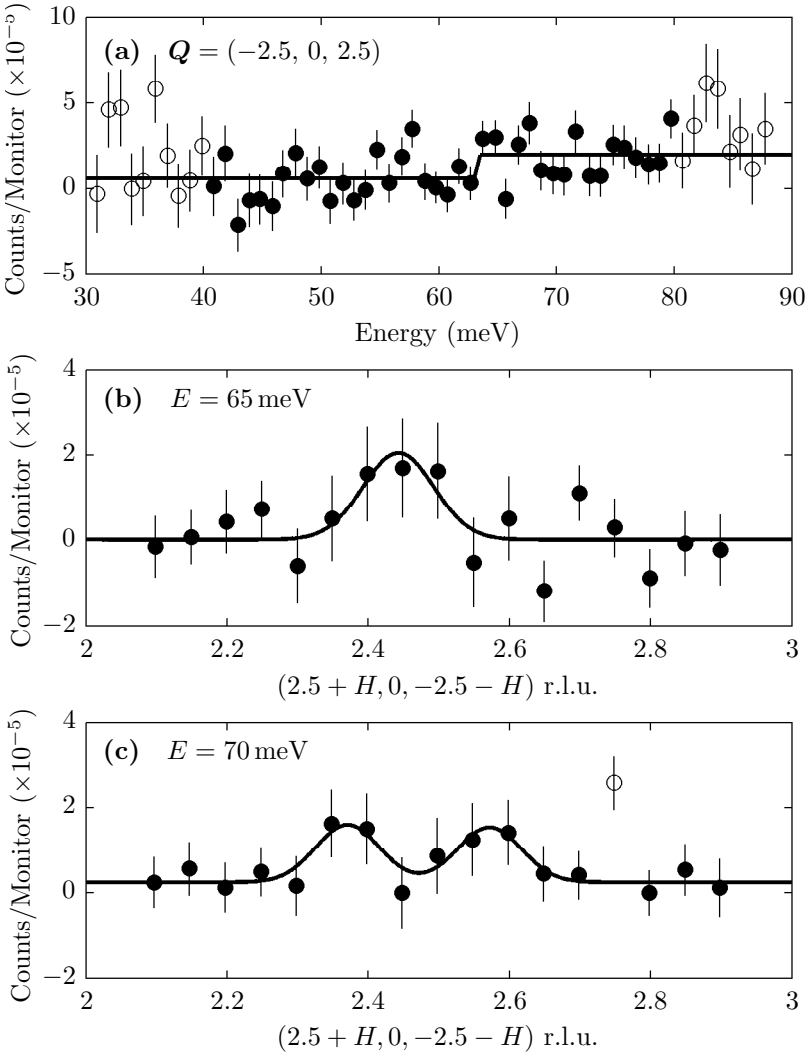

Figure 4.9: Evidence for a longitudinally fluctuating magnetic mode in CuO. (a) Energy line cut of the subtracted M_b scattering centred on the $\boldsymbol{Q}_{\mathrm{AFM}} = (-2.5, 0, 2.5)$ wave vector. A step function is fitted to the data and shown as a black line. There is an increase of intensity at 63 meV. Wave vector line cuts of the subtracted M_b intensity are presented at (b) $E = 65\,\mathrm{meV}$ and (c) $E = 70\,\mathrm{meV}$. Gaussian peaks have been fitted to both the cuts and are shown as black lines. The increased intensity above 63 meV is centred on the $\boldsymbol{Q}_{\mathrm{AFM}}$ wave vector and is consistent with a dispersive mode. Filled data points in each panel denote the points which have been included in the fits.

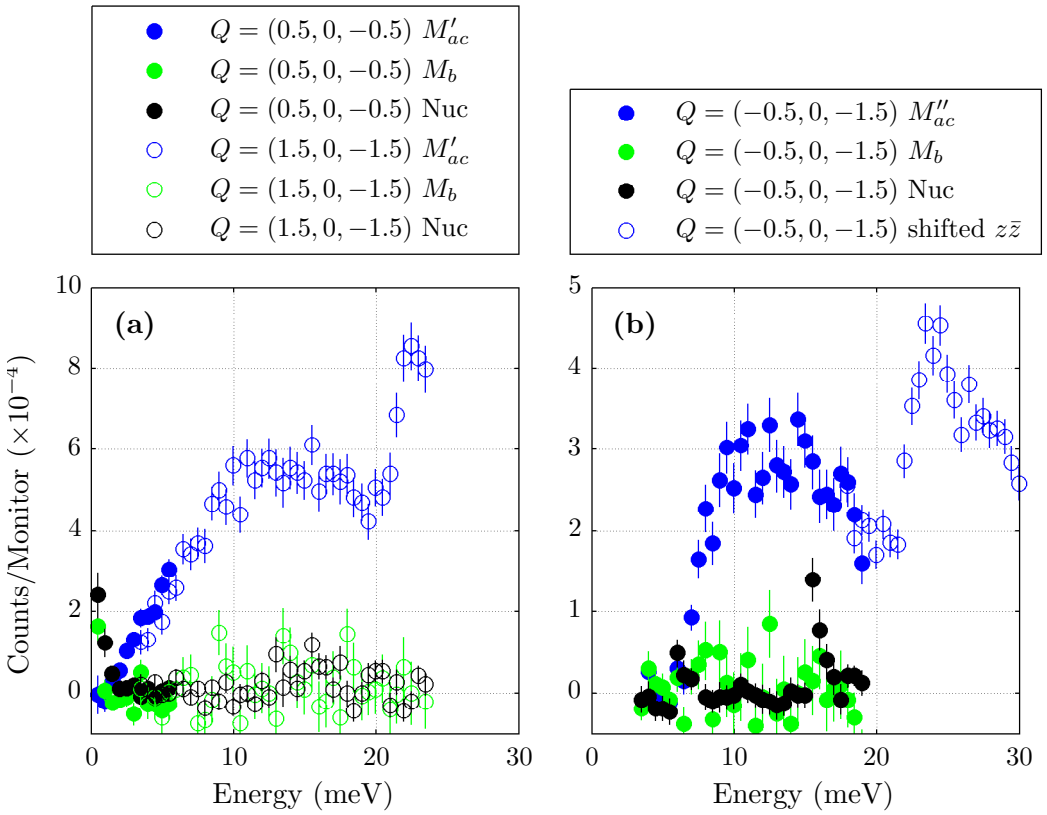

Figure 4.10: The anisotropic magnetic excitation gap of CuO. (a) The broad gap measured at $Q = (0.5, 0, -0.5)$ (filled circles) and $(1.5, 0, -1.5)$ (open circles). The subtracted intensities associated with in-plane (blue) and out-of-plane (green) magnetisation and nuclear scattering (black) are shown. (b) The sharp gap measured at $Q = (-0.5, 0, -1.5)$. Here, open blue circles denote high energy data measured in the $z\bar{z}$ channel which has had a background subtracted to match the subtracted M''_{ac} scattering at low energies. All intensities have been measured with $k_f = 2.662\,\text{Å}^{-1}$ and corrected for the effect of the magnetic form factor.

A steady onset of M'_{ac} scattering is observed, beginning at 2 meV and plateauing at 11 meV. A second, higher energy gap is measured above 21 meV. These two gaps provide evidence for a splitting of the spin wave modes at the magnetic zone centre.

Figure 4.10(b) shows both gaps measured at $\boldsymbol{Q}_{\text{AFM}} = (-0.5, 0, -1.5)$. Measurements with $\boldsymbol{Q} \parallel (H/3, 0, H)$ are sensitive to components of magnetisation M''_{ac}, which are roughly perpendicular to M'_{ac}. The magnetic scattering begins at 6.5 meV and increases up to 9 meV, revealing a much sharper low energy gap than seen in Figure 4.10(a). Not all polarisation channels could be measured at this wave vec-

tor up to the higher energy gap. Therefore, it was impossible to find M''_{ac} at high energies by subtracting the SF channels. Instead, the high energy gap shown in Figure 4.10(b) is measured in the $z\bar{z}$ channel which is only sensitive to in-plane fluctuations. This was shifted to match the subtracted M''_{ac} data at lower energies to effectively correct for a constant energy background. The onset and width of the higher energy gap is approximately equal to that measured in the $(H, 0, -H)$ direction. To better understand the significantly different low energy gap widths, simulations of the spectrometer resolution were performed using the RESCAL software [42]. These predict a broadening with a FWHM of $\sim 1.5\,\text{meV}$ across low energies at all measured wave vectors. This resolution is consistent with the M''_{ac} gap measured at $\boldsymbol{Q} = (-0.5, 0, -1.5)$ but it does not account for the broad M'_{ac} gap measured at $\boldsymbol{Q} = (0.5, 0, -0.5)$ and $(1.5, 0, -1.5)$.

The differences between M'_{ac} and M''_{ac} reveal the gap to be anisotropic. To understand why this might be the case, the nature of the spin anisotropy must be considered. The anisotropy can be a single-ion effect, created by the crystal field and spin-orbit coupling. Alternatively, it could be a two-ion effect due to exchange anisotropy. In this treatment, we shall only consider the single-ion effects. The local anisotropy experienced by an individual spin arises from the spin-orbit coupling to the crystal field produced by the square planar oxygen environment surrounding each Cu^{2+} ion. This crystal field will energetically favour the spin being perpendicular to the oxygen plaquette. As shown in Figure 4.1, these plaquettes are tilted in alternating directions along the $[1, 0, \bar{1}]$ direction. Hence, the ground state arrangement of spins lying parallel to the b axis is an energetic compromise between the local anisotropy and the strong AFM coupling between neighbouring spins [95]. Therefore, spins fluctuations may experience a lower excitation gap when fluctuations allow them to better satisfy the local anisotropy.

The effect of this alternating local anisotropy can be considered for a simplified two spin system. Each spin is placed at the centre of an alternating oxygen envi-

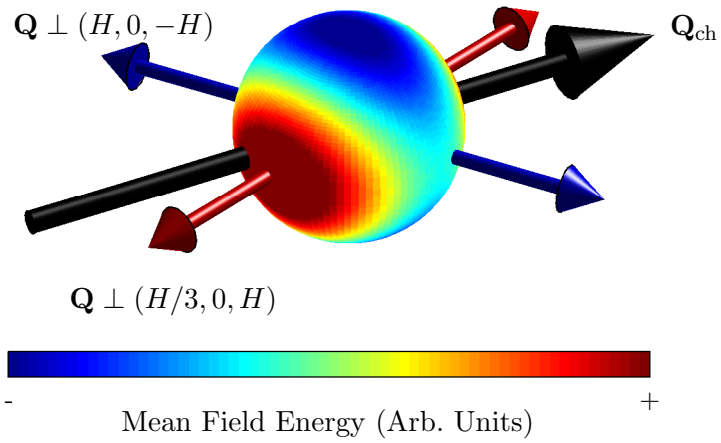

Figure 4.11: The mean field energy of all collinear spin orientations in a simplified model of CuO chains. The colour scale plotted across the surface of the sphere denotes the energy of collinear spins orientated in all possible directions. For reference the chain direction has been plotted (black arrow), alongside the directions perpendicular to the $\boldsymbol{Q} = (0.5, 0, -0.5)$ (blue arrow) and $\boldsymbol{Q} = (-0.5, 0, -1.5)$ (red arrow) directions. The blue and red arrows, therefore, represent the direction of *ac*-plane spin fluctuations probed in the two measurements of the gap.

ronment consistent with the CuO chain direction – see Figure 4.1(b). The total anisotropy is defined as the sum of the two local anisotropy terms,

$$\mathcal{H}_{\text{ani}} = \mathcal{D}' \sum_{i\in\uparrow,\, j\in\downarrow} [(S_i^{\sigma})^2 + (S_j^{\sigma'})^2]. \tag{4.5}$$

In this expression, S^{σ} and $S^{\sigma'}$ denote local easy directions, ie. the component of spin perpendicular to the two alternating oxygen plaquettes. The anisotropy strength is the same for both spins and is quantified by $\mathcal{D}'$. Using this expression in a mean field calculation, the relative energy of any two spin directions can be calculated.

The lowest energy excitations arising from an AFM ordered ground state correspond to the in-phase fluctuations of the antiferromagnetically aligned spins. These are described by the acoustic mode of the dispersion. As these fluctuations are in-phase, the spins maintain a collinear alignment. Therefore, to investigate the effect of the local anisotropy, Figure 4.11 shows the mean field energy of all possi-

ble collinear spin orientations calculated from Eq. 4.5. The sphere plotted at the origin subtends all possible orientation angles. The colour map across its surface represents the relative mean field energy of collinear spins aligned parallel to that direction. The calculation finds the ground state spin orientation is parallel to b, as measured experimentally. Away from this ground state, however, the mean-field energy is elliptically contoured. The measurements made at $\boldsymbol{Q} = (0.5, 0, -0.5)$ and $\boldsymbol{Q} = (-0.5, 0, -1.5)$ are sensitive to spin fluctuations approximately along the major and minor axes of the ellipse respectively. Therefore, the two different onset energies of the low energy gap can be understood as arising from the local anisotropy created by the crystal field.

4.4 Analysis

4.4.1 Spin Wave Model

Linear spin wave theory provides a good description of the excitation spectra of many multiferroics and frustrated systems [113–115]. Although spin wave theory is not able to reproduce an electric polarisation, it can be used to quantify the frustrated exchange interactions which give rise to incommensurate magnetic order. The DM interaction is central to many proposed mechanisms for spontaneous electric polarisation in improper multiferroics [21]. Therefore, understanding how incommensurate magnetic order arises to satisfies the DM interaction (the so called 'inverse Dyaloshinskii-Moriya' interaction) reveals much about the nature of the multiferroicity and magnetoelectric coupling in a material.

Previous theoretical investigations into the spiral magnetic ordering mechanism of CuO [89, 91, 116–118] have estimated the nature and magnitude of the dominant exchange couplings based on the results of *ab initio* calculations. The exchange parameters estimated are calculated for a Heisenberg Hamiltonian. Therefore, to analyse the data presented in the previous section, a linear spin wave model (LSWM) was derived based on the Heisenberg Hamiltonian which includes the dominant ex-

change interactions proposed by the previous theoretical studies. This allows the validity of each theoretical model to be tested.

In addition to a Heisenberg term, a single-ion anisotropy term is included in the Hamiltonian to reproduce the observed magnetic easy axis parallel to b. This is a simplified method for introducing a low energy gap in the spectrum and is not able to reproduce the splitting of the modes at low energies or the anisotropic behaviour of the low energy gap. Additionally, as CuO is a $S = 1/2$ system, introducing magnetic anisotropy via a single ion term is not formally correct. However, as outlined in Appendix A, using a single-ion form allows the Hamiltonian to be expressed as an $N_s \times N_s$ matrix (where N_s is the number of spins contained within the magnetic unit cell). This is a simplification of the general $2N_s \times 2N_s$ matrix [119] and, in the case of CuO, allows the spin wave model to be analytically solved with a phenomenological gap. Introducing anisotropy in a different way (eg. via exchange anisotropy) makes the derivation of an analytic solution unfeasible. Therefore, the LSWM is derived from a Hamiltonian of the form

$$\mathcal{H} = \sum_{\langle i,j \rangle} J_{ij} \boldsymbol{S}_i \cdot \boldsymbol{S}_j - \mathcal{D} \sum_i (S^y)^2. \tag{4.6}$$

In this expression, J_{ij} are the magnetic exchange interactions (where $J > 0$ denotes an AFM interaction and $J < 0$ denotes an FM interaction); $\boldsymbol{S}_i$ is the spin on the i^{th} site; and $\mathcal{D}$ is the strength of single-ion anisotropy whereby $\mathcal{D} > 0$ energetically favours spins orientated parallel to the b axis. The summation is over all pairs of spins, with each pair counted once, denoted by $\langle i, j \rangle$.

A simplified magnetic unit cell is used to describe CuO and is depicted in Figure 4.2(a). This unit cell describes the magnetic structure of the Cu^{2+} ions, however, it neglects their oxygen environment (for comparison, the full magnetic unit cell is described in Ref. [109]). The simplification reduces the size of the magnetic unit cell, which now only contains four Cu^{2+} ions. Such a reduced cell is valid for modelling the spin dynamics as the Hamiltonian defined in Eq. 4.6 is invariant under

translation through the unit cell vectors. The magnetic exchange interactions included in the model are shown in Figure 4.2. The dominant exchange interaction along the chain direction is J_{ch}. The next most significant exchange parameters have previously been reported as the FM inter-chain J_{perp} and J_b interactions. Frustration is predicted to arise due to the nearest neighbour exchange interactions J_a and J_c, which act between the sublattices [93]. Additionally, the third-nearest-neighbour terms J_{2a} and J_{2c} are predicted to be significant [89, 91, 116–118] and have been included. Note, that an additional exchange parameter J' is labelled in Figure 4.2(b). This has not been considered in any previous theoretical treatment and, therefore, has not been included in the current model. However, it is found to be needed to describe the inter-chain dispersion and will be discussed in more detail in Section 4.4.3.

The full derivation of the LSWM is outlined in Appendix A. The model describes a pair of doubly-degenerate magnon modes. The dispersion of the modes is given by

$$\omega_{\pm} = \sqrt{A^2 + |B|^2 - C^2 - |D|^2 \pm \sqrt{4 \mid AB - CD^* \mid^2 - \mid B^*D^* - BD \mid^2}}. \quad (4.7)$$

The variables $A,\ B,\ C$, and D are used to express the Hamiltonian in matrix form. They are defined in terms of the exchange parameters as

$$\begin{aligned}
A &= 2S(J_{\mathrm{ch}} + J_{2a} + J_{2c} + J_{\mathrm{perp}}(\cos(\pi(H+L)) - 1) + J_b(\cos(2\pi K) - 1) + 2\mathcal{D}),\\
B &= S(J_a(e^{i\pi(H+K)} + e^{i\pi(H-K)}) + J_c(e^{-i\pi(L-K)} + e^{-i\pi(L+K)})),\\
C &= 2S(J_{ch}\cos(\pi(H-L)) + J_{2c}\cos(2\pi H) + J_{2a}\cos(2\pi L),\\
D &= S(J_a(e^{i\pi(H-K)} + e^{i\pi(H+K)}) + J_c(e^{-i\pi(L+K)} + e^{-i\pi(L-K)})). \quad (4.8)
\end{aligned}$$

The scattering function for the LSWM has also been derived and is included in Appendix A for completeness. Note, that while the variables B and D are equal in above expression, they are defined separately for clarity. This is required when

they are discussed again in Section 4.5.

4.4.2 Modelling the Spinon Continuum

As observed in the Section 4.3, 1D magnetic behaviour dominates the spectrum of CuO. The chain exchange parameter J_{ch} determines the bandwidth of the 1D spectrum, while also significantly affecting the bandwidth of the low energy 3D excitations. To decouple the effect of J_{ch} from the other weaker exchange terms, its value will be found by independently modelling the 1D spectrum of CuO. Therefore, J_{ch} can be fixed in the subsequent refinements of the LSWM against the inter-chain dispersion, which are presented later.

To this end, the Müller ansatz has been used to describe the measured 1D spectrum. The Müller ansatz is an inexact, phenomenological model of the scattering function for a $S = 1/2$ Heisenberg AFM chain [102]. It has previously been shown to be a good description of the magnetic excitation spectra of quasi-1D $S = 1/2$ AFM chains [120–123]. Additionally, it has proved a good description of the data measured in a less sensitive INS experiment of the 1D spectrum of CuO [101]. The Müller ansatz has the form

$$S_{\mathrm{MA}}(Q_{\mathrm{ch}}, E) = A\frac{\Theta(E - E_{\mathrm{l}}(Q_{\mathrm{ch}}))\,\Theta(E_{\mathrm{u}}(Q_{\mathrm{ch}}) - E)}{2\pi[E_{\mathrm{u}}(Q_{\mathrm{ch}})^2 - E^2]^{1/2}}, \tag{4.9}$$

where Θ is the Heaviside function, and $A = 1$ is a constant. The intensity described by the Müller ansatz is contained between the upper and lower boundaries of the spinon continuum defined in Eqs. 4.2 and 4.3. Therefore, J in Eqs. 4.2 and 4.3 defines the bandwidth of the continuum. The value of J in this definition is related to J_{ch} by a quantum renormalisation such that $J_{\mathrm{ch}} = (\pi/2)J$.

Due to the high energy of the 1D excitations, resolution effects are expected to play a significant role. Therefore, to fit the model, the scattering function in Eq. 4.9 was convolved with the full MAPS resolution function using the Tobyfit software [40]. The model was fitted to a series of wave vector cuts between 60 <

$E < 300\,\text{meV}$, taken from the $E_\text{i} = 300$ and $500\,\text{meV}$ measured spectra. The isotropic form factor of Cu^{2+} was included in the model [35]. Additionally, the prefactors of the scattering function – defined in Eq 2.26 – were included to simulate the intensity in absolute units. The sample size and mosaic were accommodated for in the resolution function. A wave vector dependent background of the form $B(Q) = aQ^2 + bQ + c$ was refined against each cut. The parameters b and c were independently fitted in each cut to accommodate the power law decay of intensity with increasing energy. Parameter a was simultaneous refined against all cuts. This has previously been shown to provide a good description of the background scattering measured by the MAPS spectrometer for a similar experiment [124]. The constant A in Eq. 4.9 was allowed to vary to account for any discrepancies in the measured intensity.

The best-fit parameters were $J = 91.4(5)\,\text{meV}$ and $A = 0.789(1)$. These values were found by repeated fitting of the model using different starting parameters in the range $50 < J < 140\,\text{meV}$ and $0.4 < A < 2$. A series of converged parameters were found. The statistical error found in each fit did not account for the spread of converged values. Therefore, the quoted values are the average and standard deviation of all converged solutions. It should be noted that although the errors on J and A are relatively small they do not account for discrepancies from the chosen model.

The fitted exchange parameter is larger than the previous estimate of $J = 80\,\text{meV}$ given by Aïn, *et al.* [86]. This was calculated from a spin-wave analysis of low energy dispersion data in the $\boldsymbol{Q} = (H, 0, -H)$ direction. A closer agreement is found to the $J = 93.6\,\text{meV}$ exchange reported by Boothroyd, *et al.* [101] and found using the Müller ansatz to analyse basic INS measurements of the AFM chain spectrum. Estimates were also put forward from analysis of the bulk susceptibility. The fitted exchange parameter is in good agreement with $J = 90.5\,\text{meV}$ reported by O'Keefe and Stone [98], however, it differs from $J = 77 \pm 3\,\text{meV}$ estimated in a

later study by Shimizu, *et al.* [100].

The fitted amplitude A has a value of < 1 suggesting that not all the intensity is accounted for. However, a discrepancy of only $\sim 20\%$ is relatively insubstantial. Studies of the related $S = 1/2$ AFM chain compound Sr_2CuO_3 are only able to account for 80% of the intensity expected after covalency effects and higher-order multi-spinon terms are included [124]. Therefore, the refined value of A in this study supports the validity of the Müller ansatz as a description of the 1D behaviour in CuO. Expanding on this model to include the higher-order multi-spinon continuum scattering (the so-called '2+4 spinon continuum') may slightly improve the fitted values of A and J [125].

The fit to the resolution convolved Müller ansatz is shown alongside the cuts through the $E_\mathrm{i} = 300\,\mathrm{meV}$ data in Figure 4.7. Overall, the data is very well reproduced by the fit, although there are some discrepancies. In the lowest energy cut with $\langle E \rangle = 70\,\mathrm{meV}$ [Figure 4.7(a)], the model does not capture the full intensity of any of the peaks. This is most likely due the validity of the Müller ansatz breaking down in the 3D→1D crossover region [123] expected to occur at this energy. At higher energies the Müller ansatz provides an excellent reproduction of the data. However, there is a slight asymmetry of the simulated intensity about the $Q_\mathrm{ch} = -0.5$, and 0.5 positions in some lower energy cuts [Figures 4.7(b) and 4.7(c)]. This asymmetry is in the opposite direction to the Q dependent attenuation of intensity expected from the form factor as observed in the measured data. A similar asymmetry is also seen in comparable simulations using Tobyfit to convolve the MAPS resolution function with the Müller ansatz [124].

The precise origin of this asymmetry is not known. A possible cause has been proposed because two features are seemingly required to produce the asymmetry. To describe the first required feature, the details of the integration over the inter-chain wave vectors directions must be considered. The wave vector coverage of the neutron detectors show a common feature for all cuts with a simulated asymmetry.

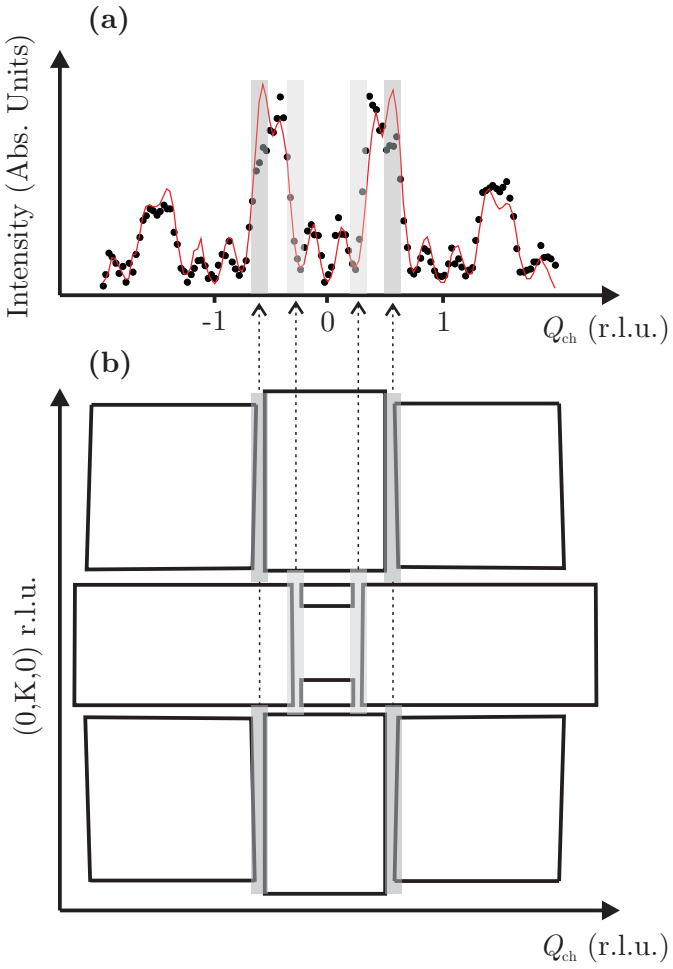

Figure 4.12: Schematic diagram of the MAPS detector bank coverage and an integrated cut with simulated intensity. (a) The $\langle E \rangle = 90\,\text{meV}$ integrated cut through the 1D spectrum measured with $E_\text{i} = 300\,\text{meV}$. The grey shaded areas show regions of the cut overlapping with vertical gaps between the MAPS spectrometer detector banks. (b) The arrangement of detector banks across low angles on the MAPS spectrometer. The vertical gaps are highlighted in grey. Cuts are found by integrating across the full range of K.

Specifically, the asymmetry only occurs when the vertical gaps between the detector banks on the MAPS spectrometer overlap with the $Q_\text{ch} = |0.5 \pm \delta q|$ peaks (where δq is the wave vector shift of the dispersing spinon lower boundary away from the 1D BZ centre). This detector geometry is illustrated in Figure 4.12 for the case of the $\langle E \rangle = 90\,\text{meV}$ cut, from the $E_\text{i} = 300\,\text{meV}$ data. Note, an asymmetry is also observed in cuts at different energies, when measured using the higher $E_\text{i} =$

500 meV experimental configuration. These different energies also coincide with the $Q_{\mathrm{ch}} = |0.5 \pm \delta q|$ peaks falling across detector gaps. The second required feature is the magnetic form factor. When it is omitted from the simulations there is no asymmetry.

In the cut in Figure 4.12(a), which is integrated across the full range of K values, the form factor will only weakly attenuate the simulated intensity in the low K detector banks. The peak at $Q_{\mathrm{ch}} = |0.5 + \delta q|$ only occurs in the low K detector bank. In contrast to this, the peak at $Q_{\mathrm{ch}} = |0.5 - \delta q|$ lies between both detector bank gaps and so, when integrated, its intensity will be more suppressed by the form factor compared to the $Q_{\mathrm{ch}} = |0.5 + \delta q|$ peak. This is because of its higher average value of K. This effect is seen in the simulation but not in the data. Therefore, its absence in the data suggests that there is some other variation of the mode intensity with K not described by the Müller ansatz. Such a variation is expected because of the significant inter-chain coupling. Unfortunately, there has been no conclusive observation of this proposed inter-chain intensity modulation as it is a small effect and only present when detector gaps obscure the relevant areas of reciprocal space. Therefore, although such asymmetry indicates deviation away from ideal 1D behaviour, the effect is very small, and overall it can be concluded that the Müller ansatz provides a good description of the 1D spectrum in CuO.

4.4.3 Comparison of the Spin Wave Model to INS Data

To compare the LSWM to the the measured inter-chain spectrum (Figure 4.8), first the dispersion relation had to be extracted from the intensity maps. This was done by fitting Gaussian line shapes to a series of wave vector and energy line cuts through the spectrum. Peak positions measured at equivalent wave vector positions were averaged to improve accuracy. A single-ion anisotropy term, such as that used in Eq. 4.6, cannot reproduce the anisotropic behaviour of the low energy acoustic gap – see Section 4.3.4. Therefore, the mid-point energy of the M_{ac} onset was

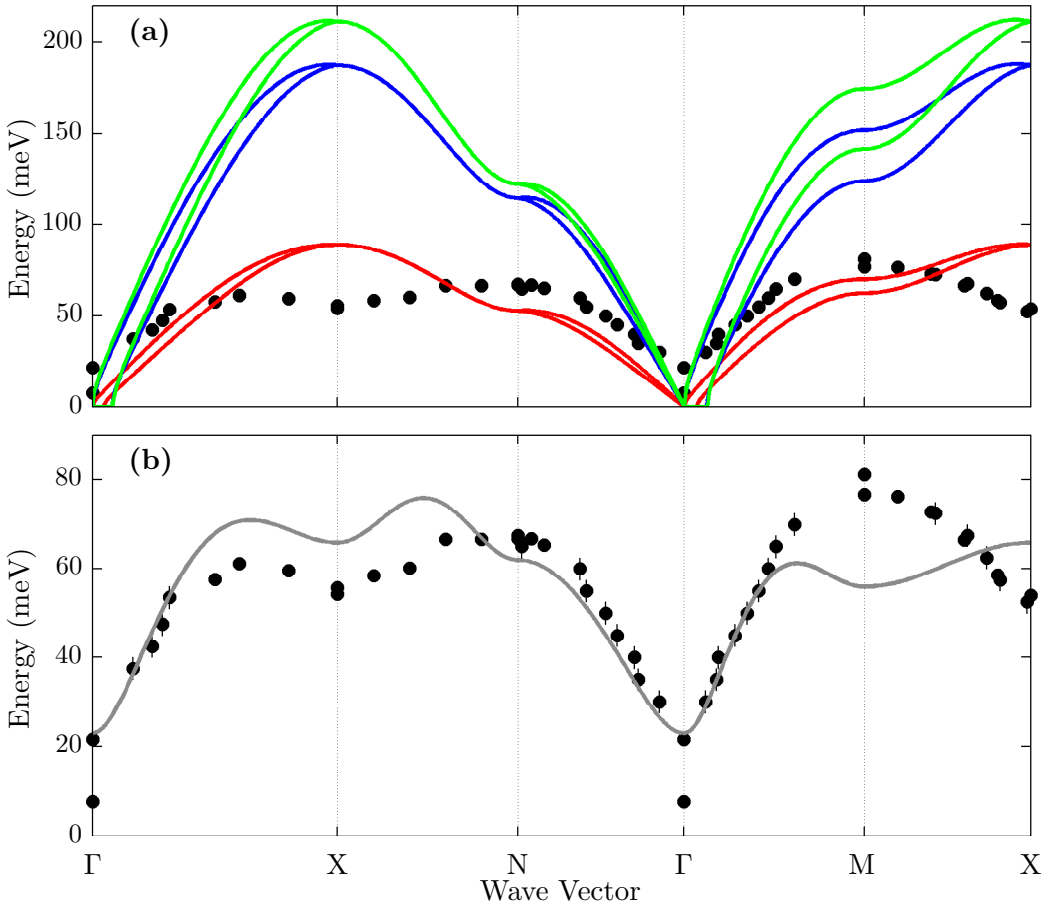

Figure 4.13: The extracted inter-chain dispersion of CuO and the results of the linear spin wave model analysis. The extracted dispersion is shown by the black circles in both panels. (a) The dispersion of the initial LSWM arising from the predicted exchange parameters of Giovannetti, *et al.* [89] (blue and green lines, calculated using $U_{\text{eff}} = 5.5$ and $\alpha = 0.15$ parameters in Ref. [89] respectively) and Jin, *et al.* [91] (red lines). (b) The lowest χ^2 fit of the initial LSWM to the extracted dispersion (grey lines). The fit fails to reproduce several features of the spectrum including the low energy mode splitting and the nature of the dispersion along the zone boundary.

found for the pair of low and high energy gaps (Figure 4.10). These values were then averaged to give a single low and high energy gap for the extracted dispersion. The resulting dispersion is shown in Figure 4.13.

Figure 4.13(a) shows a comparison of the measured dispersion to the LSWM calculated using the exchange parameters proposed in two previous theoretical studies of the origins of the AF2 phase [89, 91]. The parameters found in each of these stud-

ies can be directly mapped onto the LSWM proposed in Section 4.4.1. The values have been listed in the current notation in Table 4.2. None of the theoretical studies include anisotropy and so have been plotted as gapless. The dispersions calculated from the parameters of both theoretical studies are qualitatively similar, though the energy scales differ. The behaviour is at odds with the measured dispersion. Most prominently, the theoretical dispersions do not reproduce the softening of the magnon mode at the X position or the splitting of the modes at Γ. Additionally, the dispersions do not reproduce the expected energy minimum at the Γ position. Instead, they intersect the elastic line at two wave vector points: one at Γ, the other at an incommensurate position on the Γ →M path. If plotted to lower energies, this feature would resemble a negative energy dispersion of the modes around Γ and is unphysical. It arises, as the parameters do not lead to the accepted ground state magnetic order shown in Figure 4.2(a) and (b).

In an attempt to resolve the differences in Figure 4.13(a), I fitted the LSWM to the measured dispersion. An array of starting parameters were used to systematically test a wide range of exchange interactions. Parameters were varied such that $-30 < J_{\mathrm{perp}}, J_b < 0\,\mathrm{meV}$ and $-20 < J_a, J_c, J_{2a}, J_{2c} < 20\,\mathrm{meV}$. These limits were chosen based on the past experimental and theoretical estimates [86, 89, 91, 116]. Between these limits, values of J_{ij} were varied in 10 meV steps and all possible permutations of these exchange interactions were found. The dominant J_{ch} exchange was fixed to the renormalised value of 143.6 meV, found in the previous section. This led to an array of 16384 starting parameters sets. After the fitting, the quality of the converged solutions was quantified using the χ^2 goodness-of-fit parameter.

Performing the exhaustive fitting revealed no solutions that adequately described the experimentally measured dispersion. The best converged solution was characterised by $\chi^2 = 88$ and is shown in Figure 4.13(b). The fitted exchange parameters are listed in Table 4.2 as 'LSWM Fit 1'. Alongside this lowest-χ^2 solution, there exist many converged solutions with a near equal χ^2. Each gives raise to

a very similar dispersion. The fitted dispersion fails to quantitatively reproduce any of the high energy features in the inter-chain dispersion. Additionally, the fit shows qualitatively different dispersive behaviour along the zone boundary between X→N and M→X. Furthermore, this fit correspond to exchange parameters where $J_{\mathrm{perp}}/J_{\mathrm{ch}} \approx 2$ and $J_{2c}/J_{\mathrm{ch}} \approx 1.5$. These parameters are not consistent with the quasi-1D behaviour of CuO. Therefore, a model based on the theoretically proposed dominant exchange parameters is not consistent with the measured excitation spectrum of CuO.

4.5 Discussion

As shown in Figures 4.13, the assumed LSWM is inconsistent with the measured spectrum in three areas:

(i) It does not reproduce the softening of the magnon mode at the X position.

(ii) The fitted LSWM modes are practically degenerate at low energies where a clear splitting is observed at the zone centre Γ.

(iii) The observed anisotropy in the low energy gap cannot be not reproduced by the model.

The fact that the LSWM cannot reproduce the anisotropic behaviour of the low energy gap is expected from the simplistic method of introducing spin anisotropy using a single-ion term in Eq. 4.6. However, the failure to describe the mode splitting and the dispersive behaviour at X indicates that the particular Heisenberg Hamiltonian used does not capture all of the relevant magnetic interactions within CuO.

The softening of the magnon at X is of particular interest as it is reminiscent of the dispersive zone boundary behaviour observed in various layered cuprates which exhibit AFM order on a square lattice. Two examples of opposite dispersive behaviour are reported by Coldea, *et al.* [126] in La_2CuO_4; and Rønnow, *et al.*

Source	J_{ch}	J_{perp}	J_a	J_b	J_c	J_{2a}	J_{2c}	J'	$\mathcal{D}$
Filippetti, *et al.* [116]	38.4	-20.4	-11.6	–	-8	14	14	–	–
Rocquefelte, *et al.* [117] $\alpha = 0.15$	128.8	-2.6	18.2	–	-4.2	–	30.1	–	–
Giovannetti, *et al.* [89] $U_{\text{eff}} = 5.5$	107.8	-15.8	8	-21.5	15.8	6.9	16.2	–	–
Giovannetti, *et al.* [89] $\alpha = 0.15$	120.4	-24.3	4.2	-23.0	13.2	5	14.3	–	–
Jin, *et al.* [91]	51	-8.6	-4.9	-9.9	-7	12	-2.1	–	–
LSWM Fit 1	143.6	73.9(4)	0.0(3)	-3.5(5)	0(0)	-21.7(2)	106.1(1)	–	1.16(3)
LSWM Fit 2	143.6	-3.65(3)	–	-1.140(5)	–	–	–	-2.93(2)	0.98(5)

Table 4.2: Summary of the magnetic exchange parameters used in the comparison of the linear spin wave model with the measured dispersion. The source of each set of exchange parameters is quoted alongside the values of the interactions – as defined in Figures 4.2(a) and 4.2(b). In cases where a given exchange parameter has not been included in the model it is marked with a dash. The errors on exchange parameters fitted to the LSWM are the standard deviations arising from the fitting procedure.

[127] in $Cu(DCOO)_2{\cdot}4D_2O$ (CFTD). In La_2CuO_4, next-nearest neighbour and a higher order cyclical exchange term produce a mode softening at the mid-point on the zone boundary. In CFTD, significant wave vector dependant quantum renormalisation effects have been found to soften the magnon modes at the vertex of the zone boundary. In both cases, the same dispersive behaviour was also successfully simulated by including next-nearest neighbour exchange parameters. These examples are not directly comparable to the dispersion of CuO across the $(1/2 + H, K, -1/2 + H)$ plane where spins are ferromagnetically ordered and the planes are strongly coupled along $(H, 0, -H)$. However, including a next-nearest neighbour exchange pathway within this plane allows the dispersion around X to be reproduced. The next-nearest neighbour exchange parameter is shown in Figure 4.2(b) and labelled J'. When it is included in the LSWM, an additional term, with the form $2SJ'(\cos(\pi(2K+H+L))+\cos(\pi(2K-H-L))-2)$, must be included in the variable A, initially defined in Eq. 4.8. Fitting this expanded LSWM to the extracted dispersion reveals that the data can be well reproduced with only the J_{ch}, J_{perp}, J_b, and J' parameters. The best fit using this new LSWM is depicted in Figure 4.14(a) and the fitted parameters are recorded in Table 4.2 labelled 'LSWM Fit 2'.

The relative magnitudes of the fitted exchange parameters in this new model show $J' \approx J_{\mathrm{perp}} > J_b$. This is surprising, as no previous theoretical calculations have identified J' as a significant interaction. Additionally, while the bond lengths of the J_b and J' exchange pathways are equal, the bond angles are substantially different. The bond angle for J' is 160° compared to 91° for the J_b exchange pathway. Interpreting these angles using the GKA rules [2, 3] (which are consistent with the behaviour of the J_{ch} and J_{perp} interactions) suggests that J_b would be a ferromagnetic interaction, while J' would strongly favour being antiferromagnetic. This not being the case, the different strengths of J_b and J' suggest that while the inclusion of J' provides an excellent phenomenological model for the measured

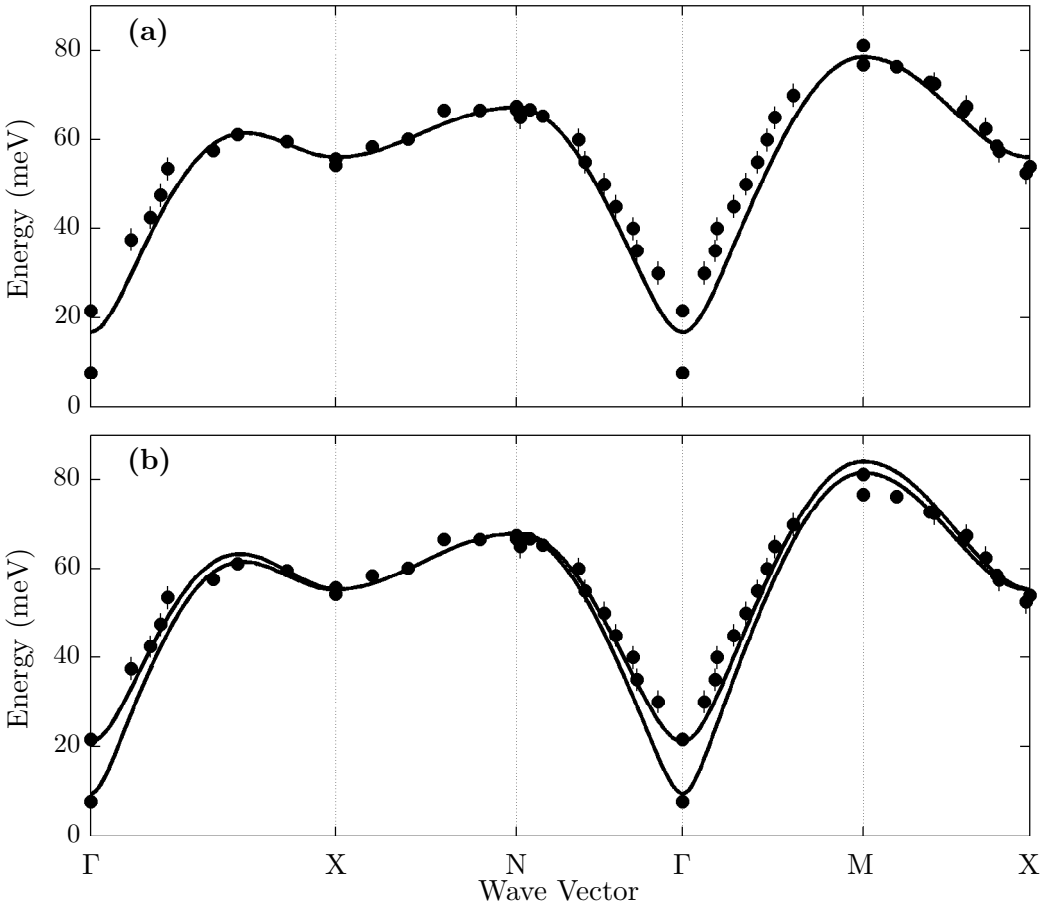

Figure 4.14: The extracted inter-chain dispersion of CuO and the expanded linear spin wave model. The extracted dispersion is shown by the black circles in both panels. (a) The line shows the best fit to the expanded spin wave model including the exchange parameter J'. This model captures the dispersive behaviour along the zone boundary. (b) The lines show the doubly degenerate acoustic and optic modes which are split when J_c is replaced with two inequivalent exchange parameters $J_{c'}$ and $J_{c''}$. This partially relieves the frustration within the system (see main text for details). A splitting of $\sim 10\,\text{meV}$ at Γ is demonstrated using exchange values $J_{c''} \approx 0.5\,\text{meV}$, $J_{c'} = J_a = 0$ and $\mathcal{D} \approx 1.5\,\text{meV}$.

dispersion, it does not prove its existence as a physically meaningful superexchange interaction. Further work is required to understand if the same softening of the mode at X can be achieved through quantum effects as seen in past studies of square-lattice quantum antiferromagnets [127].

The addition of J' has no affect on the mode splitting, and further fitting, including J_a, J_c, J_{2a}, and J_{2c}, is still unable to reproduce the two gaps measured at

the zone centre. The intensity ratio of the low energy excitation due to roughly perpendicular magnetic fluctuations (reported in Figure 4.10) is approximately equal for both the low and high energy gaps. $I_{(H,0,-H)}/I_{(-H/3,0,-H)} = 2$ in both cases, with simulations of the resolution ellipsoid indicating there is no significant difference in the broadening at the two wave vectors. Two gaps can arise from a freezing out of magnetic fluctuations in particular directions because of two contributing anisotropies (as is the case in some layered AFM insulators [75]). This is characterised by the intensities associated with different magnetic fluctuations changing at each gap. The lack of such behaviour, indicates that the mode splitting in CuO does not arise from magnetic anisotropy.

The mode splitting must therefore be due to the splitting of the doubly degenerate acoustic and optic modes. These modes relate to in-phase and anti-phase oscillations of spins on the two sublattices, respectively. As the inter-sublattice exchange parameters J_a and J_c are frustrated in the current LSWM, both acoustic and optic modes are degenerate. Therefore, to simulate the low energy mode splitting the frustration must be partially relieved. This can be achieved in the simplified magnetic unit cell by replacing J_c with two distinct exchange parameters. $J_{c'}$ acts in the $\pm 0.5\boldsymbol{b} + 0.5\boldsymbol{c}$ direction connecting two parallel spins, while $J_{c''}$ acts in the $\pm 0.5\boldsymbol{b} + 0.5\boldsymbol{c}$ direction connecting two antiparallel spins. This has the effect of changing $J_c \to J_{c'}$ in the variable D and $J_c \to J_{c''}$ in the variable B, where both variables are defined in Eq. 4.8. Additionally, the term $2S(J_{c'} - J_{c''})$ must be include in variable A in Eq. 4.8.

Figure 4.14(b) illustrates the effect of lifting the degeneracy by introducing $J_{c'}$ and $J_{c''}$. In this example $J_a = J_{c'} = 0$, $J_{c''} \approx 0.5\,\text{meV}$ and $\mathcal{D} \approx 1.5\,\text{meV}$. This small value of $|J_{c'} - J_{c''}|$ is able to produce the roughly 10 meV gap observed at Γ. A much smaller splitting is produced away from the zone centre at higher energies ($\sim 2\,\text{meV}$). Such a splitting is unresolvable in our current experimental setup but is consistent with the broad modes observed in Figure 4.8. Using this model, the

entire inter-chain dispersion can be reproduced.

This distinction between nearest neighbour exchange pathways acting parallel to the c axis breaks the inversion symmetry centred on each Cu site in CuO. This is consistent with previous optical spectroscopy studies of CuO, which suggest that the inversion symmetry at the Cu sites is broken at low temperatures [128, 129]. However, the precise mechanism causing this symmetry breaking is not known. In the absence of any microscopic model, the LSWM including $J_{c'}$ and $J_{c''}$ can only act as a proof of principal, demonstrating that any eventual model must relieve the magnetic frustration. It may be possible for non-linear interactions to create this particular splitting effect in the place of $J_{c'}$ and $J_{c''}$. The DM interaction and biquadratic (or cyclical) exchange have both been theoretically considered to explain the formation of the AF2 phase [89, 130, 131]. A recent experimental study of an electromagnon excitation measured in the multiferroic phase also suggested that biquadratic exchange interactions of the form $(\boldsymbol{S}_i \cdot \boldsymbol{S}_j)^2$ are necessary to understand the magnetic behaviour of CuO [132]. Further work is needed to explore whether the inclusion of such terms in the Hamiltonian can accurately reproduce the mode splitting at low energies.

Chapter 5

The Magnetic Excitation Spectrum of $LuFe_2O_4$

Contents

5.1 Introduction

$LuFe_2O_4$ is a controversial and complex material exhibiting a variety of orders and behaviours. Its structure can be considered as stacked Fe_2O_4 bilayers separated by LuO_2 monolayers (with these constituent parts sharing two common oxygen atoms). The room temperature crystal structure is described by the rhombohedral space group $R\bar{3}m$ in the hexagonal setting [133]. The lattice parameters are $a = b = 3.444\,\text{Å}$, $c = 25.259\,\text{Å}$ with inter-axis angles $\alpha = \beta = 90°$, $\gamma = 120°$ [134]. There are three Fe_2O_4 bilayers in the unit cell, and the Fe atoms within a monolayer form a perfect triangular net. This structure is shown in Figure 5.1. At low temperatures, there is a small monoclinic distortion of the structure below $T_L = 175\,\text{K}$ [135, 136]. Complex behaviour in $LuFe_2O_4$ arises because in the ideal rhombohedral structure all Fe sites are equivalent and the average valence state is $Fe^{2.5+}$; however, there is near-perfect valence segregation leading to an equal number of Fe^{2+} and Fe^{3+} ions in the unit cell. The triangular arrangement of Fe ions creates frustration which influences the charge order (CO) and magnetic order, the exact natures of which are still under debate.

5.1.1 Proposed Charge Order

The charge order is known to be quasi-two-dimensional (2D) below 500 K, and develops into three dimensional (3D) order below $\sim 320\,\text{K}$ [137]. Some short range 3D charge correlations have even been reported above 320 K in neutron diffraction studies [138]. In the 2D charge ordered phase, the in-plane charge density wave is characterised by the 2D wave vector $\boldsymbol{Q} = (1/3, 1/3)$ [137]. Figure 5.2 shows the elastic scattering pattern which exhibits peaks at this reduced wave vector both at 260 K and cryogenic temperatures. Such an ordering arises from the Coulomb repulsion of the Fe^{2+} and Fe^{3+} ions which distribute themselves across the two triangular monolayers making up a bilayer structure. The charge frustration can be overcome through the formation of an Fe^{2+}-rich monolayer (with 2:1 ratio of

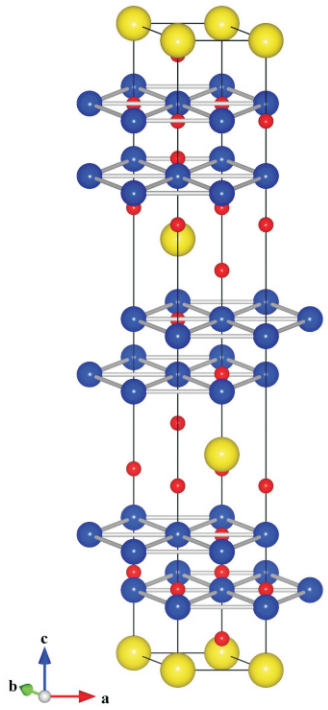

Figure 5.1: $R\bar{3}m$ crystal structure of $LuFe_2O_4$. Lu, Fe, and O atoms are depicted as yellow, blue and red spheres respectively. The grey bonds indicate the triangular coordination of Fe atoms in the monolayers. These are stacked to form bilayers, which are in turn separated by LuO_2 layers to form the unit cell.

Fe^{2+}:Fe^{3+} ions, designated as an A-layer) and an Fe^{3+}-rich monolayer (1:2 ionic ratio, B-layer) [137, 139]. The A-layer is a honeycomb network of Fe^{2+} ions, with an Fe^{3+} ion located at the centre of each hexagon. The B-layer has the opposite arrangement: Fe^{2+} ions are found at the centre of Fe^{3+} hexagons. Figure 5.3(a) shows a bilayer comprised of a stacked A- and B-layer illustrating the two monolayer orders. The charge order of each monolayer and the resulting bilayer is described by an enlarged $\sqrt{3} \times \sqrt{3}$ supercell (SC) – shown by the grey area in 5.3(a) for the AB-bilayer structure.

Exactly how these monolayers stack to form the quasi-2D bilayers and 3D structure is still under debate. Currently, contrasting models of anti-polar order with AB-BA-AB stacking [140] and charged bilayers with AA-BB-AA stacking [141] are the best descriptions of the experimental findings. Anti-polar ordering is consistent

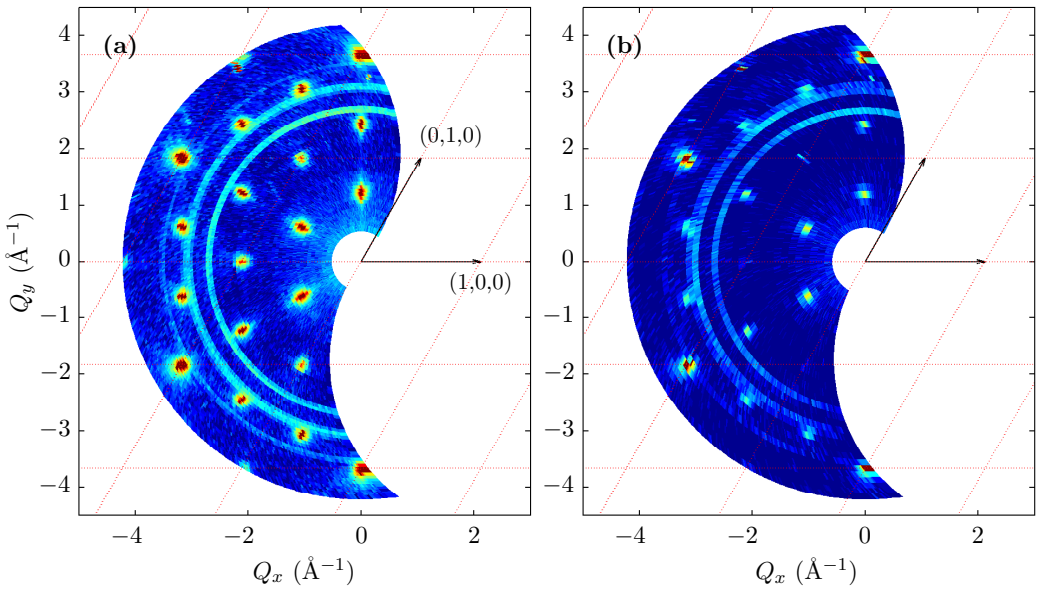

Figure 5.2: The in-plane neutron diffraction pattern of $LuFe_2O_4$. This figure is reproduced from Ref. [144]. The patterns were recorded at (a) 10 K and (b) 260 K. The hexagonal symmetry of the peaks, characterised by $\boldsymbol{Q} = (1/3, 1/3)$, is clear at both temperature. The peaks become much more intense at low temperatures, when $LuFe_2O_4$ has magnetically ordered. The patterns were measured from Sample 1 (as introduced in Section 5.2.1) using the FlatCone multidetector setup on the IN20 spectrometer at the ILL, France.

with the bilayer order shown in Figure 5.3(a), while the charged bilayers are comprised of the same ordered monolayers but stacked to form AA and BB bilayers. The proposed 3D charge ordered structures have commonly been described in enlarged C2/m monoclinic unit cells [138, 140–143]. This study aims to investigate the magnetic excitations within the bilayer, so I shall continue to refer to the structure by the hexagonal coordinates.

5.1.2 Proposed Magnetic Order

$LuFe_2O_4$ has been shown to have robust 2D ferrimagnetic (fM) order below T_N = 240 K [135, 145–147]. Fe^{2+} ($3d^6$) and Fe^{3+} ($3d^5$) ions both have a magnetic moment and adopt spin states S=2 and S=5/2 respectively in the weak crystal field environment expected in $LuFe_2O_4$. Additionally, the Fe^{2+} ion has a significant orbital angular momentum contributing to its total ordered moment [146, 147]. This arises

from the significant spin-orbit coupling present in the system due to the crystal field splitting of the Fe^{2+} ions in the trigonal bipyramidal coordination. Conversely, the orbital angular momentum is fully quenched in the Fe^{3+} ions. The significant spin-orbit coupling leads to a highly Ising-like spin structure, with the moments aligned parallel to the c axis [145]. For each monolayer, the fM spin structure [shown in Figure 5.3(c)] is highly frustrated and is characterised by the same $\boldsymbol{Q} = (1/3, 1/3)$ wave vector as the in-plane charge order [145]. It can been seen that the resulting fM moment arising in a monolayer is due to the parallel arrangement of two spins, while a third is oriented anti-parallel. This monolayer spin orientation, can be labelled as $\uparrow\uparrow\downarrow$, where the three arrows denote the orientation of any three nearest neighbour spins forming a triangle within the hexagonal structure of the monolayer.

The first experimentally consistent model for the site specific bilayer magnetic order found a ferromagnetic (FM) arrangement of all Fe^{2+} ions and an antiferromagnetic (AFM) arrangement of Fe^{3+} ions [146, 147]. This leads to a ferromagnetic stacking of the net fM moments associated with each monolayer (ie. the individual Fe-moments within the two monolayers forming the bilayer align $\uparrow\uparrow\downarrow$ and $\uparrow\uparrow\downarrow$). This is the AB-bilayer magnetic structure depicted in Figures 5.3(c) and 5.4(b). A phase mixing of these bilayers with bilayers formed from the AFM stacking of the net monolayer moments (ie. $\uparrow\uparrow\downarrow$ and $\downarrow\downarrow\uparrow$) has been reported [148]. To describe the magnetic order associated with charged-bilayer CO, two further site specific bilayer magnetic structures have been proposed (corresponding to AA- and BB-bilayers) [141, 149] – see Figure 5.4(a). There is a weak magnetic coupling between bilayers and the precise nature of the 3D magnetic ordering of the bilayers is complicated by coexisting stacking domains [148, 150] and disorder (or more specifically, spin glass behaviour, [151, 152]). An additional complicating factor is that the magnetic behaviour of $LuFe_2O_4$ has been found to be dependent on the oxygen content, with a lack of 3D magnetic order reported in off-stoichiometric samples [153].

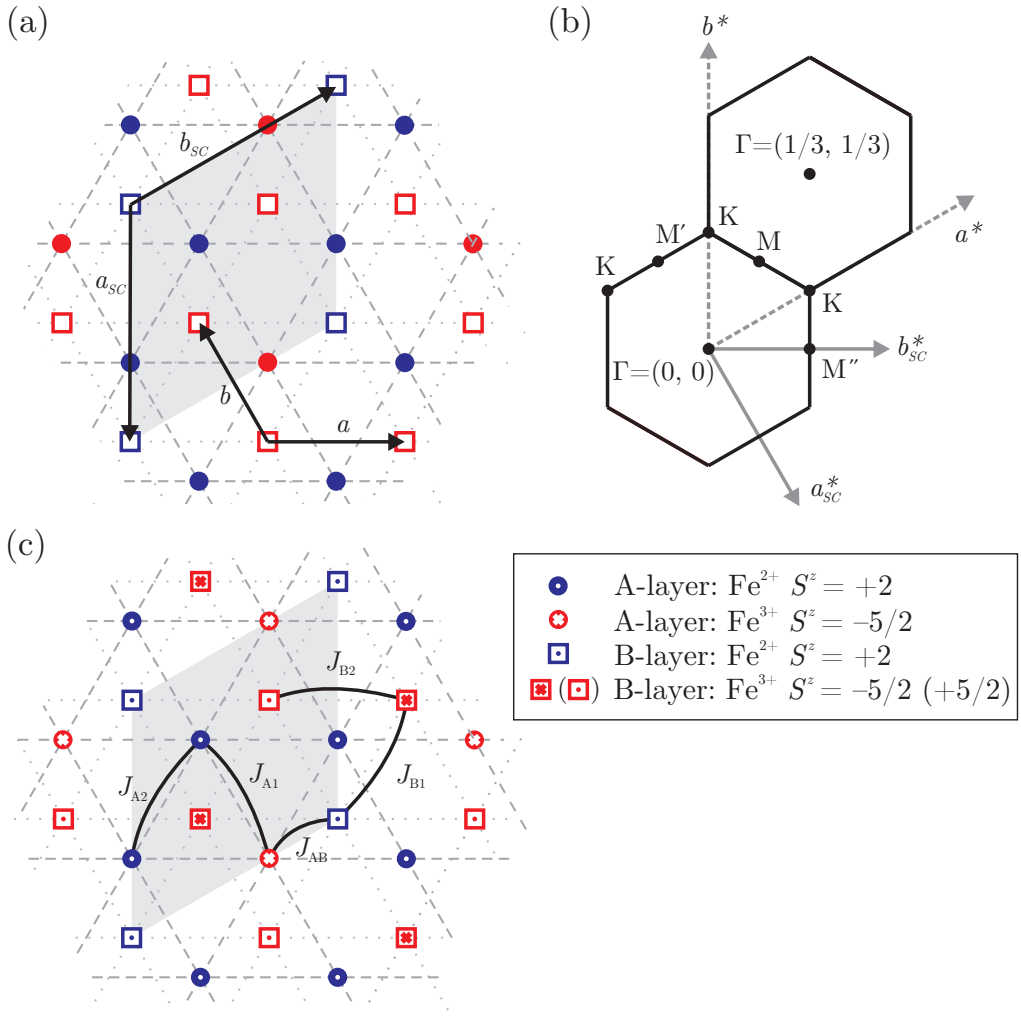

Figure 5.3: In-plane real space structure and reciprocal lattice of $LuFe_2O_4$. (a) The reduced real space structure of a single charge-ordered AB-bilayer. The lattice vectors $\boldsymbol{a}$ and $\boldsymbol{b}$ and SC lattice vectors $\boldsymbol{a}_{\mathrm{SC}}$ and $\boldsymbol{b}_{\mathrm{SC}}$ are shown as black arrows. The crystallographic and SC c axes are perpendicular to the pairs, in both cases coming out of the page. The ions in the Fe^{2+}-rich A (filled circles) and Fe^{3+}-rich B (open squares) monolayers are projected on top of each other. Oxygen atoms have been omitted for clarity. Red and blue symbols denote the Fe^{3+} and Fe^{2+} ions respectively. The $\sqrt{3} \times \sqrt{3}$ SC is depicted by the grey rhombus. (b) The reciprocal lattice of the charge and magnetically ordered supercell. The direction of the reciprocal lattice vectors for the crystallographic unit cell ($\boldsymbol{a}^*$ and $\boldsymbol{b}^*$) and supercell ($\boldsymbol{a}^*_{\mathrm{SC}}$ and $\boldsymbol{b}^*_{\mathrm{SC}}$) are shown as dashed and solid grey arrows respectively. The high symmetry positions discussed in the main text are labelled. (c) The spin structure of a ferromagnetically-coordinated AB-bilayer (see main text). The spins are parallel to the c-axis, pointing into (cross) and out-of (dot) the page. The five exchange pathways considered in the minimal model are labelled.

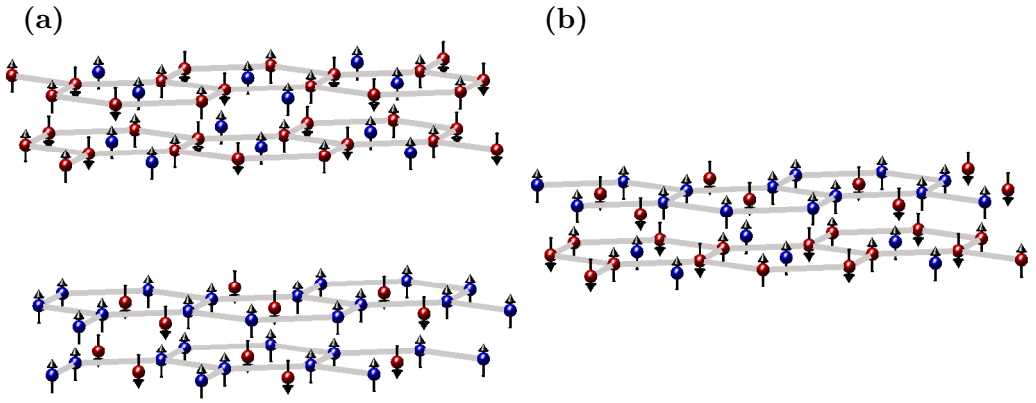

Figure 5.4: The proposed charge and magnetically ordered $LuFe_2O_4$ bilayer structures. (a) The AA-BB bilayers proposed in Ref. [148]. (b) The AB bilayer proposed in Ref. [146]. Blue (red) spheres denote the Fe^{2+} (Fe^{3+}) ions. The orientation of the magnetic moment of each ion is shown by the black arrows. Grey lines show the Fe^{2+}–Fe^{2+} bonds on the A-layer and the Fe^{3+}–Fe^{3+} bonds on the B-layer. This highlights the honeycomb structure formed by the majority ions on each layer. The minority ion is found in the middle of each hexagon.

5.1.3 The Multiferroicity of $LuFe_2O_4$

$LuFe_2O_4$ initially rose to prominence due to the findings of Ikeda, *et al.* [139] showing that it was a high-temperature multiferroic. Subsequently, Subramanian, *et al.* [154] reported a giant dielectric constant that could be manipulated through the application of relatively small magnetic fields. This indicated that a strong magnetoelectric coupling is present within $LuFe_2O_4$. However, the novel 'electronic ferroelectric' state, purported to arise from the charge ordered arrangement of Fe^{2+} and Fe^{3+} ions, has since been demonstrated as an unlikely source of polar order [141, 155]. Additionally, the dielectric response has been shown to arise principally from contact effects and grain boundaries. When these effects are taken into account, $LuFe_2O_4$ is found to have a small intrinsic dielectric constant [155–157]. It would appear that $LuFe_2O_4$ is not a multiferroic [149].

5.1.4 Magnetic Exchange Interactions

To date, there have only been theoretical estimates of the nature of the dominant exchange interactions within and between the bilayers. Iida, *et al.* [145] highlighted that nearest-neighbour AFM exchange interactions in addition to a small next-nearest neighbour FM coupling would lead to frustration and facilitate fM order (as proposed for Ising spins on a triangular lattice [158]). Nagano, *et al.* [159] attempted to predict the precise spin structure from a Hamiltonian describing charge interactions and three magnetic exchange interactions. They used the known exchange parameters from $LaFeO_3$ (which was previously thought to be magnetically similar to $LuFe_2O_4$) but the derived ordering does not agree with experiment [146]. Ko, *et al.* [146] used the Goodenough-Kanamori-Anderson (GKA) rules [2, 3] to explain the strengths of the superexchange interactions between Fe^{3+} ions within a monolayer and across the bilayer. The most comprehensive theoretical study was undertaken by Xiang, *et al.* [160], using density function theory (DFT) and Monte Carlo (MC) simulations. They calculated the exchange parameters which led to the fM ground state reported in Ref. [146] assuming AB-bilayer CO. This study used an Ising spin Hamiltonian that included 15 superexchange parameters (corresponding to intra- and inter-monolayer nearest neighbour interactions) and 19 super-superexchange parameters (next-nearest neighbour interactions).

In this Chapter, I will report measurements of the full in-plane magnetic excitation spectrum of $LuFe_2O_4$. The spectrum has an observed bandwidth of 60 meV and is consistent with six magnetic modes. This is in contrast to the twelve modes expected from the distinct AA- and BB-bilayers in a charge segregated model for the CO in $LuFe_2O_4$. For this reason, I shall present a minimal spin wave theory based on the 2D magnetic AB-bilayer structure proposed by Ko, *et al.* [146]. This simple ground state order is consistent with the six modes evidenced and provides an excellent description of the dispersion extracted from the spectrum. The strengths and weaknesses of this model shall be discussed and its implications for the debate

on the charge and spin order of $LuFe_2O_4$ shall be explored.

5.2 Sample Preparation and Characterisation

5.2.1 Crystal Growth

Single crystal samples were grown in Oxford by Dr D. Prabhakaran and in Warwick by R. A. M^{c}Kinnon under the supervision of Prof. G. Balakrishnan. Two crystals (labelled Samples 1 and 2) were grown following the same basic procedure. High purity ($> 99.999\,\%$) Lu_2O_3 and Fe_2O_3 powders were mixed in the stoichiometric ratio of $LuFe_2O_4$. This mixture was sintered at 1200°C for 12 hours under a flowing CO/CO_2 atmosphere (in a 25/75% ratio for Sample 1, 17/83% for Sample 2). This was in turn re-ground and heat treated a second time at 1200°C for 24 hours in an Ar atmosphere. The powder was subsequently pressed into a rod (8 mm diameter, 100 mm length) and sintered for 12 hours at 1200°C for Sample 1 and 1250°C for Sample 2 in a CO/CO_2 atmosphere (Sample 1: 30/70%, Sample 2: 17/83%). The single crystal growth was performed using a optical floating-zone furnace (Crystal Systems Inc.) in a flowing CO/CO_2 atmosphere (Sample 1: 5/95%, Sample 2: 17/83%). Feed and seed rods counter-rotated in this setup at 30 rpm, with the growth proceeding at 1–2 mm/hour. The first growth was performed using a polycrystalline seed rod, but in subsequent growths a cleaved single crystal was used. The growths of $LuFe_2O_4$ typically yielded multigrain samples. The two high-quality single crystals were extracted from such growths. Sample 1 was cleaved and had a mass of 0.349 g. Sample 2 was larger, with mass 2.465 g after a minority grain was cut from it using a wire saw. X-ray and neutron Laue diffraction confirmed that no secondary grain remained in either sample.

5.2.2 Magnetic Characterisation

The quality of each sample was checked using SQUID magnetometry. Figure 5.5 shows the measured susceptibilities of Samples 1 and 2. The zero-field cooled (ZFC)

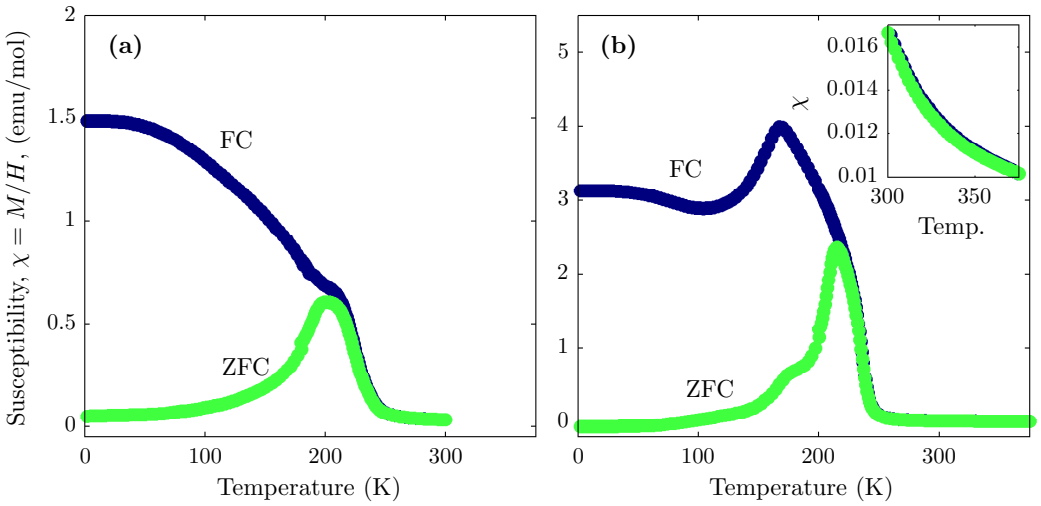

Figure 5.5: Measured susceptibility of $LuFe_2O_4$. Susceptibility measurements made using an applied magnetic field of $H = 1000\,\text{Oe}$ parallel to the c axis of (a) Sample 1 and (b) Sample 2. Insert in (b) highlights the change in gradient at $\sim 320\,\text{K}$ corresponding to the 3D charge ordering transition in Sample 2. The green (blue) points denote the ZFC (FC) data.

and field cooled (FC) data are measured by applying a magnetic field parallel to the c axis. An applied field of 1000 Oe was used for both samples. The samples exhibit an onset of magnetic order at $\sim 240\,\text{K}$ as expected for $LuFe_2O_4$. Below this onset, there is a well defined peak in the ZFC data. At even lower temperatures, the FC and ZFC susceptibilities diverge and there exists another feature, most noticeable in the FC data, at $\sim 175\,\text{K}$. Qualitatively similar behaviour has been reported in numerous other $LuFe_2O_4$ samples [134, 145, 150, 151, 161–163]. Additionally, there is faint evidence for the charge ordering transition at $\sim 320\,\text{K}$ measured in the susceptibility of Sample 2. The insert in Figure 5.5(b) shows a small change in gradient at the expected temperature.

Alongside the similarities in behaviour, there are several differences between the two samples' susceptibilities. Most noticeably, the FC data in Sample 2 shows a well defined peak at 175 K and a levelling off of the susceptibility at lower temperatures. In contrast, this peak is not observed in Sample 1 (although there is a change in gradient at $\sim 180\,\text{K}$) and the susceptibility continues to increase at lower temperatures. Additionally, Sample 2 has a distinctive shoulder emerging from the

lower temperature side of the peak in ZFC susceptibility. This is not observed in Sample 1, but its features are much broader and so it is possible this shoulder is present but unresolvable. Differences in the susceptibility of $LuFe_2O_4$ have previously been linked to the precise oxygen stoichiometry of the measured samples [153]. The measurements of Sample 1 and 2 are consistent with those reported for $LuFe_2O_4$ with a slight oxygen excess. Similar susceptibilities are observed in Refs. [145, 151] which report quasi-2D – but not 3D – magnetic order. Stoichiometric sample susceptibilities are observed in Ref. [135] alongside full 3D magnetic ordering.

The magnetic characterisation shows behaviour typical of $LuFe_2O_4$ with a slight oxygen excess in both samples. The different behaviours of samples may arise from the precise oxygen content in each. An oxygen excess is consistent with a lack of 3D magnetic order. This study is concerned with the magnetic excitations arising from the 2D static order of the bilayers in $LuFe_2O_4$. Therefore, differences in the extent of 3D magnetic order (up to its complete suppression at the 2D ordering limit) will not affect the subsequent measurements or analysis presented.

5.3 Neutron Scattering Results

Sample 1 was measured on the triple-axis spectrometer (TAS) IN8 at the ILL, France. The crystal was aligned with $(H, K, 0)$ as the horizontal scattering plane. Both horizontally focussing Si (111) and double focussing Cu (200) monochromators were used in combination with a double focussing pyrolytic graphite (002) analyser to measure with fixed final wave vectors $k_\mathrm{f} = 2.662$ and $4.1\,\text{Å}^{-1}$. Measurements were made at a temperature of 1.5 K. This experiment expanded on the previously measured elastic scattering and low energy spectrum of Sample 1 reported in Ref. [144].

The larger mass of Sample 2 allowed the use of time-of-flight (TOF) spectroscopy to survey the excitation spectrum across a wide area of the 2D BZ. Measurements

were made using the MAPS spectrometer at the ISIS facility, UK. The crystal was aligned with the c axis parallel to the incident wave vector $\boldsymbol{k}_\mathrm{i}$. In such a fixed orientation, the L component of $\boldsymbol{Q}$ varies with E – see Section 2.3.2. As $LuFe_2O_4$ exhibits very weak inter-bilayer coupling, no significant dispersion is expected parallel to L. Hence, the measured intensity is integrated over L and the bilayer spectrum is described by the 2D wave vector $\boldsymbol{Q} = (H, K)$. Preliminary high-flux measurements were made using incident energies of $E_\mathrm{i} = 60,\ 80,\ 120,\ 150$, and 200 meV to identify the total bandwidth of the spectrum. The resolution broadening in each measurement is defined by a full width at half maximum (FWHM) of approximately 6% of E_i at $E = 0$ meV. This broadening decreased with increasing energy transfer. Higher resolution configurations were used to repeat the measurements with $E_\mathrm{i} = 60$ and 80 meV. Using higher chopper frequencies, the FWHM was reduced to approximately 4% of E_i at $E = 0$ meV. Measurements were made at 7 K and 6 K for the lower and higher resolution configurations respectively. A standard vanadium sample was measured to normalise all detector efficiencies and place the intensities on an absolute scale.

Figure 5.6 illustrates the extent of the measurements and shows the bandwidth of the excitation spectrum. Figure 5.6(a) shows the excitation gap measured in Sample 1 at the $\Gamma = (1/3,\ 1/3, 0)$ zone centre. The TAS measurements have the advantage of higher resolution at low energies and clearly show a sharp peak centred on 9.4 meV. This is consistent with the gap reported in a powdered $LuFe_2O_4$ sample [148]. However, there also exists some magnetic intensity below this gap as seen from the small peak observed at 5 meV. This low energy signal is not due to intensity arising from the underlying Bragg peak (which can be seen to extend up to roughly 2 meV). This feature could not be investigated in the MAPS data because the low energy region is obscured by intensity from the Bragg peak (which extends up to 4 meV). The origin of this weak, low energy signal is not known. One possible explanation is that it arises from lower energy excitations expected from stacking

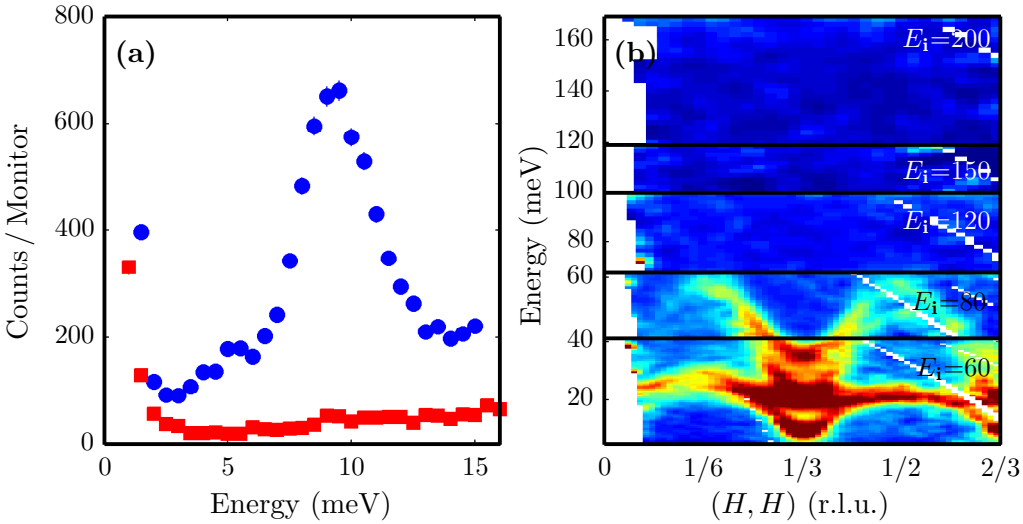

Figure 5.6: Measured gap and bandwidth of magnetic excitations in $LuFe_2O_4$. (a) IN8 energy cuts centred on the $\Gamma = (1/3, 1/3, 0)$ (blue circles) and K= $(0, 2/3, 0)$ (red circles) positions. Both cuts are measured with fixed $k_f = 2.662\,\text{Å}^{-1}$. Error bars are plotted but most are smaller than the marker size. Data at the Γ point show a prominent peak at 9.4 meV consistent with the excitation gap. Data from the K point provide a measure of the background scattering at low energies. There is a smaller magnetic peak observed at 5 meV of unknown origin. (b) Summary of the measurements made on the MAPS spectrometer. The different panels denote data collected using different incident energies (labelled) to ensures each energy range was measured with good resolution. The colour map depicts the intensity along the (H, H) direction. The intensity was scaled independently in each panel for clarity. No excitations were measured above 60 meV.

faults. This shall be discussed further in Section 5.5.

Figure 5.6(b) shows the excitations measured in Sample 2 along the (H, H) in-plane direction. Data were recorded up to 170 meV and show excitations extending up to $\sim$ 60 meV. No higher energy features were observed. The modes appear broader than expected from the instrumental resolution and overlap at various points in the spectrum. A significant structure factor modulation of intensity is also present, evidenced by the asymmetry of the intensity around the $\Gamma = (1/3, 1/3)$ zone centre position [most noticeably in the modes below 40 meV at the equivalent zone boundary positions M= (1/6, 1/6) and (1/2, 1/2)]. Note, no asymmetry would be found about the $\Gamma = (0, 0)$ zone centre but, as the magnetic unit cell is non-primitive, the structure factor is different in the neighbouring $\Gamma = (1/3, 1/3)$ BZ.

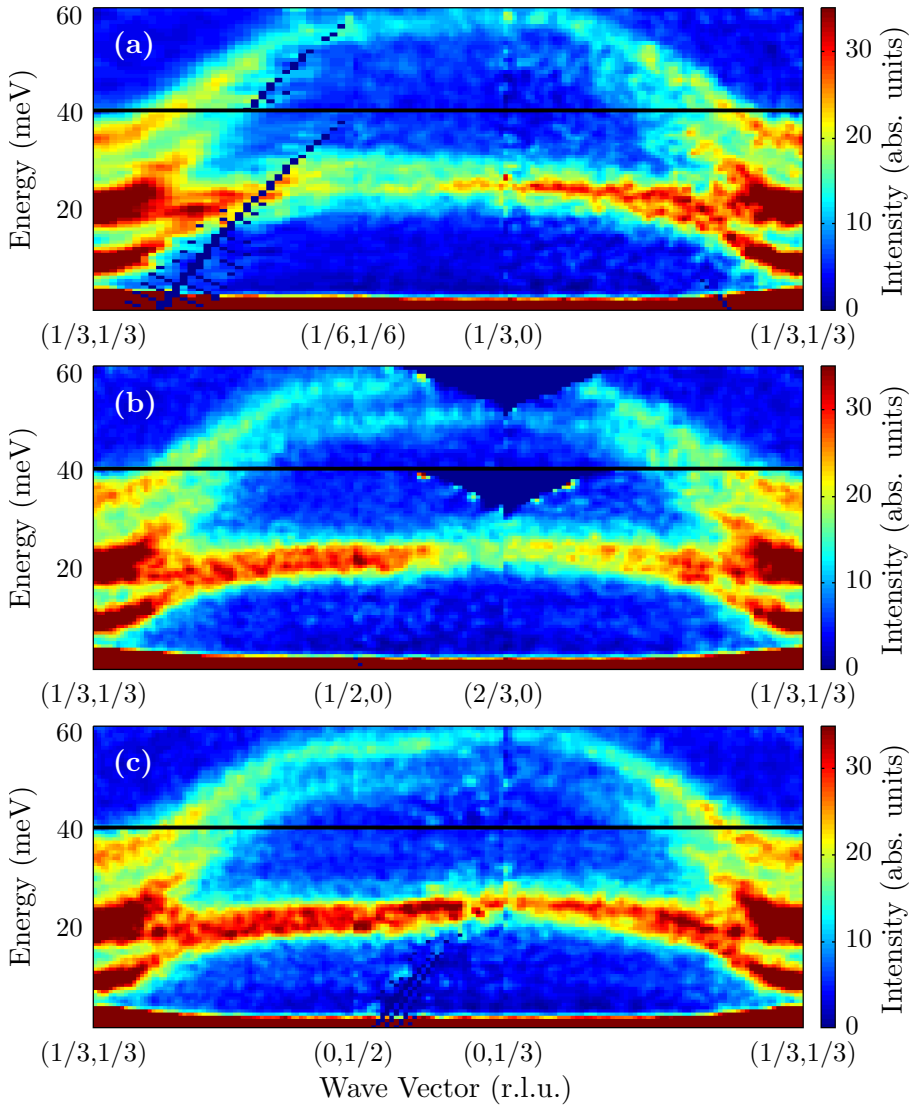

Figure 5.7: The observed magnetic excitations of $LuFe_2O_4$. Plotted spectra are along the symmetry inequivalent wave vector paths: (a) $\Gamma \rightarrow \mathrm{M} \rightarrow \mathrm{K} \rightarrow \Gamma$, (b) $\Gamma \rightarrow \mathrm{M}' \rightarrow \mathrm{K} \rightarrow \Gamma$, and (c) $\Gamma \rightarrow \mathrm{M}'' \rightarrow \mathrm{K} \rightarrow \Gamma$. The data in the bottom (top) panel of each spectra are measured from Sample 2 using the MAPS spectrometer with $E_\mathrm{i} = 60\,\mathrm{meV}$ ($E_\mathrm{i} = 80\,\mathrm{meV}$). Intensities are plotted in absolute units of $\mathrm{mb\,sr^{-1}\,meV^{-1}\,f.u.^{-1}}$.

While the structure factor significantly affects a mode's relative intensity across the BZ, the dispersion of a mode is not observed to change significantly when different wave vector paths are considered. Figure 5.7 depicts spectra along three similar but inequivalent BZ paths – distinguished by the three symmetry inequivalent zone boundary positions M, M′, and M″. The distributions of intensities is

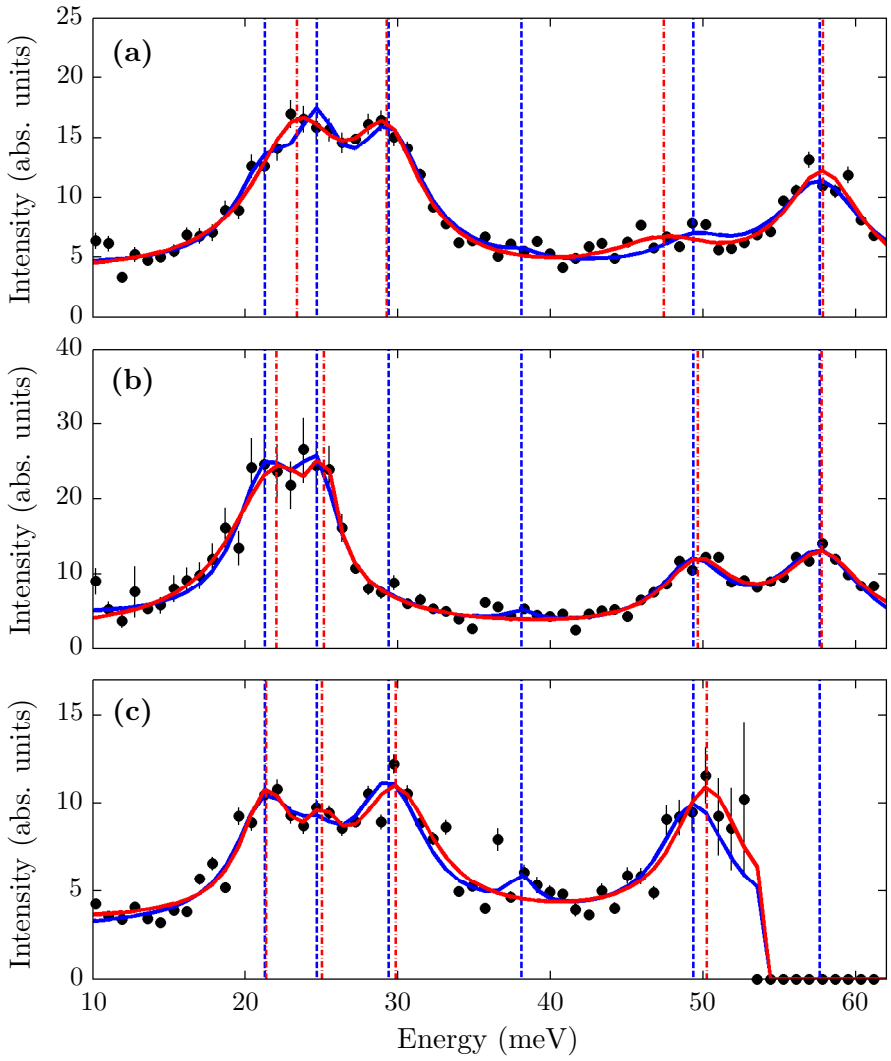

Figure 5.8: Approximately equivalent constant-Q line cuts and the fitted peak positions. The black data points show three constant-$\boldsymbol{Q}$ line cuts taken at approximately equivalent positions on the BZ boundary at (a) M= $(1/6, 1/6)$, (b) M$'$ = $(1/6, 2/3)$, and (c) M$''$ = $(2/3, 1/6)$. The data were collected from Sample 2 using the MAPS spectrometer with $E_{\mathrm{i}} = 80\,\mathrm{meV}$. All intensities are in absolute units of $\mathrm{mb\,sr^{-1}\,meV^{-1}\,f.u.^{-1}}$. The solid blue (red) lines show the semi-global (individual-$\boldsymbol{Q}$) fitted pattern. The dashed blue (red) lines show the fitted positions of the peaks using the semi-global (individual-$\boldsymbol{Q}$) fitting techniques.

very similar across the three spectra. There are differences across the zone boundary. The M$\rightarrow$K path [Figure 5.7(a)] has a much broader band of intensity between $20 - 35\,\mathrm{meV}$ than the M$'$ $\rightarrow$K and M$''$ $\rightarrow$K paths [Figures 5.7(b) and 5.7(c) respectively]. A more detailed look at the intensity distributions is given by taking

energy line cuts centred on the M, M′, and M″ positions – as presented in Figure 5.8. This figure illustrates the significant differences in the intensities of common modes (such as those found at ~ 30 and 50 meV). Additionally, some small but resolvable differences in the mode energies can be seen when the data are fit to a series of Lorentzian line shapes (shown as solid red lines). When data along all wave vector paths are examined, there is evidence for a maximum of six modes in the spectrum.

5.4 Analysis

As previously outlined, there are various proposed descriptions of the magnetic order across both the 3D structure and within the bilayers of $LuFe_2O_4$. In this analysis, a minimal spin wave model is derived from the only proposed bilayer ground state order consistent with the measured spectrum. This minimal model offers a good description of the complicated dispersive features observed in the spectrum by considering a simplified set of nearest neighbour and next-nearest neighbour exchange interactions. In this section, I shall introduce the minimal model, justify the ground state used, and outline the method for exhaustively fitting the exchange parameters.

5.4.1 Magnetic Ground State

The measured dispersion shows evidence for six magnetic excitation modes. This indicates that a 2D magnetic unit cell comprising six spins describes the majority of the sample. This is consistent with the AB-bilayer magnetic structure outlined in Figures 5.3(c) and 5.4(b). The AA-BB-bilayer model proposed in Ref. [141] is described by two distinct bilayer structures containing twelve spins and would, therefore, have twelve distinct spin wave modes.[1] While it is possible that the six modes arising from the AA- and BB- bilayer interactions will overlap, it seems very unlikely for such different structures. Additionally, the most prominent excitations

[1]Note, however, that in the absence of inter-monolayer interactions both the AB- and AA-BB-bilayer structures would give the same spectrum.

are observed to have a significant gap at the Γ position. Excitations in a BB-bilayer comprised of two Fe^{3+}-rich monolayers, are expected to be very weakly gapped because Fe^{3+} has much less orbital angular momentum and is therefore more isotropic than Fe^{2+}. Two gaps of similar intensity – consistent with excitations from equal numbers of AA- and BB-bilayers – are not experimentally observed and so this order is inconsistent with the measured spectrum. Furthermore, the AA-BB-bilayer order was proposed base on diffraction data measured at 210 K [141]. At lower temperatures, below the $T = 175$ K transition observed in the susceptibility [Figure 5.5(b)], Christianson, *et al.* [135] reported an altered magnetic diffraction pattern.

The phase mixing scenario proposed in Ref. [148], with distinct antiferromagnetically and ferromagnetically correlated bilayers, would similarly lead to more than six modes in the spectrum. Furthermore, the magnetisation for such a phase mixed sample exhibits additional features not observed in Samples 1 and 2. Most prominently, the susceptibility presented in Figure 5.5 does not include a sharp peak centred on approximately 250 K, as reported in Ref. [148]. This high temperature peak is attributed to the formation of AFM correlated bilayers. The lack of such a peak in Figure 5.5 suggests that Samples 1 and 2 are not phase mixed in this way.

Based on these considerations, I shall continue by assuming that the 2D magnetism corresponds to the ferromagnetically-correlated AB-bilayer order proposed in Refs. [146, 147]. This is consistent with the six magnetic modes measured; the single prominent excitation gaps; and reflects the good agreement between the measured susceptibility of Sample 2 (Figure 5.5(b)) and the sample of Wu, *et al.* [151] (which was subsequently used in Ref. [146]). This bilayer magnetic structure is depicted in Figure 5.3(c). It can be seen from the figure, that the charge and magnetic order of the supercell breaks the local $\bar{3}$m symmetry characteristic of the crystallographic unit cell. Therefore, this structure leads to six magnetic domains, each of which will contribute to the data measured at a given position. Figure 5.3(b) high-

lights this by showing the reciprocal lattice of one such domain, with the symmetry inequivalent M, M′, and M″ positions labelled. These are distinct high symmetry points as they are not related by a reciprocal lattice vector. The Γ and K positions are all equivalent. How the domains are accommodated in the analysis of the spectrum will be discussed in more detail in Section 5.4.3.

5.4.2 Spin Wave Model

To describe excitations away from the ground state, an anisotropic Heisenberg Hamiltonian is defined

$$\mathcal{H} = \sum_{\langle i,j \rangle} J_{ij} \boldsymbol{S}_i \cdot \boldsymbol{S}_j + \sum_i \mathcal{D}_i (S_i^z)^2, \tag{5.1}$$

where J_{ij} are the exchange parameters and $\mathcal{D}_i$ are the single ion anisotropy terms defined separately for Fe^{2+} and Fe^{3+} ions. Figure 5.3(c) specifies the exchange interactions used in the model. The different electronic structures of the Fe^{2+} and Fe^{3+} ions mean the super exchange pathways between each ion will be distinct. Therefore, the exchange parameters represent Fe^{2+}–Fe^{3+} exchanges associated with each monolayer (J_{A1} and J_{B1}); the Fe^{2+}–Fe^{2+} and Fe^{3+}–Fe^{3+} exchanges on the Fe^{2+}-rich and Fe^{3+}-rich monolayers respectively (J_{A2} and J_{B2}); and a single inter-monolayer exchange (J_{AB}). Therefore, only nearest-neighbour interactions are considered within and between the monolayers. When considering the full symmetry of the supercell, there are a total of 15 nearest-neighbour superexchange pathways [160]. However, when the different oxygen environments of each Fe site are assumed to be equivalent this contracts to the five defined above and maintains the simplicity of the model. The separate single-ion anisotropy terms introduce the c axis anisotropy that is present in $LuFe_2O_4$, while allowing the strength of the anisotropy to be different for the Fe^{2+} and Fe^{3+} ions.

This Hamiltonian expands on the three exchange parameters used by Nagano, *et al.* [159], and simplifies the model of Xiang, *et al.* [160], by defining five exchange

pathways. The exchange interactions are expected to be short range as $LuFe_2O_4$ is an insulator, and this is supported by the DFT calculations of Xiang, *et al.* [160] which found negligible super-superexchange (ie. next nearest-neighbours exchange) interactions when compared to the shorter superexchange interactions.

The validity of the proposed Hamiltonian was checked by ensuring it leads to the assumed magnetic ground state outlined in the previous section. This was done through a mean field calculation, based on the simplification of the Hamiltonian in Eq. 5.1 to the Ising limit. This has the form

$$\mathcal{H}_{\mathrm{MF}} = \sum_{\langle i,j \rangle} J_{ij} S_i^z S_j^z. \tag{5.2}$$

With six Fe ions in the magnetic unit cell, only $2^6 = 64$ Ising spin states exist (which can be simplified to 32 doubly degenerate states, when the two states linked through the reversal of all spins are considered). By considering all the exchange pathways defined in Figure 5.3(a), the ground state Ising spin structure can be identified for any given values of J_{ij}. Performing this calculation for a variety of exchange parameters reveals the accepted spin structure as the lowest energy ordering. Therefore, the chosen Hamiltonian is consistent with the proposed magnetic order for suitable choices of J_{ij} when there is strong c axis anisotropy.

5.4.3 Domains in Magnetically Ordered AB-Bilayers

As mentioned in the Section 5.4.1, the charge and magnetically ordered bilayer structure outlined in Figure 5.3(c) breaks the three-fold rotational and mirror symmetry of the crystallographic unit cell. Therefore, we expect that there will be six 2D domains present in the low-temperature ordered phase. The measured spectrum will comprise of the six domains' spectra, along directions related by the broken symmetry operations. As reciprocal space has inversion symmetry by definition, the six spectra are described by only three dispersions, each dispersion being found in two domains. Hence, the measured $\Gamma \rightarrow \mathrm{M}$ spectrum will be comprised of

intensity centred on the $\Gamma \rightarrow$ M, $\Gamma \rightarrow$ M$'$, and $\Gamma \rightarrow$ M$''$ dispersions.

The individual charge and magnetically ordered A- and B-monolayers are characterised by 6- and 3-fold symmetry, respectively. Therefore, when the monolayers are uncoupled (ie. $J_{\mathrm{AB}} = 0$), all domains have the same dispersion due to these symmetries and the inversion symmetry of reciprocal space. As previous estimates of the inter-monolayer exchange J_{AB} are small [160], the splitting of the domain dispersions is also expected to be small. With the three dispersions expected to be nearly degenerate, the inequivalent dispersion directions which are related through the broken symmetry operations can be considered as *approximately equivalent*. This is supported by the measured data, where no more than six modes are observed at any position in the BZ but approximately equivalent wave vector positions show slight energy shifts ($\sim 1 - 2\,\mathrm{meV}$) between the modes – most noticeably at the M, M$'$, and M$''$ positions as shown in Figure 5.8. It should be noted that the structure factor variation of intensity may also give rise to the shifted peak positions when two or more peaks are close in energy – this effect is described in more detail in the next section. Shifted peak positions arising from different dispersions or structure factor modulations cannot be distinguished. To accommodate for both these potential effects, an intensity-weighted domain-averaged dispersion is used to describe the spectrum. As the splitting of the domain modes is small, the spectrum can be described by a domain averaged dispersion. To reflect the differences in measured intensity, the contribution of each domain dispersion to the average is weighted by the calculated intensity at each $\boldsymbol{Q}$ position.

5.4.4 Extracting the Dispersion

The magnetic dispersion was extracted from the measured excitation spectrum by fitting probability distributions to line cuts along the high symmetry directions. Lorentzian line shapes were found to be a good description of the peaks in E line cuts, while Gaussian distributions were used for $\boldsymbol{Q}$ cuts. In both cases a linear

background was also included. The fitting of E cut data was performed in two different ways:

(i) Semi-Global Fitting

A series of peaks were simultaneously fitted to all line cuts at equivalent or approximately equivalent BZ positions. A peak's centre and width were refined against the data from all line cuts. The amplitude of a peak is refined against data from an individual line cut. The independence of the peak amplitude accommodates for the structure factor modulations across the BZ.

(ii) Individual Q-position Fitting

A series of peaks were fitted solely to an individual line cut with fixed $\boldsymbol{Q}$.

Each fitting method has its advantages. Semi-global fitting allows relatively poor counting statistics and certain modes' low intensities to be circumvented. Therefore, fitted peaks have smaller parameter errors. Individual-$\boldsymbol{Q}$ fitting avoids the averaging effect that occurs when several different cuts are fit simultaneously to a single pattern. Semi-global fits of constant-$\boldsymbol{Q}$ cuts through the $LuFe_2O_4$ data consistently allowed five modes to be resolved across the entire BZ. Six modes can be resolved at some wave vector positions when semi-global fitting is used. This represents an improvement over the individual-$\boldsymbol{Q}$ fitting, where typically only three or four modes can be accurately distinguished at any given $\boldsymbol{Q}$. However, the dispersions along approximately equivalent BZ paths are expected to be slightly different and so the semi-global fitting has the potential to smear out features.

A comparison of the resulting fits using the two methods is presented for M, M$'$, and M$''$ positions in Figure 5.8. A semi-global fit is performed using these line cuts and those related through inversion (therefore, 6 in total). The resulting fits for these three cuts are shown as solid blue lines. The positions of the six peaks

forming the fitted pattern are denoted by the vertical blue dashed lines (and are the same across the three cuts). Similarly, the individual-$\boldsymbol{Q}$ fits are shown for each line cut as solid red lines and the peak positions are marked by vertical dashed red lines.

For the case of the M, M$'$, and M$''$ positions, the increased statistics of semi-global fitting is exploited to allow six modes to be resolved while only four can be resolved at the same positions using individual-$\boldsymbol{Q}$ fitting in each. This is principally due to the structure factor modulation of intensity which suppresses certain modes at different positions in the BZ. Additionally, the weaker modes (such as that seen at $\sim 37\,\text{meV}$) cannot be accurately resolved from the background by fitting only a single line cut. There is some variation in the fitted peak positions using the individual-$\boldsymbol{Q}$ fitting technique. The peak positions are observed to fluctuate around the semi-global fitted position in each of the cuts. This is particularly noticeable for the peak at $\sim 50\,\text{meV}$. The different intensities of this peak in all three cuts makes a consistent analysis difficult. These variations are expected due to the slightly different dispersions in each domain at symmetry inequivalent wave vector positions. Furthermore, the intensities of two or more modes with similar energies can merge to form a single observable peak. As the peak intensities vary across reciprocal space, due to the structure factor modulations, the measured position of the single peak can also fluctuate. In either of these possibilities, the indivdual-$\boldsymbol{Q}$ fitting returns a more complete description of the dispersion as opposed to the semi-global fitting which is undertaken with the possibility of smearing out distinguishing features.

The dispersion was extracted from both the $E_\text{i} = 60$ and $80\,\text{meV}$ measured spectra using both fitting techniques. Figure 5.9(b) shows the dispersion found from semi-global fitting along the $\Gamma \rightarrow \text{M} \rightarrow \text{K} \rightarrow \Gamma$ path (and the related $\Gamma \rightarrow \text{M}' \rightarrow \text{K} \rightarrow \Gamma$ and $\Gamma \rightarrow \text{M}'' \rightarrow \text{K} \rightarrow \Gamma$ paths). The modes are mapped onto one such path: $\boldsymbol{Q} = (1/3, 1/3) \rightarrow (1/2, 1/2) \rightarrow (1/3, 2/3) \rightarrow (1/3, 1/3)$. Figure 5.9(c) shows the

individual-$\boldsymbol{Q}$ fit data along this specific path. Therefore, this represents only a portion of the extracted dispersion of the entire BZ found using individual-$\boldsymbol{Q}$ fitting.

5.4.5 Model Fitting

To simulate the excitation spectrum of a given exchange Hamiltonian the SPINWAVE_DISPERSIONS.M software [164] was used, which is a numerical implementation of linear spin wave theory (SWT).[2] This calculates the dispersion $\omega(\boldsymbol{Q})$ and components of the scattering function $S(\boldsymbol{Q})$. To account for the domain effects outlined in Section 5.4.2, the dispersion for each domain was calculated and an approximate dispersion was found by finding the weighted domain average for each mode. $S(\boldsymbol{Q})$ served as the $\boldsymbol{Q}$-dependent weighting factor for each domain's dispersion. The results of such an averaging are illustrated in Figure 5.9(a) where the dispersions due to all the individual domains are plotted. The modes from different domains contributing to a single weighted average are plotted in the same colour. The weighted domain average is plotted as a black line for each mode.

Preliminary fits of the domain-averaged numerical model demonstrated that there are various converged solutions corresponding to drastically different exchange parameters and final spectra. In order to conclusively find the best solution, a series of starting parameters was used to systematically cover large regions of parameter space and exhaustively fit the model. The series was found using the mean field model outlined in Section 5.4.2. Each of the J parameters was varied between 0 to 5 in 0.5 meV steps. Every possible permutation of the J values formed an array of 11^5 starting parameter sets. AFM interactions ($J \geq 0$) were chosen based on their predicted dominance [145, 146, 160]. The range and step-size of each J value was chosen to optimise the parameter space coverage while limiting the long computation times (which increase as a quintic power law with an increasing number of J-steps). Using the mean-field model, the energies of all Ising spin states

[2] This was necessary as the Hamiltonian describing the interactions of a six spin magnetic unit cell forms a 12×12 matrix. To calculate the spectrum the Hamiltonian must be diagonalised. This is unfeasible to do analytically for such a large matrix.

were calculated for each parameter set. Starting parameters which energetically favour a ground state spin structure other than that depicted in Figure 5.3(c) were discarded as unphysical. The remaining combinations formed a list of 5329 sets of starting parameters. The starting values of the anisotropy parameters were set to 3 meV for both the Fe^{2+} and Fe^{3+} ions. This choice is in contrast to the expected small and large anisotropies of the Fe^{3+} and Fe^{2+} ions respectively [146]. The same intermediate anisotropy strength was chosen for both ions so the fitting was not biased towards any specific form of anisotropy.

Fitting each of these starting parameter sets allowed parameter space to be exhaustively explored. This was done using the semi-global fitted dispersion data. Each mode was attributed various dispersion data points and, in some cases, a single data point was refined against more than one mode to accommodate for overlapping modes.[3] Each data point was weighted to the inverse square-root of its error (ie. $w_j = 1/\sqrt{\delta E_j}$ is the weighting of the j^{th} data point). This fitting produced 30–40 distinct converged solutions.

The converged parameters of the twenty best solutions (determined by the χ^2 goodness-of-fit value) formed a series of targeted starting parameters. Using the targeted parameters allows fits to focus on certain regions of parameter space known to be near a local χ^2 minima. The targeted starting parameters were used to fit the more detailed individual-$\boldsymbol{Q}$ fitted dispersion data. The same method of point weighting as the exhaustive fitting was used and, again, each data point was attributed to one or more modes. The best solution with the lowest $\chi^2 = 6.49$ value is shown in Figure 5.9. The fitted parameters are listed in Table 5.1. This solution was consistently reproduced when the data are re-fitted using starting parameters randomly shifted a small amount away from the converged values. This confirms

[3]The expectation value of the normalised goodness-of-fit parameter χ^2 when a model perfectly describes a dataset is $\chi^2 = 1$ [165]. However, in the case where a single data point is refined against two non-degenerate modes simultaneously the best achievable χ^2 is no longer 1 (as the data point cannot be perfectly described by both modes). This has the effect of making the numerical value of χ^2 inconsistent between fits performed on different datasets. Therefore, only the values of χ^2 found by fitting to the same dataset shall be considered.

Parameter	Best Fit	2nd Best Fit	Xiang, *et al.* [160]
χ^2	6.49	6.55	–
J_{AB}	-1.098(8)	-1.05(1)	0.9
J_{A1}	1.185(4)	1.184(5)	4.0
J_{A2}	0.935(8)	1.356(6)	2.75
J_{B1}	0.868(5)	-0.08(6)	1.87
J_{B2}	3.407(8)	3.405(8)	7.3
$\mathcal{D}_{\mathrm{Fe^{2+}}}$	5.53(2)	6.02(2)	–
$\mathcal{D}_{\mathrm{Fe^{3+}}}$	0.60(1)	0.84(2)	–

Table 5.1: Summary of the fitted and predicted magnetic exchange parameters of $LuFe_2O_4$. Refined parameters from the best and second best fits are listed alongside their χ^2 value. The exchange parameters are defined in Figure 5.3(c). The errors on fitted exchange parameter are the standard deviations found from the fitting procedure. The complete set of nearest neighbour superexchange parameters found by Xiang, *et al.* [160] have been simplified for comparison with the fitted results. The values quoted in the table are found by averaging all superexchange parameters that become indistinguishable in the minimal model outline in Section 5.4.2.

the solution's stability. The fit provides a good reproduction of all the features in both the semi-global fitted dispersion and individual-$\boldsymbol{Q}$ fitted dispersion data as seen in Figures 5.9(b) and 5.9(c).

The second best converged solution is characterised by $\chi^2 = 6.55$, a value very close to the lowest χ^2 found. The fitted parameters are listed for comparison in Table 5.1. While some parameters are very similar to those of the best fitted solution, others are not – most noticeable J_{A2} and J_{B1}. The dispersion arising from the parameters of the second-best fit is plotted in Figure 5.10 alongside the experimentally measured dispersion and the dispersion of the best fitted solution. It is clear from an inspection of the two fitted dispersions that the second best fit does not reproduce all the features present in experimental data. Most noticeably, the curvature and energy gap of the lowest energy mode does not match the experimental results. Therefore, while the value of χ^2 implies that the second best fit is a comparably good description of the data, it does not recreate some of the

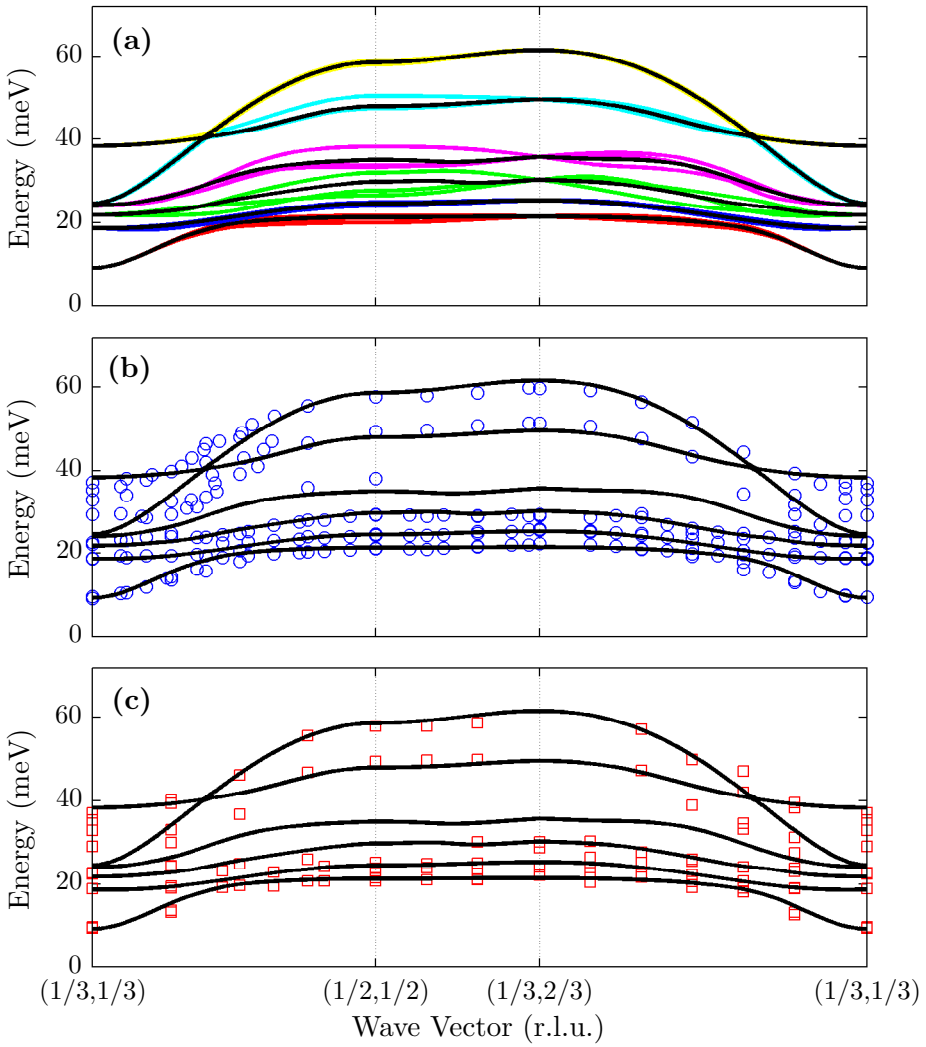

Figure 5.9: The fitted domain-averaged dispersion. (a) The simulated dispersions arising from all domains expected in the magnetic unit cell depicted in Figure 5.3(c). Each mode within a single domain's dispersion is plotted as a different coloured line. The weighted domain average of each mode used in the fitting (as described in the main text) is plotted as a solid black line in each panel. (b) The semi-global fitted dispersion data (denoted by blue circles). (c) A subset of the individual-$\boldsymbol{Q}$ fitted dispersion data, specific to the given dispersion path (red squares). In both (b) and (c), dispersion data from both the spectra measured with $E_\mathrm{i} = 60$ and 80 meV are included.

distinguishing dispersive features. The other converged solutions have significantly higher χ^2 values (≥ 8.30) in addition to badly reproducing the measured dispersion.

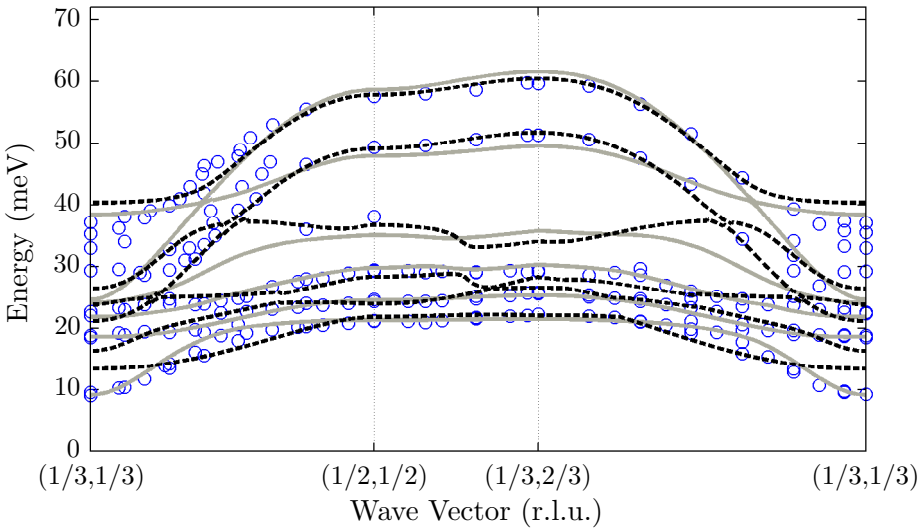

Figure 5.10: Comparison of the lowest-χ^2 and second lowest-χ^2 fitted solutions. The best (solid grey line) and second best (black dashed line) fitted solutions are plotted. For comparison, the semi-global fitted dispersion data for both the $E_i = 60$ and 80 meV spectra are also shown (blue circles). Sections of the second-best fitted dispersion do not agree with the measured data. Most noticeably, the lowest energy mode does not reproduce the curvature of the extracted dispersion near the Γ position.

5.5 Discussion

The best fitted solution provides an excellent description of the extracted dispersion. Furthermore, the converged parameters of this spin-only model successfully recover the expected strong and weak anisotropies of the Fe^{2+} and Fe^{3+} ions arising from crystal field effects. The exchange parameters are principally AFM, as expected from previous studies [145, 146, 160]. The values found using *ab initio* calculations by Xiang, *et al.* [160] have been listed for comparison with the fitted results in Table 5.1. The values have been found by averaging all those superexchange parameters listed in Ref. [160] that are indistinguishable in the minimal model used in this study. Although these results are quantitatively different from those fitted, the fitted values similarly find J_{B2} as the strongest and J_{A1} as the next-strongest interactions. The significant FM inter-layer exchange was not expected and conflicts with the averaged results of Ref [160].

Given that one of the best-fit parameters is FM, it was felt necessary to check

for the possibility of other equally good (or better) fits when negative values were included in the set of starting parameters. Therefore, a further exhaustive fit was carried out with a coarse grid of J starting parameter sets which included negative values. J was varied between -5 to 5 meV in 2.5 meV steps and all 5^5 permutations were generated. The mean field calculation was again used to remove unphysical sets and the dispersion was fit. This procedure led to some different converged solutions to those previously found, but none corresponded to a lower χ^2 minimum than that already found. Therefore, the lowest-χ^2 solution described above can be confidently stated as the best fit of the minimal model to the measured dispersion.

The analysis of the spectrum has been limited to modelling only the dispersion. This is because a refinement of the minimal model against the intensities within a line cut is made very difficult by the domain averaging. Although the model cannot be feasibly fitted against the measured intensity spectrum, the intensity arising from the fitted dispersion model can be simulated and an example 2D slice is shown in Figure 5.11(b). This has been generated by considering the measured $\boldsymbol{Q} = (1/3, 1/3) \rightarrow (1/2, 1/2) \rightarrow (1/3, 2/3) \rightarrow (1/3, 1/3)$ spectrum, shown for comparison in Figure 5.11(a). The simulated spectrum is found using the fitted parameters to calculate the dispersion and components of $S(\boldsymbol{Q})$ for each detector position contributing to the spectrum. These are then used to simulate the measured intensity at each position. An energy dependent E-broadening has been applied to the spectrum to simulate for the spectrometer resolution. An effective magnetic form factor – found by averaging the form factors of Fe^{2+} and Fe^{3+}– has been applied. Additionally, the orientation factor $(\delta_{\alpha,\beta} - \hat{Q}_\alpha \hat{Q}_\beta)$ has been applied. Finally, the intensities from all the domains are averaged and an effective g-factor of $g = 2$ is applied to express the intensities in absolute units.

Although there are discrepancies between the simulated and measured spectrum, there is a good overall agreement. The approximate factor of 2 difference in intensities can most likely be attributed to the additional experimental effects

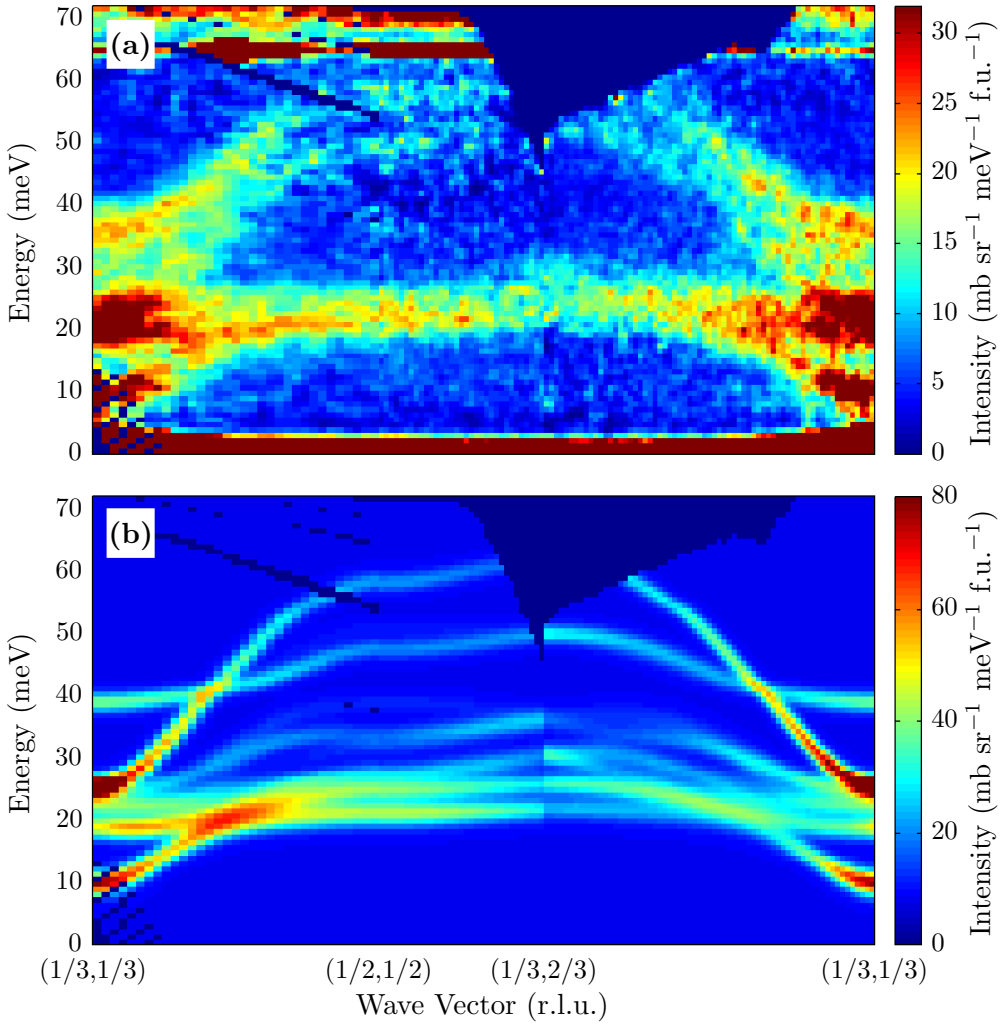

Figure 5.11: Comparison of the measured spectrum and simulated magnetic spectrum arising from the fitted dispersion. (a) Data measured on the MAPS spectrometer with $E_\mathrm{i} = 80$ meV showing an $\Gamma \rightarrow \mathrm{M} \rightarrow \mathrm{K} \rightarrow \Gamma$ path through the spectrum. The intensity is plotted in absolute units of mb sr^{-1} meV^{-1} f.u.$^{-1}$. (b) Simulations of the magnetic spectrum at the same wave vector positions. The simulations are generated using the lowest-χ^2 fitted solution's exchange and anisotropy parameters. The plotted intensity is the energy-broadened domain-averaged scattering function weighted by the orientation factor and attenuated by an averaged magnetic form factor. The g-factor ($g = 2$) and other prefactors (see Eq. 2.26) have been applied so that the intensity is in the same absolute units as (a).

of self-shielding, second-order scattering, and absorption which are not accommodated for in this simple treatment. The spectrometer resolution broadening clearly does not account for the width of the modes. A broadening of the simulated modes

would also make the cluster of domains' modes appear as single broad excitations, in better agreement with the measured spectrum.

Finally, the success of the minimal spin wave model at describing the measured spectrum indicates that the ferromagnetically-coupled AB-bilayer adopted as the ground state is a good description of the bilayer magnetic order of the majority of the crystal. The weak peak found at energies lower than the prominent gap in Figure 5.6(a) does indicate that there exists some other anisotropy within the sample. A lower gap is consistent with BB-bilayers, which have a much smaller total anisotropy because of the majority of Fe^{3+} ions. The relative weakness of the peak indicates that it is a minority phase, unlike the nearly equal phase mixing observed in Refs. [148, 150]. It may be consistent with numerous stacking faults in the sample; a theory which is consistent with the known high levels of disorder reported in $LuFe_2O_4$ [151, 152].

Chapter 6

Conclusions and Future Work

In this thesis I have used inelastic neutron scattering (INS) to measure the magnetic excitation spectra of three different and complex transition metal oxides. Modelling the spectra has revealed details of the microscopic origin of the magnetic ground state. This has been achieved, for the most part, by using linear spin wave theory (LSWT) to consider the materials as spin-only systems. While recent trends in the field of magnetic materials research have highlighted the importance of orbital physics, the results I have obtained indicate that a spin-only approach is still valid in many situations. Additionally, models based on *ab initio* calculation have been compared to measured data. These are shown to overcomplicate the description of the system – instead a minimal model is often able to capture the relevant spectral features and important energy scales. Below, I briefly summarise the findings of the three experimental studies in addition to framing some new questions that these studies have generated.

$\mathbf{La_{1.75}Sr_{0.25}CoO_4}$

The cobaltates, $La_{2-x}Sr_xCoO_4$, provide a fascinating comparison to certain cuprates, without the added complexity of superconductivity. Chapter 3 shows that the distinctive hour-glass spectrum – measured in some low-doped cuprates, manganates, and cobaltates – exists in samples of $La_{1.75}Sr_{0.25}CoO_4$ and can be simulated using LSWT based on a disordered cluster spin glass (DCSG) ground state. This result

emphasises the importance of spin-glass physics in the low doped cobaltates and adds to our current picture of the cobaltates' phase diagram.

Additionally, the findings hint that the perfect antiferromagnetic (AFM) order of the parent compound La_2CoO_4 and the checkerboard ordering seen in $La_{1.5}Sr_{0.5}CoO_4$ are connected by a steady onset of stripe correlations through a glassy intermediate phase. This hypothesis requires further experimental verification, although, it may be consistent with the proposal of Drees, *et al.* [58] that the checkerboard ordering breaks down for dopings of $x < 0.5$. This corresponds with their observations of the emergence of some chiral or non-collinear state at $x = 0.4$. Furthermore, measurements of the high energy excitations in the $x = 0.25$ doped compound may help to better understand the specifics of the AFM correlations that exist alongside the stripe correlations. The extent to which the DCSG model is valid must also be better understood. Does the disordered $x = 0.25$ state becoming increasingly more ordered at lower doping, as it approaches the AFM parent compound? Do stripe correlations exist in a similar way when $x > 0.5$? These question can only be answered by measuring and modelling the magnetic excitation spectrum.

The success of studying stripe order in cuprate-analogue systems suggests that similar approaches may help to understand other charge correlation effects observed in the cuprates. Recently, new and novel incommensurate charge fluctuations have been found in some bilayer cuprates [17]. Exploring the possibility of similar order in related bilayer cobaltate systems offers an interesting experimental challenge. If successful, such a study could reveal much more about what makes cuprates different and why they exhibit superconductivity.

CuO

Chapter 4 presents the results of an extensive INS study of CuO. Detailed measurements were made of the high energy 1D spectrum and the complete low energy 3D spectrum. The dispersion of the inter-chain magnetic excitations include several

key features. Specifically: a softening of the magnon modes at the vertex of the inter-chain Brillouin zone boundary; and an optic and acoustic mode splitting at the zone centre. These features, cannot be reproduced by a model derived from LSWT which included exchange parameters theorised to lead to the high temperature incommensurate magnetic phase in CuO. Instead, a phenomenological model is shown to reproduce the dispersion. This includes two new components. The first is an additional next-nearest neighbour interaction in the inter-chain direction. The second introduces a distinction in previously equivalent nearest neighbour interactions that relieves the frustration in the system.

Although this phenomenological model reproduces the dispersive behaviour, questions remain as to whether it represents a true microscopic model for the magnetic interactions within CuO. In other cuprate systems, next-nearest neighbour exchange interactions have been used to replicate the effects of quantum renormalisation [127] or higher-order cyclical exchange interactions [126]. Therefore, such effects must be also be investigated in the case of CuO. Quantum Monte Carlo simulations have previous been used to demonstrate the effects of quantum renormalisation in the spectrum of an AFM square lattice of $S = 1/2$ Cu^{2+} ions [127]. There are no simple cyclical (or ring) exchange pathways in CuO like there are in square lattice cuprates. However, the more complex Cu-O bonding in CuO may conceal a non-trivial higher order bonding. A model based on the true magnetic unit cell – which includes the oxygen environments – must be used in subsequent analysis to test the significance of cyclical exchange. Interestingly, cyclical exchange interactions have been proposed in a couple of previous theoretical studies of CuO [130, 131]. In these models, the cyclical exchange acts as a mechanism which stabilises the high temperature incommensurate phase.

Finally, the accurate fitting of any eventual model must accommodate the effects of the spectrometer resolution. The apparent systematic offset of all the measured points when the dispersion is steepest (ie. at intermediate energies around the zone

centre) is indicative of spectrometer resolution effects. A full resolution convolution is required to accurately fit the phenomenological model to the spectrum. This is analogous to fitting of the Müller ansatz to the high energy spectrum in Section 4.4.2. The computational tools needed to do this for multi-angle scans (such as those used to measure the inter-chain spectrum) do not exist. However, there is a current and ongoing effort to integrate the TOBYFIT resolution convolution software into the HORACE analyse suite for multi-angle scans.

LuFe2O4

Measurements of $LuFe_2O_4$ have observed a magnetic excitation spectrum which extends up to 60 meV and is consistent with six magnetic modes. A minimal spin wave model was employed to analyse the spectrum. This model was based on a previously accepted site-specific magnetic structure that has recently been called into question. Using this model and an exhaustive fitting method, the magnetic dispersion was successfully reproduced.

The success of this model, indicates that a magnetic unit cell containing six spins describes the charge and magnetic order in $LuFe_2O_4$. INS measurements appear to offer a new route to discern the possible ground state structures of $LuFe_2O_4$. With discrepancies between measured samples reported in previous studies of $LuFe_2O_4$, repeating the INS measurements on a sample exhibiting a stoichiometric oxygen content would offer an interesting comparison to the current results. Additionally, measuring the magnetic excitation spectrum at higher temperatures may also reveal new information. Diffraction studies have focussed on the data recorded between $210 - 220$ K and report sharp peaks that can be readily refined. In contrast, this neutron study has been performed at a base temperature of < 10 K. This is a region of the phase diagram with predicted spin glass effects and a 3D diffraction pattern which deviates from that at $210 - 220$ K [135].

Additionally, this study of $LuFe_2O_4$ has highlighted some interesting method-

ological points. First, the strength of a spin-only model to describe (at least in simple terms) the behaviour of a material with known orbital physics. The large fitted single-ion anisotropy found for the Fe^{2+} ions is consistent with both the Ising-like ordering of the spins and previous measurements of a significant orbital component contributing to the Fe^{2+} ion's moment. Secondly, the work presented in this thesis illustrates how the spin wave spectrum of very complex magnetic structures can be successfully modelled and parametrised using a numerical implementations of LSWT [164]. Most studies using LSWT are focussed on systems containing two magnetic sublattices. In these situations, a model Hamiltonian can be analytically solved and refined against the measured spectrum. However, analytic solutions become unfeasible when more complex magnetic unit cells are considered. The methods outlined in this thesis may improve the analysis of magnetic excitation in systems where the magnetic unit cell contains multiple magnetic sublattices.

Appendix A

CuO Spin Wave Model

Contents

A.1 Introduction

In Chapter 1, linear spin wave theory was introduced in the context of a simple antiferromagnet on a square lattice. In Chapter 4, this theory was used to develop a linear spin wave model (LSWM) for the 3D magnetic excitations measured in CuO. This appendix derives the results previously quoted in Section 4.4.1 for the LSWM of CuO. A more detailed explanation of linear spin wave theory can be found in various textbooks, such as Refs. [166, 167].

For any spin wave model, a Hamiltonian describing the system is required. In the case of CuO, this is defined in Eq. 4.6. The different exchange parameters included are defined in Figures 4.2(a) and 4.2(b). The magnetic unit cell is shown in Figure 4.2(a), and contains four spins. For clarity, these shall be identified as A (at position $\boldsymbol{r}_{\mathrm{A}} = 0\boldsymbol{a}_{\mathrm{m}} + 0\boldsymbol{b}_{\mathrm{m}} + 0\boldsymbol{c}_{\mathrm{m}}$), B ($\boldsymbol{r}_{\mathrm{B}} = 1/2\boldsymbol{a}_{\mathrm{m}} + 0\boldsymbol{b}_{\mathrm{m}} + 0\boldsymbol{c}_{\mathrm{m}}$), C ($\boldsymbol{r}_{\mathrm{C}} = 1/4\boldsymbol{a}_{\mathrm{m}} + 1/2\boldsymbol{b}_{\mathrm{m}} + 1/2\boldsymbol{c}_{\mathrm{m}}$), and D ($\boldsymbol{r}_{\mathrm{D}} = 3/4\boldsymbol{a}_{\mathrm{m}} + 1/2\boldsymbol{b}_{\mathrm{m}} + 1/2\boldsymbol{c}_{\mathrm{m}}$).

A.2 Fourier Transformation of the Hamiltonian

In order to consider the change in spin associated with a spin wave, the spin raising and lower operators are defined with respect to the spin quantisation axis y, such that

$$S^x = \frac{1}{2i}(S^+ - S^-), \qquad S^y = S^y, \qquad S^z = \frac{1}{2}(S^+ + S^-). \tag{A.1}$$

The raising and lower spin operators can then be transformed to a set of Holstein-Primakoff (HP) creation and annihilation operators. The HP operators used are approximations of the true power law expressions of S^+ and S^-. They are defined for each spin in the magnetic unit cell and their form depends on the atom's spin orientation. Therefore, for atoms A (spin up) and B (spin down)

$$S_A^+ = (2S)^{1/2}a, \qquad S_A^- = (2S)^{1/2}a^\dagger, \qquad S_A^y = S - a^\dagger a, \tag{A.2}$$

$$S_B^+ = (2S)^{1/2}b^\dagger, \qquad S_B^- = (2S)^{1/2}b, \qquad S_B^y = -S + b^\dagger b. \tag{A.3}$$

Similar expression are defined for atom C (with a spin parallel to A) and atom D (with a spin parallel to B). The operators obey the boson commutation relations $[a_n, a_m^\dagger] = \delta_{n,m}$ and $[a_{\boldsymbol{q}}, a_{\boldsymbol{q}}^\dagger] = \delta_{\boldsymbol{q},\boldsymbol{q}'}$, where $\delta_{x,y}$ is the Kronecker delta function. The HP operators associated with different spins commute, such that $[a_n, b_m] = 0$.

Using Eqs. A.1, A.2, and A.3 , neighbouring spins antiferromagnetically aligned are expressed in terms of the HP operators as

$$\boldsymbol{S}_n \cdot \boldsymbol{S}_m = -S^2 + S(a_n^\dagger a_n + b_m^\dagger b_m) + S(a_n^\dagger b_m^\dagger + a_n b_m). \tag{A.4}$$

Neighbouring spins ferromagnetically aligned are expressed as

$$\boldsymbol{S}_n \cdot \boldsymbol{S}_m = S^2 - S(a_n^\dagger a_n + a_m^\dagger a_m) + S(a_n a_m^\dagger + a_n^\dagger a_m). \tag{A.5}$$

In both, Eqs A.4 and A.5, higher order terms have been neglected. The remain-

ing terms are bilinear in creation and annihilation operators. Performing a Fourier transform on the resulting expression of the Hamiltonian defines the spin interactions in wave vector. The Fourier transforms is defined as

$$a_n = \frac{1}{\sqrt{N}} \sum_{\boldsymbol{q}} e^{i\mathbf{q}.\mathbf{r}_n} a_{\boldsymbol{q}}, \qquad a_n^\dagger = \frac{1}{\sqrt{N}} \sum_{\boldsymbol{q}} e^{-i\mathbf{q}.\mathbf{r}_n} a_{\boldsymbol{q}}^\dagger \tag{A.6}$$

In this expression, $\boldsymbol{q}$ is wave vector and $\boldsymbol{r}_n$ is the real space position of the n^{th} spin within the magnetic unit cell. N is the total number of spins in the magnetic unit cell.

This allows the Hamiltonian defined in Eq. 4.6 to be expressed in a bilinear form

$$\mathcal{H} = \mathcal{H}_0 + \mathcal{H}_{\boldsymbol{q}} = \mathcal{H}_0 + \sum_{\boldsymbol{q}} X_{\boldsymbol{q}} H_{\boldsymbol{q}} X_{\boldsymbol{q}}^\dagger. \tag{A.7}$$

The $\mathcal{H}_0$ terms contains factors that do not vary with wave vector and are, therefore, not relevant for the calculation of the dispersion and shall not be considered in the remaining derivation. The $\mathcal{H}_{\boldsymbol{q}}$ term varies with wave vector. It is defined by the vector $X_q = [a_{\boldsymbol{q}}^\dagger,\ c_{\boldsymbol{q}}^\dagger,\ b_{-\boldsymbol{q}},\ d_{-\boldsymbol{q}}]$, the adjoint of this vector $X_{\boldsymbol{q}}^\dagger$, and the matrix $H_{\boldsymbol{q}}$. For CuO, this has the form

$$H_q = \begin{pmatrix} A_{\boldsymbol{q}} & B_{\boldsymbol{q}} & C_{\boldsymbol{q}} & D_{\boldsymbol{q}} \\ B_{\boldsymbol{q}}^* & A_{\boldsymbol{q}} & D_{\boldsymbol{q}}^* & C_{\boldsymbol{q}} \\ C_{\boldsymbol{q}} & D_{\boldsymbol{q}} & A_{\boldsymbol{q}} & B_{\boldsymbol{q}} \\ D_{\boldsymbol{q}}^* & C_{\boldsymbol{q}} & B_{\boldsymbol{q}}^* & A_{\boldsymbol{q}} \end{pmatrix} \tag{A.8}$$

The matrix elements are defined in terms of the exchange parameters and wave

vector components $\boldsymbol{q} = (H, K, L)$ as

$$A = 2S(J_{\text{ch}} + J_{2a} + J_{2c} + J_{\text{perp}}(\cos(\pi(H+L)) - 1) + J_b(\cos(2\pi K) - 1) + 2\mathcal{D}),$$
$$B = S(J_a(e^{i\pi(H+K)} + e^{i\pi(H-K)}) + J_c(e^{-i\pi(L-K)} + e^{-i\pi(L+K)})),$$
$$C = 2S(J_{ch}\cos(\pi(H-L)) + J_{2c}\cos(2\pi H) + J_{2a}\cos(2\pi L),$$
$$D = S(J_a(e^{i\pi(H-K)} + e^{i\pi(H+K)}) + J_c(e^{-i\pi(L+K)} + e^{-i\pi(L-K)})).$$

A.3 Diagonalising the Hamiltonian

The wave vector dependant part of the Hamiltonian $H_{\boldsymbol{q}}$ defined in Eq. A.8 must now be diagonalised. To do this, I shall follow the method outlined by White, *et al.* [119]. This involves a Bogoliubov transformation, used to bring the Hamiltonian into a diagonal form. The Bogoluibov transformation can be defined as

$$X_{\boldsymbol{q}} = SX'_{\boldsymbol{q}}, \tag{A.9}$$

where $X'_{\boldsymbol{q}}$ diagonalises $H_{\boldsymbol{q}}$ such that, for any $\boldsymbol{q}$,

$$\mathcal{H} = XHX^{\dagger} = X'\Omega X'^{\dagger}. \tag{A.10}$$

In this equation, Ω is a diagonal matrix comprised of the eigenvalues of $H_{\boldsymbol{q}}$. Substituting Eq. A.9 into Eq. A.10, we find

$$gHS_i = \lambda_i S_i, \tag{A.11}$$

where the eigenvalue is related to the dispersion by the expression

$$\lambda_i = g'_{ii}\hbar\omega_i. \tag{A.12}$$

In the expression above, i indexes the elements of a matrix. Therefore, the value g'_{ii} is an element of the diagonal matrix g'. This, and the associated matrix g, are defined to maintain the commutation relations of the operators contained within X' and X respectively. Therefore, in this treatment, these metrics have the value

$$g = g' = \begin{pmatrix} 1 & 0 & 0 & 0 \\ 0 & 1 & 0 & 0 \\ 0 & 0 & -1 & 0 \\ 0 & 0 & 0 & -1 \end{pmatrix}. \tag{A.13}$$

The transformed vector of creation and annihilation operators is defined as $X_{\boldsymbol{q}} = [\alpha^{\dagger}_{\boldsymbol{q}},\ \kappa^{\dagger}_{\boldsymbol{q}},\ \beta_{-\boldsymbol{q}},\ \delta_{-\boldsymbol{q}}]$.

Eq. A.11 is in the form of an eigenvalue equation and can, therefore, be solved to reveal the wave vector dependant energy eigenvalues – as defined in Eq. A.12. These define the dispersion and for the case of CuO have the form

$$\omega_{\pm} = \sqrt{A^2 + |B|^2 - C^2 - |D|^2 \pm \sqrt{4 \mid AB - CD^* \mid^2 - \mid B^*D^* - BD \mid^2}}. \tag{A.14}$$

The corresponding normalised eigenvectors (ie. that satisfy $SgS^{\dagger} = g$) are

$$S = \begin{pmatrix} \bar{W}(\omega_-) & \bar{W}(\omega_+) & \bar{W}(-\omega_-) & \bar{W}(-\omega_+) \\ \bar{Y}(\omega_-) & \bar{Y}(\omega_+) & \bar{Y}(-\omega_-) & \bar{Y}(-\omega_-) \\ \bar{X}(\omega_-) & \bar{X}(\omega_+) & \bar{X}(-\omega_-) & \bar{X}(-\omega_+) \\ \bar{Z}(\omega_-) & \bar{Z}(\omega_+) & \bar{Z}(-\omega_-) & \bar{Z}(-\omega_+) \end{pmatrix}, \tag{A.15}$$

where the shorthand, $\bar{W}(\omega) = N(\omega)W(\omega)$ is used and the corresponding values are

$$W(\omega) = -(A+\omega)(A^2+|B|^2-C^2-|D|^2-\omega^2)+2A|B|^2-C(B^*D^*+BD^*)$$
$$X(\omega) = C(A^2+|B|^2-C^2+|D|^2-\omega^2)-A(B^*D+BD^*)-\omega(B^*D-BD^*)$$
$$Y(\omega) = B^*\big((A+\omega)^2-|B|^2+C^2\big)-2C(A+\omega)D^*+B|D|^2$$
$$Z(\omega) = D^*(A^2+C^2-|D|^2-\omega^2)+B^{*2}D-2AB^*C$$
$$N(\omega) = 1/\sqrt{|-|W(\omega)|^2-|Y(\omega)|^2+|X(\omega)|^2+|Z(\omega)|^2|}.$$

This solution is consistent with the results of an equivalent diagonalisation of a similar 4×4 Hamiltonian reported in Ref. [168]. Additionally, Eq. A.15 is expressed in the same format as Ref. [168].

A.4 One-Magnon Cross Section

Using the formalism of the creation and annihilation operators reveals the nature of the magnon excitations. Creating an excitation is equivalent to producing a magnon quasiparticle. Therefore, this can be used to approximate the partial differential cross section defined for neutron scattering in Section 2.2.3. Eq. 2.27, shows the scattering function is proportional to the sum of matrix elements $\langle\lambda_f|S^\alpha(\boldsymbol{Q})|\lambda_i\rangle$ which define a transition between an initial and final state. These can be calculated by considering the components of the Fourier transform of the spin operator defined for the spin on site n as

$$\boldsymbol{S}(\boldsymbol{Q}) = \sum_n e^{i\boldsymbol{Q}\cdot\boldsymbol{r}_n}\boldsymbol{S}_n. \tag{A.16}$$

The component directions $\alpha = \{x, y, z\}$ are defined with respect to the spin direction. In CuO, the spins lie parallel to the y direction, and it can be seen from Eqs. A.2 and A.3 that S^y describes a transition between two states with an equal number of magnons. Therefore, $S^{yy}(\boldsymbol{Q}, E)$ contains information relating to the elastic scattering. S^x and S^z detail a transition between states differing by one magnon

and, therefore, describes the system's response to inelastic scattering. In the case of CuO, $S^{xz}(\boldsymbol{Q}, E) = -S^{zx}(\boldsymbol{Q}, E)$ and $S^{xx}(\boldsymbol{Q}, E) = S^{zz}(\boldsymbol{Q}, E)$. Therefore, the partial differential cross section is found to be

$$\frac{d\sigma^2}{d\Omega dE} \propto (2 - \hat{Q}_x\hat{Q}_x - \hat{Q}_z\hat{Q}_z)S^{xx}(\boldsymbol{Q}, E), \tag{A.17}$$

where the dynamical correlations are again consistent with those found in Ref. [168] and expressed as

$$\begin{aligned} S^{xx}(\boldsymbol{Q},\omega) = \frac{S}{2N}\Big(&|\bar{W}(\omega_-) + \bar{Y}(\omega_-) + \bar{X}(\omega_-) + \bar{Z}(\omega_-)|^2 \\ &\times (n_\alpha + 1)\delta(\omega - \omega_+) + n_\alpha\delta(\omega + \omega_-) \\ &+|\bar{W}(\omega_+) + \bar{Y}(\omega_+) + \bar{X}(\omega_+) + \bar{Z}(\omega_+)|^2 \\ &\times (n_\kappa + 1)\delta(\omega - \omega_-) + n_\kappa\delta(\hbar\omega + \hbar\omega_+) \\ &+|\bar{W}(-\omega_-) + \bar{Y}(-\omega_-) + \bar{X}(-\omega_-) + \bar{Z}(-\omega_-)|^2 \\ &\times (n_\beta + 1)\delta(\omega - \omega_+) + n_\beta\delta(\omega + \omega_-) \\ &+|\bar{W}(-\omega_+) + \bar{Y}(-\omega_+) + \bar{X}(-\omega_+) + \bar{Z}(-\omega_+)|^2 \\ &\times (n_\delta + 1)\delta(\omega - \omega_-) + n_\delta\delta(\omega + \omega_+)\Big). \end{aligned} \tag{A.18}$$

In this expression, $n_\alpha = \alpha^\dagger\alpha$ is the number operator associated with α bosons. Equivalent number operator n_β, n_κ, and n_δ are included for the β, κ, and δ bosons. As the number operator defines the total number of excitations, in the ground state magnon vacuum $n = 0$ for all modes. The Dirac delta function $\delta(\omega + \omega_q)$ is included. However, because of the finite lifetime of excitations in real materials and the broadening of the spectrometer resolution function, the delta function is replaced in simulations with a Gaussian or Lorentzian lineshape to introduce some finite energy width.

Bibliography

[1] S. Blundell, *Magnetism in Condensed Matter*, Oxford University Press, Oxford (2012).

[2] G. T. Rado and H. Suhl, *Magnetism*, vol. 1, Academic Press, New York (1963).

[3] J. B. Goodenough, *Magnetism and the Chemical Bond*, Interscience Publisher, New York (1963).

[4] T. Giamarchi, *Quantum Physics in One Dimension*, Oxford University Press, Oxford (2004).

[5] H. Bethe, 'Zur theorie der metalle,' *Z. Phys.* **71**, 205 (1931).

[6] J. Cloizeaux and J. J. Pearson, 'Spin-wave spectrum of antiferromagnetic linear chain,' *Phys. Rev.* **128**, 2131 (1962).

[7] B. Lake, 'Quantum magnets show their hand,' *Nat. Phys.* **1**, 143 (2005).

[8] D. v. Delft and P. Kes, 'The discovery of superconductivity,' *Physics Today* **63**, 38 (2010).

[9] J. F. Annett, *Superconductivity, Superfluids, and Condensates*, Oxford University Press, Oxford (2011).

[10] J. Bardeen, L. N. Cooper, and J. R. Schrieffer, 'Microscopic theory of superconductivity,' *Phys. Rev.* **106**, 162 (1957).

[11] J. G. Bednorz and K. A. Müller, 'Possible high-T_c superconductivity in the Ba-La-Cu-O system,' *Z. Phys. B* **64**, 189 (1986).

[12] A. Schilling, M. Cantoni, J. D. Guo, and H. R. Ott, 'Superconductivity above 130 K in the Hg-Ba-Ca-Cu-O system,' *Nature* **363**, 56 (1993).

[13] L. Gao, Y. Y. Xue, F. Chen, Q. Xiong, R. L. Meng, D. Ramirez, C. W. Chu, J. H. Eggert, and H. K. Mao, 'Superconductivity up to 164 K in $HgBa_2Ca_{m-1}Cu_mO_{2m+2+\delta}$ ($m = 1, 2$, and 3) under quasi-hydrostatic pressures,' *Phys. Rev. B* **50**, 4260 (1994).

[14] C. Varma, 'High-temperature superconductivity mind the pseudogap,' *Nature* **468**, 184 (2010).

[15] M. Vojta, 'Lattice symmetry breaking in cuprate superconductors: stripes, nematics, and superconductivity,' *Adv. Phys.* **58**, 699 (2009).

[16] J. M. Tranquada, G. Y. Xu, and I. A. Zaliznyak, 'Superconductivity, antiferromagnetism, and neutron scattering,' *J. Magn. Magn. Mater.* **350**, 148 (2014).

[17] G. Ghiringhelli, M. Le Tacon, M. Minola, S. Blanco-Canosa, C. Mazzoli, N. B. Brookes, G. M. De Luca, A. Frano, D. G. Hawthorn, F. He, T. Loew, M. Moretti Sala, D. C. Peets, M. Salluzzo, E. Schierle, R. Sutarto, G. A. Sawatzky, E. Weschke, B. Keimer, and L. Braichovich, 'Long-range incommensurate charge fluctuations in (Y,Nd)$Ba_2Cu_3O_{6+x}$,' *Science* **337**, 821 (2012).

[18] D. J. Scalapino, 'A common thread: The pairing interaction for unconventional superconductors,' *Rev. Mod. Phys.* **84**, 1383 (2012).

[19] P. Monthoux, D. Pines, and G. G. Lonzarich, 'Superconductivity without phonons,' *Nature* **450**, 1177 (2007).

[20] W. Eerenstein, N. D. Mathur, and J. F. Scott, 'Multiferroic and magnetoelectric materials,' *Nature* **442**, 759 (2006).

[21] S. W. Cheong and M. Mostovoy, 'Multiferroics: a magnetic twist for ferroelectricity,' *Nat Mater* **6**, 13 (2007).

[22] P. Fischer, M. Polomska, I. Sosnowska, and M. Szymanski, 'Temperature-dependence of the crystal and magnetic-structures of $BiFeO_3$,' *J. Phys. C.* **13**, 1931 (1980).

[23] D. Khomskii, 'Classifying multiferroics: mechanism and effects,' *Physics* **2**, 20 (2009).

[24] I. E. Dzyaloshinskii, 'Theory of helicoidal structures in antiferromagnets I: Nonmetals,' *Sov. Phys. JETP* **19**, 960 (1964).

[25] T. Moriya, 'Anisotropic superexchange interaction and weak ferromagnetism,' *Phys. Rev.* **120**, 91 (1960).

[26] J. Chadwick, 'The existence of a neutron,' *Proc. R. Soc. Lond. A* **136**, 692 (1932).

[27] H. von Halban and P. Preiswerk, 'Preuve experimentale de la diffraction des neutrons,' *C.R. Acad. Sci. Paris* **203**, 73 (1936).

[28] D. P. Mitchell and N. Powers, 'Bragg reflection of slow neutrons,' *Phys. Rev.* **50**, 486 (1936).

[29] B. N. Brockhouse and A. T. Stewart, 'Scattering of neutrons by phonons in an aluminium single crystal,' *Phys. Rev.* **100**, 756 (1955).

[30] J. Als-Nielsen and D. McMorrow, *Elements of Modern X-ray Physics*, 2nd edn., John Wiley, Chichester, West Sussex (2011).

[31] R. M. Moon, T. Riste, and W. C. Koehler, 'Polarisation analysis of thermal neutron scattering,' *Phys. Rev.* **181**, 920 (1969).

[32] G. L. Squires, *Introduction to the Theory of Thermal Neutron Scattering*, Dover Publications, Mineola, NY (1996).

[33] S. W. Lovesey, *Theory of Neutron Scattering from Condensed Matter*, Oxford Clarendon Press, Oxford (1984).

[34] `http://www.ncnr.nist.gov/resources/n-lengths/` (2013).

[35] A. J. Dianoux and G. Lander, *Neutron Data Booklet*, 2nd edn., Old City Publishing Inc., Philadelphia, PA (2003).

[36] P. J. Brown, `https://www.ill.eu/sites/ccsl/ffacts/ffachtml.html` (2014).

[37] B. T. M. Willis and C. J. Carlile, *Experimental Neutron Scattering*, Oxford University Press, Oxford (2009).

[38] G. Shirane, S. M. Shapiro, and J. Tranquada, *Neutron Scattering with a Triple-Axis Spectrometer*, Cambridge University Press, Cambridge (2002).

[39] T. G. Perring, R. A. Ewings, and J. V. Duijn, 'Horace,' `http://horace.isis.rl.ac.uk/` (2013).

[40] T. G. Perring and *et al.*, 'Tobyfit,' `http://tobyfit.isis.rl.ac.uk/` (2012).

[41] C. G. Windsor, *Pulsed Neutron Scattering*, Taylor & Francis, London (1981).

[42] D. A. Tennant and D. F. McMorrow, 'Rescal,' `http://www.ill.eu/en/instruments-support/computing-for-science/cs-software/all-software/matlab-ill/rescal-for-matlab/` (1995).

[43] J. Šaroun and J. Kulda, 'Restrax,' `http://neutron.ujf.cas.cz/restrax/` (2012).

[44] S. J. B. Reed, *Electron microprobe analysis*, 2nd edn., Cambridge University Press, Cambridge (1993).

[45] J. Rodriguez-Carvajal, 'Recent advances in magnetic-structure determination by neutron powder diffraction,' *Physica B-Condensed Matter* **192**, 55 (1993).

[46] M. Arai, T. Nishijima, Y. Endoh, T. Egami, S. Tajima, K. Tomimoto, Y. Shiohara, M. Takahashi, A. Garrett, and S. M. Bennington, 'Incommensurate spin dynamics of underdoped superconductor $YBa_2Cu_3O_{6.7}$,' *Phys. Rev. Lett.* **83**, 608 (1999).

[47] P. Bourges, Y. Sidis, H. F. Fong, L. P. Regnault, J. Bossy, A. Ivanov, and B. Keimer, 'The spin excitation spectrum in superconducting $YBa_2Cu_3O_{6.85}$,' *Science* **288**, 1234 (2000).

[48] J. M. Tranquada, H. Woo, T. G. Perring, H. Goka, G. D. Gu, G. Xu, M. Fujita, and K. Yamada, 'Quantum magnetic excitations from stripes in copper oxide superconductors,' *Nature* **429**, 534 (2004).

[49] S. M. Hayden, H. A. Mook, P. C. Dai, T. G. Perring, and F. Dogan, 'The structure of the high-energy spin excitations in a high-transition-temperature superconductor,' *Nature* **429**, 531 (2004).

[50] V. Hinkov, S. Pailhes, P. Bourges, Y. Sidis, A. Ivanov, A. Kulakov, C. T. Lin, D. P. Chen, C. Bernhard, and B. Keimer, 'Two-dimensional geometry of spin excitations in the high-transition-temperature superconductor $YBa_2Cu_3O_{6+x}$,' *Nature* **430**, 650 (2004).

[51] D. Reznik, P. Bourges, L. Pintschovius, Y. Endoh, Y. Sidis, T. Masui, and S. Tajima, 'Dispersion of magnetic excitations in optimally doped superconducting $YBa_2Cu_3O_{6.95}$,' *Phys. Rev. Lett.* **93**, 207003 (2004).

[52] N. B. Christensen, D. F. McMorrow, H. M. Ronnow, B. Lake, S. M. Hayden, G. Aeppli, T. G. Perring, M. Mangkorntong, M. Nohara, and H. Takagi, 'Dispersive excitations in the high-temperature superconductor $La_{2-x}Sr_xCuO_4$,' *Phys. Rev. Lett.* **93**, 147002 (2004).

[53] C. Stock, W. J. L. Buyers, R. A. Cowley, P. S. Clegg, R. Coldea, C. D. Frost, R. Liang, D. Peets, D. Bonn, W. N. Hardy, and R. J. Birgeneau, 'From incommensurate to dispersive spin-fluctuations: The high-energy inelastic spectrum in superconducting $YBa_2Cu_3O_{6.5}$,' *Phys. Rev. B* **71**, 024522 (2005).

[54] O. J. Lipscombe, S. M. Hayden, B. Vignolle, D. F. McMorrow, and T. G. Perring, 'Persistence of high-frequency spin fluctuations in overdoped superconducting $La_{2-x}Sr_xCuO_4$ ($x = 0.22$),' *Phys. Rev. Lett.* **99**, 067002 (2007).

[55] M. Matsuda, M. Fujita, S. Wakimoto, J. A. Fernandez-Baca, J. M. Tranquada, and K. Yamada, 'Magnetic dispersion of the diagonal incommensurate phase in lightly doped $La_{2-x}Sr_xCuO_4$,' *Phys. Rev. Lett.* **101**, 197001 (2008).

[56] G. Y. Xu, G. D. Gu, M. Hucker, B. Fauque, T. G. Perring, L. P. Regnault, and J. M. Tranquada, 'Testing the itinerancy of spin dynamics in superconducting $Bi_2Sr_2CaCu_2O_{8+\delta}$,' *Nature Phys.* **5**, 642 (2009).

[57] A. T. Boothroyd, P. Babkevich, D. Prabhakaran, and P. G. Freeman, 'An hour-glass magnetic spectrum in an insulating, hole-doped antiferromagnet,' *Nature* **471**, 341 (2011).

[58] Y. Drees, D. Lamago, A. Piovano, and A. C. Komarek, 'Hour-glass magnetic spectrum in a stripeless insulating transition metal oxide,' *Nat. Commun.* **4**, 2449 (2013).

[59] H. Ulbrich, P. Steffens, D. Lamago, Y. Sidis, and M. Braden, 'Hourglass dispersion in overdoped single-layered manganites,' *Phys. Rev. Lett.* **108**, 247209 (2012).

[60] M. Fujita, H. Goka, K. Yamada, J. M. Tranquada, and L. P. Regnault, 'Stripe order, depinning, and fluctuations in $La_{1.875}Ba_{0.125}CuO_4$ and $La_{1.875}Ba_{0.075}Sr_{0.050}CuO_4$,' *Phys. Rev. B* **70**, 104517 (2004).

[61] J. M. Tranquada, B. J. Sternlieb, J. D. Axe, Y. Nakamura, and S. Uchida, 'Evidence for stripe correlations of spins and holes in copper-oxide superconductors,' *Nature* **375**, 561 (1995).

[62] C. H. Chen, S. W. Cheong, and A. S. Cooper, 'Charge modulations in $La_{2-x}Sr_xNiO_{4+y}$ – ordering of polarons,' *Phys. Rev. Lett.* **71**, 152461 (1993).

[63] J. M. Tranquada, D. J. Buttrey, V. Sachan, and J. E. Lorenzo, 'Simultaneous ordering of holes and spins in $La_2NiO_{4.125}$,' *Phys. Rev. Lett.* **73**, 1003 (1994).

[64] H. Yoshizawa, T. Kakeshita, R. Kajimoto, T. Tanabe, T. Katsufuji, and Y. Tokura, 'Stripe order at low temperatures in $La_{2-x}Sr_xNiO_4$ with $0.289 \lesssim x \lesssim 0.5$,' *Phys. Rev. B* **61**, R854 (2000).

[65] H. Ulbrich, D. Senff, P. Steffens, O. J. Schumann, Y. Sidis, P. Reutler, A. Revcolevschi, and M. Braden, 'Evidence for charge orbital and spin stripe order in an overdoped manganite,' *Phys. Rev. Lett.* **106**, 157201 (2011).

[66] M. Cwik, M. Benomar, T. Finger, Y. Sidis, D. Senff, M. Reuther, T. Lorenz, and M. Braden, 'Magnetic correlations in $La_{2-x}Sr_xCoO_4$ studied by neutron scattering: Possible evidence for stripe phases,' *Phys. Rev. Lett.* **102**, 057201 (2009).

[67] F. C. Chou, N. R. Belk, M. A. Kastner, R. J. Birgeneau, and A. Aharony, 'Spin-glass behavior in $La_{1.96}Sr_{0.04}CuO_4$,' *Phys. Rev. Lett.* **75**, 112204 (1995).

[68] P. G. Freeman, A. T. Boothroyd, D. Prabhakaran, and J. Lorenzana, 'Magnetization of $La_{2-x}Sr_xNiO_{4+\delta}$ ($0 \leq x \leq 0.5$): Spin-glass and memory effects,' *Phys. Rev. B* **73**, 014434 (2006).

[69] T. Lancaster, S. R. Giblin, G. Allodi, S. Bordignon, M. Mazzani, R. De Renzi, P. G. Freeman, P. J. Baker, F. L. Pratt, P. Babkevich, S. J. Blundell, A. T. Boothroyd, J. S. Moeller, and D. Prabhakaran, 'Stripe disorder and dynamics in the hole-doped antiferromagnetic insulator $La_{5/3}Sr_{1/3}CoO_4$,' *Phys. Rev. B* **89**, 020405 (2013).

[70] E. C. Andrade and M. Vojta, 'Disorder, cluster spin glass, and hourglass spectra in striped magnetic insulators,' *Phys. Rev. Lett.* **109**, 147201 (2012).

[71] N. Hollmann, M. W. Haverkort, M. Cwik, M. Benomar, M. Reuther, A. Tanaka, and T. Lorenz, 'Anisotropic susceptibility of $La_{2-x}Sr_xCoO_4$ related to the spin states of cobalt,' *New J. Phys.* **10**, 023018 (2008).

[72] I. A. Zaliznyak, J. P. Hill, J. M. Tranquada, R. Erwin, and Y. Moritomo, 'Independent freezing of charge and spin dynamics in $La_{1.5}Sr_{0.5}CoO_4$,' *Phys. Rev. Lett.* **85**, 204353 (2000).

[73] L. M. Helme, A. T. Boothroyd, R. Coldea, D. Prabhakaran, C. D. Frost, D. A. Keen, L. P. Regnault, P. G. Freeman, M. Enderle, and J. Kulda, 'Magnetic order and dynamics of the charge-ordered antiferromagnet $La_{1.5}Sr_{0.5}CoO_4$,' *Phys. Rev. B* **80**, 134414 (2009).

[74] H. Ulbrich and M. Braden, 'Neutron scattering studies on stripe phases in non-cuprate materials,' *Physica C* **481**, 31 (2012).

[75] P. Babkevich, D. Prabhakaran, C. D. Frost, and A. T. Boothroyd, 'Magnetic spectrum of the two-dimensional antiferromagnet La_2CoO_4 studied by inelastic neutron scattering,' *Phys. Rev. B* **82**, 184425 (2010).

[76] A. T. Boothroyd, D. Prabhakaran, P. G. Freeman, S. J. S. Lister, M. Enderle, A. Hiess, and J. Kulda, 'Spin dynamics in stripe-ordered $La_{5/3}Sr_{1/3}NiO_4$,' *Phys. Rev. B* **67**, 100407(R) (2003).

[77] H. J. Woo, A. T. Boothroyd, K. Nakajima, T. G. Perring, C. D. Frost, P. G. Freeman, D. Prabhakaran, K. Yamada, and J. M. Tranquada, 'Mapping spin-wave dispersions in stripe-ordered $La_{2-x}Sr_xNiO_4$ ($x = 0.275$, 0.333),' *Phys. Rev. B* **72**, 064437 (2005).

[78] J. D. Jorgensen, B. Dabrowski, S. Y. Pei, D. G. Hinks, L. Soderholm, B. Morosin, J. E. Schirber, E. L. Venturini, and D. S. Ginley, 'Superconducting phase of $La_2CuO_{4+\delta}$ – a superconducting composition resulting from phase-separation,' *Phys. Rev. B* **38**, 11337 (1988).

[79] D. E. Rice and D. J. Buttrey, 'An X-ray-diffraction study of the oxygen-content phase-diagram of $La_2NiO_{4+\delta}$,' *J. Solid State Chem.* **105**, 197 (1993).

[80] S. M. Gaw, E. C. Andrade, M. Vojta, C. D. Frost, D. T. Adroja, D. Prabhakaran, and A. T. Boothroyd, 'Hour-glass magnetic spectrum arising from a striped cluster spin-glass ground state in $La_{1.75}Sr_{0.25}CoO_4$,' *Phys. Rev. B* **88**, 165121 (2013).

[81] K. H. Fischer and J. A. Hertz, *Spin Glasses*, Cambridge University Press, Cambridge (1991).

[82] I. A. Campbell, 'Critical exponents of spin-glass systems,' *Phys. Rev. B* **37**, 169800 (1988).

[83] P. Babkevich, *Quantum Materials Explored by Neutron Scattering*, D.Phil. Thesis, University of Oxford and Paul Scherrer Institute (2012).

[84] B. N. Brockhouse, 'Antiferromagnetism in cupric oxide,' *Phys. Rev.* **94**, 781 (1954).

[85] B. X. Yang, T. R. Thurston, J. M. Tranquada, and G. Shirane, 'Magnetic neutron-scattering study of single-crystal cupric oxide,' *Phys. Rev. B* **39**, 4343 (1989).

[86] M. Ain, W. Reichardt, B. Hennion, G. Pepy, and B. M. Wanklyn, 'Magnetic excitations in CuO,' *Physica C* **162**, 1279 (1989).

[87] T. Kimura, Y. Sekio, H. Nakamura, T. Siegrist, and A. P. Ramirez, 'Cupric oxide as an induced-multiferroic with high-T_c,' *Nat. Mater.* **7**, 291 (2008).

[88] P. Babkevich, A. Poole, R. D. Johnson, B. Roessli, D. Prabhakaran, and A. T. Boothroyd, 'Electric field control of chiral magnetic domains in the high-temperature multiferroic CuO,' *Phys. Rev. B* **85**, 134428 (2012).

[89] G. Giovannetti, S. Kumar, A. Stroppa, J. van den Brink, S. Picozzi, and J. Lorenzana, 'High-T_c ferroelectricity emerging from magnetic degeneracy in cupric oxide,' *Phys. Rev. Lett.* **106**, 026401 (2011).

[90] P. Tolédano, N. Leo, D. D. Khalyavin, L. C. Chapon, T. Hoffmann, D. Meier, and M. Fiebig, 'Theory of high-temperature multiferroicity in cupric oxide,' *Phys. Rev. Lett.* **106**, 257601 (2011).

[91] G. X. Jin, K. Cao, G. C. Guo, and L. X. He, 'Origin of ferroelectricity in high-T_c magnetic ferroelectric CuO,' *Phys. Rev. Lett.* **108**, 187205 (2012).

[92] S. Asbrink and L. J. Norrby, 'A refinement of crystal structure of copper(II) oxide with a discussion of some exceptional E.s.d.'s,' *Acta Cryst.* **B26**, 8 (1970).

[93] J. B. Forsyth, P. J. Brown, and B. M. Wanklyn, 'Magnetism in cupric oxide,' *J. Phys. C: Solid State Phys.* **21**, 2917 (1988).

[94] P. J. Brown, T. Chattopadhyay, J. B. Forsyth, V. Nunez, and F. Tasset, 'Antiferromagnetism in CuO studied by neutron polarimetry,' *J. Phys. Condens. Matter* **3**, 4281 (1991).

[95] M. Ain, A. Menelle, B. M. Wanklyn, and E. F. Bertaut, 'Magnetic-structure of CuO by neutron-diffraction with polarization analysis,' *J. Phys. Condens. Matter* **4**, 5327 (1992).

[96] R. Villarreal, G. Quirion, M. L. Plumer, M. Poirier, T. Usui, and T. Kimura, 'Magnetic phase diagram of CuO via high-resolution ultrasonic velocity measurements,' *Phys. Rev. Lett.* **109**, 167206 (2012).

[97] A. Rebello, Z. C. M. Winter, S. Viall, and J. J. Neumeier, 'Multiple phase transitions in CuO observed with thermal expansion,' *Phys. Rev. B* **88**, 094420 (2013).

[98] M. O'Keefe and F. S. Stone, 'The magnetic suscepticility of cupric oxide,' *J. Phys. Chem. Solids* **23**, 261 (1962).

[99] M. Steiner, J. Villain, and C. G. Windsor, 'Theoretical and experimental studies on one-dimensional magnetic systems,' *Adv. Phys.* **25**, 87 (1976).

[100] T. Shimizu, T. Matsumoto, A. Goto, T. V. C. Rao, K. Yoshimura, and K. Kosuge, 'Spin susceptibility and superexchange interaction in the antiferromagnet CuO,' *Phys. Rev. B* **68**, 224433 (2003).

[101] A. T. Boothroyd, A. Mukherjee, S. Fulton, T. G. Perring, R. S. Eccleston, H. A. Mook, and B. M. Wanklyn, 'High-energy magnetic excitations in CuO,' *Physica B* **234**, 731 (1997).

[102] G. Muller, H. Thomas, H. Beck, and J. C. Bonner, 'Quantum spin dynamics of the anti-ferromagnetic linear-chain in zero and nonzero magnetic-field,' *Phys. Rev. B* **24**, 1429 (1981).

[103] F. Wang, T. Zou, Y. Liu, L. Q. Yan, and Y. Sun, 'Persistent multiferroicity without magnetoelectric effects in CuO,' *J. Appl. Phys.* **110**, 054106 (2011).

[104] T. Kimura, T. Goto, H. Shintani, K. Ishizaka, T. Arima, and Y. Tokura, 'Magnetic control of ferroelectric polarization,' *Nature* **426**, 55 (2003).

[105] G. Lawes, A. B. Harris, T. Kimura, N. Rogado, R. J. Cava, A. Aharony, O. Entin-Wohlman, T. Yildirim, M. Kenzelmann, C. Broholm, and A. P. Ramirez, 'Magnetically driven ferroelectric order in $Ni_3V_2O_8$,' *Phys. Rev. Lett.* **95**, 087205 (2005).

[106] K. Taniguchi, N. Abe, T. Takenobu, Y. Iwasa, and T. Arima, 'Ferroelectric polarization flop in a frustrated magnet $MnWO_4$ induced by a magnetic field,' *Phys. Rev. Lett.* **97**, 097203 (2006).

[107] D. Prabhakaran and A. T. Boothroyd, 'Single crystal growth of Zn-doped CuO by the floating-zone method,' *J. Cryst. Growth* **250**, 77 (2003).

[108] X. G. Zheng, C. N. Xu, E. Tanaka, Y. Tomokiyo, H. Yamada, Y. Soejima, Y. Yamamura, and T. Tsuji, 'Evidence of charge stripes, charge-spin-orbital coupling and phase transition in a simple copper oxide CuO,' *J. Phys. Soc. Jpn* **70**, 1054 (2001).

[109] B. X. Yang, J. M. Tranquada, and G. Shirane, 'Neutron-scattering studies of the magnetic-structure of cupric oxide,' *Phys. Rev. B* **38**, 174 (1988).

[110] H. J. Schulz, 'Dynamics of coupled quantum spin chains,' *Phys. Rev. Lett.* **77**, 2790 (1996).

[111] F. H. L. Essler, A. M. Tsvelik, and G. Delfino, 'Quasi-one-dimensional spin-1/2 heisenberg magnets in their ordered phase: Correlation functions,' *Phys. Rev. B* **56**, 11001 (1997).

[112] B. Lake, D. A. Tennant, and S. E. Nagler, 'Longitudinal magnetic dynamics and dimensional crossover in the quasi-one-dimensional spin-1/2 heisenberg antiferromagnet $KCuF_3$,' *Phys. Rev. B* **71**, 134412 (2005).

[113] F. Ye, J. A. Fernandez-Baca, R. S. Fishman, Y. Ren, H. J. Kang, Y. Qiu, and T. Kimura, 'Magnetic interactions in the geometrically frustrated triangular lattice antiferromagnet $CuFeO_2$,' *Phys. Rev. Lett.* **99**, 157201 (2007).

[114] H. J. Lewtas, A. T. Boothroyd, M. Rotter, D. Prabhakaran, H. Muller, M. D. Le, B. Roessli, J. Gavilano, and P. Bourges, 'Magnetic excitations in multiferroic $LuMnO_3$ studied by inelastic neutron scattering,' *Phys. Rev. B* **82**, 184420 (2010).

[115] J. Jeong, E. A. Goremychkin, T. Guidi, K. Nakajima, G. S. Jeon, S. A. Kim, S. Furukawa, Y. B. Kim, S. Lee, V. Kiryukhin, S. W. Cheong, and J. G. Park, 'Spin wave measurements over the full brillouin zone of multiferroic $BiFeO_3$,' *Phys. Rev. Lett.* **108**, 077202 (2012).

[116] A. Filippetti and V. Fiorentini, 'Magnetic ordering in CuO from first principles: A cuprate antiferromagnet with fully three-dimensional exchange interactions,' *Phys. Rev. Lett.* **95**, 086405 (2005).

[117] X. Rocquefelte, M. H. Whangbo, A. Villesuzanne, S. Jobic, F. Tran, K. Schwarz, and P. Blaha, 'Short-range magnetic order and temperature-dependent properties of cupric oxide,' *J. Phys.: Condens. Matter* **22**, 045502 (2010).

[118] A. M. Pradipto, R. Maurice, N. Guihery, C. de Graaf, and R. Broer, 'First-principles study of magnetic interactions in cupric oxide,' *Phys. Rev. B* **85**, 014409 (2012).

[119] R. M. White, M. Sparks, and Ortenbur.I, 'Diagonalization of antiferromagnetic magnon-phonon interaction,' *Phys. Rev.* **139**, A450 (1965).

[120] S. E. Nagler, D. A. Tennant, R. A. Cowley, T. G. Perring, and S. K. Satija, 'Spin dynamics in the quantum antiferromagnetic chain compound $KCuF_3$,' *Phys. Rev. B* **44**, 12361 (1991).

[121] D. A. Tennant, R. A. Cowley, S. E. Nagler, and A. M. Tsvelik, 'Measurement of the spin-excitation continuum in one-dimensional $KCuF_3$ using neutron-scattering,' *Phys. Rev. B* **52**, 13368 (1995).

[122] I. A. Zaliznyak, H. Woo, T. G. Perring, C. L. Broholm, C. D. Frost, and H. Takagi, 'Spinons in the strongly correlated copper oxide chains in $SrCuO_2$,' *Phys. Rev. Lett.* **93**, 087202 (2004).

[123] B. Lake, D. A. Tennant, C. D. Frost, and S. E. Nagler, 'Quantum criticality and universal scaling of a quantum antiferromagnet,' *Nat. Mater.* **4**, 329 (2005).

[124] A. C. Walters, T. G. Perring, J. S. Caux, A. T. Savici, G. D. Gu, C. C. Lee, W. Ku, and I. A. Zaliznyak, 'Effect of covalent bonding on magnetism and the missing neutron intensity in copper oxide compounds,' *Nat. Phys.* **5**, 867 (2009).

[125] B. Lake, D. A. Tennant, J. S. Caux, T. Barthel, U. Schollwock, S. E. Nagler, and C. D. Frost, 'Multispinon continua at zero and finite temperature in a near-ideal heisenberg chain,' *Phys. Rev. Lett.* **111**, 137205 (2013).

[126] R. Coldea, S. M. Hayden, G. Aeppli, T. G. Perring, C. D. Frost, T. E. Mason, S. W. Cheong, and Z. Fisk, 'Spin waves and electronic interactions in La_2CuO_4,' *Phys. Rev. Lett.* **86**, 5377 (2001).

[127] H. M. Ronnow, D. F. McMorrow, R. Coldea, A. Harrison, I. D. Youngson, T. G. Perring, G. Aeppli, O. Syljuasen, K. Lefmann, and C. Rischel, 'Spin dynamics of the 2D spin 1/2 quantum antiferromagnet copper deuteroformate tetradeuterate (CFTD),' *Phys. Rev. Lett.* **87**, 037202 (2001).

[128] A. B. Kuz'menko, D. van der Marel, P. J. M. van Bentum, E. A. Tishchenko, C. Presura, and A. A. Bush, 'Infrared spectroscopic study of CuO: Signatures of strong spin-phonon interaction and structural distortion,' *Phys. Rev. B* **63**, 094303 (2001).

[129] K. Y. Choi, W. J. Lee, A. Glamazda, P. Lemmens, D. Wulferding, Y. Sekio, and T. Kimura, 'Competing lattice fluctuations and magnetic excitations in CuO,' *Phys. Rev. B* **87**, 184407 (2013).

[130] D. A. Yablonskii, 'Mean-field theory of magnetic order in cupric oxide,' *Physica C* **171**, 454 (1990).

[131] K. Pasrija and S. Kumar, 'High-temperature noncollinear magnetism in a classical bilinear-biquadratic heisenberg model,' *Phys. Rev. B* **88**, 144418 (2013).

[132] S. P. P. Jones, S. M. Gaw, K. I. Doig, D. Prabhakaran, E. M. Hétroy Wheeler, A. T. Boothroyd, and J. Lloyd-Hughes, 'High-temperature electromagnons in the magnetically induced multiferroic cupric oxide driven by intersublattice exchange,' *Nat. Comm.* (2014).

[133] M. Isobe, N. Kimizuka, J. Iida, and S. Takekawa, 'Structures of lufecoo4 and $LuFe_2O_4$,' *Acta Cryst.* **C46**, 1917 (1990).

[134] Y. Zhang, H. X. Yang, C. Ma, H. F. Tian, and J. Q. Li, 'Charge-stripe order in the electronic ferroelectric $LuFe_2O_4$,' *Phys. Rev. Lett.* **98**, 247602 (2007).

[135] A. D. Christianson, M. D. Lumsden, M. Angst, Z. Yamani, W. Tian, R. Jin, E. A. Payzant, S. E. Nagler, B. C. Sales, and D. Mandrus, 'Three-dimensional magnetic correlations in multiferroic $LuFe_2O_4$,' *Phys. Rev. Lett.* **100**, 107601 (2008).

[136] X. S. Xu, M. Angst, T. V. Brinzari, R. P. Hermann, J. L. Musfeldt, A. D. Christianson, D. Mandrus, B. C. Sales, S. McGill, J. W. Kim, and Z. Islam, 'Charge order, dynamics, and magnetostructural transition in multiferroic $LuFe_2O_4$,' *Phys. Rev. Lett.* **101**, 227602 (2008).

[137] Y. Yamada, K. Kitsuda, S. Nohdo, and N. Ikeda, 'Charge and spin ordering process in the mixed-valence system $LuFe_2O_4$: Charge ordering,' *Phys. Rev. B* **62**, 12167 (2000).

[138] M. Angst, R. P. Hermann, A. D. Christianson, M. D. Lumsden, C. Lee, M. H. Whangbo, J. W. Kim, P. J. Ryan, S. E. Nagler, W. Tian, R. Jin, B. C. Sales, and D. Mandrus, 'Charge order in $LuFe_2O_4$: Antiferroelectric ground state and coupling to magnetism,' *Phys. Rev. Lett.* **101**, 227601 (2008).

[139] N. Ikeda, H. Ohsumi, K. Ohwada, K. Ishii, T. Inami, K. Kakurai, Y. Murakami, K. Yoshii, S. Mori, Y. Horibe, and H. Kito, 'Ferroelectricity from iron valence ordering in the charge-frustrated system $LuFe_2O_4$,' *Nature* **436**, 1136 (2005).

[140] X. S. Xu, J. de Groot, Q. C. Sun, B. C. Sales, D. Mandrus, M. Angst, A. P. Litvinchuk, and J. L. Musfeldt, 'Lattice dynamical probe of charge order and antipolar bilayer stacking in $LuFe_2O_4$,' *Phys. Rev. B* **82**, 014304 (2010).

[141] J. de Groot, T. Mueller, R. A. Rosenberg, D. J. Keavney, Z. Islam, J. W. Kim, and M. Angst, 'Charge order in $LuFe_2O_4$: An unlikely route to ferroelectricity,' *Phys. Rev. Lett.* **108**, 187601 (2012).

[142] F. M. Vitucci, A. Nucara, D. Nicoletti, Y. Sun, C. H. Li, J. C. Soret, U. Schade, and P. Calvani, 'Infrared study of the charge-ordered multiferroic $LuFe_2O_4$,' *Phys. Rev. B* **81**, 195121 (2010).

[143] J. Bourgeois, M. Hervieu, M. Poienar, A. M. Abakumov, E. Elkaim, M. T. Sougrati, F. Porcher, F. Damay, J. Rouquette, G. Van Tendeloo, A. Maignan, J. Haines, and C. Martin, 'Evidence of oxygen-dependent modulation in $LuFe_2O_4$,' *Phys. Rev. B* **85**, 064102 (2012).

[144] H. J. Lewtas, *A Muon and Neutron Study of Multiferroic Materials*, D.Phil. Thesis, University of Oxford (2010).

[145] J. Iida, M. Tanaka, Y. Nakagawa, S. Funahashi, N. Kimizuka, and S. Takekawa, 'Magnetization and spin correlation of 2-dimensional triangular antiferromagnet $LuFe_2O_4$,' *J. Phys. Soc. Jpn.* **62**, 1723 (1993).

[146] K. T. Ko, H. J. Noh, J. Y. Kim, B. G. Park, J. H. Park, A. Tanaka, S. B. Kim, C. L. Zhang, and S. W. Cheong, 'Electronic origin of giant magnetic anisotropy in multiferroic $LuFe_2O_4$,' *Phys. Rev. Lett.* **103**, 207202 (2009).

[147] K. Kuepper, M. Raekers, C. Taubitz, M. Prinz, C. Derks, M. Neumann, A. V. Postnikov, F. M. F. de Groot, C. Piamonteze, D. Prabhakaran, and S. J. Blundell, 'Charge order, enhanced orbital moment, and absence of magnetic frustration in layered multiferroic $LuFe_2O_4$,' *Phys. Rev. B* **80**, 220409(R) (2009).

[148] J. Bourgeois, G. Andre, S. Petit, J. Robert, M. Poienar, J. Rouquette, E. Elkaim, M. Hervieu, A. Maignan, C. Martin, and F. Damay, 'Evidence of magnetic phase separation in $LuFe_2O_4$,' *Phys. Rev. B* **86**, 024413 (2012).

[149] M. Angst, 'Ferroelectricity from iron valence ordering in rare earth ferrites?' *Phys. Status Solidi* **7** (2013).

[150] J. de Groot, K. Marty, M. D. Lumsden, A. D. Christianson, S. E. Nagler, S. Adiga, W. J. H. Borghols, K. Schmalzl, Z. Yamani, S. R. Bland, R. de Souza, U. Staub, W. Schweika, Y. Su, and M. Angst, 'Competing ferri- and antiferromagnetic phases in geometrically frustrated $LuFe_2O_4$,' *Phys. Rev. Lett.* **108**, 037206 (2012).

[151] W. Wu, V. Kiryukhin, H. J. Noh, K. T. Ko, J. H. Park, W. Ratcliff, P. A. Sharma, N. Harrison, Y. J. Choi, Y. Horibe, S. Lee, S. Park, H. T. Yi, C. L. Zhang, and S. W. Cheong, 'Formation of pancakelike ising domains and giant magnetic coercivity in ferrimagnetic $LuFe_2O_4$,' *Phys. Rev. Lett.* **101**, 137203 (2008).

[152] F. Wang, J. Kim, Y. J. Kim, and G. D. Gu, 'Spin-glass behavior in $LuFe_2O_{4+\delta}$,' *Phys. Rev. B* **80**, 024419 (2009).

[153] F. Wang, J. Kim, G. D. Gu, Y. Lee, S. Bae, and Y. J. Kim, 'Oxygen stoichiometry and magnetic properties of $LuFe_2O_{4+\delta}$,' *J. Appl. Phys.* **113**, 063909 (2013).

[154] M. A. Subramanian, T. He, J. Z. Chen, N. S. Rogado, T. G. Calvarese, and A. W. Sleight, 'Giant room-temperature magnetodielectric response in the electronic ferroelectric $LuFe_2O_4$,' *Adv. Mater.* **18**, 1737 (2006).

[155] A. Ruff, S. Krohns, F. Schrettle, V. Tsurkan, P. Lunkenheimer, and A. Loidl, 'Absence of polar order in $LuFe_2O_4$,' *EPJ B* **85**, 290 (2012).

[156] P. Ren, Z. Yang, W. G. Zhu, C. H. A. Huan, and L. Wang, 'Origin of the colossal dielectric permittivity and magnetocapacitance in $LuFe_2O_4$,' *J. Appl. Phys.* **109**, 074109 (2011).

[157] D. Niermann, F. Waschkowski, J. de Groot, M. Angst, and J. Hemberger, 'Dielectric properties of charge-ordered $LuFe_2O_4$ revisited: The apparent influence of contacts,' *Phys. Rev. Lett.* **109**, 016405 (2012).

[158] M. Mekata, 'Antiferro-ferrimagnetic transition in triangular ising lattice,' *J. Phys. Soc. Jpn* **42**, 76 (1977).

[159] A. Nagano, M. Naka, J. Nasu, and S. Ishihara, 'Electric polarization, magnetoelectric effect, and orbital state of a layered iron oxide with frustrated geometry,' *Phys. Rev. Lett.* **99**, 217202 (2007).

[160] H. J. Xiang, E. J. Kan, S. H. Wei, M. H. Whangbo, and J. L. Yang, 'Origin of the ising ferrimagnetism and spin-charge coupling in $LuFe_2O_4$,' *Phys. Rev. B* **80**, 132408 (2009).

[161] J. Y. Park, J. H. Park, Y. K. Jeong, and H. M. Jang, 'Dynamic magnetoelectric coupling in "electronic ferroelectric" $LuFe_2O_4$,' *Appl. Phys. Lett.* **91**, 152903 (2007).

[162] M. H. Phan, N. A. Frey, M. Angst, J. de Groot, B. C. Sales, D. G. Mandrus, and H. Srikanth, 'Complex magnetic phases in $LuFe_2O_4$,' *Solid State Commun.* **150**, 341 (2010).

[163] F. Wang, C. H. Li, T. Zou, Y. Liu, and Y. Sun, 'Electrically driven magnetic relaxation in multiferroic $LuFe_2O_4$,' *J. Phys. Condens. Mat.* **22**, 496001 (2010).

[164] R. Coldea, SPINWAVE_DISPERSIONS.M, program (2013).

[165] P. R. Bevington and D. K. Robinson, *Data Reduction and Error Analysis for the Physical Sciences*, 3rd edn., McGraw Hill, New York (2003).

[166] G. T. Rado and H. Suhl, *Magnetism*, vol. 1, Academic Press Inc., London, UK (1963).

[167] C. Kittel, *Quantum Theory of Solids*, 2nd edn., Wiley, New York (1987).

[168] E. M. Wheeler, R. Coldea, E. Wawrzyńska, T. Sörgel, M. Jansen, M. M. Koza, J. Taylor, P. Adroguer, and N. Shannon, 'Spin dynamics of the frustrated easy-axis triangular antiferromagnet $2H$-$AgNiO_2$ explored by inelastic neutron scattering,' *Phys. Rev. B* **79**, 104421 (2009).